JSCSEN 91(10)981-1111(2026)

ISSN 1820-7421(Online)

Journal of the Serbian Chemical Society

Electronic version

VOLUME 91

No 10

BELGRADE 2026

Available on line at

www.shd.org.rs/JSCS/

The full search of JSCS is available through

DOAJ DIRECTORY OF OPEN ACCESS JOURNALS

www.doaj.org

The **Journal of the Serbian Chemical Society** (formerly Glasnik Hemijskog društva Beograd), one volume (12 issues) per year, publishes articles from the fields of chemistry. The **Journal** is financially supported by the **Ministry of Science, Technological Development and Innovation of the Republic of Serbia.**
Articles published in the **Journal** are indexed in **Clarivate Analytics products: Science Citation Index-Expanded™** – accessed *via* **Web of Science®** and **Journal Citation Reports®**.
Impact Factor announced for the year 2024: **0.700; 5-year Impact Factor**: **0.900**.
Articles appearing in the **Journal** are also abstracted by: **Scopus, Chemical Abstracts Plus (CAplus℠), Directory of Open Access Journals, Referativnii Zhurnal (VINITI), RSC Analytical Abstracts, EuroPub, Pro Quest** and **Asian Digital Library.**

Publisher:	**Serbian Chemical Society**, Karnegijeva 4/III, P. O. Box 36, 1120 Belgrade 35, Serbia tel./fax: +381–11–3370–467, E-mails: **Society** – shd@shd.org.rs; **Journal** – jscs@shd.org.rs Home Pages: **Society** – http://www.shd.org.rs/, **Journal** – http://www.shd.org.rs/JSCS/
Internet Service:	Contents, Abstracts and full papers (from Vol. 64, No. 1, 1999) are available in the electronic form at the Web Site of the **Journal** (http://www.shd.org.rs/JSCS/).
Former Editors:	**Nikola A. Pušin** (1930–1947), **Aleksandar M. Leko** (1948–1954), **Panta S. Tutundžić** (1955–1961), **Miloš K. Mladenović** (1962–1964), **Đorđe M. Dimitrijević** (1965–1969), **Aleksandar R. Despić** (1969–1975), **Slobodan V. Ribnikar** (1975–1985), **Dragutin M. Dražić** (1986–2006), **Branislav Ž. Nikolić** (2006-2026).
Editor-in-Chief:	DUŠAN **SLADIĆ**, Faculty of Chemistry, University of Belgrade
Deputy Editors:	MARIO **ZLATOVIĆ**, Faculty of Chemistry, University of Belgrade, VLADIMIR **PANIĆ**, Institute of Chemistry, Technology and Metallurgy, University of Belgrade
Sub editors:	
,	
Organic Chemistry	DEJAN **OPSENICA**, Institute of Chemistry, Technology and Metallurgy, University of Belgrade
	JÁNOS **CSANÁDI**, Faculty of Science, University of Novi Sad
Biochemistry and Biotechnology	OLGICA **NEDIĆ**, INEP – Institute for the Application of Nuclear Energy, University of Belgrade
Inorganic Chemistry	BILJANA **GLIŠIĆ**, Faculty of Science, University of Kragujevac
Theoretical Chemistry	MATIJA **ZLATAR**, Institute of Chemistry, Technology and Metallurgy, University of Belgrade
	MILOŠ **MILIČIĆ**, Faculty of Chemistry, University of Belgrade
Physical Chemistry	LJILJANA **DAMJANOVIĆ-VASILIĆ**, Faculty of Physical Chemistry, University of Belgrade
Electrochemistry	SNEŽANA **GOJKOVIĆ**, Faculty of Technology and Metallurgy, University of Belgrade
Analytical Chemistry	RADA **BAOŠIĆ**, Faculty of Chemistry, University of Belgrade
Polymers	BRANKO **DUNJIĆ**, Faculty of Technology and Metallurgy, University of Belgrade
Thermodynamics	MIRJANA **KIJEVČANIN**, Faculty of Technology and Metallurgy, University of Belgrade
Chemical Engineering	TATJANA **KALUĐEROVIĆ RADOIČIĆ**, Faculty of Technology and Metallurgy, University of Belgrade
Materials	RADA **PETROVIĆ**, Faculty of Technology and Metallurgy, University of Belgrade
Metallic Materials and Metallurgy	ANA **KOSTOV**, Mining and Metallurgy Institute Bor, University of Belgrade
Environmental and Geochemistry	VESNA **ANTIĆ**, Faculty of Agriculture, University of Belgrade
History of and Education in Chemistry	DRAGICA **TRIVIĆ**, Faculty of Chemistry, University of Belgrade
English Language Editors:	VLATKA **VAJS**, Serbian Chemical Society
	MIROSLAV **PAVLOVIĆ**, Institute of Chemistry, Technology and Metallurgy, University of Belgrade
Journal Manager & Web Master:	MARIO **ZLATOVIĆ**, Faculty of Chemistry, University of Belgrade
Office:	VERA **ĆUŠIĆ**, Serbian Chemical Society

Editorial Board

From abroad: **R. Adžić**, Brookhaven National Laboratory (USA); **A. Casini**, University of Groningen (The Netherlands); **G. Cobb**, Baylor University (USA); **D. Douglas**, University of British Columbia (Canada); **G. Inzelt**, Etvos Lorand University (Hungary); **J. Kenny**, University of Perugia (Italy); **Ya. I. Korenman**, Voronezh Academy of Technology (Russian Federation); **M. D. Lechner**, University of Osnabrueck (Germany); **S. Macura**, Mayo Clinic (USA); **M. Spiteller**, INFU, Technical University Dortmund (Germany); **M. Stratakis**, University of Crete (Grecce); **M. Swart**, University de Girona (Cataluna, Spain); **G. Vunjak-Novaković**, Columbia University (USA); **P. Worsfold**, University of Plymouth (UK); **J. Zagal**, Universidad de Santiago de Chile (Chile).

From Serbia: **B. Abramović**, **V. Antić**, **R. Baošić**, **V. Beškoski**, **J. Csanadi**, **Lj. Damjanović-Vasilić**, **A. Dekanski**, **V. Dondur**, **B. Dunjić**, **M. Đuran, B. Glišić, S. Gojković**, **I. Gutman**, **B. Jovančićević**, **I. Juranić**, **T. Kaluđerović Radiočić**, **L. Katsikas**, **M. Kijevčanin**, **A. Kostov**, **V. Leovac**, **S. Milonjić**, **V.B. Mišković-Stanković**, **O. Nedić**, **D. Opsenica**, **V. Panić**, **M. Pavlović**, **M. Petkovska**, **R. Petrović**, **I. Popović**, **B. Radak**, **S. Ražić**, **D. Sladić**, **S. Sovilj**, **S. Šerbanović**, **B. Šolaja**, **Ž. Tešić**, **D. Trivić**, **V. Vajs, M. Zlatović**.

Subscription: The annual subscription rate is **150.00 €** including postage (surface mail) and handling. For Society members from abroad rate is **50.00 €**. For the proforma invoice with the instruction for bank payment contact the Society Office (E-mail: shd@shd.org.rs) or see JSCS Web Site: http://www.shd.org.rs/JSCS/, option Subscription.
Godišnja pretplata: Za članove SHD: **2.500,00 RSD**, za penzionere i studente: **1000,00 RSD**, a za ostale: **3.500,00 RSD**:za organizacije i ustanove: **16.000,00 RSD**. Uplate se vrše na tekući račun Društva: **205-13815-62**, poziv na broj **320**, sa naznakom "pretplata za JSCS".

Nota: Radovi čiji su svi autori članovi SHD prioritetno se publikuju.
Odlukom Odbora za hemiju Republičkog fonda za nauku Srbije, br. 66788/1 od 22.11.1990. godine, koja je kasnije potvrđena odlukom Saveta Fonda, časopis je uvršten u kategoriju međunarodnih časopisa (**M-23**). Takođe, aktom Ministarstva za nauku i tehnologiju Republike Srbije, 413-00-247/2000-01 od 15.06.2000. godine, ovaj časopis je proglašen za publikaciju od posebnog interesa za nauku. **Impact Factor** časopisa objavljen za 2024. godinu je **0,700**, a petogodišnji **Impact Factor 0,900**.

Journal of the Serbian Chemical Society
JSCS-info@shd.org.rs • www.shd.org.rs/JSCS

J. Serb. Chem. Soc. Vol. 91, No. 10 (2026)

CONTENTS*

Organic Chemistry

N. R. Ningsih, *Jumina*, *T. D. Wahyuningsih* and *Y. S. Kurniawan*: Dioleate and trioleate epoxides from palm oil as anticancer agents through *in vitro* and molecular docking studies (Short communication) 981

Inorganic Chemistry

E. L. Tikhonova, *T. D. Bolkhovskaya*, *P. V. Kortikova* and *E. N. Bulanov*: Investigation of the isomorphic P–V substitution in the structure of calcium hydroxyapatite by X-ray and spectral methods 995

Physical Chemistry

C. Liu, *C. Jie*, *J. Yu*, *Y. Guo1*, *F. Li1*, *S. Liu* and *H. Cheng*: Systematic investigation into the physicochemical properties of deep eutectic $AlCl_3$/amide electrolytes with additives 1007

Thermodynamics

H. Bayraktar and *İ. Sezer*: A detailed thermodynamic analysis of a diesel engine at different compression ratios 1025

Materials

G. G. Stanojević, *M. M. Komljenović*, *J. Lj. Petrović* and *R. D. Petrović*: Influence of fly ash fineness on cesium immobilization in geopolymers 1043

Chemical Engineering

A. V. Gasimzade, *V. Kh. Nurullayev* and *R. R. Khalilzade*: Chemical technology aspects of non-equilibrium microwave heating for phase separation in multiphase liquid systems 1059

Metallic Materials and Metallyrgy

M. S. Shaikh, *A. M. Shariff*, *I. Bhatti*, *Abdul Qadeer LagharI*, *A. S. Jatoi*, *Arshad Iqbal*, *G. M. Memon* and *T. Hussain*: Corrosion studies of stainless steel and carbon steel in aqueous solutions of sodium glycinate used for CO_2 capture 1083

Enviromental Chemistry

R. D. Đurović-Pejčev, *Lj. R. Šantrić*, *L. M. Kaluđerović* and *S. B. Radmanović*: Adsorption–desorption behaviour of clomazone in Planosol and Vertisol agricultural soils 1099

Published by the Serbian Chemical Society
Karnegijeva 4/III, P.O. Box 36, 11120 Belgrade, Serbia
Printed by the Faculty of Technology and Metallurgy
Karnegijeva 4, P.O. Box 35-03, 11120 Belgrade, Serbia

* For colored figures in this issue please see electronic version at the Journal Home Page: http://www.shd.org.rs/JSCS/

(CC) 2026 Serbian Chemical Society.

Journal of the Serbian Chemical Society
JSCS-info@shd.org.rs • www.shd.org.rs/JSCS
J. Serb. Chem. Soc. 91 (10) 981–994 (2026)
JSCS–5539
Short communication
Published 23 November, 2026

SHORT COMMUNICATION

Dioleate and trioleate epoxides from palm oil as anticancer agents through *in vitro* and molecular docking studies

NUNUNG RATNA NINGSIH, JUMINA*, TUTIK DWI WAHYUNINGSIH and YEHEZKIEL STEVEN KURNIAWAN

Department of Chemistry, Faculty of Mathematics and Natural Sciences, Universitas Gadjah Mada, Yogyakarta 55281, Indonesia

(Received 7 April, revised 22 May, accepted 7 August 2026)

Abstract: Dioleate and trioleate epoxides were successfully obtained from palm oil through several steps and evaluated as anticancer agent *via in vitro* assays and studies of their binding to the FASN protein. At first, fatty acid methyl esters (FAMEs) were isolated through the transesterification reaction from palm oil. Next, the methyl oleate from FAME was purified through urea inclusion method and then hydrolyzed into oleic acid. The oleic acid was further reacted with 1,2-propanediol and glycerol to produce 1,2-propanediol dioleate (dioleate) and glyceryl-1,2,3-trioleate (trioleate) derivatives, respectively. The dioleate and trioleate compounds were epoxidized with performic acid reagent to yield dioleate and trioleate epoxides, respectively. Trioleate epoxide generated a more potent anticancer activity against T47D and WiDr cancer cells with IC_{50} values of 27.40 and 32.41 mg L^{-1}, respectively. In comparison, the IC_{50} values of dioleate epoxide against T47D and WiDr cancer cells are 35.66 and 38.25 mg L^{-1}. Trioleate epoxide and dioleate epoxide were non-toxic for normal cells with selectivity index values of 9.19–10.87 and 7.60–8.16, respectively. The molecular docking showed that dioleate and trioleate epoxides could inhibit the function of the FASN enzyme with binding affinity values of –27.11 and –27.61 kJ mol^{-1}, respectively.

Keywords: FAME; methyl oleate; epoxidation; selectivity index; FASN.

INTRODUCTION

Cancer has become one of the leading causes of death in the world, whereas the mortality rates of approximately 1 in 9 among men and 1 in 12 among women.[1] Human lifestyles such as smoking, lack of physical activity, and being obese can

* Corresponding author. E-mail: jumina@ugm.ac.id
https://doi.org/10.2298/JSC260407046N

Available online at https://www.shd.org.rs/JSCS/
(CC) 2026 Serbian Chemical Society.

trigger cancer disease.[2] In general, cancer can be treated by chemotherapy, radiotherapy, anti-endocrine therapy, specialized targeted therapy and surgery.[3] Prolonged use of chemotherapeutic agents could cause serious side effects due to longer exposure to normal cells.[4] In addition, around 70–95 % of the population in developing countries use traditional medicine for cancer treatment due to the high cost of modern therapies.[5] Thus, identifying natural compounds that can act as anticancer agents, with low toxicity and side effects, is urgently needed.

Palm oil is a natural product with 99.6 % triglycerides, 0.4 % free fatty acids, and minor ingredients, such as carotenoids, phytosterols and vitamin E.[6] The triglycerides consist of saturated and unsaturated fatty acids.[7] Oleic acid, an unsaturated fatty acid with the highest content in palm oil, around 36.4–41.2 %,[8] can be isolated *via* a transesterification reaction and purified by the urea inclusion complex (UIC) method. The principle of the UIC method is the separation of saturated and unsaturated fatty acids based on their size.[9] The oleic acid can be further modified by epoxidation reaction[9], in which the double bond is converted to an oxirane ring,[10] which is a three-membered ring ether cyclic.[11] Fatmayanti *et al.* reported that epoxidized oleic acid exhibited potent anticancer activity against the WiDr and T47D cancer cell lines with an IC_{50} value of less than 20 mg L^{-1} and below 31 mg L^{-1}.[12] This epoxide ring can interact with nucleophilic groups in the proteins and nucleic acids, making them promising candidates for cancer treatment.[13] Therefore, epoxide compounds show good antiproliferative activities such as enzyme inhibition, induction of cell cycle arrest and apoptosis.[14]

Cancer cells proliferate faster and therefore have higher metabolic demands than normal cells. Cancer cells obtain lipids from the abnormal activity of the de novo fatty acid synthesis pathway, characterised by increased fatty acid synthesis and the production of palmitoleic acid. The lipid causes cancer cells to experience excessive proliferation, cancer cell metastasis, and triggers death in cancer patients four times faster.[15] Activation of these signalling pathways increases the activity of sterol regulatory element-binding protein-1 (SREBP-1), which in turn induces the expression of fatty acid synthase (FASN). Consequently, FASN has recently been recognised as an oncoprotein that is overexpressed in various cancer types. The administration of FASN inhibitors can prevent the synthesis of long-chain saturated fatty acids to reduce the ability of cancer cells to survive and support apoptosis in cancer cells. Disrupted FASN activity can cause metabolic stress, causing damage to cells (cytotoxicity).[16]

One of the FASN inhibitors that has been developed is cerulenin. The epoxide ring of cerulenin inhibits FASN activity by binding to the enzyme's activity, disturbing the fatty acid synthesis process. This binding involves covalent interactions of epoxide with cysteine residues in the active site β-ketoacyl-ACP synthase (KS) domain of FASN. However, cerulenin has serious side effects, as revealed by the *in vivo* results, especially in the form of anorexia and weight loss.[17] This study

(CC) 2026 Serbian Chemical Society.

aims to synthesize dioleate and trioleate epoxides from oleic acid isolated from palm oil through a series of chemical reactions, as shown in Scheme 1. Then, the *in vitro* anticancer activity of epoxides were investigated against breast (T47D) and colon (WiDr) cancer cells, as well as against normal cells (Vero). In addition, the interaction of the epoxides in the active site of the FASN was examined by *in silico* molecular docking.

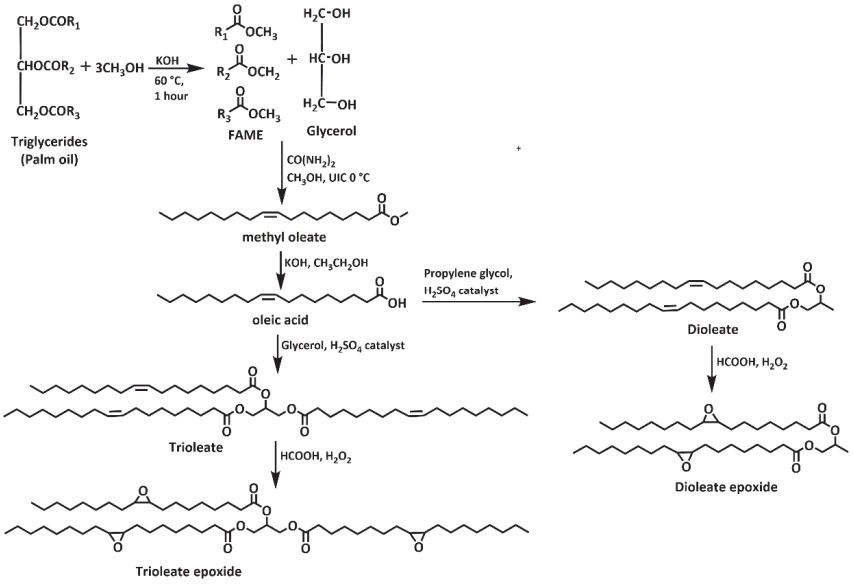

Scheme 1. Synthesis scheme of dioleate epoxide and trioleate epoxide from palm oil.

EXPERIMENTAL

Materials

Palm oil was purchased from a local market in Yogyakarta, Indonesia. All chemicals and solvents in this work were of pro analysis grade, obtained from Merck (Germany) and used without further purification. The chemicals included: carbamide ($CO(NH_2)_2$), propane-1,2,3-triol, propane-1,2-diol, methanoic acid, hydrogen peroxide (H_2O_2, 30 %), potassium hydroxide, sodium hydroxide, hydrochloric acid, sodium hydrogen carbonate, ethanol, methanol, ethyl ethanoate, *n*-hexane and anhydrous sodium sulfate. The cell lines used for the cytotoxic evaluation were T47D, WiDr and Vero. The materials used for the cytotoxic assay included Dulbecco's modified eagle medium (DMEM), medium 199 (M199), fetal bovine serum (FBS), penicillin–streptomycin (Pen–Strep), fungizone, trypsin-EDTA solution, dimethyl sulfoxide (DMSO), phosphate-buffered saline (PBS), mycoexpert mycoplasma, 3-(4,5-dimethylthiazol-2--yl)-2,5-diphenyltetrazolium bromide (MTT), 0.01 M HCl and sodium dodecyl sulfate (SDS).

Instrumentation

The purity and molecular weight of the products were measured by gas chromatography––mass spectrometry (GC–MS) using a Shimadzu-QP 2010S and Agilent GC type 6890-MS type 5973. Liquid chromatography–mass spectrometry (LC–MS) analysis was performed using

(CC) 2026 Serbian Chemical Society.

Acquity UPLC®H-Class System (Waters, USA) equipped with an LC Acquity UPLC®HSS C18 (1.8 µm, 2.1 mm×100 mm) and a Xevo G2-S QTOF mass spectrometer. The nuclear magnetic resonance (NMR) spectra were recorded on a JEOL JNM-ECZ 500R spectrometer at 500 and 125 MHz, respectively, using CD_3OD as solvent. Fourier-transform infrared (FTIR) spectra were recorded using a Shimadzu Prestige 21 with NaCl plate. The formazan absorbance solution was measured using a Bio-Rad Benchmark ELISA reader. Molecular docking simulations were done using the AutoDock Vina approach implemented in YASARA Structure (version 23.519; license number 645289713). Ligand–receptor interactions was visualized using Discovery Studio Visualizer (ver. 19.1.0.18287, ©2019).

Synthesis of fatty acid methyl esters (FAME)

Palm oil (50 g, 50 mmol) and KOH (1 g, 18 mmol) were dissolved in methanol (12.15 mL, 30 mmol). The mixture was refluxed and the reaction progress was monitored by GC–MS. The optimum reaction time of FAME was 60 min. After completion, the mixture was extracted with *n*-hexane and washed with distilled water (3×15 mL). The organic phase was dried over anhydrous sodium sulfate and the organic solvents were removed by a vacuum evaporator.

Purification of FAME by urea inclusion complex

The urea inclusion complex was carried out to produce a high purity of methyl oleate from FAME. Urea solution in methanol (12.5 g/50 mL) was heated at 50 °C for 15 min. Immediately, FAME (6.25 g) were added to the urea solution and stirred for 10–15 min. The solution was allowed to reach room temperature and kept in the freezer for 24 h. The formed crystals were filtered and rinsed with *n*-hexane (3×15 mL). The filtrate was acidified with distilled water and 6 M HCl to pH 1. The organic phase was separated and evaporated to obtain enriched-methyl oleate product.

Hydrolysis of oleic acid

Methyl oleate (2.95 g, 10 mmol) and KOH (1.68 g, 30 mmol) were dissolved in ethanol (10 mL). The mixture was refluxed for 120 min. The mixture was acidified with H_2SO_4 to pH 1–3. Afterward, the mixture was extracted by using *n*-hexane and washed by distilled water (3×20 mL) to remove excess H_2SO_4 and K_2SO_4. The organic solvents were removed with the help of a vacuum evaporator.

Synthesis of 1,2-propanediol dioleate (dioleate)

Oleic acid (6.21 g, 22 mmol) was reacted with 1,2-propanediol (0.76 g, 10 mmol) with sulfuric acid catalyst (200 µL) at 90–100 °C. After reaction for 4 h, the mixture was extracted with *n*-hexane and washed with distilled water (3×20 mL) to remove impurities. The organic phase was dried over anhydrous sodium sulphate and then removed in vacuum to produce the title compound.

Synthesis of glyceryl-1,2,3-trioleate (trioleate)

Oleic acid (9.04 g, 32 mmol) was reacted with glycerol (0.92 g, 10 mmol) in the presence of sulfuric acid catalyst (300 µL) at 90–100 °C for 6 h. Then, the mixture was extracted with *n*-hexane and washed with distilled water (3×15 mL) to remove undesired compounds. The organic phase was dried over anhydrous sodium sulphate and then removed by a vacuum evaporator to produce the title compound.

Epoxidation of dioleate and trioleate

The synthesis of dioleate epoxide was done with a mole ratio of dioleate (0.076 g), formic acid (0.276 g) and 30 % hydrogen peroxide (0.714 g) of 1:6:21. Meanwhile, the synthesis of

(CC) 2026 Serbian Chemical Society.

trioleate epoxide was carried out with a mole ratio of trioleate (0.89 g), formic acid (0.41 g), and 30 % hydrogen peroxide (1.05 g) was 1:9:31. Formic acid (1.08 g, 24 mmol) and hydrogen peroxide 30 wt% (2.86 g, 84 mmol) were firstly mixed in a closed Erlenmeyer at 28 °C for 1 h to generate performic acid. Afterwards, dioleate and trioleate compounds were separately added and the mixture was stirred at 28 °C for 24 h. The product was extracted with ethyl acetate (3×20 mL) and then the organic phase was washed with sodium bicarbonate 5 wt. % and sodium chloride 5 wt. %. The organic phase was dried over anhydrous sodium sulphate, filtered and evaporated to yield epoxide product.

Analytical and spectral data of the synthesized compounds are given in the Supplementary material to this paper.

Cytotoxicity evaluation

The cytotoxic evaluation was conducted in the Laboratory of Parasitology, Faculty of Medicine, Universitas Gadjah Mada. The ethical clearance approval letter is shown in Fig. S--26, Supplementary material. The MTT assay was performed to examine the cytotoxic activity and selectivity of all synthesized epoxides. The T47D, WiDr and Vero cell line were separately cultured in a 10 % FBS medium at 37 °C with a flow of 5 % CO_2. Each cell line (100 μL/well) was incubated at 37 °C with 5 % CO_2 flow for 24 h. Doxorubicin and 5-fluorouracil were chosen as positive controls. The evaluated compounds were examined at two-fold serial dilutions in DMSO. After exposing the cell with the tested compounds for 24 h, the MTT solution (100 μL) was added to each well and placed in an incubator for 4 h. Then, the SDS reagent stopper solution (100 μL) was added and the mixture was stored in a darkroom overnight. The absorbance was measured by using an Elisa reader at 595 nm. Each sample concentration was assayed in triplicate. The cell viability percentage was evaluated and expressed in half-maximal inhibitory concentration (IC_{50}). The IC_{50} value represents the effective concentration required to inhibit 50 % of cell viability. The selectivity of tested compounds was determined by calculating selectivity index (*SI*) value. The *SI* represents the safety of epoxidized oleate in cancer and normal cells.

RESULTS AND DISCUSSION

FAME isolation and purification

Fatty acid methyl esters (FAMEs) were successfully isolated from palm oil through the transesterification reaction. Base catalyst (KOH) was selected due to its higher reaction rate and lower operating temperature compared to acid-catalyzed processes.[18] The used mole ratio of palm oil and alcohol was 1:6 to accelerate the reaction rate to form the ester product, as reported earlier.[19] The methoxide ion attacks the carbonyl carbon of triglyceride, forming a tetrahedral intermediate. This intermediate then undergoes a nucleophilic substitution reaction, where one of the acyl chains on the triglyceride is released, producing methyl ester (FAME) and diacylglyceride (DAG) as intermediate products. This reaction continues until the entire acyl chain on the triglyceride is converted to methyl ester, with glycerol as a by-product.[20] Based on the results of the GC–MS analysis, six methyl ester peaks were detected, comprised four saturated fatty acids (myristate, palmitate, stearate, and eicosanoate) and two unsaturated fatty acids (oleate and linoleate).

(CC) 2026 Serbian Chemical Society.

The unsaturated fatty acid fraction was further purified using the UIC method. Urea has a tetragonal lattice with a diameter of 5.67 Å. The large size of the urea crystal can accommodate the aliphatic chain of fatty acid esters with more than six carbon atoms to form a hexagonal complex through van der Waals interactions. In contrast, urea crystal canals cannot accommodate unsaturated fatty acid esters due to their non-linear form.[21] In this work, methyl oleate was purified using the UIC method with a mole ratio of FAME:urea:methanol of 1:2:8 at 0 °C for 24 h. Based on GC–MS results, the purity of methyl oleate was significantly increased from 51.0 to 89.9 %. A slight increase was detected also for methyl linoleate, from 8.8 to 9.8 %. The concentration of methyl palmitate decreased from 36.3 to 3.3 %, while methyl myristate, methyl stearate, and methyl eicosanoate were no longer detected (see Table I).

TABLE I. Compositions of FAME before and after purification by UIC method

Entry	Methyl ester	Percentage (%)	
		Before purification	After purification
1	Myristate	0.4	0.0
2	Palmitate	36.3	3.3
3	Linoleate	8.8	9.8
4	Oleate	51.0	89.9
5	Stearate	3.3	0.0
6	Eicosanoate	0.2	0.0

The FTIR spectra of FAME before and after purification showed no significant changes (Fig. 1), except for an increase in the intensity of the =C–H sp^2 stretching band at 3008 cm^{-1}. The FAME sample after purification had a sharper intensity with a typical peak of C=O and C–O ester vibrations appearing at 1743 and 1165 cm^{-1}, respectively.

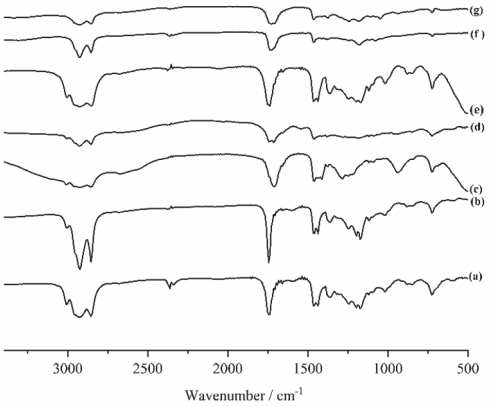

Fig. 1. FTIR spectra of: a) FAME, b) purified FAME, c) oleic acid, d) dioleate, e) trioleate, f) dioleate epoxide and g) trioleate epoxide.

(CC) 2026 Serbian Chemical Society.

Hydrolysis of methyl oleate

The refined methyl oleate was hydrolyzed at a mole ratio of methyl oleate to KOH of 1:3, respectively. The FTIR spectrum (Fig. 1) confirmed the formation of oleic acid by the appearance of a broad O–H stretching band of the carboxylic group at 3100 cm^{-1}. In addition, a strong absorption at 1712 cm^{-1} (shifted from 1743 cm^{-1} in methyl oleate) corresponds to the C=O of the carboxylic group. In the ^{1}H-NMR spectrum (Fig. 2), the double bond of oleic acid appeared as a multiplet at δ 5.32 ppm (J = 6.3 Hz) indicating a cis configuration. The hydroxyl proton peak on oleic acid does not appear in the ^{1}H-NMR spectrum because this proton easily exchanges with protons from the solvent or water present in the sample, causing the signal to broaden or disappear.[22] The α-methylene protons (H_α) appeared as a triplet at δ 2.35 ppm, while the β-methylene protons (H_β) were observed as a multiplet at δ 1.59 ppm.

The ^{13}C-NMR spectrum confirmed the presence of 18 carbon atoms in oleic acid. The carbonyl carbon appeared at δ 180 ppm because it binds to a hydroxy group, making it the least protected shift. The olefinic carbons were observed at δ 129 and 130 ppm, while fourteen other carbon peaks are found at a chemical shift range of 20–30 ppm.

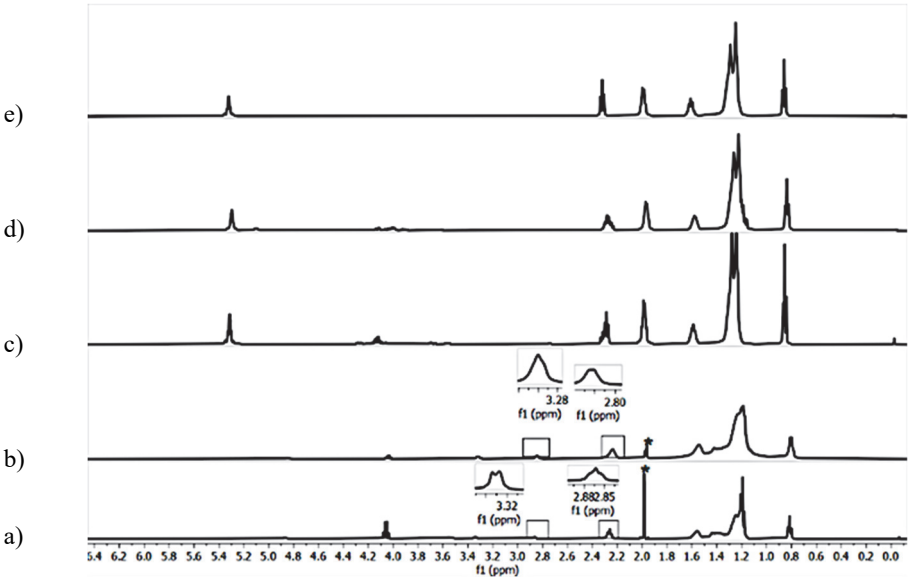

Fig. 2. ^{1}H-NMR spectra of: a) dioleate epoxide, b) trioleate epoxide, c) trioleate, d) dioleate, and e) oleic acid.

(CC) 2026 Serbian Chemical Society.

Synthesis of dioleate and trioleate

Dioleate was synthesized by reacting an excess amount of oleic acid with 1,2--propanediol at a mole ratio of 2.3:1.0 in the presence of sulfuric acid as a catalyst at 100 °C for 4 h. Oleic acid was added in excess to reduce the possibility of the monoester formation as the side product. The FTIR spectrum confirmed the formation of dioleate by the disappearance of the O–H stretching band at 3100 cm^{-1} from oleic acid and propanediol. The formation of dioleate product is proven by the absence of OH protons of oleic acid and 1,2-propanediol in the ^{1}H-NMR profile, which appear at δ 10–13 ppm. The alkene proton (–CH=) appeared at δ 5.30 ppm. On the other hand, the ^{13}C-NMR analysis showed that the carbon in the unsaturated double bond remains at δ 129 and 130 ppm while C=O carbon appears at δ 173 ppm.

Trioleate was also synthesized by esterification of oleic acid and glycerol at a mole ratio of oleic acid and glycerol of 3.3:1.0, respectively, at 100 °C for 6 h. In the ^{1}H-NMR spectrum, trioleate showed 8 proton signals. The formation of trioleate was confirmed by the absence of hydroxyl proton signals from oleic acid and glycerol, which appear at a chemical shift of δ 10–13 ppm. The FTIR data also support this evidence by showing no signal at 3100 cm^{-1} regions, which are found only for oleic acid and glycerol. Moreover, the characteristic ester absorptions at 1713 (C=O) and 1226 cm^{-1} (C–O) are observed. The alkene protons (–CH=) appeared at δ 5.32 ppm, while the alkene and carbonyl carbons appeared at δ 129––130 and 180 ppm in the ^{13}C-NMR spectrum. Although similar compound has been prepared by Radojčić *et al*. in 2022, no further epoxidation reaction is performed.[23] Furthermore, the previous work did not provide sufficient structural elucidation for the synthesized target compound.

Synthesis of dioleate and trioleate epoxides

At first, formic acid and hydrogen peroxide were reacted *in situ* for 1 h to produce performic acid (Fig. S-23, Supplementary material). Performic acid was then reacted with dioleate and trioleate compounds to yield targeted epoxide product (Figs. S-24 and S-25, Supplementary material). The mole ratio of dioleate, formic acid and hydrogen peroxide (30 wt. %) was 1:6:21 mmol, while the mole ratio of trioleate, formic acid and hydrogen peroxide (30 wt. %) was 1:9:31. Due to high molecular weights of dioleate and trioleate (636.53 and 932.77 g mol^{-1}), respectively, LC–MS analysis was employed to identify the purity of the products. The purities of dioleate epoxide and trioleate epoxide were 86.49 and 93.51 %, respectively. The LC chromatogram showed dioleate epoxide as the major component at a retention time of 12.28 min with an *m*/*z* value of 722.49, corresponding to the $[M+CH_3CN+HCOO]^-$ (Fig S-14, Supplementary material). Trioleate epoxide was detected at 12.10 min with an *m*/*z* value of 985.74, assigned to the $[M+NH_4Cl]^-$ (Fig S-18, Supplementary material). In the ^{1}H-NMR spectra,

(CC) 2026 Serbian Chemical Society.

the epoxide ring protons of the dioleate epoxide appeared as a multiplets at δ 2.85–3.55 ppm (J = 7 Hz), in agreement with another report.[31] The alkene proton at 5.32 ppm no longer appears in the ^{1}H-NMR spectra of both epoxides. Additionally, the alkene carbon peaks disappeared after the epoxidation reaction. Instead, the epoxide carbon signals appeared at δ 57.41–57.50 ppm. This is in accordance with Mai *et al.*, stating that the ^{13}C-NMR peaks of the epoxide ring of vegetable oil is observed at δ 54–58 ppm.[24] The characteristic =C–H and C=C bands at 3008 and 1658 cm^{-1} were also absent in the FTIR spectra. Meanwhile, a new peak showing the C–O–C oxirane appeared at 840 cm^{-1}, in which agree with previous work.[24] The disappearance of alkene groups and the appearance of oxirane groups indicate the presence of epoxide moieties. These results revealed that both dioleate and trioleate epoxides have been successfully obtained.

In vitro *cytotoxic evaluation*

Cytotoxicity tests of epoxides were evaluated against T47D, WiDr and Vero cells using the *in vitro* MTT assay (Tables S-I–S-IV, Supplementary material). The principle of the MTT method is based on color measurement.[25] The IC_{50} values of both epoxides (Table II) fall into the moderate category in killing cancer cells, according to National Cancer Institute of the United States.[26]

TABLE II. IC_{50} value of tested compounds against cancer and normal cell lines

Compound	IC_{50} / μg mL^{-1}			Index selectivity	
	T47D	WiDr	Vero	T47D	WiDr
Dioleate epoxide	35.66	38.25	291.04	8.16	7.60
Trioleate epoxide	27.40	32.41	297.93	10.87	9.19
Doxorubicin	12.58	–	–	–	–
5-fluorouracil	–	1.58	–	–	–
Epoxidized methyl oleate[12]	12.63	1.56	226.53	17.94	145.13
Epoxidized ethyl oleate[12]	30.13	10.05	244.10	8.10	24.28

Trioleate epoxide exhibited a lower IC_{50} value than dioleate epoxide against both T47D and WiDr cells. This difference in cytotoxic activity is thought to be related to the differences in the molecular structures of both compounds. Trioleate epoxide has a greater number of oxirane rings than dioleate epoxide, thereby providing more reactive centers capable of interacting with intracellular biomolecules, thus disruption of lipid metabolism in cancer cells. WiDr and T47D cancer cells are known to undergo metabolic reprogramming, characterised by increased *de novo* fatty acid synthesis to meet high proliferation demands. This increased demand for lipids is primarily mediated by the overexpression of FASN, which functions to produce palmitate as a precursor for various structural lipids and signaling molecules.[15] Structurally, dioleate epoxide and trioleate epoxide retain the lipophilic characteristics of the long oleate chain, thereby enabling both molecules to

(CC) 2026 Serbian Chemical Society.

interact with the hydrophobic environment of FASN. These interactions may disrupt FASN activity, leading to a reduction in palmitate production and endogenous lipid synthesis, thereby impairing the formation of membrane phospholipids and lipid rafts required to maintain the activation of pro-survival signaling pathways, such as PI3K/Akt/mTOR and MAPK/ERK.[16]

Compared with the methyl ester and ethyl ester derivatives previously reported – namely, epoxidized methyl oleate and epoxidized ethyl oleate[12] – both dioleate epoxide and trioleate epoxide exhibited lower cytotoxic activity against both T47D and WiDr cells. This finding indicates that structural modification of the monoester compound into glycerol-based diester and triester derivatives does not enhance cytotoxic potential due to bulky three-dimensional structures. Larger molecular size also has the potential to reduce the efficiency of penetration into the cell or limit the access of the epoxide group to intracellular biological targets, resulting in lower cytotoxic activity compared to monoester compounds. The results of cytotoxicity tests on dioleate and trioleate epoxides against normal Vero cells showed the IC_{50} values of 291.04 and 297.93 mg L^{-1}, respectively. This indicates that dioleate and trioleate epoxide compounds are non-toxic for normal cells. Furthermore, all test compounds exhibited a $SI > 6$ against T47D and WiDr cancer cells. These data indicate that dioleate and trioleate epoxide compounds are selective anti-cancer agents, as they are capable of inhibiting the growth of cancer cells without significantly inhibit the growth of normal cells.

Molecular docking study

The cytotoxic activities of dioleate and trioleate epoxides were further supported by molecular docking studies against the thioesterase domain of FASN. FASN has a co-crystallized ligand, orlistat, which is a lipid-derived molecule possessing a long aliphatic hydrocarbon chain and a highly lipophilic character. Orlistat was previously known as a weight-loss drug and is now recognised as a promising candidate for an anti-cancer agent due to its ability to irreversibly inhibit FASN by forming a covalent bond with the thioesterase domain.[27] Orlistat bears a structural resemblance to the epoxide compounds, both possess long-chain alkyl groups that are lipophilic, and are therefore thought to be capable of interacting with the hydrophobic pockets of FASN, which naturally accommodate long-chain fatty acid substrates. In this work, the redocking of native ligands against the FASN enzyme was performed within a cube-shaped grid box with a distance of 5 Å from the vicinity of the selected ligand. The root-mean square deviation (*RMSD*) value obtained from the redocking of native ligand (*i.e.*, orlistat) was 1.40 Å. When the *RMSD* value is smaller than 2 Å, it indicates that the pose of orlistat after redocking has no significant difference from the experimental pose from the crystallographic data. The re-docking results show that the orlistat interacts with various amino acid

(CC) 2026 Serbian Chemical Society.

residues in the FASN enzyme, generating a binding affinity value of –22.87 kJ mol^{-1}.

After confirming the redocking of orlistat, the next stage is the molecular docking of dioleate and trioleate epoxides against FASN. Docking of dioleate epoxide and trioleate epoxide in the active site of FASN resulted in a binding affinity value of –27.11 and –27.61 kJ mol^{-1}. The dioleate epoxide, trioleate epoxide and native ligand interacted with the identical amino acid residues, namely Leu2222, Ile2250, Ser2308, Tyr2309, Ala2367, Phe2370, Phe2371, Gln2374, Phe2375, Phe2423, Lys2426, Leu2427, His2481 and Arg2482. The oxygen atom on the oxirane ring of both epoxides interacts with Ser2308 residue through a hydrophobic interaction. Based on the results, trioleate epoxide has a stronger bond affinity value because trioleate epoxide has 2 hydrogen bonds and 2 C–H bonds, while epoxide dioleate only has 2 C–H bonds. Hydrogen and C–H bonds have the most important role in stabilizing enzyme–ligand bonds, whereas the energy of hydrogen bonds and C–H bonds is 10–63 and 4 kJ mol^{-1}.[28] Trioleate epoxide is more stable for FASN binding through Ser2308 residue compared to dioleate epoxide. This computational finding agrees with the experimental *in vitro* result, in which trioleate epoxide exhibits a stronger anticancer activity than dioleate epoxide. The interactions in the docking results are listed in Table III.

TABLE III. Molecular docking results of the native ligand and epoxide compounds

Compound	Binding affinity kJ mol^{-1}	Interaction			
		Hydrogen	C–H	Hydrophobic	Electrostatic
Native ligand (orlistat)	–22.87	Ile2250, Ser2308, His2481	–	Leu2222, Pro2249, Val2256, Tyr2307, Tyr2309, Tyr2343, Ala2367, Phe2370, Phe2371, Gln2374, Phe2375, Ala2419, Ser2422, Phe2423, Lys2426, Leu2427, Arg2482	Glu2251
Dioleate epoxide	–27.11	–	Thr2342, Ala2363	Leu2222, Ile2250, Glu2251, Ser2308, Tyr2309, Asp2338, Gly2339, Ser2340, Val2343, Leu2344, Ala2345, Tyr2350, Ala2363, Glu2364, Glu2366, Ala2367, Phe2370, Phe2371, Gln2374, Phe2375, Phe2423, Tyr2424, Lys2426, Leu2427, Arg2428, Ala2430, Glu2431, Ala2452, Tyr2453, Gly2454, Asp2456, Tyr2462, His2481,Arg2482	–
Trioleate epoxide	–27.61	Ser2308, Arg2351	Thr2342, Ala2367	Leu 2222, Ile2250, Glu2251, Tyr2309, Val2343, Ala2345, Tyr2350, Glu2366, Phe2370, Phe2371, Gln2374, Phe2375, Ala2419, Phe2423, Lys2426, Leu2427, Arg2428, Ala2430, Glu2431, Ala2452, Tyr2453, Tyr2462, His2481, Arg2482	–

(CC) 2026 Serbian Chemical Society.

Compared with previously reported oleate epoxide derivatives – namely, epoxidized methyl oleate (–30.54 kJ mol^{-1}) and epoxidized ethyl oleate (–33.89 kJ mol^{-1})[12] – the two compounds synthesised in this study exhibited weaker binding affinity for FASN. This strengthen that structural modification of monoester compounds into glycerol-based diester and triester derivatives does not enhance the strength of interaction with the target protein due to steric effect, which is in agreement with the cytotoxic results.

CONCLUSION

Dioleate and trioleate epoxides have been successfully prepared from palm oil through five consecutive steps with a purity of 86.49 and 93.51 %, respectively. Based on the *in vitro* and *in silico* tests, trioleate epoxide generated more potent *in vitro* anticancer activity in killing T47D and WiDr cancer cells than dioleate epoxide. Meanwhile, the cytotoxicity results revealed that SI values of dioleate and trioleate epoxides were found in a range of 7.60–10.87 demonstrating their non-toxic category towards Vero normal cells. The docking results revealed that both epoxides were able to interact with key amino acid residues, *i.e.*, Ser2308, Thr2342, Arg2351, Ala2363 and Ala2367, in the FASN's active site. In future, *in vivo* tests of these oleate epoxides need to be carried out for further development as new anticancer agents.

SUPPLEMENTARY MATERIAL

Additional data and information are available electronically at the pages of journal website: https://www.shd-pub.org.rs/index.php/JSCS/article/view/13896, or from the corresponding author on request.

Acknowledgement. The authors sincerely thanks to the Austrian–Indonesian Centre for Computational Chemistry for supporting the molecular docking studies.

ИЗВОД

ЕПОКСИДИ ИЗВЕДЕНИ ИЗ ДИОЛЕАТА И ТРИОЛЕАТА ПАЛМИНОГ УЉА КАО АНТИТУМОРСКИ АГЕНСИ ИСПИТИВАЊЕМ *IN VITRO* АКТИВНОСТИ И МОЛЕКУЛСКОГ ДОКИНГА

NUNUNG RATNA NINGSIH, JUMINA, TUTIK DWI WAHYUNINGSIH и YEHEZKIEL STEVEN KURNIAWAN

Department of Chemistry, Faculty of Mathematics and Natural Sciences, Universitas Gadjah Mada, Yogyakarta 55281, Indonesia

Епоксиди изведени из диолеата и триолеата палминог уља добијени су у неколико корака, и испитан им је антитуморски потенцијал у *in vitro* тестовима, а молекулским докингом је испитано могуће везивање за FASN протеин. Прво, поступком трансестерификације палминог уља добијени су метил-естри масних киселина (FAME). Затим су метил-олеати из FAME пречишћени инклузионом методом помоћу урее и затим је пречишћен метил-олеат хидролизован до олеинске киселине. Олеинска киселина је у поступку естерификације са 1,2-пропандиолом и глицеролом преведена у 1,2-пропандиол-диолеат (диолеат) и глицерил-1,2,3-триолеат (триолеат), редом. Диолеат и триолеат су

(CC) 2026 Serbian Chemical Society.

помоћу пермрављe киселине преведени у одговарајуће епоксиде. Триолеат-епоксид показује бољу антитуморску активност према T47D и WiDr ћелијама рака са IC_{50} вредностима 27,40 и 32,41 mg L^{-1}, редом. У поређењу са њим, диолеат-епоксид према T47D и WiDr ћелијама ракаа има активност 35,66 и 38,25 mg L^{-1}, редом. Триолеат- и диолеат-епоксиди нису токсични према нормалним ћелијама са вредностима индекса селективности 9,19–10,87 и 7,60–8,16, редом. Молекулским докингом је показано да би диолеат- и триолеат-епоксиди могли да инхибирају функционисање ензима FASN са вредностима афинитета везивања од –27,11 и –27,61 kJ mol^{-1}, редом.

(Примљено 7. априла, ревидирано 22. маја, прихваћено 7. августа 2026)

REFERENCES

1. F. Bray, M. Laversanne, H. Sung, J. Ferlay, R. L. Siegel, I. Soerjomataram, A. Jemal, *CA Cancer J. Clin.* **74** (2024) 229 (https://doi.org/10.3322/caac.21834)
2. P. Marino, M. Mininni, G. Deiana, G. Marino, R. Divella, I. Bochicchio, A. Giuliano, S. Lapadula, A. R. Lettini, F. Sanseverino, *Nutrients* **16** (2024) 800 (https://doi.org/10.3390/nu16060800)
3. R. Baskar, K. A. Lee, R. Yeo, K. W. Yeoh, *Int. J. Med. Sci.* **9** (2012) 193 (https://doi.org/10.7150/ijms.3635)
4. J. Cox, S. Weinman, *Hepat. Oncol.* **3** (2016) 57 (https://doi.org/10.2217/hep.15.41)
5. M. Fridlender, Y. Kapulnik, H. Koltai, *Front. Plant Sci.* **6** (2015) 799 (https://doi.org/10.3389/fpls.2015.00799)
6. A. Mancini, E. Imperlini, E. Nigro, C. Montagnese, A. Daniele, S. Orrù, P. Buono, *Molecules* **20** (2015) 17339 (https://doi.org/10.3390/molecules200917339)
7. D. Perdana, M. N. Rohman, M. Choifin, *Int. J. Appl. Power Eng.* **14** (2025) 980 (https://doi.org/10.11591/ijape.v14.i4.pp980-987)
8. K. A. Sampaio, R. Ceriani, S. M. Silva, T. Taham, A. J. A. Meirelles, *Food Bioprod. Process.* **89** (2011) 383 (https://doi.org/10.1016/j.fbp.2010.11.012)
9. J. Selvaraj, in *Fatty Acids*, A. Catala, Ed., InTechOpen, Rijeka, 2017 (https://doi.org/10.5772/intechopen.68171)
10. B. R. Moser, S. C. Cermak, K. M. Doll, J. A. Kenar, B. K. Sharma, *J. Am. Oil Chem. Soc.* **99** (2022) 801 (https://doi.org/10.1002/aocs.12623)
11. P. T. Wai, P. Jiang, Y. Shen, P. Zhang, Q. Gu, Y. Leng, *RSC Adv.* **9** (2019) 38119 (https://doi.org/10.1039/C9RA05943A)
12. B. R. Fatmayanti, J. Jumina, B. Purwono, Y. S. Kurniawan, H. D. Pranowo, E. N. Sholikhah, *ChemistrySelect* **9** (2024) 202400752 (https://doi.org/10.1002/slct.202400752)
13. V. M. Dembitsky, *Biomedicines* **11** (2023) 2237 (https://doi.org/10.3390/biomedicines11082237)
14. A. Lewinska, P. Chochrek, K. Smolag, E. Rawska, M. Wnuk, *Redox Report* **20** (2015) 116 (https://doi.org/10.1179/1351000214Y.0000000113)
15. C. W. Fhu, A. Ali, *Molecules* **25** (2020) 3935 (https://doi.org/10.3390/molecules25173935)
16. J. A. Menendez, E. Cuyàs, J. A. Encinar, T. Vander Steen, S. Verdura, À. Llop-Hernández, J. López, E. Serrano-Hervás, S. Osuna, B. Martin-Castillo, R. Lupu, *Mol. Oncol.* **18** (2024) 479 (https://doi.org/10.1002/1878-0261.13582)
17. R. Flavin, S. Peluso, P. L. Nguyen, M. Loda, *Future Oncology* **6** (2010) 551 (https://doi.org/10.2217/fon.10.11)
18. D. Singh, P. Patidar, A. Ganesh, S. Mahajani, *Ind. Eng. Chem. Res.* **52** (2013) 14776 (https://doi.org/10.1021/ie401636v)

(CC) 2026 Serbian Chemical Society.

19. I. A. Musa, *Egyptian J. Petrol.* **25** (2016) 21 (https://doi.org/10.1016/j.ejpe.2015.06.007)
20. I. M. Rizwanul Fattah, H. H. Masjuki, M. A. Kalam, M. Mofijur, M. J. Abedin, *Energy Convers. Manage.* **79** (2014) 265 (https://doi.org/10.1016/j.enconman.2013.12.024)
21. J. Liu, B. Tao, *Biofuel Res. J.* **9** (2022) 1617 (https://doi.org/10.18331/BRJ2022.9.2.3)
22. P. Charisiadis, V. G. Kontogianni, C. G. Tsiafoulis, A. G. Tzakos, M. Siskos, I. P. Gerothanassis, *Molecules* **19** (2014) 13643 (https://doi.org/10.3390/molecules190913643)
23. D. Radojčić, J. Hong, Z. S. Petrović, *J. Polym. Environ.* **30** (2022) 765 (https://doi.org/10.1007/s10924-021-02228-w)
24. L. L. T. Mai, M. M. Aung, S. A. M. Saidi, P. S. H'ng, M. Rayung, A. M. Jaafar, *Polymers (Basel)* **13** (2021) 2177 (https://doi.org/10.3390/polym13132177)
25. N. Ganot, S. Meker, L. Reytman, A. Tzubery, E. Y. Tshuva, *J. Vis. Exp.* **81** (2013) e50767 (https://doi.org/10.3791/50767)
26. T. Widiandani, T. Tandian, B. D. Zufar, A. Suryadi, B. T. Purwanto, S. Hardjono, S. Siswandono, *J. Public Health Afr.* **14** (2023) 2516 (https://doi.org/10.4081/jphia.2023.2516)
27. V. E. Fako, J. T. Zhang, J. Y. Liu, *ACS Catal.* **4** (2014) 3444 https://doi.org/10.1021/cs500956m
28. S. J. Grabowski, *Ann. Rep. Prog. Chem. Sect. C* **102** (2006) 131 (https://doi.org/10.1039/B417200K).

(CC) 2026 Serbian Chemical Society.

Journal of the Serbian Chemical Society
JSCS-info@shd.org.rs • www.shd.org.rs/JSCS
J. Serb. Chem. Soc. 91 (10) S278–S299 (2026) *Supplementary material*

SUPPLEMENTARY MATERIAL TO

Dioleate and trioleate epoxides from palm oil as anticancer agents through *in vitro* and molecular docking studies

NUNUNG RATNA NINGSIH, JUMINA*, TUTIK DWI WAHYUNINGSIH and YEHEZKIEL STEVEN KURNIAWAN

Department of Chemistry, Faculty of Mathematics and Natural Sciences, Universitas Gadjah Mada, Yogyakarta 55281, Indonesia

J. Serb. Chem. Soc. 91 (10) (2026) 981–994

ANALYTICAL AND SPECTRAL DATA

Fatty acid methyl esters (FAME)

Bright yellow liquid (41.09 g, 95.69 %). FTIR (NaCl, ν_max/cm^{-1}): 3008 (=C–H), 2924, 2854 (C–H), 1743 (C=O), 1658 (C=C), 1458, 1435 (CH_2), 1381 (CH_3), 1165 (C–O), 1118 (=C–H), 725 ((CH_2) n) (Fig. S-1). GC–MS (EI, 70 eV): methyl myristate (0.42 %, R_t = 30.43 min, m/z 242 $[M]^+$), methyl palmitate (36.30 %, R_t = 35.02 min, m/z 270 $[M]^+$), methyl linoleate (8.75 %, R_t = 38.40 min, m/z 294 $[M]^+$), methyl oleate (51.01 %, R_t = 38.62 min, m/z 264 $[M - CH_3OH]^+$), methyl stearate (3.27 %, R_t = 39.00 min, m/z 298 $[M]^+$), and methyl icosanoate (0.25 %, R_t = 42.70 min, m/z 326 $[M]^+$) (Fig. S-2).

Purified FAME

Pale yellow liquid (5.56 g, 88.96 %). FTIR (NaCl, ν_max/cm^{-1}): 3008 (=C–H), 2924, 2854 (C–H), 1743 (C=O), 1658 (C=C), 1458, 1435 (CH_2), 1381 (CH_3), 1165 (C–O), 1118 (=C–H), 725 ((CH_2)_n) (Fig. S-3). GC–MS (EI, 70 eV): methyl palmitate (3.26 %, R_t=29.24 min, m/z 270 $[M]^+$), methyl linoleate (9.84 %, R_t=32.47 min, m/z 294 $[M]^+$), and methyl oleate (89.90%, R_t=32.67 min, m/z 296 $[M]^+$) (Fig. S-4).

Oleic acid

Light yellow liquid (2.59 g, 92%). FTIR (NaCl, ν_max/cm^{-1}): 3100 (O–H), 2924, 2854 (C–H), 1712 (C=O), 1458 (CH_2), 1373 (CH_3), 1280 (C–O), 725 ((CH_2)$_n$) (Fig. S-5). ^{1}H NMR (500 MHz, $CDCl_3$, δ): 0.85 (t, *J* = 7.0 Hz, 3H), 1.20–1.32 (m, 20H), 1.56–1.63 (m, 2H), 1.95 (q, *J* = 7.0 Hz, 4H), 2.35 (t, *J* = 8.0 Hz, 2H), 5.30–5.35 (m, 2H) (Fig. S-6). ^{13}C NMR (125 MHz, $CDCl_3$, δ): 14.18, 22.77, 24.74, 27.23, 27.29, 29.12, 29.15, 29.24, 29.42, 29.62, 29.76, 29.85, 32.00, 34.15, 34.20, 127.79, 130.08, 180.53 (Fig. S-7).

1,2-Propanediol dioleate

Yellow liquid (6.01 g, 82.8%). FTIR (NaCl, ν_max/cm^{-1}): 3008 (=C–H), 2924, 2854 (C–H), 1736, 1712 (C=O), 1658 (C=C), 1458 (CH_2), 1381 (CH_3), 1180 (C–O), 725 ((CH_2)$_n$) (Fig. S-8). ^{1}H NMR (500 MHz, $CDCl_3$, δ): 0.81–0.84 (m, 6H), 1.14–1.32 (m, 43H), 1.54–1.61 (m,

* Corresponding author. E-mail: jumina@ugm.ac.id

Available online at https://www.shd.org.rs/JSCS/

(CC) 2026 Serbian Chemical Society.

4H), 1.92 (q, J = 6.8 Hz, 8H), 2.25–2.30 (m, 4H), 3.95–4.05 (m, 2H), 5.08–5.12 (m, 1H), 5.28–5.32 (m, 4H) (Fig. S-9). ^{13}C NMR (125 MHz, $CDCl_3$, δ): 14.17, 16.55, 22.76, 24.80, 27.23, 27.28, 29.02, 29.11, 29.18, 29.34, 29.42, 29.47, 29.58, 29.68, 31.98, 34.19, 65.98, 68.07, 129.78, 130.06, 173.64 (Fig. S-10).

Glyceryl trioleate

Yellow liquid (7.08 g, 80 %). FTIR (NaCl, ν_max/cm^{-1}): 3008 (=C–H), 2924, 2854 (C–H), 1736 (C=O), 1658 (C=C), 1458, 1435 (CH_2), 1357 (CH_3), 1172 (C–O), 725 ($(CH_2)_n$) (Fig. S-11). ^{1}H NMR (500 MHz, $CDCl_3$, δ): 0.85 (t, J = 7.1 Hz, 9H), 1.18–1.30 (m, 60H), 1.55–1.63 (m, 6H), 1.98 (q, J = 7.2 Hz, 12H), 2.28 (t, J = 8.4 Hz, 6H), 4.09–4.16 (m, 4H), 4.73–4.77 (m, 1H), 5.28–5.33 (m, 6H) (Fig. S-12). ^{13}C NMR (125 MHz, $CDCl_3$, δ): 14.18, 24.81, 24.94, 27.24, 27.29, 29.17, 29.25, 29.41, 29.61, 29.77, 29.85, 31.68, 31.99, 34.16, 34.26, 65.09, 70.34, 129.87, 130.08, 180.03 (Fig. S-13).

Dioleate diepoxide

White solid (0.60 g, 94.49 %). FTIR (NaCl, ν_max/cm^{-1}): 2924, 2854 (C–H), 1735 (C=O), 1465 (CH_2), 1381 (CH_3), 1172 (C–O), 840 (oxirane C–O), 725 ($(CH_2)^n$) (Fig. S-14,. LC–MS (ESI, negative ion mode): purity 86.49 %, R_t=12.28 min, m/z 722 ($[M + CH_3CN + HCOO]^-$) (Fig. S-15). ^{1}H NMR (500 MHz, CD_3OD, δ/ppm): 0.80 (t, J = 7.0 Hz, 6H), 1.23–1.27 (m, 43H), 1.40 (q, J = 5.5 Hz, 4H), 1.55 (q, J = 8.0 Hz, 8H), 2.25 (t, J = 7.2 Hz, 4H), 2.85–3.32 (m, 4H), 4.04–4.07 (m, 2H), 4.84–4.90 (m, 1H) (Fig. S-16). ^{13}C NMR (125 MHz, CD_3OD, δ/ppm): 14.18, 24.81, 24.94, 27.24, 27.29, 29.17, 29.25, 29.41, 29.61, 29.73, 29.77, 29.85, 30.53, 31.88, 33.50, 34.01, 57.41, 57.50, 65.95, 68.07, 178.13 (Fig. S-17).

Trioleate triepoxide

White solid (0.81 g, 92.04 %). FTIR (NaCl, ν_max/cm^{-1}): 2924, 2854 (C–H), 1728 (C=O), 1465 (CH_2), 1373 (CH_3), 1242 (C–O), 840 (oxirane C–O), 725 ($(CH_2)_n$) (Fig. S-18). LC–MS (ESI, negative ion mode): purity 93.51 %, R_t=12.10 min, m/z 985 ($[M+ NH_4Cl]^-$) (Fig. S-19). ^{1}H NMR (500 MHz, CD_3OD, δ/ppm): 0.81 (t, J = 7.0 Hz, 9H), 1.21–1.25 (m, 60H), 1.40–1.44 (m, 6H), 1.56 (q, J = 8.3 Hz, 12H), 2.26 (t, J = 7.2 Hz, 6H), 2.87–3.34 (m, 6H), 4.06–4.08 (m, 4H), 4.81–4.87 (m, 1H) (Fig. S-20). ^{13}C NMR (125 MHz, CD_3OD, δ/ppm): 14.14, 21.06, 22.70, 24.72, 26.60, 27.79, 28.99, 29.05, 29.25, 29.35, 29.56, 29.73, 31.89, 33.49, 34.03, 57.43, 57.48, 60.53, 72.24, 171.44 (Fig. S-21).

SYNTHESIS OF FAME

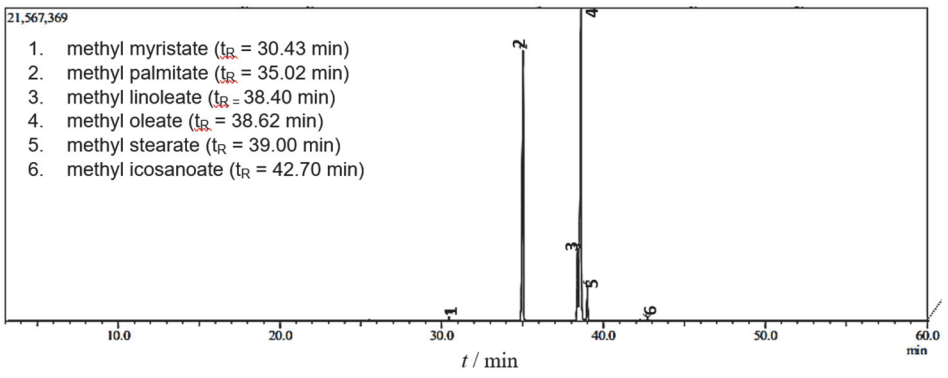

Fig. S-1. GC chromatograms of FAME

(CC) 2026 Serbian Chemical Society.

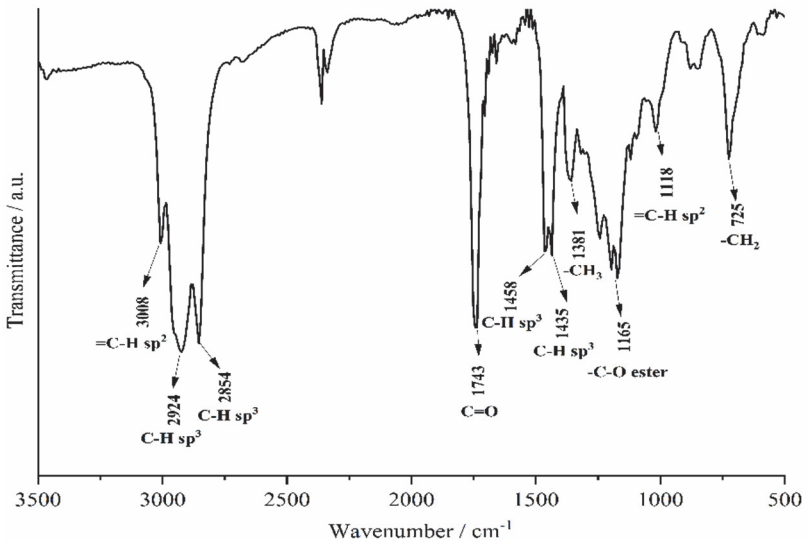

Fig. S-2. FTIR spectra of FAME

Synthesis of FAME: The FAME product was obtained as a yellow liquid (41.09 g, 95.69%). FTIR (ν, cm^{-1}): 3008 (C–H sp^2), 2924 and 2854 (C–H sp^3), 1743 (C=O), 1658 (C=C sp^2), 1458 and 1435 (–CH_2– sp^3), 1381 (–CH_3 sp^3), 1165 (C–O ester), 725 (–CH_2– sp^3). GC–MS: methyl myristate ($C_{15}H_{30}O_2$, 0.42%, retention time (t_R) 30.43 min, m/z 242 $[M]^+$), methyl palmitate ($C_{17}H_{34}O_2$, 36.30%, t_R 35.02 min, m/z 270 $[M]^+$), methyl linoleate ($C_{19}H_{34}O_2$, 8.75%, t_R 38.40 min, m/z 294 $[M]^+$), methyl oleate ($C_{19}H_{36}O_2$, 51.01%, t_R 38.62 min, m/z 264 $[M\text{-}CH_4O]^+$), methyl stearate ($C_{19}H_{38}O_2$, 3.27%, t_R 39.00 min, m/z 298 $[M]^+$), and methyl icosanoate ($C_{21}H_{42}O_2$, 0.25%, t_R 42.70 min, m/z 326 $[M]^+$).

Purified FAME

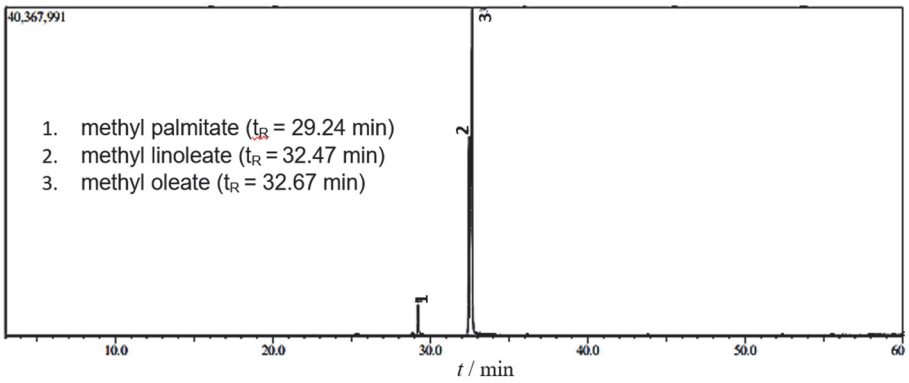

Fig. S-3. GC chromatograms of purified FAME

(CC) 2026 Serbian Chemical Society.

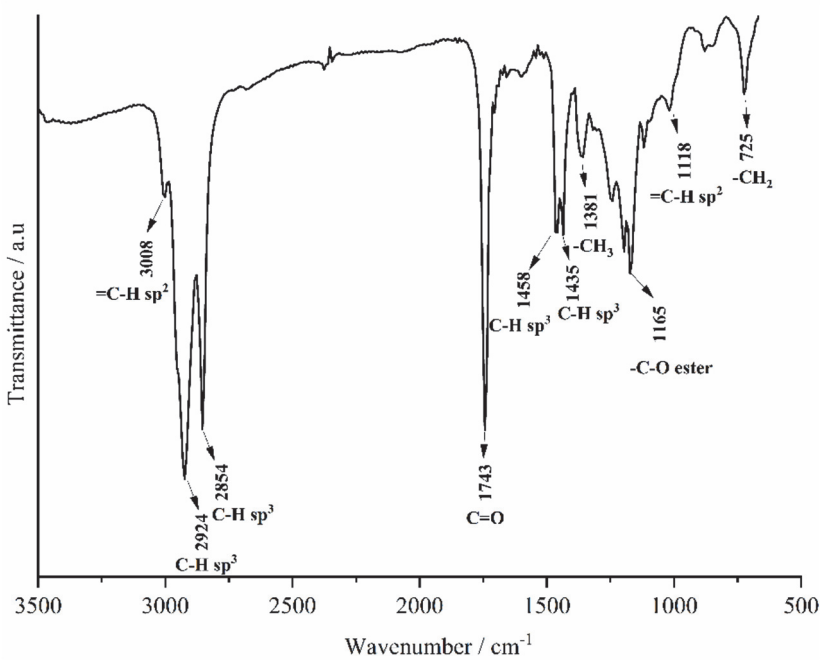

Fig. S-4. FTIR spectra of purified FAME

Purified FAME: The product was obtained as a pale yellow liquid (5.56 g, 88.96%). FTIR (ν, cm^{-1}): 3008 (C–H sp^2), 2924 and 2854 (C–H sp^3), 1743 (C=O), 1658 (C=C sp^2), 1458 and 1435 (–CH_2– sp^3), 1381 (–CH_3 sp^3), 1165 (C–O ester), 725 (–CH_2– sp^3). GC–MS: methyl palmitate ($C_{17}H_{34}O_2$, 3.26%, t_R 29.24 min, m/z 270 $[M]^+$), methyl linoleate ($C_{19}H_{34}O_2$, 9.84%, t_R 32.47 min, m/z 294 $[M]^+$), and methyl oleate ($C_{19}H_{36}O_2$, 89.90%, t_R 32.67 min, m/z 296 $[M]^+$).

(CC) 2026 Serbian Chemical Society.

SYNTHESIZED OLEIC ACID

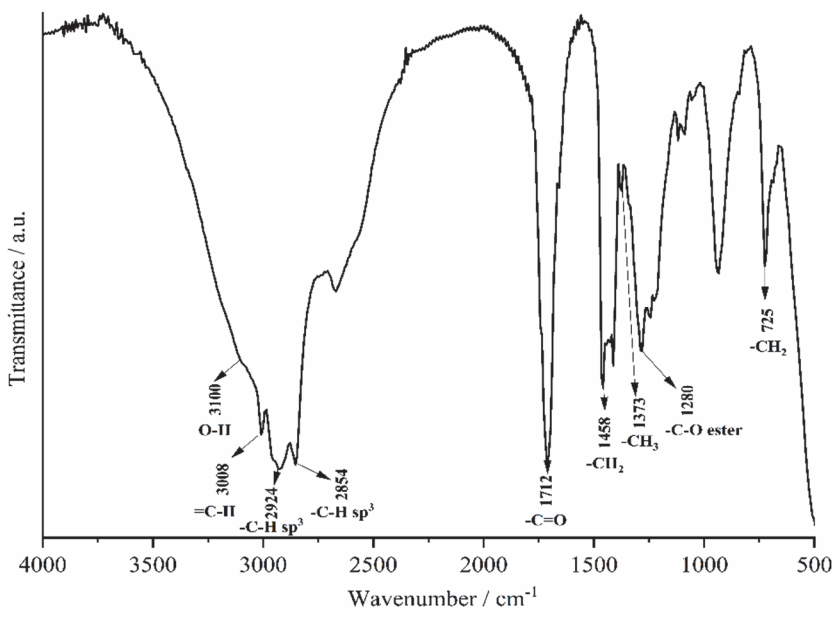

Fig. S-5. FTIR spectra of oleic acid

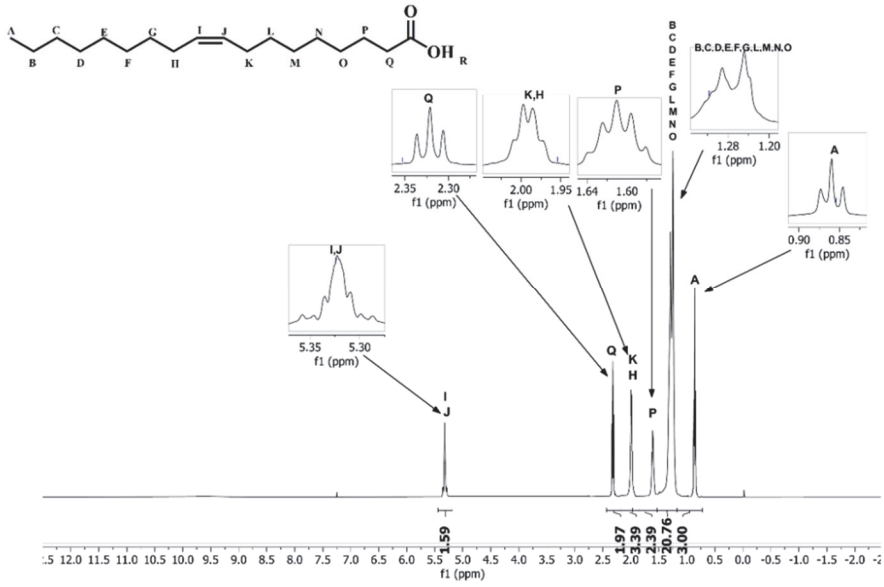

Fig. S-6. ^{1}H-NMR spectra of oleic acid

(CC) 2026 Serbian Chemical Society.

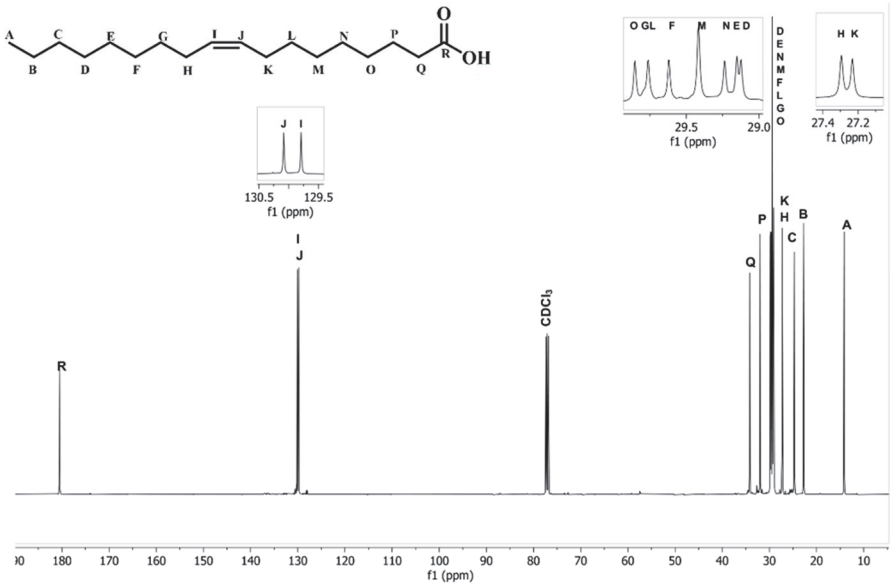

Fig. S-7. ^{13}C-NMR spectra of oleic acid

Synthesized oleic acid: Oleic acid ($C_{18}H_{34}O_2$) product was obtained as a light yellow liquid (2.59 g, 92%). FTIR (ν, cm^{-1}): 3100 (O–H), 2924 and 2854 (C–H sp^3), 1712 (C=O), 1458 (–CH_2– sp^3), 1373 (–CH_3 sp^3), 1280 (C–O ester), 725 (–CH_2– sp^3).

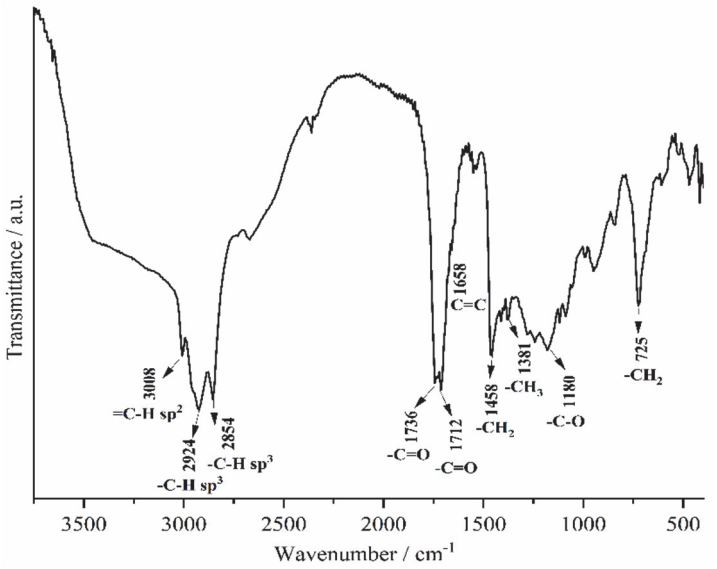

Fig. S-8. FTIR spectra of dioleate

(CC) 2026 Serbian Chemical Society.

SYNTHESIZED DIOLEATE

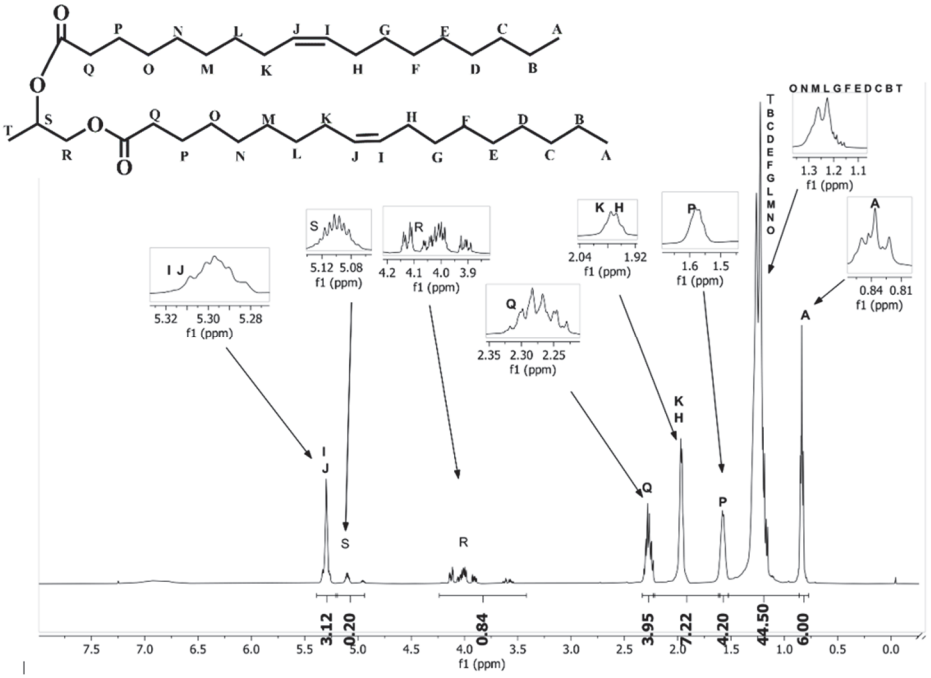

Fig. S-9. ^{1}H-NMR spectra of dioleate

(CC) 2026 Serbian Chemical Society.

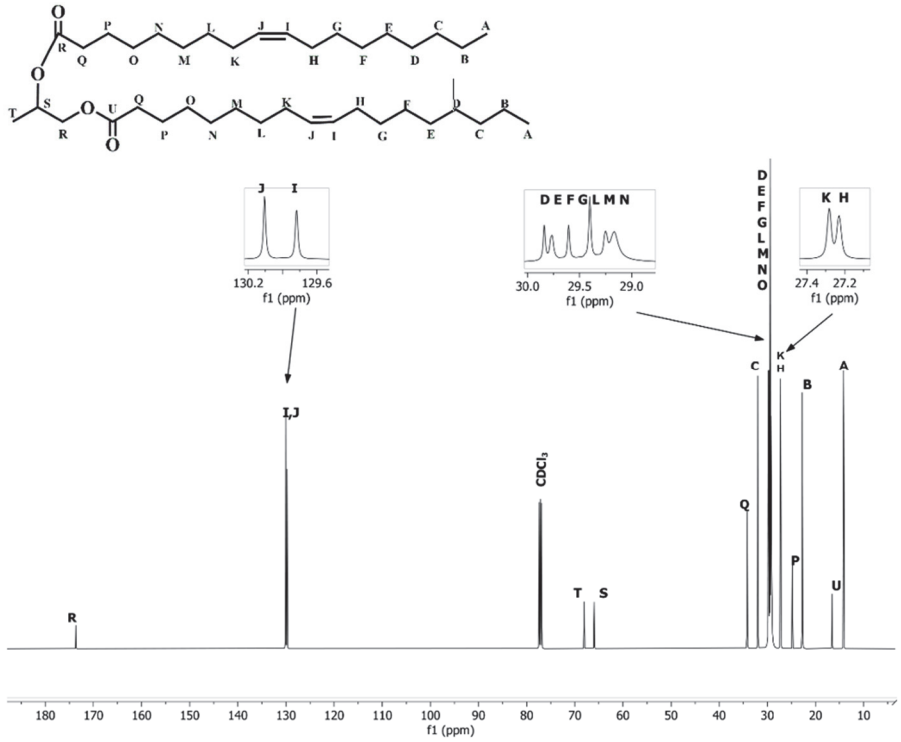

Fig. S-10. ^{13}C-NMR spectra of dioleate

Synthesized dioleate: Dioleate ($C_{39}H_{72}O_4$) product was obtained as a yellow liquid (6.01 g, 82.8%). FTIR (ν, cm^{-1}): 3008 (C–H sp^2), 2924 and 2854 (C–H sp^3), 1736 and 1712 (C=O), 1658 (C=C sp^2), 1458 (–CH_2– sp^3), 1381 (–CH_3 sp^3), 1180 (C–O ester), 725 (–CH_2– sp^3).

(CC) 2026 Serbian Chemical Society.

SYNTHESIZED TRIOLEATE

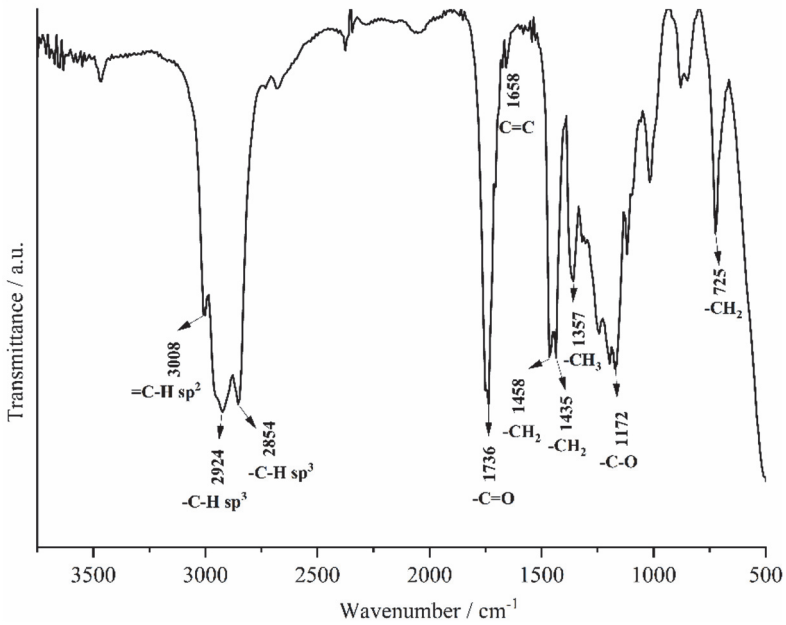

Fig. S-11. FTIR spectra of trioleate

(CC) 2026 Serbian Chemical Society.

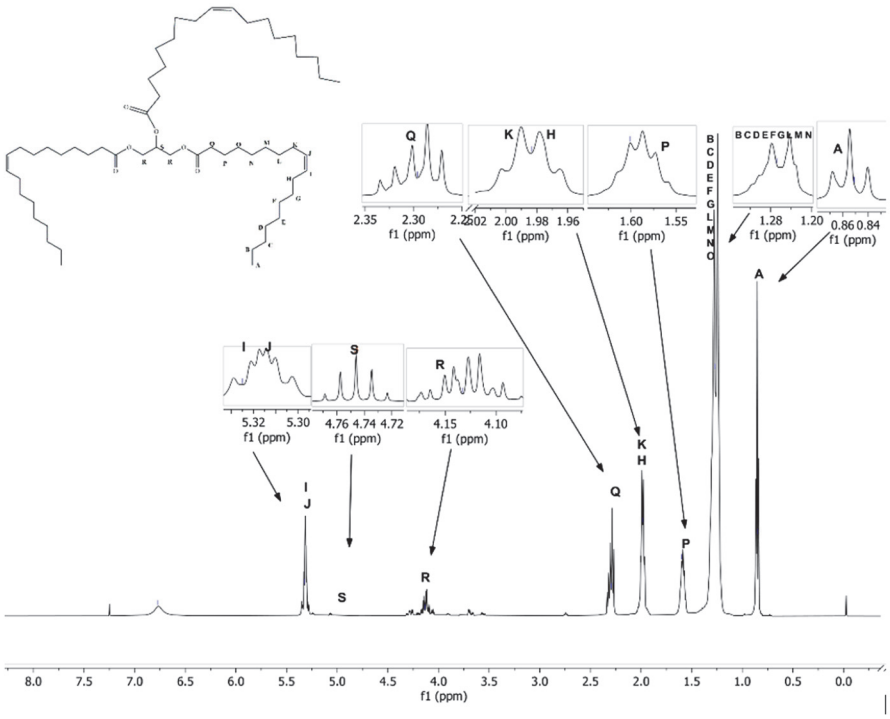

Fig. S-12. ^{1}H-NMR spectra of trioleate

(CC) 2026 Serbian Chemical Society.

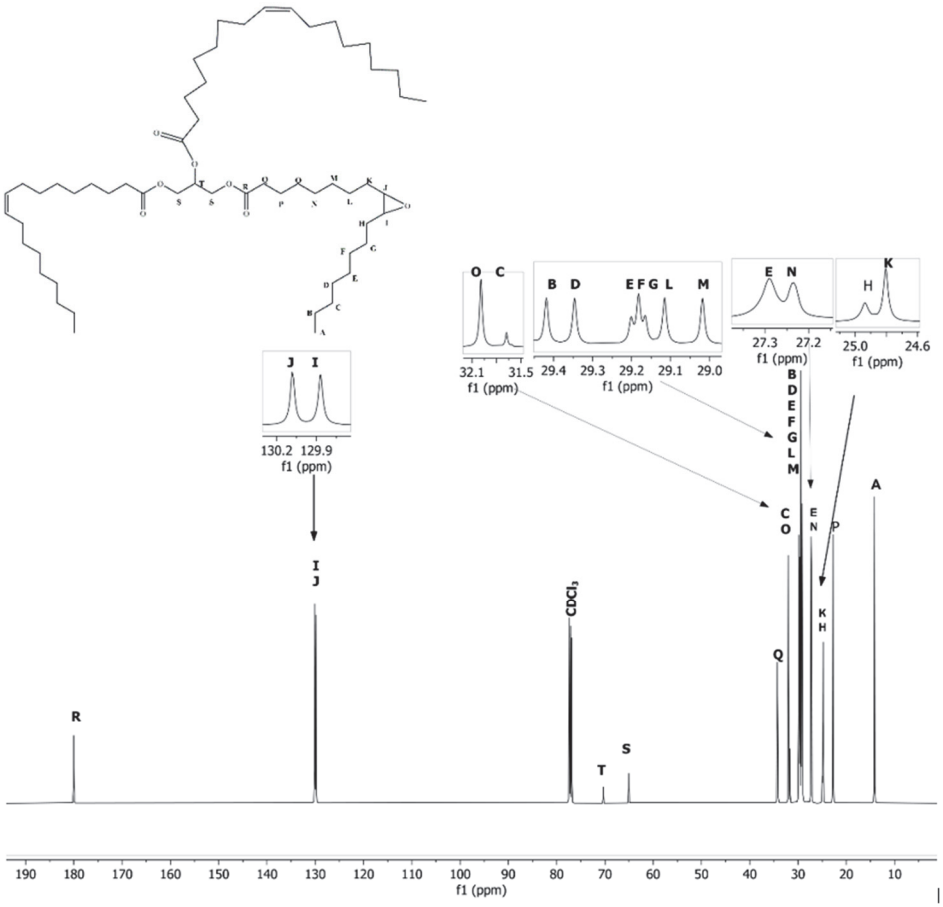

Fig. S-13. ^{13}C-NMR spectra of trioleate

Synthesized trioleate: Trioleate ($C_{57}H_{104}O_6$) product was obtained as a yellow liquid (7.08 g, 80%). FTIR (ν, cm^{-1}): 3008 (C–H sp^2), 2924 and 2854 (C–H sp^3), 1736 (C=O), 1658 (C=C sp^2), 1458 and 1435 (–CH_2– sp^3), 1357 (–CH_3 sp^3), 1172 (C–O ester), 725 (–CH_2– sp^3).

(CC) 2026 Serbian Chemical Society.

SYNTHESIZED DIOLEATE EPOXIDE

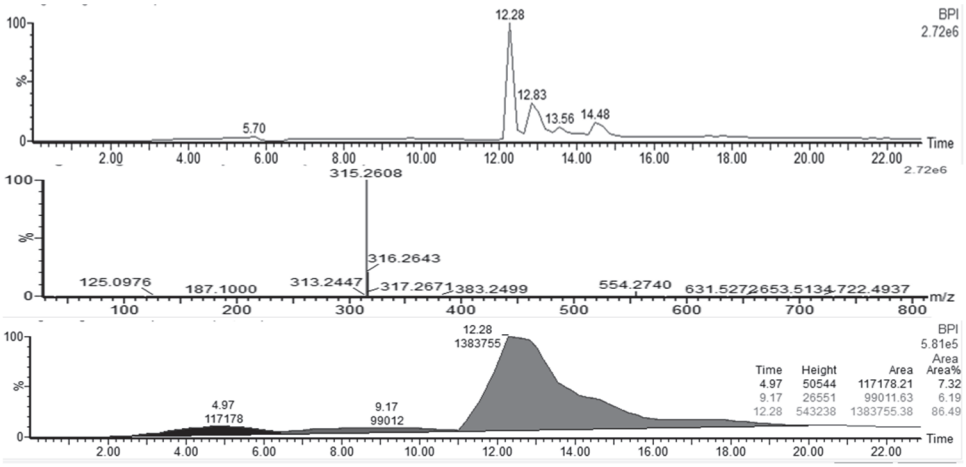

Fig. S-14. LC chromatograms and mass spectrum of dioleate epoxide

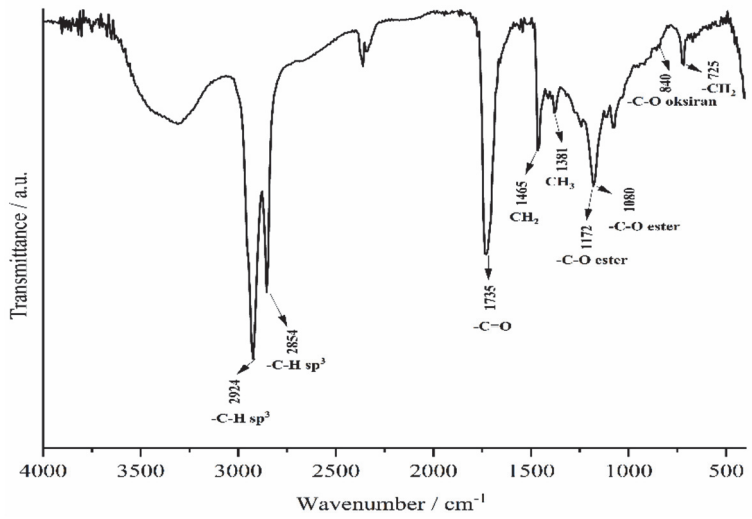

Fig. S-15. FTIR spectra of dioleate epoxide

(CC) 2026 Serbian Chemical Society.

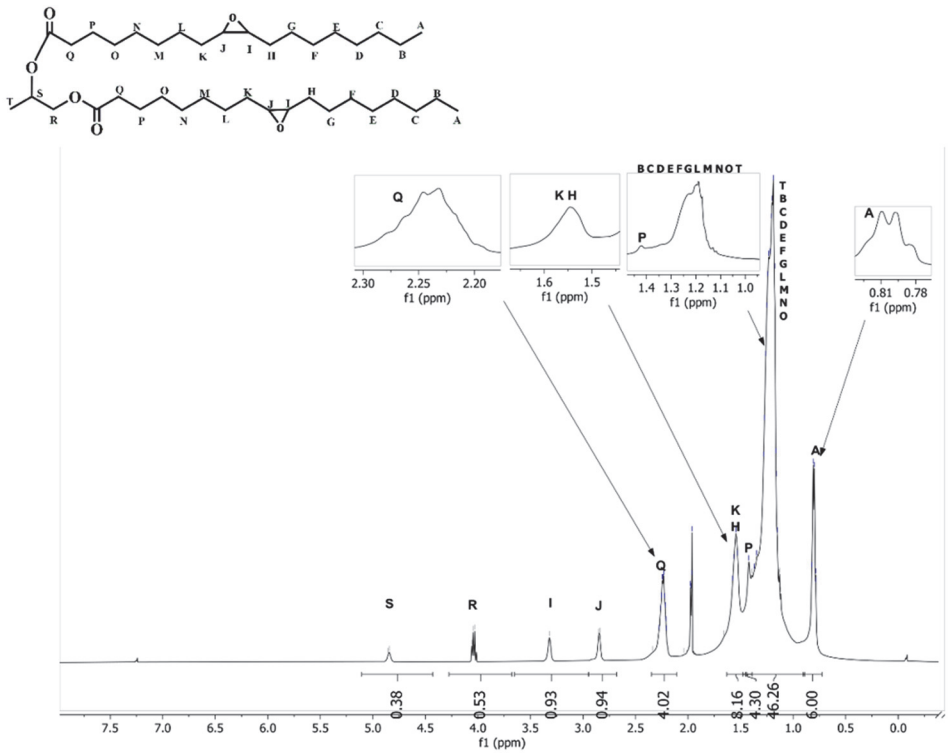

Fig. S-16. ^{1}H-NMR spectra of dioleate epoxide

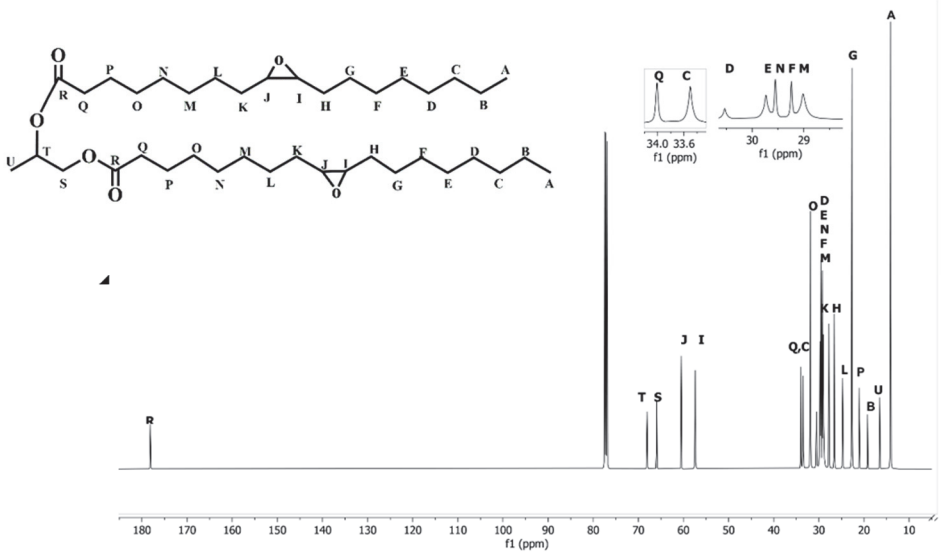

Fig. S-17. ^{13}C-NMR spectra of dioleate epoxide

(CC) 2026 Serbian Chemical Society.

Dioleate epoxide: Dioleate epoxide ($C_{39}H_{72}O_6$) product was obtained as a white solid (0.6 g, 94.49 %). FTIR (ν, cm^{-1}): 2924 and 2854 (C–H sp^3), 1735 (C=O ester), 1465 (–CH_2– sp^3), 1381 (–CH_3 sp^3), 1172 (C–O ester), 840 (C–O oxirane), 725 (–CH_2– sp^3). LC-MS: dioleate epoxide (86.49% purity, t_R 12.28 min, MS: 722 ([M+CH_3CN+HCOO]$^-$). ^{1}H-NMR (CD_3OD, 500 MHz, δ/ppm): 0.80 (6H, 2 –CH_3 oleate, *triplet*, *J* = 7 Hz), 1.23–1.27 (43H, 20 –CH_2–, –CH_3 1,2-propanediol, *multiplet*), 1.40 (4H, –C**H$_2$**–CH_2–C=O, *quintet*, *J* = 5.5 Hz), 1.55 (8H, 2 –C**H$_2$**–CH–O–CH–C**H$_2$**–, *quartet*, *J* = 8 Hz), 2.25 (4H, 2 –CH_2–C=O, *triplet*, *J* = 7.2 Hz), 2.85 and 3.32 (4H, 2 –CH–O–CH– oxirane, *multiplet*), 4,04 (2H, –CH_2–, multiplet) and 4,84 (1H, –CH–, multiplet). ^{13}C-NMR (CD_3OD, 125 MHz, δ/ppm): 14.18 (–CH_3 oleate), 24.81 (–CH_3 propanediol), 24,94, 27.24, 27.29, 29.17, 29.25, 29.41, 29.61, 29.77, 29.85, 29.73, 30.53, 31.88, 33.50, 34.01 (–CH_2– oleate), 65.95 (–CH_2– propanediol), 57.41 and 57.50 (–CH– oxirane), 68.07 (–CH– propanediol), and 178.13 (C=O).

SYNTHESIZED TRIOLEATE EPOXIDE

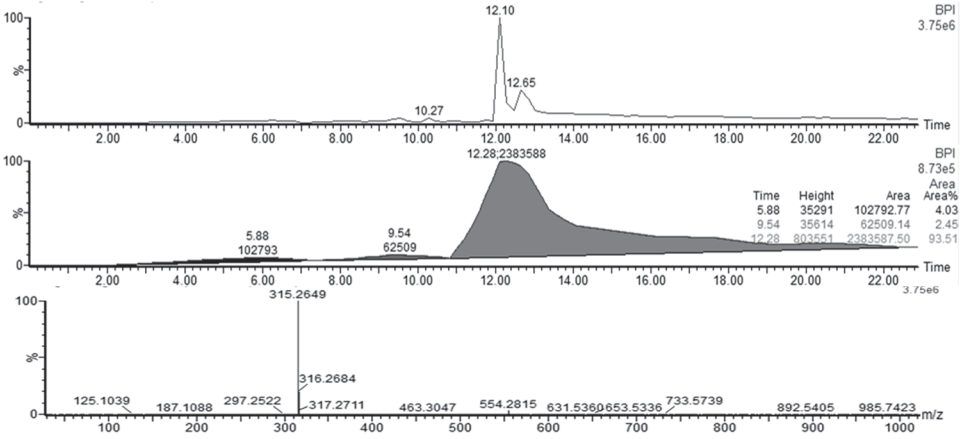

Fig. S-18. LC chromatograms and mass spectrum of trioleate epoxide

(CC) 2026 Serbian Chemical Society.

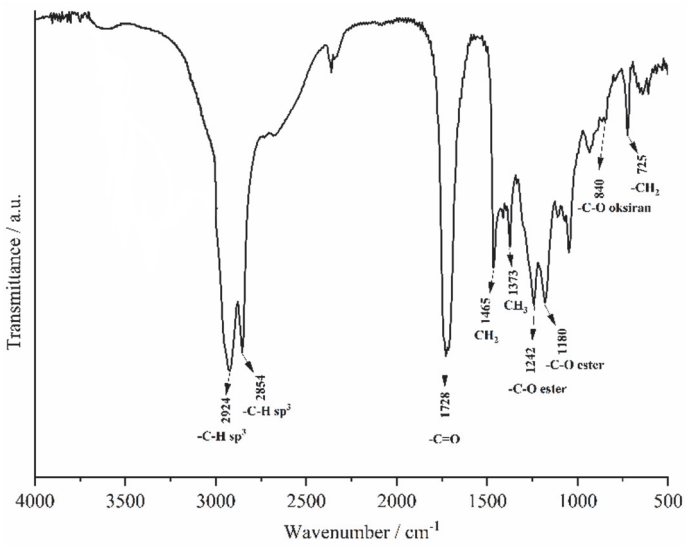

Fig. S-19. FTIR spectra of trioleate epoxide

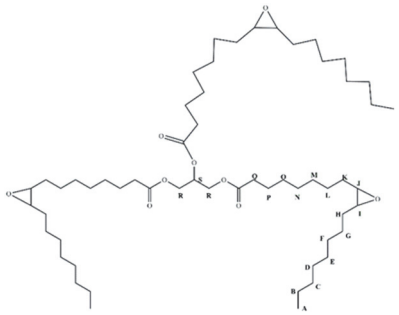

(CC) 2026 Serbian Chemical Society.

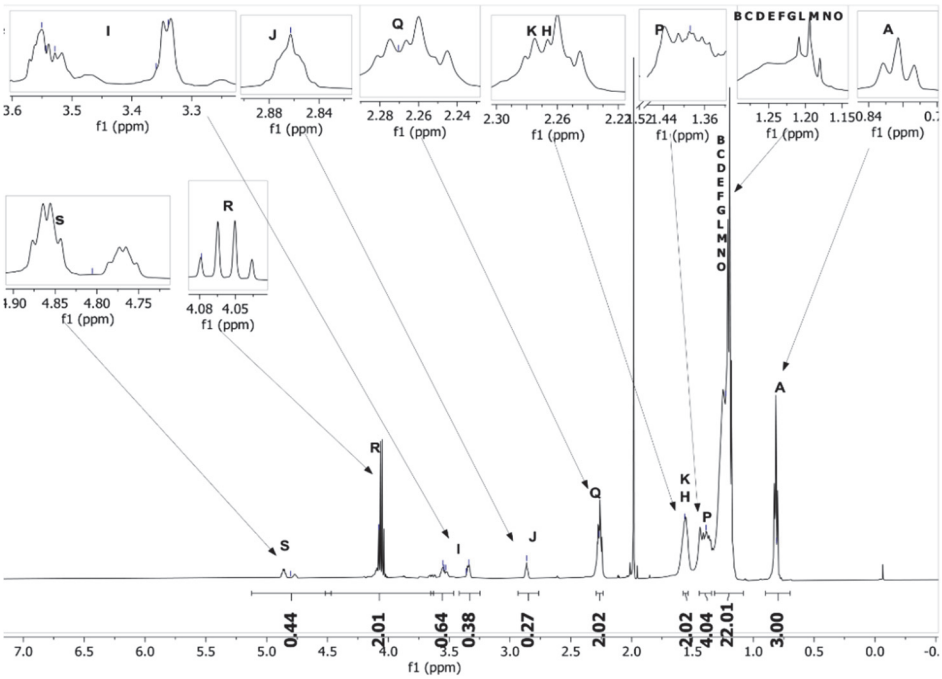

Fig. S-20. ^{13}H-NMR spectra of trioleate epoxide

(CC) 2026 Serbian Chemical Society.

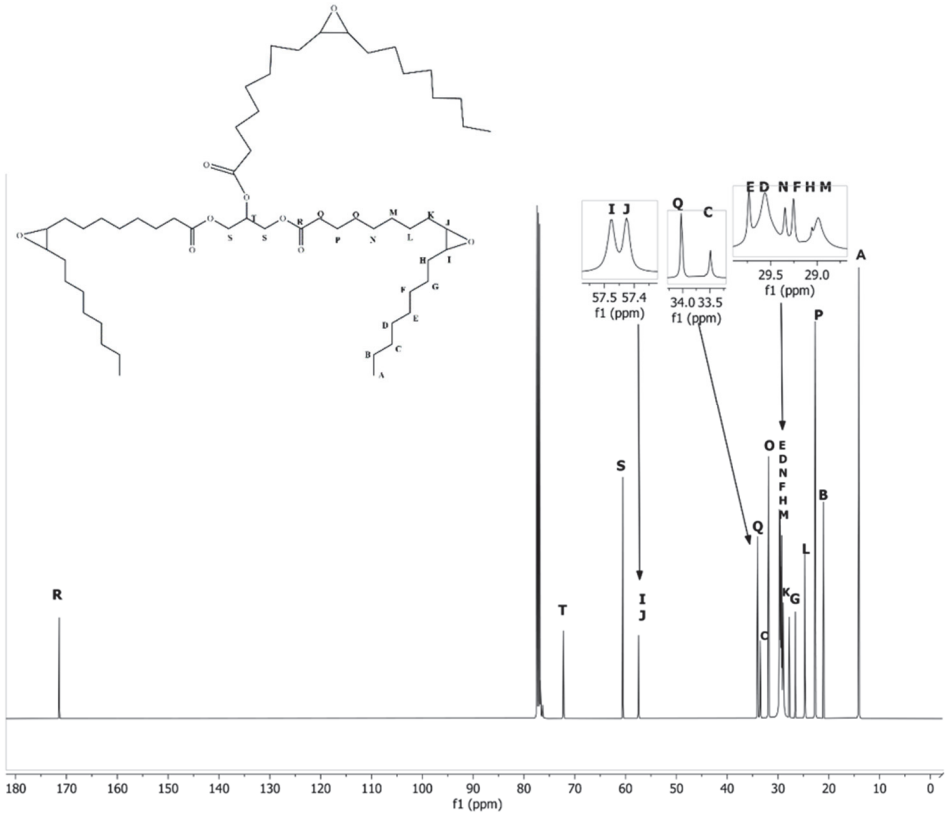

Fig. S-21. ^{13}C-NMR spectra of trioleate epoxide

Trioleate epoxide: Trioleate epoxide ($C_{57}H_{104}O_9$) product was obtained as a white solid (0.81 g, 92.04%). FTIR (ν, cm^{-1}): 2924 and 2854 (C–H sp^3), 1728 (C=O ester), 1465 (–CH_2– sp^3), 1373 (–CH_3 sp^3), 1242 (C–O ester), 840 (C–O oxirane), 725 (–CH_2– sp^3). LC-MS: trioleate epoxide (93.51% purity, t_R 12.10 min, MS: 985 $[M+NH_4Cl]^-$). ^{1}H-NMR (CD_3OD, 500 MHz, δ/ppm): 0.81 (9H, 3 –CH_3 oleate, *triplet*, J = 7 Hz), 1.21–1.25 (60H, 30 –CH_2–, *multiplet*), 1.40 (6H, 3 –C**H$_2$**–CH_2–C=O, *multiplet*), 1.56 (12H, 3 –C**H$_2$**–CH–O–CH–C**H$_2$**–, *quartet*, J = 8.3 Hz), 2.26 (6H, 3 –CH_2–C=O, *triplet*, J = 7.2 Hz), 2.87 and 3.34 (6H, 3 –CH–O–CH– oxirane, *multiplet*), 4,06 (4H, –CH_2– glycerol, multiplet), and 4,81 (1H, –CH– glycerol, multiplet). ^{13}C-NMR (CD_3OD, 125 MHz, δ/ppm): 14.14 (–CH_3), 21.06, 22.70, 24.72, 26.60, 27.79, 28.99, 29.05, 29.25, 29.35, 29.56, 29.73, 31.89, 33.49, and 34.03 (–CH_2– oleate), 57.43 and 57.48 (–CH– oxirane), 60.53 (–CH_2– glycerol), 72.24 (–CH– glycerol), and 171.44 (C=O).

(CC) 2026 Serbian Chemical Society.

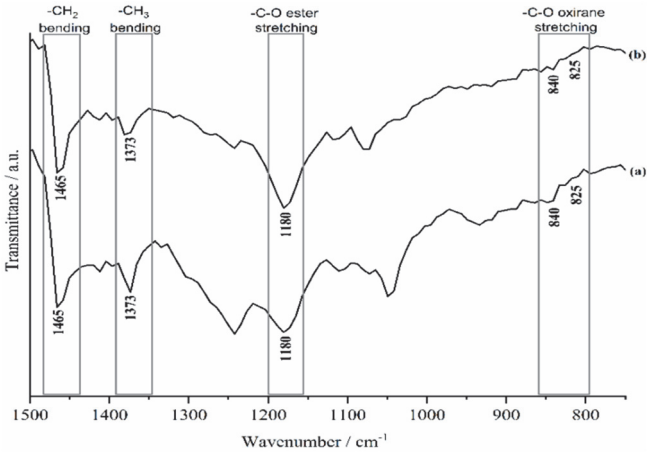

Fig S-22. FTIR profile spectra at 1500–750 cm^{-1} of (a) dioleate epoxide and (b) trioleate epoxide

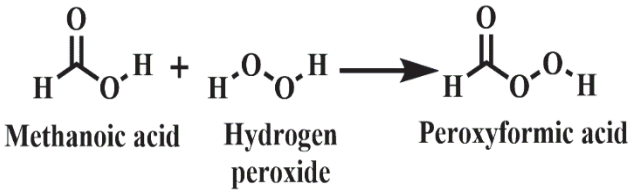

Fig S-23. Reaction scheme of performic acid

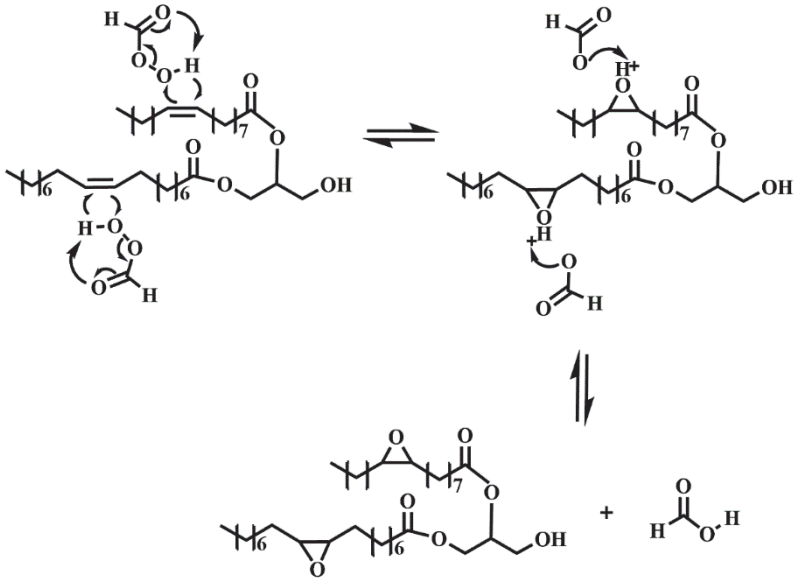

Fig S-24. Reaction scheme of the synthesis of dioleate

(CC) 2026 Serbian Chemical Society.

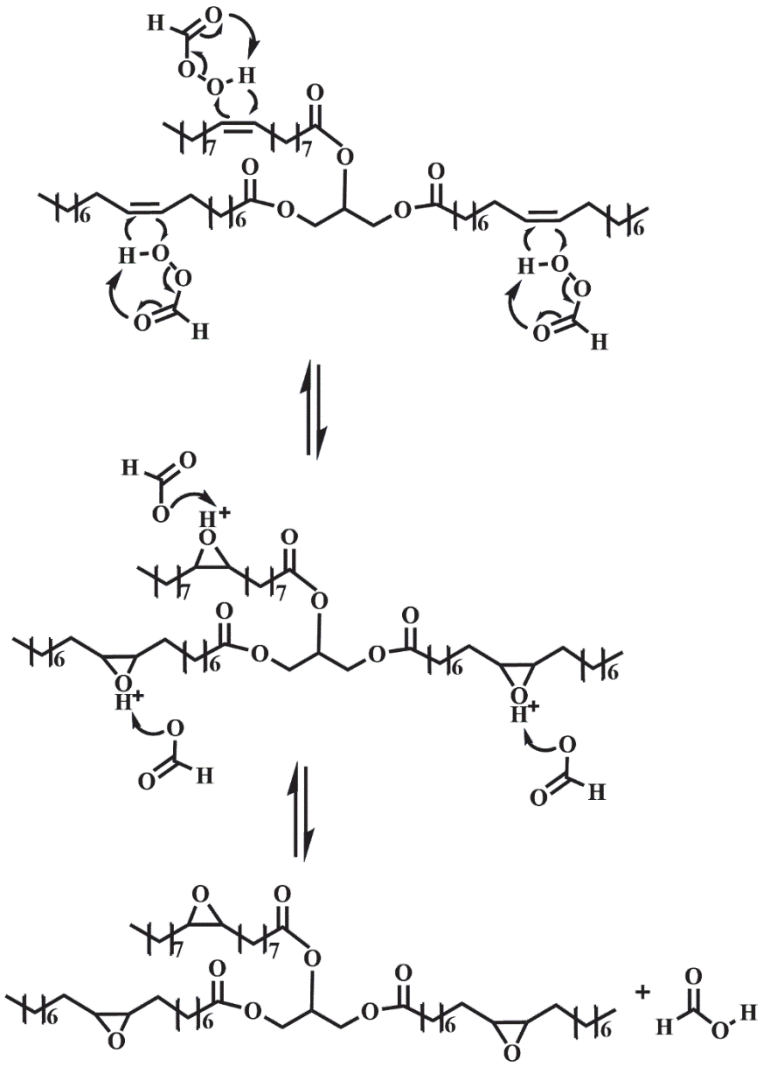

Fig S-25. Reaction scheme of the synthesis of trioleate

(CC) 2026 Serbian Chemical Society.

LINEAR REGRESSION OF DIOLEATE EPOXIDE CYTOTOXIC EVALUATION

Table S-I. Table concentration of dioleate epoxide versus cell viability

Concentration (ppm)	Log concentration	Cell viability (%)		
		T47D	WiDr	Vero
6.25	0.796	64.18	60.39	86.54
12.5	1.097	55.74	52.17	78.02
25	1.398	51.48	54.11	86.71
50	1.699	43.57	45.41	75.98
100	2.000	32.85	39.13	78.88
200	2.301	27.83	31.40	66.95
400	2.602	16.58	26.81	32.88

Table S-II. IC_{50} and SI values of dioleate epoxide

Cells	Linear regression equation	IC_{50} (ppm)	SI
T47D	y = -0.1062x + 53.787 R^2 = 0.8159	35.66	8.16
WiDr	y = -0.0777x + 52.953 R^2 = 0.8006	38.25	7.60
Vero	y = -0.1062x + 53.787 R^2 = 0.8159	291,04	

Linear Regression of Trioleate Epoxide Cytotoxic Evaluation

Table S-III. The concentration of trioleate epoxide versus cell viability

Concentration (ppm)	Log conc.	Cell viability (%)		
		T47D	WiDr	Vero
6.25	0.796	62.36	62.08	89.27
12.5	1.097	56.73	56.04	79.05
25	1.398	51.56	53.62	73.25
50	1.699	39.47	43.96	73.25
100	2.000	34.60	32.61	79.90
200	2.301	25.48	23.19	64.40
400	2.602	16.81	17.15	39.95

(CC) 2026 Serbian Chemical Society.

Table S-IV. IC_{50} and SI values of trioleate epoxide

Cells	Linear regression equation	IC_{50} (ppm)	SI
T47D	y = -0.1046x + 52.866 R^2 = 0.8016	27.40	10.87
WiDr	y = -0.0977x + 50.585 R^2 = 0.8148	38.41	9.19
Vero	y = -0.1123x + 83.458 R^2 = 0.8839	297.93	

(CC) 2026 Serbian Chemical Society.

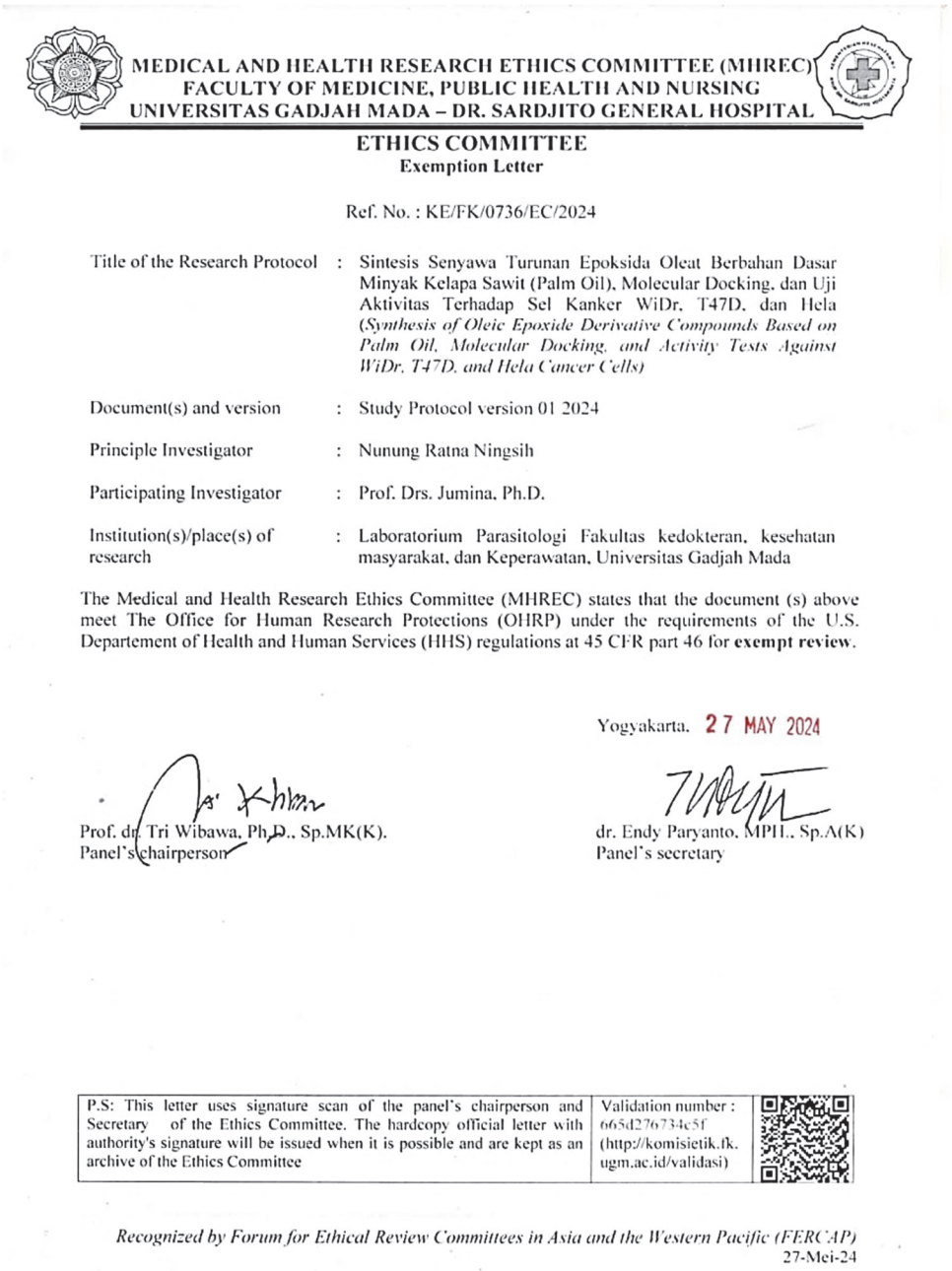

MEDICAL AND HEALTH RESEARCH ETHICS COMMITTEE (MHREC)
FACULTY OF MEDICINE, PUBLIC HEALTH AND NURSING
UNIVERSITAS GADJAH MADA – DR. SARDJITO GENERAL HOSPITAL

ETHICS COMMITTEE
Exemption Letter

Ref. No. : KE/FK/0736/EC/2024

Title of the Research Protocol	:	Sintesis Senyawa Turunan Epoksida Oleat Berbahan Dasar Minyak Kelapa Sawit (Palm Oil), Molecular Docking, dan Uji Aktivitas Terhadap Sel Kanker WiDr, T47D, dan Hela (*Synthesis of Oleic Epoxide Derivative Compounds Based on Palm Oil, Molecular Docking, and Activity Tests Against WiDr, T47D, and Hela Cancer Cells*)
Document(s) and version	:	Study Protocol version 01 2024
Principle Investigator	:	Nunung Ratna Ningsih
Participating Investigator	:	Prof. Drs. Jumina, Ph.D.
Institution(s)/place(s) of research	:	Laboratorium Parasitologi Fakultas kedokteran, kesehatan masyarakat, dan Keperawatan, Universitas Gadjah Mada

The Medical and Health Research Ethics Committee (MHREC) states that the document (s) above meet The Office for Human Research Protections (OHRP) under the requirements of the U.S. Departement of Health and Human Services (HHS) regulations at 45 CFR part 46 for **exempt review**.

Yogyakarta, 27 MAY 2024

Prof. dr. Tri Wibawa, Ph.D., Sp.MK(K).
Panel's chairperson

dr. Endy Paryanto, MPH., Sp.A(K)
Panel's secretary

P.S: This letter uses signature scan of the panel's chairperson and Secretary of the Ethics Committee. The hardcopy official letter with authority's signature will be issued when it is possible and are kept as an archive of the Ethics Committee	Validation number : 665d276734c5f (http://komisietik.fk.ugm.ac.id/validasi)

Recognized by Forum for Ethical Review Committees in Asia and the Western Pacific (FERCAP)
27-Mei-24

Fig S-26. Ethical clearance approval letter for cytotoxic evaluation

(CC) 2026 Serbian Chemical Society.

Journal of the Serbian Chemical Society
JSCS-info@shd.org.rs • www.shd.org.rs/JSCS
J. Serb. Chem. Soc. 91 (10) 995–1006 (2026)
JSCS–5540
Original scientific paper
Published 9 November, 2026

Investigation of the isomorphic P–V substitution in the structure of calcium hydroxyapatite by X-ray and spectral methods

ELENA L. TIKHONOVA, TAISIYA D. BOLKHOVSKAYA, POLINA V. KORTIKOVA and EVGENY N. BULANOV*

Lobachevsky University, 23 Gagarin ave., Nizhny Novgorod, 603022, Russia

(Received 1 May, revised 20 May, accepted 28 August 2026)

Abstract: The paper considers the possibility of forming a continuous series of solid solutions in the binary system $Ca_{10}(PO_4)_6(OH)_2$–$Ca_{10}(VO_4)_6(OH)_2$, the extreme members of which belong to the structural type of apatite. The objects of the study were obtained by solid-phase reaction, the monophasicity of the products was confirmed by powder X-ray and IR spectroscopy. The detected anomalous deviations of the dependence of unit cell parameters on linearity (Vegard's rule) confirm the hypothesis of a possible ordering of phosphorus and vanadium atoms in solid solutions. The constancy of the volumetric coefficient of thermal expansion of the composition $Ca_{10}(PO_4)_3(VO_4)_3(OH)_2$ has been established with a change in temperature.

Keywords: apatite; isomorphism; phase analysis; IR spectroscopy; *in situ* thermo X-ray diffraction.

INTRODUCTION

Materials based on stoichiometric synthetic calcium hydroxyapatite $Ca_{10}(PO_4)_6(OH)_2$ are currently considered as the basis for the creation of implants for bone restoration due to the crystallochemical identity of native bone.[1,2]

However, despite the proximity of the structure and composition parameters, such materials do not meet the requirements of resorbability after implantation.[3,4] In addition, there are more general problems associated with the implantation of materials, such as the risk of periprosthetic infection. Currently, antibiotics added to the implant material or applied to the surgical site on a resorbable carrier are used to eliminate this risk factor.[5,6] This approach is also not without drawbacks – it is difficult to control the dosage of antibiotics and their toxic effect on the body.

To solve these problems, a number of scientific groups are developing approaches for chemical modification of the hydroxyapatite matrix to form additional

* Corresponding author. E-mail: bulanoven@chem.unn.ru
https://doi.org/10.2298/JSC260501053T

Available online at https://www.shd.org.rs/JSCS/
(CC) 2026 Serbian Chemical Society.

properties of the material, including increased strength, improved resorbability, antibacterial properties, *etc.*[7]

However, works focused on achieving specific properties, as a rule, have the disadvantage of lacking a theoretical foundation for the possibility of such modifications of compositions from the point of view of the crystallochemical features of the system, which leads to a phenomenological description of the results.[8,9]

In this paper, the theoretical and practical possibility of modifying synthetic hydroxyapatite with vanadium which is considered one of the most promising antimicrobial agents, including being a necessary ultramicroelement for the formation and normal functioning of solid tissues of the human body.[10] In addition, thermal deformations of the crystal structure during isomorphic P–V substitution have been studied, and the results are necessary in the development of ceramic materials based on the solid solutions under consideration as well as modelling their behaviour at varying temperatures.

EXPERIMENTAL

Individual compounds of the compositions $Ca_{10}(PO_4)_6(OH)_2$ and $Ca_{10}(VO_4)_6(OH)_2$ were considered as the object of the study. The possibility of obtaining a continuous series of solid solutions of the composition $Ca_{10}(PO_4)_{6-x}(VO_4)_x(OH)_2$ was also studied (x from 0 to 6, step 1).

The synthesis of individual compounds and solid solutions was carried out by the solid phase reaction method according to the reaction scheme indicated below:

$$9Ca(NO_3)_2 \cdot 4H_2O + Ca(OH)_2 + (6-x)(NH_4)_2HPO_4 + xNH_4VO_4 \rightarrow$$
$$\rightarrow Ca_{10}(PO_4)_{6-x}(VO_4)_x(OH)_2 + \text{gaseous products}$$

The reagent mixture was weighed (analytical electronic scales BEL DA-723C, BEL Engineering, weighing accuracy ±0.001 g) in the required stoichiometric ratio, placed in a porcelain crucible and heated to a temperature of 150 °C, since calcium nitrate tetrahydrate begins to dissolve in its own water at a temperature of 42.7 °C and finally loses crystallization water at 132 °C; the decomposition temperatures of ammonium metavanadate and ammonium dihydrogen phosphate are 138 °C and 100–155 °C, respectively. Next, the temperature was raised at a rate of 25 °C/h to 600 °C, followed by exposure at 600 °C for 6 h to decompose calcium nitrate. Further heat treatment involved stepwise heating to 1000 °C in increments of 100 °C with exposure for 6–8 h, dispersion in an agate mortar and control using X-ray diffraction at each stage. At a temperature of 1000 °C, the samples were calcined for 12 h.

The proposed approach is based on our previous studies on the synthesis of solid solutions with an apatite-type structure, including those involving the substitution of phosphate ions by vanadate groups.[10-14] The periodic alternation of heating and grinding cycles helps to prevent the formation of secondary phases and to control the reaction rate. In essence, this constitutes a necessary condition for carrying out the synthesis of solid solutions under uniform conditions, since the end-member compositions are obtained at lower temperatures, whereas the intermediate compositions require higher temperatures. Therefore, the final synthesis temperature was chosen as the minimum temperature at which all of the investigated solid solutions can be obtained.

The chemical purity and elemental composition of the prepared samples were examined by energy-dispersive X-ray fluorescence analysis carried out in air on a long-wavelength

(CC) 2026 Serbian Chemical Society.

dispersive X-ray fluorescence spectrometer (Shimadzu LAB Center XRF-1800). The quantification was performed using the fundamental parameters (FP) approach with a single certified reference material. The Kα emission line intensities were recorded in triplicate at an accelerating voltage of 40 kV and a tube current of 50 mA, employing a Rh anode, as well as flow proportional counter (FPC) and scintillation (SC) detectors.

X-ray phase analysis was performed using a Shimadzu XRD-6000 powder diffractometer (CuKα radiation, λ = 1.5406 Å, Bragg–Brentano focusing, 2θ 10–60°, scanning speed 2°/min). The Topas 3.0 software package was used for processing the results.[15] X-ray diffraction data of individual compounds $Ca_{10}(PO_4)_6(OH)_2$[16] (this model is a more general case of the hydroxyapatite structure, because the oxygen of the OH group is specified in position 4*e* rather than 2*a*/2*b*) and $Ca_{10}(VO_4)_6(OH)_2$,[17,18] with the apatite structure were used as models for phase analysis as well as other substances that can be formed in the system under consideration under the specified synthesis conditions (α-$Ca_2P_2O_7$,[19] β-$Ca_2P_2O_7$,[20] α-$Ca_3(PO_4)_3$,[21] β-$Ca_3(PO_4)_3$[22] and $Ca_3(VO_4)_3$[23]).

Scanning electron microscopy (SEM) in the secondary electron detection mode (Signal A = = SE1) was used to obtain surface images of all compounds under study. Instrumental parameters: accelerating voltage 8.00 kV, probe current 2 pA. The SE1 mode provides high topographic contrast, which is ideally suited for examining the surface morphology of powder particles.

Determination of thermal expansion features of compounds under investigation realized using Shimadzu HA-1001 attachment (for the same diffractometer) in the range of 2θ angles from 10 to 60° with 100K step. Thermal expansion of compounds under study was analyzed using program complex ThetaToTensor 2.0.[24]

The IR spectra of the study objects were recorded on a Shimadzu FTIR Prestige-21 spectrometer (wavelength range 400–4000 cm^{-1}, signal accumulation – 20 scans) from suspensions in petroleum jelly placed between ZnSe plates. The assignment of vaseline bands was carried out using the AIST Spectral Database for Organic Compounds.[25]

RESULT AND DISCUSSION

As it follows from Table I the composition of the resulting compounds was confirmed to be stoichiometric within a relative error of no more than 0.5 %.

TABLE I. X-Ray fluorescence analysis data (wt. %) for $Ca_{10}(PO_4)_{6-x}(VO_4)_x(OH)_2$ samples (*x* from 0 to 6)

x	CaO		P_2O_5		V_2O_5	
	Calcd.	Found	Calcd.	Found	Calcd.	Found
0	55.8	55.8	42.4	42.4	0	0
1	54.7	54.7	34.6	34.6	8.9	8.8
2	53.7	53.6	27.2	27.2	17.4	17.5
3	52.7	52.7	20.0	20.1	25.6	25.6
4	51.7	51.8	13.1	13.0	33.5	33.5
5	50.8	50.7	6.4	6.2	41.2	41.1
6	49.9	49.9	0	0	48.5	48.6

According to the results of the X-ray diffraction analysis, the $Ca_{10}(PO_4)_6(OH)_2$–$Ca_{10}(VO_4)_6(OH)_2$ system is characterized by the formation of a continuous series

(CC) 2026 Serbian Chemical Society.

of solid solutions over the entire range of the studied compositions at temperatures above 1000 °C, as evidenced by the characteristic diffraction pattern of the structural type of apatite, which changes monotonously with changes in the composition of the object (Fig. 1). The observed shift of the diffraction maxima toward lower 2θ angles with increasing vanadium content is in full agreement with the previously established unit cell parameters for the individual compounds,[16–18] as well as with the Bragg–Wolff equation, which describes the inverse relationship between the interplanar spacing (and, consequently, the lattice parameters) and the diffraction angle.

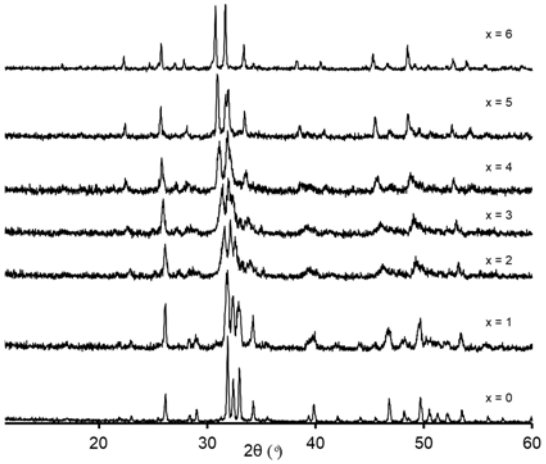

Fig. 1. XRD patterns of $Ca_{10}(PO_4)_{6-x}(VO_4)_x(OH)_2$ samples (x, 0–6) after calcination at 1000 °C.

The monophasicity of the obtained samples is confirmed not only by the absence of diffraction peaks impurity phases, but also with the results of the analysis of IR spectra recorded after calcination of substances at 1000 °C (Figs. 2 and 3).

Despite the presence of bands in the spectra in the wavenumber ranges of 650––150 and 1300–1500 cm^{-1} due to the presence of petroleum jelly oil in the system, the identification of the main modes of the phosphate and vanadates under consideration can be carried out unambiguously. Thus, in the recorded spectra, the following are observed:

– stretching modes of slightly distorted phosphate tetrahedra ($\nu(PO_4^{3-})$) in the range of wavenumbers of 900–1150 cm^{-1},

– deformation modes of phosphate tetrahedra ($\delta(PO_4^{3-})$) in the range of wavenumbers of 500–150 cm^{-1} and

– stretching modes of vanadium tetrahedra ($\nu(VO_4^{3-})$) in the range of wavenumbers of 750–930 cm^{-1}.

The bands of deformation modes of vanadium tetrahedra are not visible, since they are outside the range of operation of the used spectrometer (below 400 cm^{-1}).[26]

(CC) 2026 Serbian Chemical Society.

At the same time, bands of pyrophosphate ($P_2O_7^{4-}$)[27] and pyrovanadate groups ($V_2O_7^{4-}$)[28] are not observed.

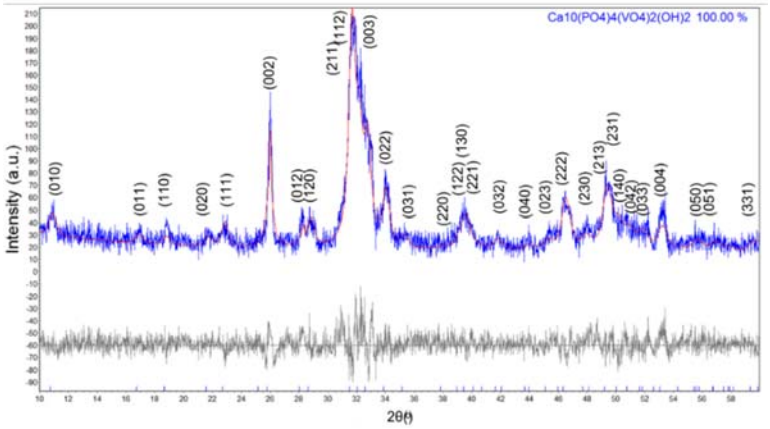

Fig. 2. X-Ray phase analysis of the solid solution of composition $Ca_{10}(PO_4)_4(VO_4)_2(OH)_2$ with Miller indices assigned to the diffraction maxima of the apatite phase (blue – experimental diffraction pattern, red – simulated pattern, grey – difference pattern, blue triangles – positions of diffraction maxima).

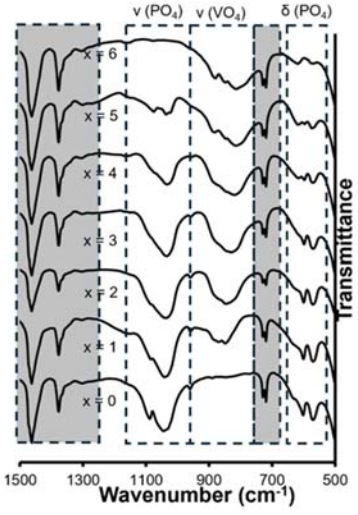

Fig. 3. IR spectra of $Ca_{10}(PO_4)_{6-x}(VO_4)_x(OH)_2$ samples (x, 0–6); grey colour indicates the areas of vibrations of the functional groups of petroleum jelly.

The morphology of a powdered sample was investigated using SEM at a magnification of 5000×. All samples under study were found to consist of polydisperse, irregularly shaped particles, predominantly in the size range of 0.5 to 7 μm, with a tendency to form loose agglomerates. The particle surfaces display pronounced micro-roughness, indicative of a high specific surface area. The uniform contrast and the absence of bright inclusions suggest compositional homogeneity (Fig. 4).

(CC) 2026 Serbian Chemical Society.

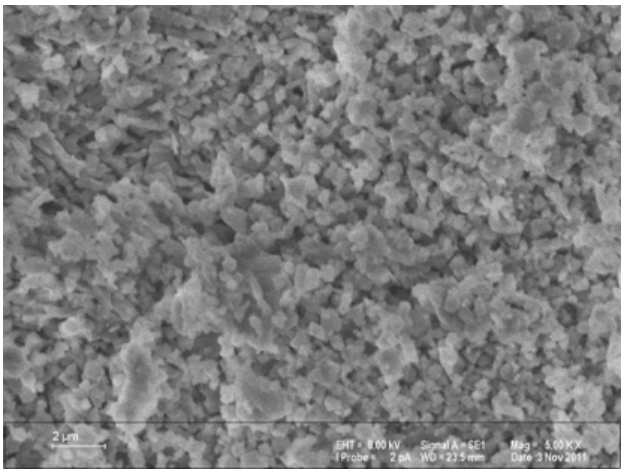

Fig. 4. Typical scanning electron microscopy (SEM) image of the powdered sample of $Ca_{10}(PO_4)_3(VO_4)_3(OH)_2$ (SE1 mode).

Based on the analytical indexing of powder XRD patterns, the dependences of the parameters of the unit cells of the objects of study on the composition were calculated.

As can be seen from Fig. 5, deviations from both the Vegard rule and the Retgers rule are observed in this system.

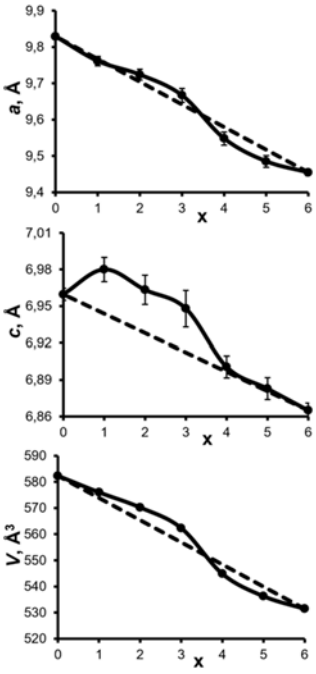

Fig. 5. Dependences of the unit-cell parameters of the of samples $Ca_{10}(PO_4)_{6-x}(VO_4)_x(OH)_2$ (x, 0–6, step 1) on the composition (the dotted line shows the theoretical dependencies in accordance with the rules of Vegard and Retgers).

(CC) 2026 Serbian Chemical Society.

Positive deviations from the empirical rules of isomorphism are observed for compositions $0 < x < 3$, *i.e.*, when phosphate ions are introduced into the calcium hydroxyvanadate matrix. A similar situation was observed with the substitution of phosphate and vanadium ions in the structure of $Pb_{10}(AO_4)_6Cl_2$.[11] Subsequently, this apparent contradiction to the Goldschmidt–Fersman principle of directed substitution[29] was hypothetically explained by the ordering of phosphate and vanadium tetrahedra, indirectly experimentally confirmed by the anomalous thermal expansion of a solid solution of the composition $Pb_{10}(PO_4)_3(VO_4)_3Cl_2$.[30]

The minimal deviations from linearity in the dependences for parameters *a* and *V* indicate that atomic substitutions in the tetrahedral position of the crystal structure of apatite (even at $\Delta r/r = 1$ for phosphorus and vanadium)[31,32] do not affect the size of atomic layers perpendicular to the direction *c* (Fig. 6), which is determined in this structural type exclusively by the cationic sublattice.

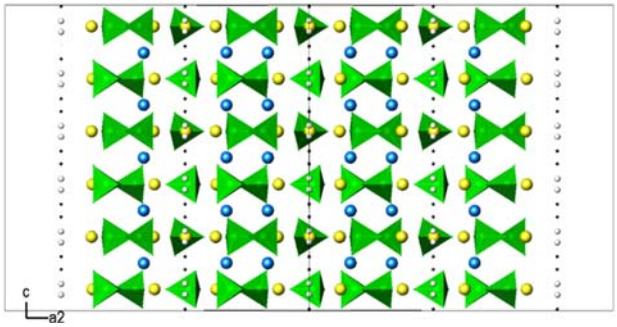

Fig. 6. Fragment of the crystal structure of $Ca_{10}(PO_4)_6(OH)_2$: the blue spheres are Ca cations at 4*f* position, the yellow ones are Ca cations at 6*h* position, the white ones are oxygens of hydroxyl groups and the black ones are hydrogens of hydroxyl groups. Orthophosphate groups are represented as polyhedra.

The study of thermal deformations of the crystal structure of synthesized solid solutions also confirms the hypothesis of the ordering of tetrahedral groups PO_4 and VO_4 (Table II, Fig. 7). The typical values and linear dependences of the volumetric coefficients of thermal expansion[33,34] for the extreme terms of the series degenerate into a constant α_V with a temperature change in the composition $Ca_{10}(PO_4)_3(VO_4)_3(OH)_2$.

Possible variants of the structure ordering are shown in Fig. 8. Option **a**, similar to the result of the "order-disorder" transition in the Cu–Au alloy,[35] seems less likely, as does option **b**. In the case of variant **c**, a tetrahedron vanadate layer "isolated" from phosphate arises, which, due to the greater deformability of the electron shell of vanadium atoms compared to phosphorus, will ensure not only the stability of volumetric thermal expansion, but also the predominance of expansion along the crystallographic direction *a* compared to the direction *c*, which is typical for purely vanadic apatites.

(CC) 2026 Serbian Chemical Society.

TABLE II. Thermal dependencies of unit-cell parameters and linear and volumetric thermal expansion coefficients for apatites under study

T/K	a/Å	$\alpha_a/10^{-6}$ K^{-1}	c/Å	$\alpha_c/10^{-6}$ K^{-1}	V/Å^3	$\alpha_V/10^{-6}$ K^{-1}
			$x = 0$			
298	9.829(1)	7.1(5)	6.9596(8)	10.3(9)	582.2(1)	24.4(1)
373	9.836(1)	8.6(4)	6.967(1)	12.4(7)	583.7(1)	29.5(9)
473	9.843(1)	10.6(3)	6.978(1)	15.1(5)	585.4(1)	36.4(6)
573	9.856(1)	12.7(2)	6.989(1)	17.8(4)	587.9(1)	43.1(4)
673	9.868(2)	14.7(1)	7.001(2)	20.5(3)	590.4(2)	49.9(3)
773	9.886(2)	16.7(2)	7.016(2)	23.2(3)	593.8(2)	56.6(4)
873	9.903(2)	18.7(3)	7.032(2)	25.8(5)	597.2(2)	63.3(6)
973	9.922(2)	20.7(4)	7.053(2)	28.5(7)	601.3(2)	70.0(8)
1073	9.943(3)	22.7(5)	7.075(3)	31.1(9)	605.7(3)	76.6(1)
			$x = 1$			
298	9.7613(8)	7.9(8)	6.980(1)	8.8(5)	575.9(1)	24.6(2)
373	9.768(1)	9.4(6)	6.985(1)	10.3(4)	577.1(1)	29.2(1)
473	9.777(1)	11.5(5)	6.991(1)	12.3(3)	578.7(1)	25.4(1)
573	9.787(1)	13.6(6)	7.00(1)2	14.3(2)	580.8(1)	41.5(7)
673	9.805(2)	15.7(2)	7.013(2)	16.2(1)	583.8(2)	47.7(5)
773	9.822(2)	17.8(3)	7.025(2)	18.2(2)	586.9(2)	53.8(6)
873	9.839(2)	19.9(4)	7.038(2)	20.1(3)	590.0(2)	59.8(7)
973	9.861(3)	21.9(6)	7.053(3)	22.1(4)	593.9(3)	65.9(1)
1073	9.881(3)	23.9(7)	7.069(3)	24.0(5)	597.7(3)	71.8(3)
			$x = 2$			
298	9.7239(8)	5.9(8)	6.9633(9)	6.4(6)	570.1(1)	18.1(2)
373	9.729(1)	7.2(6)	6.968(1)	7.9(6)	571.1(1)	22.3(2)
473	9.738(1)	9.0(5)	6.974(1)	9.8(4)	572.7(1)	27.7(2)
573	9.745(1)	10.7(3)	6.980(1)	11.8(3)	574.0(1)	33.2(6)
673	9.756(2)	12.5(2)	6.991(2)	13.7(2)	576.2(2)	38.6(5)
773	9.770(2)	14.2(3)	6.999(2)	15.6(2)	578.5(2)	44.1(7)
873	9.788(2)	16.0(4)	7.013(2)	17.6(4)	581.8(2)	49.5(3)
973	9.802	17.7(6)	7.025(3)	19.5(5)	584.5(3)	54.8(4)
1073	9.819(3)	19.4(7)	7.039(3)	21.3(6)	587.7(3)	60.2(5)
			$x = 3$			
298	9.667(1)	18.0(2)	6.948(1)	6.2(5)	562.3(1)	41.1(4)
373	9.684(1)		6.951(1)		564.5(1)	
473	9.701(1)		6.95(1)		566.8(1)	
573	9.718(1)		6.958(1)		569.1(1)	
673	9.735(2)		6.962(2)		571.4(2)	
773	9.752(2)		6.9655(2)		573.7(2)	
873	9.769(2)		6.969(2)		575.9(2)	
973	9.786(3)		6.972(3)		578.2(3)	
1073	9.803(3)		6.976(3)		580.5(3)	
			$x = 4$			
298	9.5482(8)	6.3(6)	6.9006(9)	7.9(6)	544.8(1)	20.5(4)

(CC) 2026 Serbian Chemical Society.

TABLE II. Continued

T/K	a/Å	$\alpha_a/10^{-6}$ K^{-1}	c/Å	$\alpha_c/10^{-6}$ K^{-1}.	V/Å^3	$\alpha_V/10^{-6}$ K^{-1}
			$x = 4$			
373	9.552(1)	7.8(6)	6.905(1)	9.2(5)	545.6(1)	24.8(2)
473	9.560(1)	9.7(4)	6.913(1)	10.9(3)	547.1(1)	30.4(6)
573	9.571(1)	11.7(3)	6.919(1)	12.6(2)	548.8(1)	35.9(6)
673	9.582(2)	13.6(2)	6.929(2)	14.3(2)	550.9(2)	41.5(4)
773	9.599(2)	15.5(2)	6.941(2)	16.0(2)	553.8(2)	47.1(5)
873	9.612(2)	17.4(4)	6.952(2)	17.7(3)	556.2(2)	52.6(8)
973	9.632(3)	19.3(5)	6.964(3)	19.4(5)	559.5(3)	58.0(3)
1073	9.649(3)	21.2(6)	6.979(3)	21.2(5)	562.7(3)	63.5(4)
			$x = 5$			
298	9.4852(9)	4.9(7)	6.8829(9)	5.8(2)	536.2(1)	15.6(3)
373	9.489(1)	6.9(6)	6.888(1)	8.0(2)	537.1(1)	21.8(2)
473	9.498(1)	9.5(4)	6.892(1)	11.0(2)	538.4(1)	30.0(2)
573	9.505(1)	12.1(3)	6.899(1)	13.9(6)	539.7(1)	38.2(3)
673	9.521(2)	14.7(2)	6.910(2)	16.8(5)	542.4(2)	46.3(5)
773	9.535(2)	17.3(3)	6.925(2)	19.8(6)	545.2(2)	54.4(4)
873	9.553(2)	19.9(4)	6.943(2)	22.7(7)	548.7(2)	62.5(2)
973	9.575(3)	22.5(5)	6.958(3)	25.5(2)	552.4(3)	70.5(2)
1073	9.595(3)	25.1(7)	6.972(3)	28.4(4)	555.8(3)	78.5(3)
			$x = 6$			
298	9.454(1)	10.7(6)	6.865(1)	7.0(6)	531.4(1)	28.5(2)
373	9.462(1)	11.4(6)	6.866(1)	8.0(5)	532.5(1)	30.7(2)
473	9.471(1)	12.2(4)	6.874(1)	9.3(4)	534.0(1)	33.6(7)
573	9.486(1)	13.0(3)	6.880(1)	10.5(3)	536.2(1)	36.5(5)
673	9.500(2)	13.8(2)	6.889(2)	11.8(2)	538.4(2)	39.4(4)
773	9.510(2)	14.6(3)	6.898(2)	13.1(3)	540.3(2)	42.3(5)
873	9.525(2)	15.4(4)	6.906(2)	14.3(4)	542.7(2)	45.2(7)
973	9.541(3)	16.2(5)	6.915(3)	15.5(4)	545.2(3)	48.0(2)
1073	9.557(3)	17.0(6)	6.928(3)	16.8(6)	548.1(3)	50.9(2)

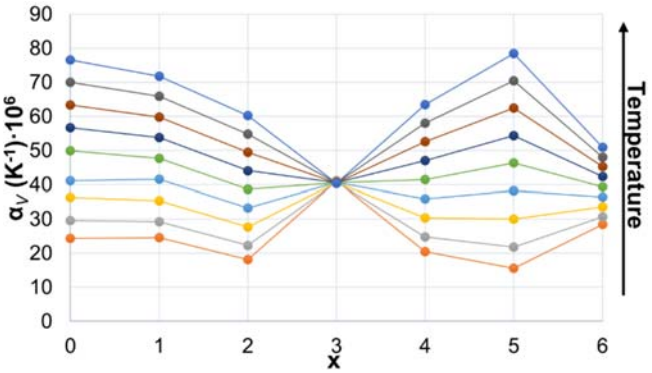

Fig. 7. Thermal dependencies of volume thermal expansion coefficient for $Ca_{10}(PO_4)_{6-x}(VO_4)_x(OH)_2$ solid solutions

(CC) 2026 Serbian Chemical Society.

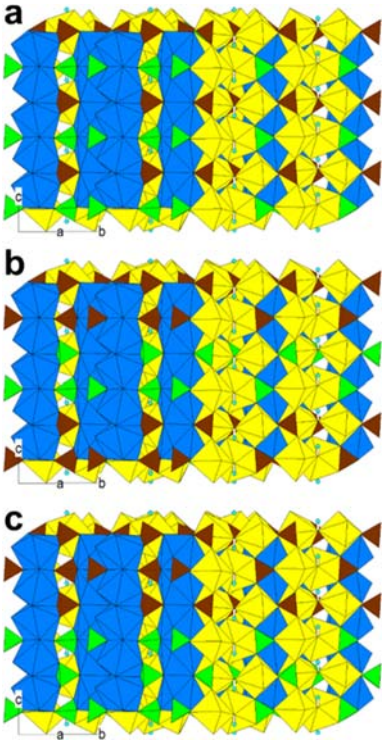

Fig. 8. Possible ordering options for phosphate (green) and vanadium (brown) tetrahedra in the crystalline structure of $Ca_{10}(PO_4)_3(VO_4)_3(OH)_2$ solid solution.

CONCLUSION

Thus, when considering the possibility of forming solid solutions in the binary system $Ca_{10}(PO_4)_6(OH)_2$–$Ca_{10}(VO_4)_6(OH)_2$ it has been established that a continuous series of phases of variable composition can be formed, despite the contradiction to the empirical rules of isomorphism (Goldschmidt's rule of 15 % difference in radii of substituted atoms). This result indicates the importance of considering isomorphic substitutions without taking into account the structural type and layout features of a particular crystal lattice.

In turn, the established continuous substitution of vanadium for phosphorus in the hydroxyapatite structure makes it possible to develop biomaterials based on substances of the chemical compositions under consideration with controlled, *i.e.*, a priori set properties.

The features of thermal deformations of the crystal structure associated with the possible ordering of isomorphically replaceable structural units make it possible to control the sintering processes of ceramic materials, avoiding the accumulation of stresses in the structure and, as a result, cracking of the material at the manufacturing stage.

Acknowledgements. The research was carried out with financial support *via* State assignment in Research scientific laboratory of "Chemistry of natural products and their synthetic

(CC) 2026 Serbian Chemical Society.

analogues", grant number FSWR-2024-0002. The authors express their sincere gratitude to the Candidate of Chemical Sciences, Assoc. Permin D.A., graduate student Krasnov M.V. for their help in conducting experiments.

ı æ ª ¹ Ø

ı ó– ı Öı ª—" Œ ı æ¹ œ ¹ °Ê ß Œ ó ö– ó Öı Öö¼ ı ‰Œ P·V ö ó Ö° ö ł Öö° ı ł—ø¼ ı ‰öœ -
-û ı Ø° ¹ ł ó ı ––– Öı Ö– – ° ı œ Œß ¹ œ °Œß ØŁŒß ó ł ı û ı ó– Œł Ö°—ø ß ı û œ Œö¹ Ø—

ELENA L.TIKHONOVA,TAISIYA D.BOLKHOVSKAYA,POLINA V.KORTIKOVA | EVGENY N.BULANOV

Lna`bgdurjx Umhudqrhsx,12 G`f`qhm `ud.,N hygmx N nufnqnc,5/2/11,Rtrrh`

ö ð½íÙ Ð ð½®ý ÇµðÐÁ½ ý ÇéÙ»ÁÇÅµ È Çðý | ð½" ½ þÇÁµ | ÁÙ | ð½ÁÇé Á | ®½ ÑúðÅµ | Š ð½ÅµúÇð½ Ù Õ | Á½ðÁÇý Å | ÅµÐý Ù C`1/ (PO4)5 (OH)1·C`1/ (VO4)5 (OH)1, Ñ | ˇ | þð½˘" | Å½Åµ½ú | ñð | ñ½í½Ù ÅµðÙ- þµÙðÁÇý µ | ñÙ ½ñ½µ | µ½. ı Åñ | µ | ú½Á | Ù®Çðõ | íÇÕ | ÐÁ | ÅÙ ðÐ½þõ | ˇÇý Ù ÑúðÅµÇˇ È ½® | , ½ ý ÇÁÇ- È ½®Á | Å½Åµ½ú ñðÇ | ®úÇí½ ñÇµúð›ÐÁ Ð ðÐÁíéÐÁÅþÇý í | È ð½þõ | ˇÇý Á½ ñð½ŠÙ | IR ÅñÐþµðÇÅþÇ- ñ | ˇÇý . öÇÑÐÁ½ ½ÁÇý½ÃÁ½ ÇíÅµÙñ½" ½ ®½ú | ÅÁÇÅµ | ñ½ð½ý Ðµ½ð½ ˇÐí | Á | ÑÁÐ »ÐÃ | Ð Çí Ã | ÁÐ½ðÁÇÅµ | (ªÐé½ðíÇúÇ ñð½ú | ÃÇ) ñÇµúð›ÙÙ ñðÐµñÇÅµ½úþÙ Ç ý ÇéÙ»Ðý ÙðÐ›Ð" Ù ½µÇý½ È ÇÅÈ Çð½ | ú½Á½í | ˇÙý½ Ù ÑúðÅµ | ý ð½ÅµúÇð | ý½. öµúð›ÐÁ½ Ð þÇÁÅµ½ÁµÁÇÅµ ®½ñðÐý | ÁÅþÇé þÇÐÈ | õ | ˇÐÁµ½µÐðý | ÑþÇéÚ | ðÐ" ½Å½Åµ½ú½ C`1/ (PO4)2 (VO4)2 (OH)1 ñð | ñðÇý ÐÁ | µÐý ñÐð½µÙðÐ.

(– ð | ý , ÐÁÇ 1.ý½˘½,ðÐú | í | ð½ÁÇ 1/.ý½˘½,ñð | Šú½»ÐÁÇ 18.½úéÙÅµ½ 1/15)

REFERENCES

1. S. V. Dorozhkin, *J. Compos. Sci.* **8** (2024) 218 (https://doi.org/10.3390/jcs8060218)
2. T. H. M. Mysore, A. Y. Patil, C. Hegde, M. A. Sudeept, R. Kumar, M. E. M. Soudagar, I. M. R. Fattah, *Eur. Polym. J.* **209** (2024) 112842 (https://doi.org/10.1016/j.eurpolymj.2024.112842)
3. T. J. Webster, E. A. Massa-Schlueter, J. L. Smith, E. B. Slamovich, *Biomaterials* **25** (2004) 2111 (https://doi.org/10.1016/j.biomaterials.2003.09.001)
4. S. Sumathi, B. Gopal, *J. Cryst. Growth* **422** (2015) 36 (https://doi.org/10.1016/j.jcrysgro.2015.04.022)
5. L. Oezel, C. Büren, A. O. Scholz, J. Windolf, C. D. Windolf, *PLoS One* **14** (2019) e0213590 (https://doi.org/10.1371/journal.pone.0213590)
6. I. Karacan, B. Ben-Nissan, J. Santos, S. Yiu, P. Bradbury, S. M. Valenzuela, J. Chou, *J. Tissue Eng. Regen. Med.* **16** (2022) 1149 (https://doi.org/10.1002/term.3353)
7. S. Shanmugam, B. Gopal, *Appl. Surf. Sci.* **303** (2014) 277 (https://doi.org/10.1016/j.apsusc.2014.02.166)
8. S. Sumathi, B. Gopal, *Ceram. Int.* **41** (2015) 4852 (https://doi.org/10.1016/j.ceramint.2014.12.043)
9. E. N. Bulanov, O. N. Golitsyna, Y. V. Ostrovskaya, M. N. Egorikhina, M. I. Zaslavskaya, D. Y. Aleynik, *Ceram. Int.* **50** (2024) 11150 (https://doi.org/10.1016/j.ceramint.2024.01.016)
10. E. N. Bulanov, K. S. Stasenko, M. N. Egorikhina, M. I. Zaslavskaya, D. Y. Aleynik, *Solid State Sci.* **151** (2024) Article number 107527 (https://doi.org/10.1016/j.solidstatesciences.2024.107527)
11. N. G. Chernorukov, A. V. Knyazev, E. N. Bulanov, *Russ. J. Inorg. Chem.* **55** (2010) 1463 (https://doi.org/10.1134/S0036023610090226)

(CC) 2026 Serbian Chemical Society.

12. A. V Knyazev, N. G. Chernorukov, E. N. Bulanov, *Thermochim. Acta* **513** (2011) 112 (https://doi.org/10.1016/j.tca.2010.11.020)
13. A. V. Knyazev, N. G. Chernorukov, E. N. Bulanov, *Thermochim. Acta* **526** (2011) 72 (https://doi.org/10.1016/j.tca.2011.08.028)
14. E. N. Bulanov, A. A. Vasileva, S. A. Kazakovtsev, O. N. Golitsyna, E. V. Syrov, A. V. Knyazev, *Ceram. Int.* **49** (2023) 34097 (https://doi.org/10.1016/j.ceramint.2023.08.113)
15. A. A. Coelho, *J. Appl. Crystallogr.* **51** (2018) 210 (https://doi.org/10.1107/S1600576718000183)
16. A. T. Sänger, W. F. Kuhs, *Zeitsch. Krist.* **199** (1992) 123 (https://doi.org/10.1524/ZKRI.1992.199.1-2.123)
17. A. Kutoglu, *Neues Jahrb. Mineral.* **1974** (1974) 210 (https://doi.org/10.1127/njmm/1974/1974/210)
18. C. B. Boechat, J.-G. Eon, A. M. Rossi, C. A. de Castro Perez, R. A. da Silva San Gil, *Phys. Chem. Chem. Phys.* **2** (2000) 4225 (https://doi.org/10.1039/B004339G)
19. C. Calvo, *Inorg. Chem.* **7** (1968) 1345 (https://doi.org/10.1021/ic50065a019)
20. N. C. Webb, *Acta Crystallogr.* **21** (1966) 942 (https://doi.org/10.1107/s0365110x66004225)
21. R. M. Thompson, X. Xie, S. Zhai, R. T. Downs, H. Yang, *Am. Mineral.* **98** (2013) 1585 (https://doi.org/10.2138/am.2013.4435)
22. P. A. Henning, E. Adolfsson, J. Grins, *Zeitsch. Krist.* **215** (2000) 226 (https://doi.org/10.1524/zkri.2000.215.4.226)
23. R. Gopal, C. Calvo, *Zeitsch. Krist. Crist. Mat.* **137** (1973) 67 (https://doi.org/10.1524/zkri.1973.137.16.67)
24. R. S. Bubnova, V. A. Firsova, S. K. Filatov, *Glas. Phys. Chem.* **39** (2013) 347 (https://doi.org/10.1134/S108765961303005X)
25. *AIST Spectral Database for Organic Compounds*, https://sdbs.db.aist.go.jp/ (accessed: May 1, 2026)
26. K. Nakamoto, *Infrared and Raman Spectra of Inorganic and Coordination Compounds*, fourth ed., John Wiley and Sons, Inc., New York, 1986
27. G. Buvaneswari, U. V. Varadaraju, *J. Solid State Chem.* **149** (2000) 133 (https://doi.org/10.1006/jssc.1999.8510)
28. I. E. Glazov, V. K. Krut'ko, O. N. Musskaya, A. I. Kulak, *Russ. J. Inorg. Chem.* **67** (2022) 173 (https://doi.org/10.1134/S0036023622020048)
29. V. S. Urusov, *Theoratical crystall chemistry*, Moscow State University Press, Moscow, 1987
30. A. V. Knyazev, E. N. Bulanov, V. Z. Korokin, *Mater. Res. Bull.* **61** (2014) 47 (https://doi.org/10.1016/j.materresbull.2014.09.089)
31. R. D. Shannon, *Acta Crystallogr., A* **32** (1976) 751 (https://doi.org/10.1107/S0567739476001551)
32. *Database of Ionic Radii*, http://abulafia.mt.ic.ac.uk/shannon/ptable.php (accessed: November 27, 2025)
33. N. G. Chernorukov, A. V. Knyazev, E. N. Bulanov, *Inorg. Mater.* **47** (2011) 172 (https://doi.org/10.1134/S002016851101002X)
34. A. V. Knyazev, N. G. Chernorukov, E. N. Bulanov, *Mater. Chem. Phys.* **132** (2012) (https://doi.org/10.1016/j.matchemphys.2011.12.011)
35. A. V. Glukhov, V. A. Kazantsev, A. Y. Volkov, B. D. Antonov, *Tech. Phys.* **65** (2020) 87 (https://doi.org/10.1134/S1063784220010065).

(CC) 2026 Serbian Chemical Society.

Journal of the Serbian Chemical Society
JSCS-info@shd.org.rs • www.shd.org.rs/JSCS
J. Serb. Chem. Soc. 91 (10) 1007–1024 (2026)
JSCS–5541
Original scientific paper
Published 16 November, 2026

Systematic investigation into the physicochemical properties of deep eutectic $AlCl_3$/amide electrolytes with additives

CHENGYUAN LIU[1]*, CHAOYANG JIE[1], JIANGYU YU[2], YAN GUO[1], FENGCUI LI[1], SHIYAN LIU[1] and HONGLIANG CHENG[1]

[1]*Henan University of Urban Construction, Pingdingshan, 467036, China and* [2]*School of Metallurgy, Northeastern University, Shenyang, 110819, China*

(Received 18 March, revised 4 June, accepted 21 July 2026)

Abstract: This study comprehensively examines the physicochemical characteristics, including density, viscosity, electrical conductivity, and electrochemical behavior, of two deep eutectic electrolytes, $AlCl_3$/acetamide and $AlCl_3$/urea, with the incorporation of various additives (LiCl, LiBr, NaCl, NaBr, EC, THF, DCE, and EMIC). The measurements were conducted across a temperature range of 313–373 K. The findings reveal that, with the exception of LiBr and NaBr, all other additives contribute to expanding the electrochemical windows of the $AlCl_3$/amide electrolytes. The addition of alkali metal halides leads to an increase in density, while EMIC and THF exert a more pronounced density-lowering effect compared to other organic additives. Inorganic additives enhance the viscosity of $AlCl_3$/acetamide but produce the opposite effect in $AlCl_3$/urea. Conversely, DCE, THF, and EMIC reduce the viscosity of both electrolytes. All investigated additives, except EC, improve electrical conductivity. Among these, EMIC demonstrates the most significant positive impact on optimizing the overall physicochemical properties of the deep eutectic $AlCl_3$/amide electrolytes.

Keywords: deep eutectic solvent; ionic conductivity; electrochemical window; Walden product.

INTRODUCTION

Deep eutectic $AlCl_3$/amide electrolytes are formed by the heterolytic cleavage of $AlCl_3$ with the assistance of amides.[1,2] Owing to their adjustable acidity, high catalytic activity, cost-effectiveness, and facile preparation, these electrolytes have emerged as promising alternatives to conventional $AlCl_3$-based electrolytes.[3,4] Numerous studies have focused on aluminum electrodeposition from $AlCl_3$/amide deep eutectic systems,[5,6] and research attention has shifted toward the structural characterization of these electrolytes,[7–10] their application as liquid catalysts,[11–14]

* Corresponding author. E-mail: liu_chy@126.com
https://doi.org/10.2298/JSC260318037L

Available online at https://www.shd.org.rs/JSCS/
(CC) 2026 Serbian Chemical Society.

and their use as electrolytes in aluminum-ion batteries.[15–20] However, only a limited number of studies have systematically explored the fundamental physicochemical properties, such as density, viscosity, and electrical conductivity, of $AlCl_3$/amide deep eutectic electrolytes.[10,21,22] Among the various $AlCl_3$/amide combinations, $AlCl_3$/acetamide and $AlCl_3$/urea have been the most extensively studied for applications in aluminum deposition and AIBs.

Compared to $AlCl_3$/imidazolium electrolytes, which are commonly used in aluminum-ion batteries,[23] $AlCl_3$/amide deep eutectic electrolytes suffer from narrower electrochemical stability windows, lower conductivities, and the formation of dendritic aluminum deposits during electrodeposition.[6,7] These drawbacks adversely affect the electrochemical performance of AIBs, including specific capacity, cycle stability and operational safety. To address these issues, several studies have proposed modifying $AlCl_3$/amide electrolytes with additives, such as alkali metal chlorides, rare-earth chlorides, and small organic molecules, to enhance the quality of aluminum deposits[4] and improve the electrochemical performance of aluminum-ion batteries.[18,22,24] Additionally, the physicochemical properties of certain $AlCl_3$/amide electrolytes blended with CuCl have been investigated to support the development and scale-up of deep eutectic electrolyte-catalyzed alkylation processes.[25]

Recent studies have made significant progress in this direction. For instance, Lee *et al.* characterized the electrochemical deposition of Al from $AlCl_3$/urea containing NaCl, demonstrating that alkali metal halides can modulate plating behavior.[26] Higashino *et al*. revealed the long-term stability of amide-based $AlCl_3$ electrolytes in dry air, highlighting that short-term tests may overlook oxygen-induced degradation that accumulates during repeated cycling.[27] Furthermore, deep eutectic electrolytes have been successfully employed in rechargeable aluminum batteries with graphite cathodes, achieving over 8,000 cycles with a specific capacity of approximately 50 mA h g^{-1} at 2 A g^{-1}.[28] From a fundamental perspective, the structural chemistry of $AlCl_3$/amide has been systematically investigated by combined Raman spectroscopy, NMR, and quantum chemical calculations, providing new insights into the complex speciation and hydrogen-bonding networks.[29] Guo *et al.* further developed a hypercoordinated chloroaluminate electrolyte with a chain-assisted ion transport mechanism, achieving an ionic conductivity of 0.89 mS cm^{-1} and an electrochemical window exceeding 2.6 V.[30] These recent advances underscore the critical importance of understanding how additives affect electrolyte properties, yet systematic comparative studies across multiple additive types remain scarce.

In the present work, we conduct a detailed investigation into the density, viscosity, electrical conductivity, and electrochemical behavior of two $AlCl_3$/amide deep eutectic electrolytes ($AlCl_3$/acetamide and $AlCl_3$/urea) in the presence of various additives. The additives are categorized into two groups: alkali metal

(CC) 2026 Serbian Chemical Society.

halides (LiCl, LiBr, NaCl, NaBr) and organic compounds (ethylene carbonate (EC), tetrahydrofuran (THF), 1,2-dichloroethane (DCE) and 1-ethyl-3-methylimidazole chloride (EMIC)). The selection of these additives is supported by recent literature. For instance, the incorporation of NaCl into $AlCl_3$-urea DES has been shown to influence aluminum electrodeposition behavior. Meanwhile, the use of EMIC as an ionic liquid additive for chloroaluminate electrolytes has been extensively validated in solid-state AIB applications. Polar organic solvents such as EC, THF, and DCE are widely used as co-solvents in battery electrolyte engineering, as summarized in recent reviews on deep eutectic electrolytes, while EMIC is a classic imidazolium ionic liquid with excellent ionic conductivity. All additives were added at a fixed dosage of 5 mol %, which is a moderate concentration that can effectively modify electrolyte properties while avoiding phase separation and excessive viscosity increase caused by high additive content.[26,30,31]

EXPERIMENTAL

Materials

Acetamide (AcA, Sinopharm Chemical Reagent Co. Ltd., China, 99.5 %), urea (Ur, Sinopharm Chemical Reagent Co. Ltd., China, 99.5 %) and 1-ethyl-3-methylimidazole chloride (EMIC, Aladdin, 99 %) were dried under vacuum at 333 K for 72 h. LiCl (Alfa Aesar, 99 %), LiBr (Alfa Aesar, 99 %), NaCl (Alfa Aesar, 99 %) and NaBr (Alfa Aesar, 99 %) were dried under vacuum at 393 K for 72 h. Anhydrous aluminum chloride ($AlCl_3$, Aladdin, 99 %), ethylene carbonate (EC, Aladdin, 99 %), tetrahydrofuran (THF, Aladdin, 99 %) and 1,2-dichloroethane (DCE, Aladdin, 99 %) were used without further treatment.

Preparation of $AlCl_3$/amide electrolyte with various additives

$AlCl_3$/amide (amide = urea (UR), acetamide (AcA)) with a mole ratio of 1.3 was prepared by gradually adding a predetermined mass of amide to $AlCl_3$ at room temperature. Subsequently, 5 mol % of the selected additive was introduced into the liquid electrolyte, which was then stirred until a homogeneous solution was obtained. All experimental operations were performed in an argon-filled glove box (MBraun MB 200B, Germany) to prevent moisture and air contamination.

Raman spectroscopy analysis

Raman spectra of $AlCl_3$/amide electrolyte containing additives were recorded using an HR 800 Raman spectrometer (Horiba Jobin Yvon LabRAM) equipped with a 633 nm He–Ne laser. The electrolytes were sealed in L-shaped quartz tubes to ensure stability during measurement.

Physicochemical behavior measurement

Electrochemical behavior of the $AlCl_3$/amide electrolytes (with and without additives) was evaluated using cyclic voltammetry (CV) and linear sweep voltammetry (LSV) on a tungsten working electrode at room temperature (CHI660E, Shanghai Chenhua Instrument Co., Ltd., China). The scan rates were set to 10 mV s^{-1} for both cathodic and anodic processes. High-purity aluminum wire and aluminum sheet were employed as the reference and counter electrodes, respectively. Prior to use, all electrodes were polished with emery paper, cleaned with anhydrous ethanol, and dried thoroughly. The anodic limit potential (E_{lim}) of each electrolyte was defined as the potential at which the anodic background current increased sharply during cyclic voltammetry (CV) and linear sweep voltammetry (LSV) measurements, corresponding

(CC) 2026 Serbian Chemical Society.

to the onset of oxidative decomposition of the electrolyte system and marking the upper boundary of the electrochemical stability window.

The densities of $AlCl_3$/amide electrolytes (with and without additives) were determined via Archimedes' principle over the temperature range of 313–373 K in the glove box (MBraun GmbH, Germany). The schematic of the experimental setup is presented in Fig. S-1 of the Supplementary material to this paper. Prior to liquid density measurement, the volume of the platinum sinker was firstly calibrated using anhydrous ethanol at 293 K and further verified with deionized water, yielding a volumetric measurement error below 0.1 %. Given that the maximum experimental temperature was limited to 373 K, the thermal expansion of the platinum sinker was negligible. The electrolyte density was calculated using the Eq. (1):

$$\rho = \frac{M_1 - M_2}{V} \tag{1}$$

where M_1 denotes the mass of the platinum sinker before immersion in the target electrolyte, M_2 is the sinker mass after immersion and V represents the pre-calibrated volume of the platinum sinker. The density of anhydrous ethanol at ambient temperature measured by this method was compared with reported literature values, with a relative deviation less than 1 %, which verifies the reliability of the established Archimedes-based measurement method.

Viscosities of $AlCl_3$/amide electrolytes (with and without additives) were measured by the capillary tube method inside a glove box over the temperature range of 313–373 K. As illustrated in Fig. S-2 of the Supplementary material, the experimental apparatus consists of a glass capillary viscometer, a stirring impeller and a thermostated oil bath. The viscosity was calculated from the efflux time required for a fixed volume of liquid to flow through the capillary under gravity. The correlation between viscosity and flow time is defined by Eq. (2):

$$\eta = C\rho t \tag{2}$$

where C stands for the viscometer constant, ρ is the liquid density and t denotes the recorded efflux time. To validate the measurement system, the viscosity was determined using the above setup, and the measured data agreed well with previously reported literature values within acceptable experimental error, confirming the validity of the present viscosity testing approach for subsequent measurements. The temperature-dependent viscosity data were fitted to the Arrhenius equation *via* nonlinear least-squares regression using Origin software.

Electrical conductivities of $AlCl_3$/amide electrolytes (with and without additives) were measured *via* the capillary impedance method in a glove box from 313 to 373 K. The experimental setup is displayed in Fig. S-3 of the Supplementary material. The electrical resistance of liquid samples was measured using an Agilent impedance analyzer (4263B LCR Meter, Agilent Technologies, USA) at a fixed excitation frequency of 1000 Hz and an applied voltage of 1 V. The ionic conductivity was calculated according to Eq. (3):

$$\sigma = \frac{K}{R} \tag{3}$$

where K is the cell constant and R denotes the experimentally measured resistance of the liquid sample. The cell constant was first determined with a 0.1 mol·L^{-1} aqueous KCl solution and further calibrated using an 1 mol·L^{-1} KCl standard solution, with the resulting calibration error lower than 0.5 %. The conductivity of the $AlCl_3$–EMImCl electrolyte with a mole ratio of 1.3 was measured by the aforementioned method. The measured data were compared with literature

(CC) 2026 Serbian Chemical Society.

results, and all deviations fell within acceptable experimental ranges, which verified the reliability of the present apparatus for subsequent conductivity tests. The temperature dependence of electrical conductivity was fitted to the Arrhenius equation by nonlinear least-squares fitting in Origin.

RESULTS AND DISCUSSION

Raman spectra

The Raman spectra of the $AlCl_3$/amide electrolytes with various additives are presented in Fig. 1. All spectra exhibit two characteristic peaks appearing at 347 and 310 cm^{-1}, which are assigned to the $[AlCl_4]^-$ and $[Al_2Cl_7]^-$ complexes, respectively. As reported in previous studies,[2] dynamic equilibria (4)–(6) exist in $AlCl_3$/amide electrolytes. Eq. (4) describes the reversible equilibrium between $[AlCl_4]^-$ and $[Al_2Cl_7]^-$. Eqs. (5) and (6) illustrate the mutual transformation between various aluminum–amide complex cations and anions inside the electrolytes. To assess the effect of additives on the relative content ratrio of $[Al_2Cl_7]^-$ to $[AlCl_4]^-$ in the $AlCl_3$/amide electrolytes, the ratios of the integral area of the $[Al_2Cl_7]^-$ peak (310 cm^{-1}) to that of the $[AlCl_4]^-$ (347 cm^{-1}) peak, denoted as I_{310}/I_{347}, were calculated (Table I). Similar Raman spectral features were reported in $AlCl_3$-N--methylformamide DES, where the I_{310}/I_{347} ratio was found to be highly sensitive to the amide species and $AlCl_3$ mole ratio:[29]

$$2\left[AlCl_4\right]^- \rightleftharpoons \left[Al_2Cl_7\right]^- + Cl^- \quad (4)$$

$$\left[AlCl_2 \cdot 2Amide\right]^+ + \left[AlCl_4\right]^- \rightleftharpoons 2\left[AlCl_3 \cdot Amide\right] \quad (5)$$

$$\left[AlCl_2 \cdot 2Amide\right]^+ + \left[Al_2Cl_7\right]^- \rightleftharpoons \left[AlCl_3 \cdot Amide\right] + \left[Al_2Cl_6 \cdot Amide\right] \quad (6)$$

Eqs. (7) and (8) depict the interactions between alkali metal halides (MX) and the intrinsic ionic species of the electrolytes. The added halide salts react with aluminum complexes and generate new halogen-containing complex ions. Eq. (9) shows the complexation reaction between neutral organic additives (L) and aluminum complex anions. Organic molecules first form adducts and then decompose into different aluminum complex species. Eqs. (10) and (11) illustrate the reactions between EMIC and electrolyte ions. EMIC dissociates into imidazolium cations and participates in ion recombination and rearrangement. Compared to the additive-free (blank) systems, almost all additives cause a slight decrease in the relative content of $[Al_2Cl_7]^-$. This phenomenon can be attributed to chemical reactions between the additives and species in the electrolyte, as described by Eqs. (7) and (8) for inorganic additives, Eq. (9) for DCE/EC/THF and Eqs. (10) and (11) for EMIC. The decreasing trend of the I_{310}/I_{347} ratio after adding halide salts in this work is consistent with the findings for NaCl-doped $AlCl_3$/urea DES, which further verifies that alkali metal halides can react with $[Al_2Cl_7]^-$ and reduce its relative content. For organic additives including THF, DCE and EC, the weak influence of

(CC) 2026 Serbian Chemical Society.

these additives on the ratio of the two aluminum complex ions is also in line with the structural characteristics of polar organic co-solvents in chloroaluminate electrolytes reported in previous reviews.[26]

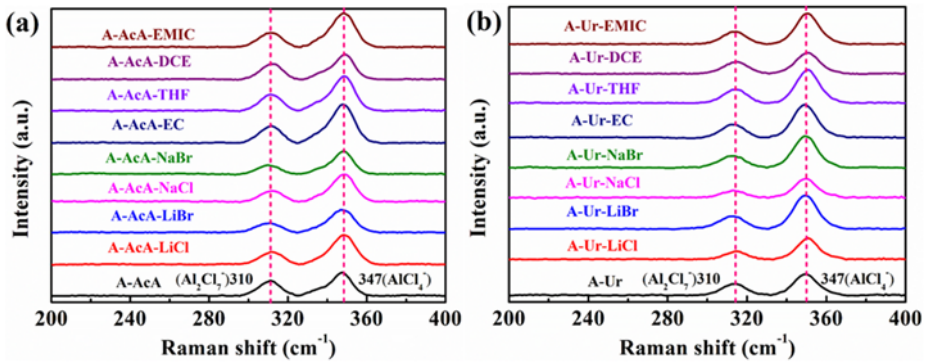

Fig. 1. Raman spectra of: a) $AlCl_3$–AcA and b) $AlCl_3$–Ur electrolytes with various additives.

TABLE I. The integral area ratio of $[Al_2Cl_7]^-$ to $[AlCl_4]^-$ (I_{310}/I_{347}) for $AlCl_3$/amide electrolytes containing various additives

Additive	Electrolite	
	$AlCl_3$–AcA	$AlCl_3$–Ur
Blank	0.65	0.54
LiCl	0.42	0.39
LiBr	0.42	0.36
NaCl	0.42	0.37
NaBr	0.41	0.37
EC	0.44	0.42
THF	0.46	0.42
DCE	0.66	0.57
EMIC	0.43	0.41

$$\left[Al_2Cl_7\right]^- + MX \rightleftharpoons \left[AlCl_4\right]^- + \left[AlCl_3X\right]^- + M^+ \left(M = Li,Na;\ X = C1,Br\right) \quad (7)$$

$$\left[AlCl_2 \cdot x\text{Amide}\right]^+ + 2MX \rightleftharpoons \left[2M \cdot AlCl_2X_2 \cdot x\text{Amide}\right]^+ \left(M = Li,Na;\ X = C1,Br\right) \quad (8)$$

$$\left[Al_2Cl_7\right]^- + nL \rightleftharpoons \left[Al_2Cl_7 \cdot nL\right]^- \rightleftharpoons \left[AlCl_4\right]^- + \left[AlC1nL\right] \left(L = EC,THF,DCE\right) \quad (9)$$

$$\left[Al_2Cl_7\right]^- + EMIC \rightleftharpoons 2\left[AlCl_4\right]^- + EMI^+ \quad (10)$$

$$\left[AlCl_2 \cdot x\text{Amide}\right]^+ + 2EMIC \rightleftharpoons \left[2EMI \cdot AlCl_4 \cdot x\text{Amide}\right]^+ \rightleftharpoons \rightleftharpoons \left[AlCl_4\right]^- + \left[EMI \cdot x\text{Amide}\right]^+ \quad (11)$$

(CC) 2026 Serbian Chemical Society.

Electrochemical behavior

The electrochemical behavior of $AlCl_3$/amide electrolytes (with and without additives) was investigated using a tungsten electrode (Fig. 2). Additives exert a similar influence on both $AlCl_3$–AcA and $AlCl_3$–Ur electrolytes. No consistent trend was observed in the initial reduction potential (E_0) following the addition of additives. For the $AlCl_3$–AcA electrolytes, the initial reduction potentials ranged from –0.135 to –0.053 V, while those of $AlCl_3$–Ur electrolytes varied between –0.126 and –0.049 V. A distinct reduction peak in the cathodic region is assigned to the deposition of metallic aluminum, while the oxidation peak in the anodic region corresponds to aluminum stripping. The addition of additives leads to a decrease in redox current densities, which is attributed to the reduced concentration of electrochemically active species ($[Al_2Cl_7]^-$). The anodic limit potential (E_{lim}), defined as the potential at which the anodic background current rises sharply on voltammograms and representing the oxidative decomposition potential of the electrolytes, is a critical parameter for the application of $AlCl_3$/amide electrolytes in AIBs. For both $AlCl_3$–AcA and $AlCl_3$–Ur, the addition of LiBr and NaBr shifts E_{lim} to a more negative value (~1.90 V). In contrast, all other additives tend to increase E_{lim}, with a more pronounced effect in $AlCl_3$–Ur, where E_{lim} increases from 2.23 V to approximately 2.40 V.

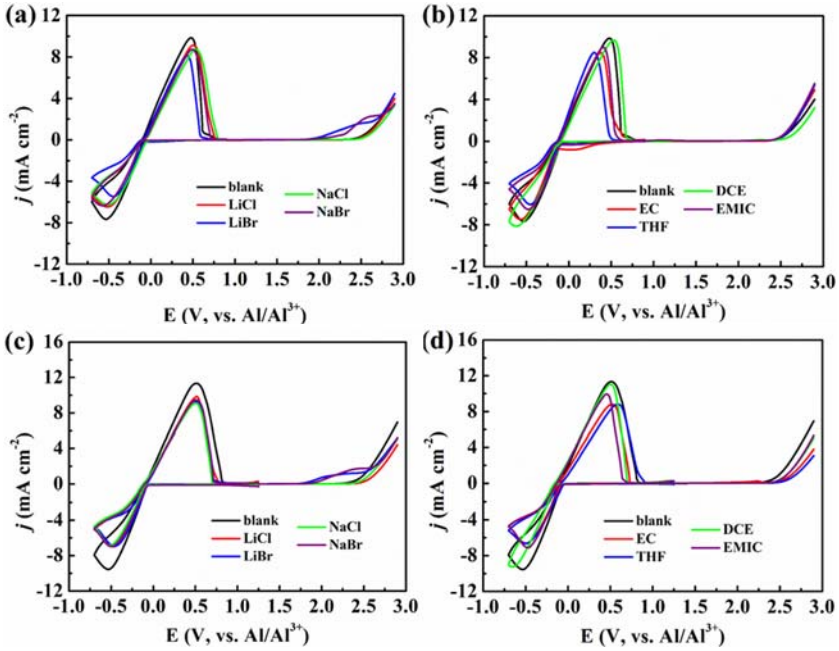

Fig. 2. Electrochemical behavior of: a, b) $AlCl_3$–AcA and c, d) $AlCl_3$–Ur IL analogs with various additives.

(CC) 2026 Serbian Chemical Society.

The plating-stripping efficiency, defined as $\mu_{CV} = Q^+/Q^-$, was calculated to evaluate the reversibility of aluminum electrodeposition.[32] As shown in Table II, all additives improve the reversibility of aluminum deposition/stripping in both electrolytes, which is consistent with the beneficial effect of alkali metal halides on aluminum electrodeposition reversibility.[26] Additionally, underpotential deposition (UPD) was observed in $AlCl_3$–AcA after the addition of EC, THF, or EMIC, a phenomenon previously reported for $AlCl_3$–EMIC electrolytes on tungsten electrodes.[33] However, UPD was not detected in any $AlCl_3$–Ur systems. This discrepancy may be associated with the unique electric double layer formed at the $AlCl_3$––Ur/W interface, as urea (with two NH_2 groups) exhibits stronger electrophilicity and thus a higher adsorption capacity on the electrode surface compared to acetamide.

TABLE II. The initial reduction potential (E_0), redox peak current densities (j_c and j_a), anodic limit potential (E_{lim}) and plating-stripping efficiency (μ_{CV}) obtained from the electrochemical curves in Fig. 2

Additive	E_0 / V	j_c / mA cm^{-2}	j_a / mA cm^{-2}	E_{lim} / V	μ_{CV} / %	Deposition
			$AlCl_3$–AcA			
Blank	–0.089	–7.669	9.931	2.37	88.68	–
LiCl	–0.059	–6.518	9.194	2.44	96.60	–
LiBr	–0.072	–5.464	8.148	1.93	90.78	–
NaCl	–0.053	–6.307	8.885	2.45	94.19	–
NaBr	–0.078	–6.356	8.885	1.95	93.71	–
EC	–0.135	–7.508	8.520	2.37	90.33	UPD
THF	–0.102	–6.040	8.520	2.37	92.08	UPD
DCE	–0.083	–8.189	9.721	2.45	93.30	–
EMIC	–0.096	–6.567	9.040	2.37	94.84	UPD
			$AlCl_3$–Ur			
Blank	–0.069	–9.502	11.448	2.23	91.58	–
LiCl	–0.075	–6.988	9.875	2.39	95.64	–
LiBr	–0.054	–6.932	9.299	1.85	98.28	–
NaCl	–0.088	–6.883	9.145	2.37	96.16	–
NaBr	–0.066	–6.988	9.510	1.87	94.05	–
EC	–0.077	–6.616	8.885	2.40	94.94	–
THF	–0.049	–6.721	8.885	2.42	95.94	–
DCE	–0.126	–9.229	11.086	2.39	97.38	–
EMIC	–0.097	–7.143	9.980	2.39	95.27	–

Density

The density of $AlCl_3$–AcA and $AlCl_3$–Ur electrolytes with various additives is shown in Fig. 3. For all systems, density decreases linearly with increasing temperature, which can be described by the following equation:

$$\rho = a + bT \tag{12}$$

where a (g cm^{-3}) and b (g cm^{-3} K^{-1}) are adjustable parameters. The experimental density data and fitted parameters are provided in Tables S-I and S-II of the

(CC) 2026 Serbian Chemical Society.

Supplementary material. The observed temperature dependence of density is attributed to enhanced molecular vibration, weakened coulombic interactions and increased free volume at higher temperatures. At the same temperature, the density of $AlCl_3$–AcA is lower than that of $AlCl_3$–Ur, which aligns with the density of the pure amides (AcA: 1.16 g cm^{-3}; Ur: 1.32 g cm^{-3}), suggesting that the density of the electrolytes is strongly influenced by the density of the parent amide.

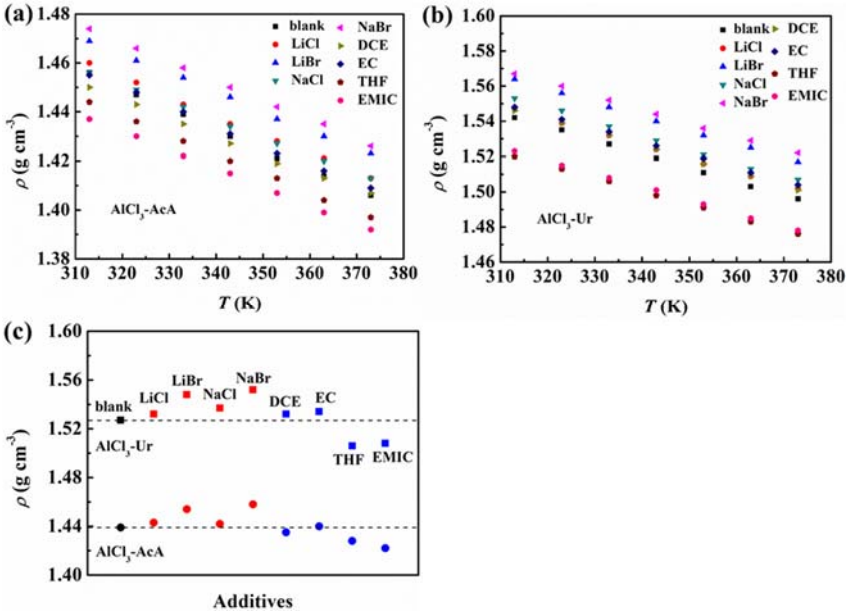

Fig. 3. Density of: a) $AlCl_3$–AcA and b) $AlCl_3$–Ur electrolytes with various additives; c) the density of $AlCl_3$/amide with various additives at 343 K.

As illustrated in Fig. 3c, the addition of alkali metal halides increases the density of both $AlCl_3$–AcA and $AlCl_3$–Ur electrolytes, following the order of NaBr, LiBr > NaCl, LiCl. This indicates that the anion has a more significant impact on density than the cation. The density increase may be explained by two factors: 1) small-sized cations occupy interstitial spaces in the electrolyte, increasing the mass per unit volume; 2) additives coordinate with anions to form species with higher densities than the original $AlCl_3$/amide complexes. Additionally, reactions between additives and electrolyte species reduce the average pore radius, further contributing to a slight density increase. For organic additives, the effect on density follows the order: EC > DCE ≥ blank > THF, which matches the density order of the pure organic compounds. EMIC causes a significant decrease in density due to its large imidazolium cation, which increases free volume and reduces the concentration of species per unit volume. Raman spectroscopy results further confirm that EMIC addition decreases the concentration of the heavier $[Al_2Cl_7]^-$, which also

(CC) 2026 Serbian Chemical Society.

contributes to the density reduction. The density-increasing effect of alkali metal halides observed here is consistent with the finding of a density increase upon NaCl addition to $AlCl_3$–urea DES.[26] Furthermore, recent studies on other DES systems have similarly reported that the addition of lithium salts tends to increase density while decreasing free volume, in agreement with the present results.[34]

Viscosity

Viscosity data for $AlCl_3$/amide electrolytes with various additives are presented in Table S-III of the Supplementary material, and the temperature dependence of viscosity is shown in Fig. 4a and b. Viscosity follows an Arrhenius relationship with temperature:

$$\eta = \eta_0 \exp\left(-E_\eta / RT\right) \tag{13}$$

where η_0 (mPa s) and E_η (kJ mol^{-1}) are empirical constants. Fitted parameters are listed in Table III. All fitting results show high R^2 values (> 0.99), confirming the excellent correlation between viscosity and temperature following the Arrhenius rule. The apparent activation energy E_η for viscosity reflects the energy barrier for ion and molecular migration. For both electrolytes, EMIC, THF and DCE present lower E_η values than blank samples, indicating reduced flow resistance. In contrast, EC gives a much higher activation energy, which is consistent with its viscosity-increasing effect. The fitted pre-exponential factor η_0 also varies with the type of additive, further proving the regulation effect of additives on the fluidity of the electrolytes.

The viscosity of deep eutectic electrolytes is influenced by factors such as the hydrogen bond network among the components, ion size, void volume and intermolecular forces (*e.g.*, electrostatic and van der Waals interactions).[35] As shown in Fig. 4a and b, the viscosity of each electrolyte decreases sharply with increasing temperature, suggesting that the increase in temperature significantly reduces the polymerization energy and hydrogen bonds among the species in the liquids. On the other hand, increased free volume results in easier movement of ions into vacant sites.[36]

The effect of additives on the viscosity of $AlCl_3$/amide electrolytes was analyzed by comparing values at 343 K (Fig. 4c and d). For $AlCl_3$–AcA, alkali metal halides increase viscosity. This is because the addition of these salts increases the relative molecular mass of the electrolyte, enhancing Van der Waals forces,[25] and reduces void volume, thereby decreasing the mobility of free species.[35] In contrast, DCE, THF and EMIC reduce the viscosity of $AlCl_3$–AcA by solvating constituent ions and reducing ion aggregation.[37,38] EMIC exhibits a more pronounced viscosity-lowering effect than DCE or THF, as its large cation increases void volume in the electrolyte. Notably, EC increases the viscosity of $AlCl_3$–AcA, likely due to the formation of an extensive hydrogen-bond network between the three oxygen

(CC) 2026 Serbian Chemical Society.

TABLE III. Arrhenius equation fitting parameters of viscosity and temperature for $AlCl_3$–AcA and $AlCl_3$–Ur electrolytes with various additives

Additive	$\eta = \eta_0 \exp(-E_\eta/RT)$		
	η_0 / Pa s	E_η / kJ mol^{-1}	R^2
	$AlCl_3$–AcA		
Blank	0.00065	28.975	0.9906
LiCl	0.00055	29.382	0.9928
LiBr	0.00114	27.592	0.9973
NaCl	0.00118	27.418	0.9975
NaBr	0.00102	27.937	0.9975
DCE	0.00138	26.766	0.9960
EC	0.00118	27.490	0.9976
THF	0.00132	26.898	0.9971
EMIC	0.00131	26.732	0.9973
	$AlCl_3$–Ur		
Blank	0.00113	27.750	0.9971
LiCl	0.00108	27.619	0.9974
LiBr	0.00133	27.239	0.9963
NaCl	0.00096	28.266	0.9970
NaBr	0.00099	28.109	0.9952
DCE	0.00214	25.591	0.9926
EC	0.00017	33.612	0.9952
THF	0.00132	27.140	0.9970
EMIC	0.00179	25.954	0.9954

atoms in EC and species in the electrolyte. For $AlCl_3$–Ur, organic additives exert a similar effect on viscosity to that observed in $AlCl_3$–AcA. However, alkali metal halides decrease the viscosity of $AlCl_3$–Ur, an opposite trend to that in $AlCl_3$––AcA. This difference arises from the stronger 3D hydrogen–bond network in $AlCl_3$–Ur, which is formed by the two NH_2 groups in urea (compared to one in acetamide). The addition of alkali metal halides partially disrupts this network, which becomes the dominant factor overriding other force-enhancing effects, leading to a net decrease in viscosity. The viscosity-reducing effect of organic additives observed here aligns with the findings of the FNMA–LiTFSI DES system, where the incorporation of small organic molecules was shown to significantly reduce viscosity while enhancing ionic conductivity.[34] Meanwhile, the inverse effect of alkali metal halides in $AlCl_3$–AcA versus $AlCl_3$–Ur is reminiscent of the composition-dependent viscosity behavior reported in EMIC–$AlCl_3$ systems with varying Lewis acidity.[39]

Electrical conductivity

The electrical conductivities of $AlCl_3$/amide electrolytes with various additives are listed in Table S-IV of the Supplementary material. The temperature dependence of electrical conductivity is shown in Fig. 5. As expected, the electrical con-

(CC) 2026 Serbian Chemical Society.

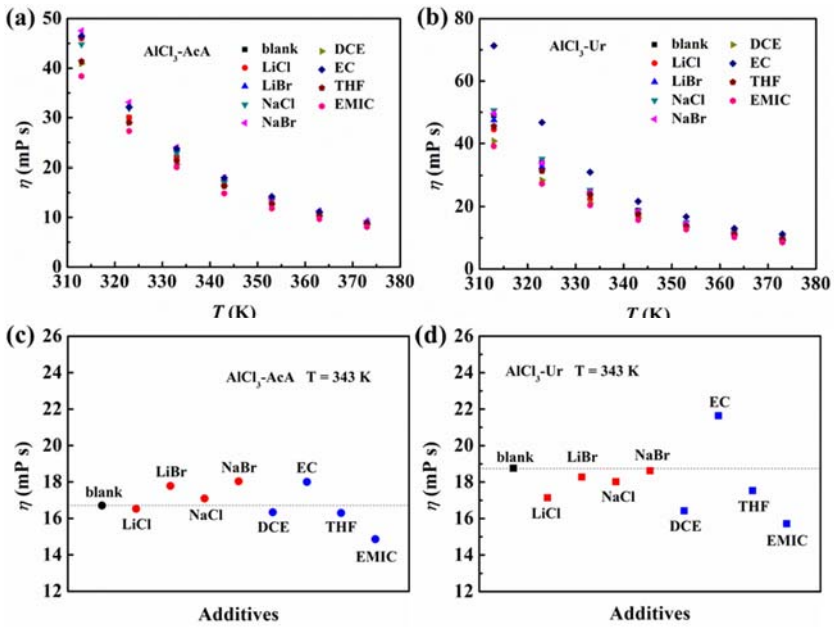

Fig. 4. Temperature dependence of the viscosity of: a) $AlCl_3$–AcA, b) $AlCl_3$–Ur electrolytes with various additives, c) $AlCl_3$–AcA and d) $AlCl_3$–Ur electrolytes with various additives at 343 K.

ductivities increase with temperature for all $AlCl_3$/amide electrolytes, as higher temperatures weaken intermolecular interactions, increase average pore radius, and enhance ion mobility. The experimental data have been fitted to the Arrhenius equation:

$$\sigma = \sigma_0 \exp\left(-E_\sigma / RT\right) \tag{14}$$

where σ_0 ($S \cdot cm^{-1}$) and E_σ (kJ mol^{-1}) are adjustable parameters. The values of the best-fit parameters are presented in Table IV. The electrical conductivity data were well fitted by the Arrhenius equation with all $R^2 > 0.99$. The activation energy E_σ for ionic migration represents the energy required for ion transport. It is found that EMIC has the lowest E_σ among all additives, which explains its optimal conductivity improvement. Most inorganic halides show moderate E_σ values, while EC corresponds to a relatively higher migration barrier, leading to its negative effect on conductivity.

As shown in Fig. 5c and d, all additives except EC improve the electrical conductivity of both $AlCl_3$/amide electrolytes. For organic additives (DCE, THF, EMIC), conductivity is inversely proportional to viscosity, which indicates that weakened intermolecular interactions and enhanced ion mobility are the primary

(CC) 2026 Serbian Chemical Society.

drivers of conductivity improvement. Furthermore, EMIC exhibits the most significant conductivity-enhancing effect among organic additives, which is attributed to its ionic liquid nature (unlike molecular DCE and THF). Alkali metal halides also increase the electrical conductivity of $AlCl_3$–AcA and $AlCl_3$–Ur electrolytes, but through a different mechanism. The addition of these salts increases the concentration of small, highly mobile ions (Li^+ and Na^+), which migrate more easily through the free volume than large complex species in the electrolyte, thereby improving overall conductivity.

TABLE IV. Arrhenius equation fitting parameters of conductivity and temperature for $AlCl_3$––AcA and $AlCl_3$–Ur electrolytes with various additives

Additive	$\sigma = \sigma_0 \exp(-E_\sigma/RT)$		
	σ_0 / 10^{-4} S m^{-1}	E_σ / kJ mol^{-1}	R^2
$AlCl_3$–AcA			
Blank	1.5651	22.796	0.9970
LiCl	1.7957	22.783	0.9986
LiBr	1.4901	22.444	0.9958
NaCl	1.6354	22.811	0.9975
NaBr	1.3631	22.280	0.9967
DCE	1.6957	22.951	0.9993
EC	1.0741	22.036	0.9987
THF	0.8980	21.262	0.9991
EMIC	0.8506	20.562	0.9967
$AlCl_3$–Ur			
Blank	0.9189	21.347	0.9978
LiCl	1.4994	22.339	0.9986
LiBr	1.2155	21.722	0.9990
NaCl	1.3696	22.144	0.9976
NaBr	1.0820	21.471	0.9975
DCE	0.7415	20.772	0.9967
EC	1.0827	22.198	0.9972
THF	0.7631	20.772	0.9964
EMIC	0.7131	20.028	0.9961

Molar conductivity (Λ) is a key parameter for evaluating ion mobility. Based on electrical conductivity and density values, the molar conductivities of $AlCl_3$/amide electrolytes with various additives were calculated using the following equation:

$$\Lambda = \frac{\sigma M}{\rho} \tag{15}$$

where M represents the molar mass of $AlCl_3$/amide electrolytes. The molar conductivity data are provided in Table S-V of the Supplementary material, and the temperature dependence of molar conductivity (Λ) is shown in Fig. 6a and b. As

(CC) 2026 Serbian Chemical Society.

observed for electrical conductivity, molar conductivity increases with temperature and is improved by all additives except EC. This confirms that smaller charge carriers and larger void volume are beneficial for electrolyte conductivity.

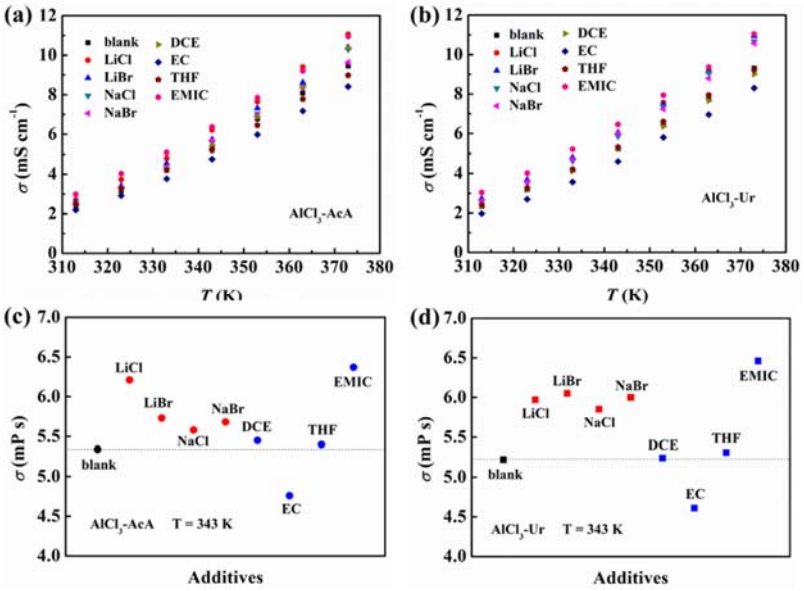

Fig. 5. Temperature dependence on the conductivity of: a) $AlCl_3$–AcA, b) $AlCl_3$–Ur electrolytes with various additives, c) $AlCl_3$–AcA and d) $AlCl_3$–Ur electrolytes with various additives at 343 K.

To further assess ionic transport efficiency, Walden plots were constructed by plotting log Λ against log η^{-1} (Fig. 7). The Walden product ($\Lambda\eta = k$) is a tempe–rature-dependent constant that reflects the degree of ion dissociation or ionicity of a liquid. A dilute 0.01 M KCl solution, where ions are fully dissociated and exhibit equal mobility, was used as a reference. "Good ionic liquids" lie near the ideal KCl line, while those above the line are classified as "superionic" and those below as "poor ionic liquids" (characterized by significant cation-anion pairing or correlated ion motion).[40,41]

As shown in Fig. 7, all $AlCl_3$/amide electrolytes fall into the "poor ionic liquids" classification region. In contrast, the behavior of the $AlCl_3$–EMIC ionic liquids model lies near the ideal KCl line on the Walden plot and is classified as a "true ionic liquid". Notably, all $AlCl_3$/amide electrolytes deviate from the ideal KCl line by less than 20 %, indicating a high degree of ion association and their classification as "associated ionic liquids", an intermediate class between true ionic liquids and molecular species.[41] For instance, the FNMA–LiTFSI DES was shown to exhibit vehicular transport as the main ion transport mechanism, with a strong coupling between ionic conductivity and viscous flow.[34] The present Walden plot

(CC) 2026 Serbian Chemical Society.

results further support that all investigated additives maintain the associated ionic liquid character while improving ionic conduction efficiency. As will be discussed shortly, the aluminum species in $AlCl_3$/amide electrolytes are chemically separated, and there is some coordination between the cation and anion mobility. This also accounts for the lower conductivity of $AlCl_3$/amide deep eutectic electrolytes compared to the $AlCl_3$–EMIC ionic liquid. The Walden product provides a valuable benchmark for selecting additives to enhance the ionic conduction efficiency of electrolytes in future studies.

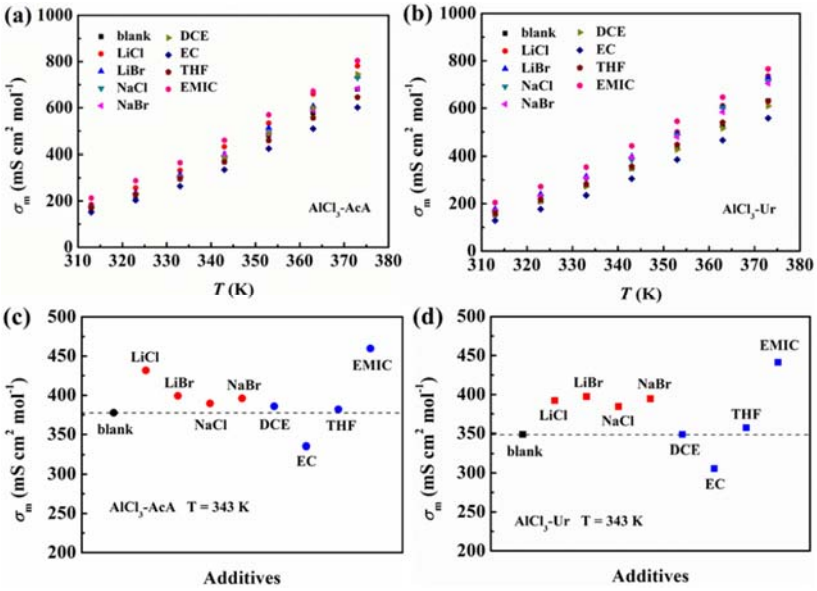

Fig. 6. Temperature dependence of the molar conductivity of: a) $AlCl_3$–AcA, b) $AlCl_3$–Ur electrolytes with various additives, c) $AlCl_3$–AcA and d) $AlCl_3$–Ur electrolytes with various additives at 343 K.

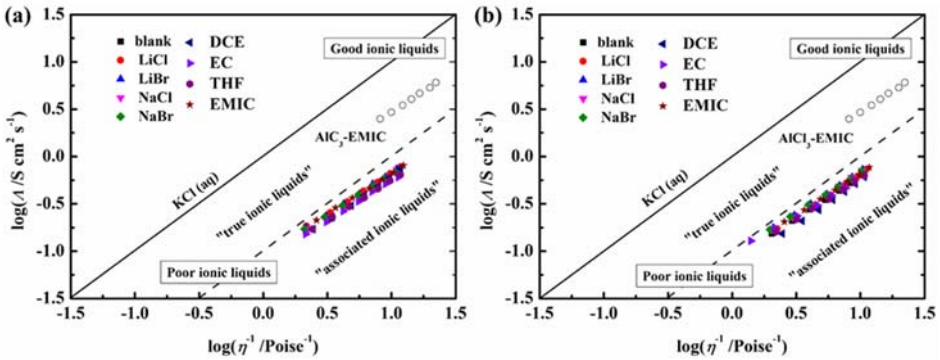

Fig. 7. Walden plot for: a) $AlCl_3$–AcA and b) $AlCl_3$–Ur electrolytes with various additives.

(CC) 2026 Serbian Chemical Society.

CONCLUSION

This study systematically investigates the density, viscosity, electrical conductivity and electrochemical behavior of $AlCl_3$–AcA and $AlCl_3$–Ur deep eutectic electrolytes with eight additives (LiCl, LiBr, NaCl, NaBr, EC, THF, DCE and EMIC) over a temperature range of 313–373 K. The key findings are as follows. All additives improve the reversibility of aluminum deposition/stripping in both electrolytes. Except for LiBr and NaBr, all additives expand the electrochemical windows of the $AlCl_3$/amide electrolytes. Alkali metal halides increase electrolyte density, while EMIC and THF produce the most significant density-lowering effects among organic additives. Inorganic additives increase the viscosity of $AlCl_3$–AcA but decrease that of $AlCl_3$–Ur; DCE, THF and EMIC reduce the viscosity of both electrolytes. All additives except EC enhance electrical conductivity, with EMIC exhibiting the most pronounced effect on reducing viscosity and increasing conductivity. These results provide valuable insights for optimizing $AlCl_3$/ /amide deep eutectic electrolytes for applications in AIBs and catalytic processes.

SUPPLEMENTARY MATERIAL

Additional data and information are available electronically at the pages of journal website: https://www.shd-pub.org.rs/index.php/JSCS/article/view/13845, or from the corresponding author on request.

Acknowledgements. This work was supported by the Natural Science Foundation of Henan Province of China (252300420759), the Key Scientific Research Project of Colleges and Universities in Henan Province (26B630005), Henan Key Science and Technology Research (262102230097) and Henan University of Urban Construction Young Backbone Teacher Training Program (YCJQNGGJS202507, YCJQNGGJS202503).

| ®úÇí

ó1óÖŒœ—Öó Ł¹ 1ó–1Ö1ª—" Œ Ê1æ1¬Ł¹ûŒœ1%óŁ1ûó ª1%óÖ—ª— ØöÆ¹Ł1û
ŒöÖŒŁÖ1¬Ł1ûAlCl₃/—œ1ØßŁ1ûŒøŒŁÖ°¹ø1Ö—ó——Ø1Ö1ª1œ—

CHENGYUAN LIU[1],CHAOYANG JIE[1],JIANGYU YU[2],YAN GUO[1],FENGCUILI[1],SHIYAN LIU[1] | HONGLIANG CHENG[1]

[1]Hdn‘m Umhudqphsx neUqa‘m Cnmrsqtbshnm,Ohmfchmfrg‘m 356/35,Cghm‘ | [2]Sbgnnlne L ds‘llt qfx, Nnqsgd‘rsdqm Umhudqphsx,Sgdmx‘mf 11/718,Cghm‘

¹ú½ÅµÙí|Ÿ½ñðÐíÅµ½ú,½ÅúÐÇÕÙŠú½µÁÇ|Åñ|µ|ú½"ÐÈ|®|ÑþÇŠÐý|Ÿåþ|Šþ½ð½þuÐð|Åµ|þ½,Ùþ,ÙÑÙŸÙ»|êÙÅµ|ÁÙ,ú|ÅþÇ®ÁÇÅµ,ÐÃÐþuð|ÑÁÙñðÇúÇí,|úÇÅµ|ÐÃÐþuðÇŠÐý|Ÿåþç ñÇÁ½Ú½"Ð,íúý íÙÕÇþ½ÐÙµÐþµ|Ñþ½ÐÃÐþuðÇÃ|µ½,AlCl₃/½ôÐµý|í|AlCl₃/ŸðÐý,Ù®Ùéð½í"Ùð½®Ã|Ñ|µ|Š½í|µ|ú½(LhCl,LhBq,N‘Cl,N‘Bq,EC,THF,DCE|EL IC).œÐðÐ"½ÅÙÅñðÇúÐíÐÁ½ÙµÐýñÐ-ð½µÙðÁÇý ÇñÅÐêÙÇí 313 íÇ 363 K.ØÇÕ|ŸÐÁ|ðÐ®ÙÃµ½µ|ñÇþ½®ÙŸÙí½,Å½|®Ù®ÐuþÇý LhBq|N‘Bq,Åú|ÇÅµ½Ã|½í|µ|ú|íÇñð|ÁÇÅÐ ñðÇÚ|ðÐ"ÙÐÃÐþuðÇŠÐý|Ÿåþ|Š ÇñÅÐê½AlCl₃/½ý|íÁ|Š ÐÃÐþuðÇÃ|µ½.ØÇí½µ½þŠ½ÃÇêÐÁ|í½½Ãþ½ÃÁ|ŠýÐµ½Ã½íÇúÇí|íÇñÇúÐ»½"½êÙÅµ|ÁÐ,íÇþEL IC|THF ñÇþ½®ÙŸÙ|®ð½îÐÁ|Ÿ|ÐÈÐþ½µÅý½"Ð"½êÙÅµ|ÁÐÙñÇðÐ›Ð"ÙÅ½íðÙé|ý ÇêÅÁåþ|ý½í|µ|ú|ý½.ßŠÐÇðê½ÁÅþ|½í|µ|ú|ñÇúÐ»½ú½ŸÙú|ÅþÇ®ÁÇÅµAlCl₃/½ôÐµý|í½,½Ã|ñðÇ|®úÇíÐÅÙñðÇµµ½ÁÐÈÐþ½µþÇíAlCl₃/ŸðÐÐ.ß½ÅÙñðÇµµÇýÐ,DCE,THF|EL IC Åý½"ŸÙú|ÅþÇ®ÁÇÅµçÕ½ÐÃÐþuðÇÃ|µ½.óú||Åñ|µ½Ã|½í|µ|ú|,ÇÅ|ý EC,ñÇÕÇ,Ú½ú½ŸÙ ÐÃÐþuð|ÑÁÙ ñðÇúÇí,|úÇÅµ.

(CC) 2026 Serbian Chemical Society.

œ Ð›Ù ″ |ý½, EL IC ñÇþ½®ÙÐ Á½˜®Á½Ñ½Á|˘| ñÇ®|µ|ú½Á Ùµ|õ½˘ Á½ Çñµ|ý|®½õ|˘Ù ÙþÙñÁ|Š È|®|ÑþÇŠÐý|˘Åþ|Š ÅúÇ˘Åµ½ú½ íÙÕÇþ|Š ÐÙµÐþµ|Ñþ|Š A lC l3/½ý|íÁ|Š ÐÃÐþµðÇÃ|µ˙.

(– ð|ý, ÐÁÇ 17.ý½ðµ½,ðÐú|í|ð½ÁÇ 3.˘ÙÁ½,ñð|Šú½»ÐÁÇ 21.˘ÙÃ½ 2/25)

REFERENCES

1. H. M. A. Abood, A. P. Abbott, A. D. Ballantyne, K. S. Ryder, *Chem. Commun.* **47** (2011) 3523 (https://doi.org/10.1039/C0CC04989A)
2. F. Coleman, G. Srinivasan, M. S. Kwaśny, *Angew. Chem.* **52** (2013) 12582 (https://doi.org/10.1002/anie.201306267)
3. J. Wang, *PhD Thesis*, CUNY City College, CUNY Academic Works, New York, 2025 (https://academicworks.cuny.edu/cc_etds_theses/1259)
4. A. Zobeid, F. Abbasi, S. Azadi, *Adv. Appl. NanoBio Tech.* **6** (2025) 18615 (https://doi.org/10.18502/AANBT.V6I2.18615)
5. V. S. Cvetković, N. M. Vukićević, N. Jovićević, J. S. Stevanović, J. N. Jovićević, *Trans. Nonferrous Met. Soc. China* **30** (2020) 823 (https://doi.org/10.1016/S1003-6326(20)65257-8)
6. S. Prabu, H. W. Wang, *Chin. J. Chem. Eng.* **28** (2020) 854 (https://doi.org/10.1016/j.cjche.2019.11.002)
7. P. C. Hu, R. Zhang, X. H. Meng, H. Y. Liu, C. M. Xu, Z. C. Liu, *Inorg. Chem.* **55** (2016) 2374 (https://doi.org/10.1021/acs.inorgchem.5b02744)
8. P. C. Hu, W. Jiang, L. J. Zhong, S. F Zhou, *RSC Adv.* **8** (2018) 13248 (https://doi.org/10.1039/C8RA01845F)
9. M. Malik, K. L. Ng, G. Azimi, *Electrochim. Acta* **354** (2020) 136708 (https://doi.org/10.1016/j.electacta.2020.136708)
10. Y. Liu, R. S. Hu, C. M. Xu, H. Q. Su, *Appl. Catal., A* **346** (2008) 189 (https://doi.org/10.1016/j.apcata.2008.05.024)
11. J. M. Hogg, F. Coleman, A. F. Ugalde, M. P. Atkins, M. S. Kwaśny, *Green Chem.* **17** (2015) 1831 (https://doi.org/10.1039/C4GC02080D)
12. P. C. Hu, Y. D. Wang, X. H. Meng, R. Zhang, H. Y. Liu, C. M. Xu, Z. C. Liu, *Fuel* **189** (2017) 203 (https://doi.org/10.1016/j.fuel.2016.10.099)
13. P. C. Hu, J. W. Zheng, W. Jiang, L. J. Zhong, S. F. Zhou, *Chinese J. Chem. Eng.* **28** (2020) 152 (https://doi.org/10.1016/j.cjche.2019.04.018)
14. K. Matuszek, A. Chrobok, J. M. Hogg, F. Colemanb, M. S. Kwaśny, *Green Chem.* **17** (2015) 4255 (https://doi.org/10.1039/C5GC00749F)
15. M. Angell, C. J. Pan, Y. M. Rong, C. Z. Yuan, M. C. Lin, B. J. Hwang, H. J. Dai, *PNAS* **114** (2017) 834 (https://doi.org/10.1073/pnas.1619795114)
16. Y. T. Kao, S. B. Patil, C. Y. An, S. K. Huang, J. C. Lin, T. S. Lee, Y. C. Lee, H. L. Chou, C. W. Chen, Y. J. Chang, Y. H. Lai, D. Y. Wang, *ACS Appl. Mater. Interfaces* **12** (2020) 25853 (https://doi.org/10.1021/acsami.0c04640)
17. X. Y. Bao, Z. S. Wang, D. Zhang, R. Y. Hong, M .L. Li, C. M. Smithc, J. J. Xu, *New J. Chem.* **48** (2024) 5893 (https://doi.org/10.1039/d4nj00147h)
18. N. Canever, N. Bertrand, T. Nann, *Chem. Commun.* **54** (2018) 11725 (https://doi.org/10.1039/C8CC04468F)
19. C. Xu, T. Diemant, X. Liu, S. Passerini, *Adv. Mater.* **36** (2024) 2400263 (https://doi.org/10.1002/adma.202400263)
20. M. Raić, O. Lužanin, I. Jerman, R. Dominko, J. Bitenc, *J. Power Sources* **624** (2024) 235575 (https://doi.org/10.1016/j.jpowsour.2024.235575)

(CC) 2026 Serbian Chemical Society.

21. M. Angell, G. Z. Zhu, M. C Lin, Y. M. Rong, H. J. Dai, *Adv. Funct. Mater.* **30** (2019) 1901928 (https://doi.org/10.1002/adfm.201901928)
22. J. F. Li, J.G. Tu, H. D. Jiao, C. Wang, S. Q. Jiao, *J. Electrochem. Soc.* **164** (2017) A3093 (https://doi.org/10.1149/2.0811713jes)
23. K. V. Kravchyk, M. V. Kovalenko, *Commun. Chem.* **3** (2020) 120 (https://doi.org/10.1038/s42004-020-00365-2)
24. F. C. Li, C. Y. Liu, R. J. Liu, J. Y. Yu, Z. W. Liu, *Electrochemistry* **91** (2023) 057005 (https://doi.org/10.5796/electrochemistry.23-00028)
25. P. C. Hu, W. Jiang, L. J. Zhong, S. F. Zhou, *Chin. J. Chem. Eng.* **27** (2019) 144 (https://doi.org/10.1016/j.cjche.2018.06.018)
26. J. Lee, Y.R. Gwon, S. Kim, J. Lee, S. Choe, P.K. Song, B. Yoo, *J. Appl. Electrochem.* **55** (2025) 2999 (https://doi.org/10.1007/s10800-025-02356-4)
27. S. Higashino, T. Yamamoto, T. Ikenoue, T. Hirato, M. Miyake, *J. Electrochem. Soc.* **173** (2026) 112503 (https://doi.org/10.1149/1945-7111/ae7476)
28. F. Jach, M. Wassner, M. Bamberg, E. Brendler, G. Frisch, U. Wunderwald, J. Friedrich, *ChemElectroChem* **8** (2021) 1988 (https://doi.org/10.1002/celc.202100183)
29. Q. L. Meng, X. W. Hu, R. D. Guo, A. M. Liu, J. Y. Yu, Z. N. Shi, Z. W. Wang. *Inorg. Chem.* **64** (2025) 17722 (https://doi.org/10.1021/acs.inorgchem.5c01791)
30. K. Guo, W. Wang, H. D. Jiao, W. L. Song, S. Q. Jiao, *ACS Nano* **19** (2025) 32595 (https://doi.org/10.1021/acsnano.5c09979)
31. D. C. Wu, X. L. Wang, S. J. Yang, Y. H. Zhu, Z. H. Zuo, Z. Liao, J. Liu, H. Yuan, J. Q. Huang, *Adv. Sci.* **13** (2026): e17939 (https://doi.org/10.1002/advs.202517939)
32. M. Torrero, P. Leung, E. G. Quismondo, E. Ventosa, M. Anderson, J. Palma, R. Marcilla, *J. Power Sources* **374** (2018) 77 (https://doi.org/10.1016/j.jpowsour.2017.11.032)
33. T. Jiang, M. J. C. Brym, G. Dubé, A. Lasia, G. M. Brisard, *Surf. Coat. Tech.* **201** (2006) 1 (https://doi.org/10.1016/j.surfcoat.2005.10.046)
34. G. Lyu, C. Korte, J. Luo, *Materials* **18** (2025) 2048 (https://doi.org/10.3390/ma18092048)
35. Q. H. Zhang, K. D. O. Vigier, S. Royer, F. Jérôme, *Chem. Soc. Rev.* **41** (2012) 7108 (https://doi.org/10.1039/C2CS35178A)
36. R. L. Perry, K. M. Jones, W. D. Scott, Q. Liao, C. L. Hussey, *J. Chem. Eng. Data* **40** (1995) 615 (https://doi.org/10.1021/je00019a017)
37. Y. Z. Jia, *Ionic liquid analogues*, Chemical Industry Press, Beijing, 2015 (ISBN 978-7-122-22060-8)
38. A. García, L. C. T. González, K. P. Padmasree, M. G. B. Garcia, E. M. Sánchez, *J. Molecular Liq.* **178** (2013) 57 (https://doi.org/10.1016/j.molliq.2012.11.007)
39. K. Venkatesh, A. Ispas, A. Bund, *Meet. Abstr.* **MA2025-01** (2025) 1406 (https://doi.org/10.1149/MA2025-01231406mtgabs)
40. R. E. Ramírez, L. C. T. González, A. Hernández, A. García, E. M. Sánchez, *J. Phys. Chem., B* **114** (2010) 4271 (https://doi.org/10.1021/jp910706m)
41. D. R. MacFarlane, M. Forsyth, E. I. Izgorodina, A. P. Abbott, G. Annata, K. Fraser, *Phys. Chem. Chem. Phys.* **11** (2009) 4962 (https://doi.org/10.1039/B900201D).

(CC) 2026 Serbian Chemical Society.

Journal of the Serbian Chemical Society
JSCS-info@shd.org.rs • www.shd.org.rs/JSCS
J. Serb. Chem. Soc. 91 (10) S300–S304 (2026) *Supplementary material*

SUPPLEMENTARY MATERIAL TO

Systematic investigation into the physicochemical properties of deep eutectic $AlCl_3$/amide electrolytes with additives

CHENGYUAN LIU[1]*, CHAOYANG JIE[1], JIANGYU YU[2], YAN GUO[1], FENGCUI LI[1], SHIYAN LIU[1] and HONGLIANG CHENG[1]

[1]*Henan University of Urban Construction, Pingdingshan 467036, China and*
[2]*School of Metallurgy, Northeastern University, Shenyang 110819, China*

J. Serb. Chem. Soc. 91 (10) (2026) 1007–1024

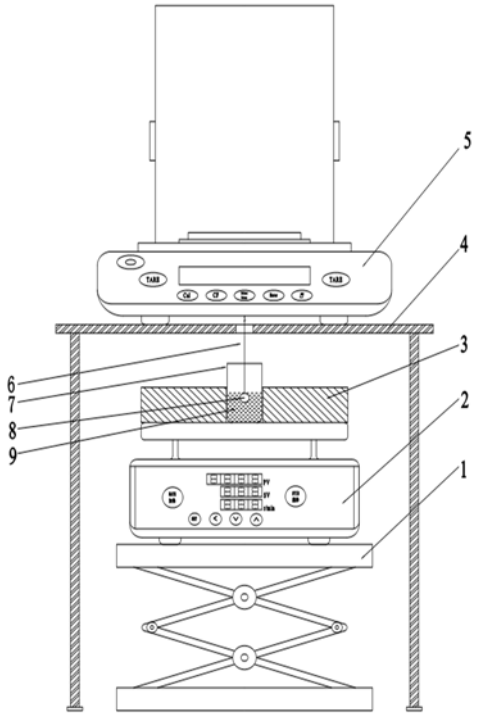

1- lifting table; 2- intelligent digital display magnetic heating plate; 3- insulation cotton; 4- trestle table; 5- electronic balance; 6- platinum wire; 7- beaker; 8- platinum ball; 9- electrolyte

Fig. S-1. Schematic diagram for the density measurement.

* Corresponding author. E-mail: liu_chy@126.com

Available online at https://www.shd.org.rs/JSCS/

(CC) 2026 Serbian Chemical Society.

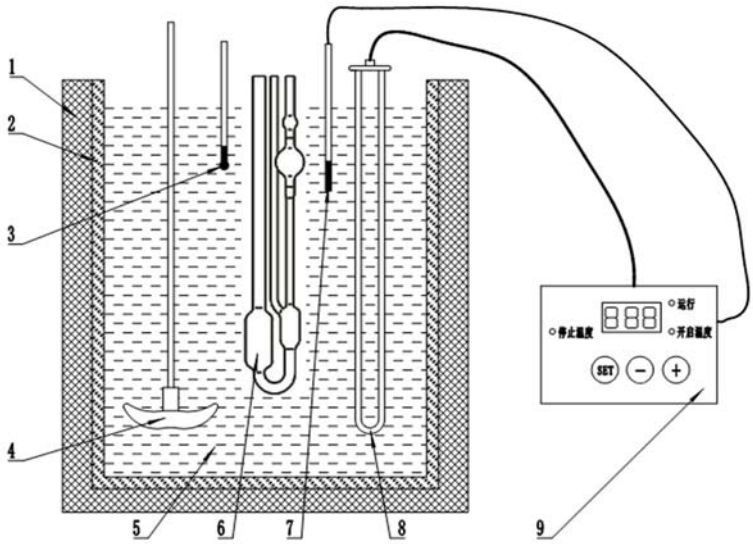

1- insulation cotton; 2- quartz cell; 3- thermometer; 4- stirring paddle; 5- dimethicone; 6- ubbelodhe viscometer; 7- temperature sensor; 8- heating bar; 9- microcomputer intelligent temperature controller

Fig. S-2. Schematic diagram for the viscosity measurement.

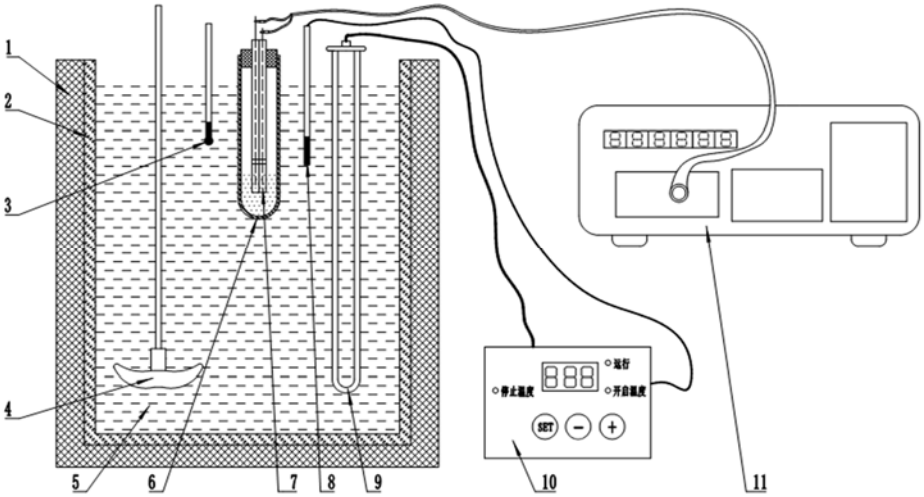

1- insulation cotton; 2- quartz cell; 3- thermometer; 4- stirring paddle; 5- dimethicone; 6- quartz tube; 7- conductance cell; 8- temperature sensor; 9- heating bar; 10- microcomputer intelligent temperature controller; 11- agilent impedance meter

Fig. S-3. Schematic diagram for the electrical conductivity measurement.

(CC) 2026 Serbian Chemical Society.

TABLE S-I. Density of $AlCl_3$-AcA and $AlCl_3$-Ur electrolytes with various additives at different temperatures

T (K)	ρ (g·cm^{-3})								
	blank	LiCl	LiBr	NaCl	NaBr	DCE	EC	THF	EMIC
	$AlCl_3$-AcA								
313	1.456	1.460	1.469	1.456	1.474	1.450	1.455	1.444	1.437
323	1.447	1.452	1.461	1.449	1.466	1.443	1.448	1.436	1.430
333	1.439	1.443	1.454	1.442	1.458	1.435	1.440	1.428	1.422
343	1.430	1.435	1.446	1.434	1.450	1.427	1.431	1.420	1.415
353	1.421	1.428	1.437	1.427	1.442	1.419	1.423	1.413	1.407
363	1.414	1.421	1.430	1.420	1.435	1.413	1.416	1.404	1.399
373	1.406	1.413	1.423	1.413	1.426	1.407	1.409	1.397	1.392
	$AlCl_3$-Ur								
313	1.542	1.547	1.564	1.553	1.567	1.546	1.548	1.520	1.523
323	1.535	1.539	1.556	1.546	1.560	1.539	1.541	1.513	1.515
333	1.527	1.532	1.548	1.537	1.552	1.532	1.534	1.506	1.508
343	1.519	1.524	1.540	1.529	1.544	1.524	1.526	1.498	1.501
353	1.511	1.516	1.532	1.521	1.536	1.516	1.519	1.491	1.493
363	1.503	1.509	1.525	1.513	1.529	1.509	1.511	1.483	1.485
373	1.496	1.502	1.517	1.507	1.522	1.501	1.504	1.476	1.478

TABLE S-II. Least-squares fitted parameters of density equation for $AlCl_3$-AcA and $AlCl_3$-Ur electrolytes with various additives

Additives	$\rho = a+bT$ (g·cm^{-3})		
	a	$-b\times10^{-4}$	R^2
	$AlCl_3$-AcA		
blank	1.7144	8.2786	0.9987
LiCl	1.7015	7.7429	0.9981
LiBr	1.7106	7.7214	0.9988
NaCl	1.6795	7.1500	0.9997
NaBr	1.7221	7.9286	0.9995
DCE	1.6789	7.3214	0.9964
EC	1.6986	7.7857	0.9983
THF	1.6898	7.8571	0.9994
EMIC	1.6743	7.5714	0.9996
	$AlCl_3$-Ur		
blank	1.7866	7.8000	0.9991
LiCl	1.7814	7.5000	0.9983
LiBr	1.8086	7.8214	0.9996
NaCl	1.7990	7.8571	0.9978
NaBr	1.8052	7.6074	0.9992
DCE	1.7810	7.5000	0.9997
EC	1.7797	7.3929	0.9996
THF	1.7517	7.3929	0.9996
EMIC	1.7577	7.5000	0.9995

(CC) 2026 Serbian Chemical Society.

TABLE S-III. Viscosity of $AlCl_3$-AcA and $AlCl_3$-Ur electrolytes with various additives at different temperatures

T (K)	η (mPa·s)								
	blank	LiCl	LiBr	NaCl	NaBr	DCE	EC	THF	EMIC
	$AlCl_3$-AcA								
313	46.144	45.960	46.537	44.799	47.528	40.904	46.478	41.364	38.372
323	30.017	30.033	32.387	31.880	33.112	28.952	32.121	28.995	27.301
333	22.060	21.998	23.613	22.857	24.040	20.635	23.769	21.271	20.154
343	16.709	16.524	17.783	17.092	18.033	16.339	18.007	16.301	14.858
353	13.132	12.831	14.039	13.630	13.809	12.625	14.216	12.705	11.829
363	10.587	10.222	11.185	10.769	11.351	10.348	11.157	10.257	9.686
373	8.745	8.445	9.156	9.108	9.247	8.533	8.862	8.548	8.084
	$AlCl_3$-Ur								
313	48.967	44.455	47.483	49.627	50.558	40.782	71.298	45.531	39.131
323	33.931	31.711	32.741	33.741	35.061	28.449	46.736	31.366	27.327
333	24.575	22.377	24.378	24.587	25.318	21.097	31.016	23.798	20.446
343	18.760	17.137	18.274	18.013	18.618	16.421	21.638	17.526	15.716
353	14.716	13.264	14.483	14.662	14.885	13.303	16.710	13.698	12.671
363	11.844	10.591	11.572	11.698	11.760	10.946	12.992	11.144	10.169
373	9.307	8.945	9.618	9.699	9.748	9.336	11.133	9.356	8.538

TABLE S-IV. Conductivity of $AlCl_3$-AcA and $AlCl_3$-Ur electrolytes with various additives at different temperatures

T (K)	σ (mS·cm^{-1})								
	blank	LiCl	LiBr	NaCl	NaBr	DCE	EC	THF	EMIC
	$AlCl_3$-AcA								
313	2.35	2.70	2.58	2.52	2.50	2.45	2.19	2.46	2.99
323	3.16	3.73	3.41	3.28	3.33	3.26	2.92	3.27	4.03
333	4.21	4.81	4.55	4.27	4.37	4.30	3.77	4.21	5.09
343	5.34	6.21	5.73	5.58	5.68	5.45	4.76	5.40	6.37
353	6.77	7.64	7.32	7.04	6.96	6.87	5.98	6.87	7.85
363	8.08	9.40	8.62	8.41	8.36	8.39	7.17	8.21	9.21
373	9.46	11.06	10.39	10.30	9.64	10.38	8.41	9.98	10.96
	$AlCl_3$-Ur								
313	2.34	2.66	2.73	2.60	2.61	2.34	1.97	2.42	3.04
323	3.19	3.60	3.69	3.52	3.57	3.57	2.70	3.27	4.02
333	4.18	4.73	4.82	4.63	4.72	4.22	3.57	4.22	5.21
343	5.22	5.97	6.05	5.85	6.00	5.24	4.61	5.31	6.46
353	6.50	7.57	7.48	7.36	7.24	6.76	5.80	6.60	7.94
363	7.81	9.20	9.14	9.07	8.79	7.96	6.95	7.95	9.37
373	9.31	11.04	10.95	10.67	10.57	9.41	8.30	9.42	11.04

(CC) 2026 Serbian Chemical Society.

TABLE S-V. Molar conductivity of $AlCl_3$-AcA and $AlCl_3$-Ur electrolytes with various additives at different temperatures

T (K)	σ_m (mS·cm^2·mol^{-1})								
	blank	LiCl	LiBr	NaCl	NaBr	DCE	EC	THF	EMIC
	$AlCl_3$-AcA								
313	163.19	184.50	176.98	173.30	171.52	170.72	151.71	171.10	212.47
323	220.80	256.28	235.19	226.65	229.71	228.27	203.26	228.71	287.77
333	295.80	332.55	315.33	296.49	303.10	302.76	263.88	296.10	365.50
343	377.56	431.74	399.30	389.62	396.14	385.89	335.28	381.94	459.68
353	481.70	533.76	513.30	493.97	488.10	489.17	423.58	488.31	569.86
363	577.75	659.96	607.42	593.01	589.15	599.94	510.37	587.30	672.13
373	680.28	780.90	735.75	729.87	683.64	745.41	601.62	717.49	803.98
	$AlCl_3$-Ur								
313	153.87	172.13	176.52	168.21	169.05	153.49	128.73	160.47	204.60
323	210.86	234.01	239.82	228.76	232.27	208.87	177.23	217.83	271.99
333	277.74	309.07	314.88	302.66	308.67	272.71	235.41	282.42	354.13
343	348.68	392.14	397.29	384.42	394.42	348.66	305.58	357.27	441.15
353	436.48	499.86	493.75	486.18	478.40	425.42	386.24	446.14	545.12
363	527.23	610.31	606.10	602.31	583.48	514.75	465.27	540.30	646.76
373	631.43	735.78	729.95	711.38	704.87	608.70	558.23	643.24	765.64

(CC) 2026 Serbian Chemical Society.

Journal of the Serbian Chemical Society
JSCS-info@shd.org.rs • www.shd.org.rs/JSCS
J. Serb. Chem. Soc. 91 (10) 1025–1041 (2026)
JSCS–5542
Original scientific paper
Published 18 November, 2026

A detailed thermodynamic analysis of a diesel engine at different compression ratios

HAKAN BAYRAKTAR[1] and İSMET SEZER[2]*

[1]*Karadeniz Technical University, Department of Mechanical Engineering, Faculty of Engineering, Trabzon, Türkiye and* [2]*Gümüşhane University, Department of Mechanical Engineering, Faculty of Engineering and Natural Sciences, Gümüşhane, Türkiye*

(Received 31 March, revised 25 May, accepted 6 October 2026)

Abstract: This study experimentally investigates the effects of compression ratio (*CR*) on the combustion, energy and exergy characteristics of a diesel engine. A four-stroke, naturally aspirated, water-cooled, direct-injection, single-cylinder diesel engine with variable *CR* capability was employed. Experiments were conducted at a constant speed of 1500 rpm under various loads, with *CR*s set to 15:1, 16:1 and 17:1. The software in the experimental setup calculated the arithmetic mean of ten cycles to minimize the effects of cycle-to-cycle variations and enhance the accuracy of the results. A detailed thermodynamic analysis was carried out to examine the combustion, energy and exergy characteristics of the tested *CR*s using data obtained from the experiments. The results demonstrated that *CR* has a significant influence on combustion, energy, and exergy characteristics. Combustion parameters such as mass burned fraction, heat release rate, cylinder pressure and gas temperature increased with rising *CR*. Similarly, performance indicators including efficiency, fuel consumption and the overall energy and exergy performance of the engine also tended to improve as *CR* increased. Among the tested *CR*s, a *CR* of 16 provided the most favorable exergetic outcomes. Specifically, exergy efficiency, exergy performance coefficient and sustainability index improved by 9.9–22.1, 45.3–110.9 and 0.6–6.9 %, respectively, depending on engine load for a *CR* of 16.

Keywords: combustion; exergy analysis; irreversibility; sustainability.

INTRODUCTION

Diesel engines are extensively employed in heavy duty applications such as transportation, construction and agriculture due to their low fuel consumption, high torque output and overall efficiency.[1] Single-cylinder diesel engines are frequently preferred as power sources in the agricultural sector, where they are commonly used to operate farming machinery such as water pumps, generators and tillers, as

* Corresponding author. E-mail: isezer@gumushane.edu.tr
https://doi.org/10.2298/JSC260331060B

Available online at https://www.shd.org.rs/JSCS/
(CC) 2026 Serbian Chemical Society.

well as in fishing activities.[2] However, the continuous rise in oil prices and the growing problem of environmental pollution have made it necessary to strengthen legal regulations and conduct technical studies aimed at improving the efficiency and environmental sustainability of internal combustion engines (ICEs).[3,4] Hence, intensive efforts have been directed toward utilizing renewable alternative fuels, improving the properties of fossil fuels, and developing ICEs in line with current technological advancements.[5,6] Improving fuel properties has made research on enhancing and optimizing engine design features increasingly important.[7,8] The compression ratio (*CR*) is one of the fundamental design parameters of ICEs and has a significant impact on combustion, performance and emission characteristics. Therefore, *CR* must be determined appropriately in accordance with the engine's structure and type, its charging system and the fuel characteristics.[9–11] Conversely, research on engines is conducted through theoretical and/or experimental approaches. While experimental studies provide more realistic results, they are often time-consuming and costly. Advances in computer and software technologies have increased the reliability of theoretical studies, making it possible to achieve desired outcomes with fewer experimental studies.[12,13] Theoretical and experimental studies on engines are primarily grounded in the principles of thermodynamics and fluid mechanics. Thermodynamics-based investigations often employ energy analysis derived from the first law of thermodynamics. However, it has been emphasized that exergy analysis, which supplements first-law approaches with those of the second law of thermodynamics, can yield more accurate results. Moreover, exergy analysis enables the identification of losses caused by system irreversibilities and supports efficiency improvements through studies aimed at reducing these losses.[14–16] For all these reasons, a detailed thermodynamic analysis was conducted in this study to investigate the effects of *CR* on the combustion, performance, energy and exergy characteristics of a diesel engine.

EXPERIMENTAL

The experimental setup comprises three primary components: the engine, the dynamometer and the measurement and control panel. An image of the test system is provided in Fig. 1. As illustrated, an electric dynamometer was incorporated into the system to impose a load on the engine, with the load being regulated through a dedicated switch.

The system is equipped with air, fuel and coolant tanks, along with measurement devices for air, fuel and coolant flow rates, torque, rotational speed, cylinder gas and fuel pressures and temperatures at various points. A data acquisition unit is integrated to transfer the recorded measurements to a computer. The performance parameters are subsequently calculated from the collected data using Enginesoft software, which operates on the Labview platform. The engine employed in the system is a four-stroke, naturally aspirated, water-cooled, direct-injection diesel engine, with its technical specifications presented in Table I. The *CR* of the engine can be adjusted through a mechanism located on the cylinder block. Experiments were carried out at a constant speed of 1500 rpm under varying load conditions ranging from 0 to 100 %. Measurements were recorded once the engine reached a steady–state operating regime, and the collected

(CC) 2026 Serbian Chemical Society.

data were utilized for a comprehensive thermodynamic analysis covering the combustion, performance, energy and exergy characteristics.[17]

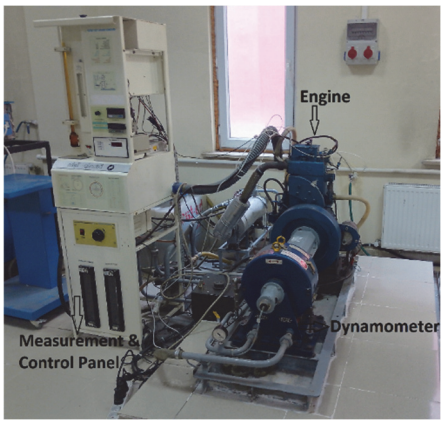

Fig. 1. Image of the experimental setup.

TABLE I. The specifications of the test engine[17]

Brand and model	Kirloskar TV1
Number of cylinders	1
Bore×Stroke	87.5 mm×110 mm
Cylinder volume	661 cm^3
Compression ratio	Variable
Engine power	3.5 kW @ 1500 rpm

The combustion, performance, energy, and exergy characteristics were identified and thoroughly analyzed using the equations provided below within the framework of thermodynamic evaluation. Various engine performance parameters, including power, efficiency, specific fuel consumption and the air excess coefficient, were determined accordingly. The indicated (in-cylinder) power (*IP*), brake power (*BP*) and friction (lost) power (*FP*) were calculated as follows:[18,19]

$$IP = \frac{WNZ}{60 \times CC \times 1000} \tag{1}$$

$$BP = \frac{2\pi N\tau}{60 \times 1000} \tag{2}$$

$$FP = IP - BP \tag{3}$$

The indicated specific fuel consumption (*ISFC*) and brake specific fuel consumption (*BSFC*) were calculated as follows:[18,19]

$$ISFC = \frac{\dot{m}_f}{IP} \tag{4}$$

$$BSFC = \frac{\dot{m}_f}{BP} \tag{5}$$

(CC) 2026 Serbian Chemical Society.

The indicated thermal efficiency (*ITE* or η_i), mechanical efficiency (*ME* or η_m) and brake thermal efficiency (*BTE* or η_e) were calculated as follows:[18,19]

$$ITE = \eta_i = \frac{3600IP}{\dot{m}_f LHV_f} \tag{6}$$

$$BTE = \eta_e = \frac{3600BP}{\dot{m}_f LHV_f} \tag{7}$$

In the energy analysis, the fuel energy (E_f), energy converted into work (E_W), energy lost with heat transfer (E_{cw}), energy lost with exhaust (E_{exh}) and other energy losses (E_{other}) were determined as follows:[19–21]

$$E_f = \dot{m}_f LHV_f \tag{8}$$

$$E_w = 3600BP \tag{9}$$

$$E_{cw} = \dot{m}_{cw} c_{p,cw} (T_2 - T_1) \tag{10}$$

$$E_{exh} = \left(\dot{m}_f + \dot{m}_h\right) c_{p,exh} (T_3 - T_0) \tag{11}$$

$$E_{other} = E_f - \left(E_w + E_{cw} + E_{exh}\right) \tag{12}$$

In the exergy analysis, the fuel exergy ($E_{\chi f}$), exergy converted into work ($E_{\chi w}$), exergy lost with heat transfer ($E_{\chi cw}$), exergy lost with exhaust ($E_{\chi exh}$) and exergy destruction ($E_{\chi dest}$) were determined as follows:[19–21]

$$E_{\chi_f} = \dot{m}_f \left[1.0401 + 0.1728\frac{h}{c} + 0.2169\frac{s}{c}\left(1 - 2.0628\frac{h}{c}\right)\right] \tag{13}$$

$$E_{\chi_w} = E_w \tag{14}$$

$$E_{\chi_{cw}} = E_{cw} + \left[\dot{m}_{cw} c_{p,w} T_2 \ln\left(\frac{T_1}{T_2}\right)\right] \tag{15}$$

$$E_{\chi_{exh}} = E_{exh} + \left[\left(\dot{m}_f + \dot{m}_h\right) c_{p,exh} T_0 \ln\left(\frac{T_0}{T_3}\right)\right] \tag{16}$$

$$E_{\chi_{dest}} = E_{\chi_f} - \left(E_{\chi_w} + E_{\chi_{cw}} + E_{\chi_{exh}}\right) \tag{17}$$

The exergy efficiency (η_{ex}), exergy performance coefficient (*EPC*) and sustainability index (*SI*) were also calculated as follows:[20–22]

$$\eta_{ex} = \frac{E_{\chi_w}}{E_{\chi_f}} \tag{18}$$

$$EPC = \frac{E_{\chi_w}}{E_{\chi_{dest}}} \tag{19}$$

$$SI = \frac{1}{1 - \eta_{ex}} \tag{20}$$

(CC) 2026 Serbian Chemical Society.

Uncertainties inevitably arise during experimental measurements due to the sensitivity of instruments, possible measurement errors and environmental conditions. Hence, uncertainty analysis is essential to demonstrate the accuracy of experimental results. In this study, the uncertainty analysis was carried out using the method described below. Any result parameter R is expressed as a function of the independent variables $x_1, x_2,\ldots,x_n$ as follows:[22]

$$R = R(x_1, x_2, \ldots, x_n) \tag{21}$$

Accordingly, the uncertainty U_R associated with any result parameter is determined as follows:

$$U_R = \sqrt{U_{R,1}^2 + U_{R,2}^2 + \ldots + U_{R,n}^2} = \sqrt{\sum_{i=1}^{n} U_{R,i}^2} \tag{22}$$

This approach, also referred to as the partial uncertainty method, determines the uncertainty $U_{R,i}$ arising from any independent variable x_i as follows:[22]

$$U_{R,i} = \left|\frac{\partial R}{\partial x_i}\right| U_i \qquad (1 \le i \le n) \tag{23}$$

The scale, sensitivity, and uncertainty values of the measurement devices, along with the uncertainty values of the main parameters calculated using this method, are shown in Table II.

TABLE II. Uncertainty values of devices and parameters

Measured parameter	Device	Scale	Sensitivity	Uncertainty, %
Engine load	Strain gauge	0–50 kg	±0.1 kg	±0.5
Engine speed	Magnetic sensor	0–10000 rpm	±10 rpm	±1
Pressure	Piezo sensor	0–5000 psi	±0.1 psi	±1
Crank angle	Magnetic sensor	–	±1 °CA	±0.2
Air flow rate	Pressure transducer	200 mm	1 mm	±1
Fuel flow rate	Pressure transducer	500 mmWC	1 mm	±1
Exhaust gas temperature	K-type thermocouple	0–1200 °C	±1 °C	±0.2
Brake torque	–	–	–	±0.5
Brake power	–	–	–	±1
Air excess coefficient	–	–	–	±1
Specific fuel consumption	–	–	–	±1.1
Brake thermal efficiency	–	–	–	±1.2

RESULTS AND DISCUSSION

Fig. 2a presents the variation in mass burned fraction (*MBF*) with crank angle at full load for different *CR*s. For all *CR*s, MBF increases rapidly with increasing crank angle, as shown in the figure. However, MBF begins to rise earlier at higher *CR*s. This behavior is attributed to the shortening of the ignition delay period, which leads to earlier and faster combustion since the in–cylinder gas pressure and temperature reach higher values as the *CR* increases. Fig. 2b illustrates the variation in heat release rate (*HRR*) with crank angle at full load for different *CR*s. Similar to *MBF*, the *HRR* rises earlier with increasing *CR* and it begins to decline sooner due to the shorter combustion duration, as shown in the figure. Moreover,

(CC) 2026 Serbian Chemical Society.

the maximum *HRR* value increases with higher *CR*s as a result of the reduced ignition delay period. The maximum *HRR* values were determined to be 63.65, 67.34 and 67.49 J $^{-}$°CA for *CR*s of 15, 16, and 17, respectively. Fig. 2c depicts the variation in pressure rise rate (*PRR*) at full load for different *CR*s. As the *CR* increases, the *PRR* begins to rise earlier and reaches its highest value at a *CR* of 17, as shown in the figure. The maximum *PRR* values were determined to be 6.04, 6.15 and 7.05 bar $^{-}$°CA for *CR*s of 15, 16, and 17, respectively. These results indicate that increasing the *CR* beyond a certain level may lead to knocking, which adversely affects engine performance.

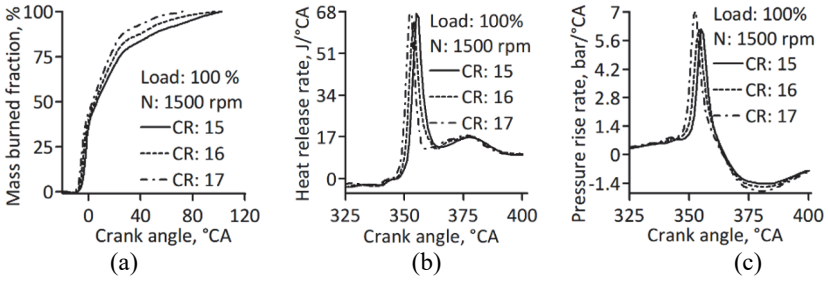

Fig. 2. Variations in: a) mass burned fraction, b) heat release rate and c) pressure rise rate.

Fig. 3a and b shows the variations in cylinder pressure and temperature with crank angle at full load for different *CR*s. Both cylinder pressure and temperature rise rapidly with the onset of combustion, and this increase occurs earlier as the *CR* rises, as illustrated in the figures. This behavior is attributed to the shortened ignition delay period at higher *CR*s, resulting in earlier combustion. Consequently, higher maximum values of cylinder pressure and temperature were achieved with increasing *CR*. Conversely, cylinder pressure and temperature began to decline earlier during the expansion process due to a shorter ignition delay and combustion duration, leading to lower values at the end of the expansion. The maximum cylinder pressures were determined to be 61.81, 65.07 and 69.31 bar, while the maximum cylinder temperatures were found to be 1319.31, 1424.63 and 1456.38 °C for *CR*s of 15, 16, and 17, respectively.

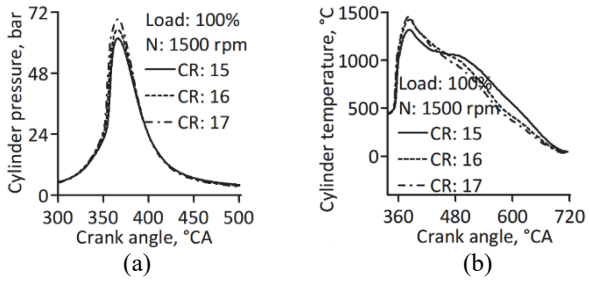

Fig. 3. Variations in: a) cylinder pressure and b) cylinder temperature.

(CC) 2026 Serbian Chemical Society.

Fig. 4a and b presents the variations in energy converted to work (E_W) and the ratio of E_W (E_W/E_f) with engine load at 1500 rpm for different *CR*s. Both E_W and its ratio increase significantly with rising engine load, which is attributed to the greater amount of fuel supplied to the cylinder at higher loads. Conversely, while the absolute E_W values did not vary considerably with *CR*, the ratio of E_W generally exhibited an increasing trend at higher *CR*s. This improvement is explained by enhanced combustion efficiency at elevated *CR*s, resulting in a larger fraction of fuel energy being converted into useful work.[23] It was determined that the E_W ratio increased by 4.7–9.9 and 4.6–17.4 % for *CR*s of 16 and 17, respectively, compared to a *CR* of 15 depending on engine load, while a reduction of 2.3 % was also observed at a *CR* of 16.

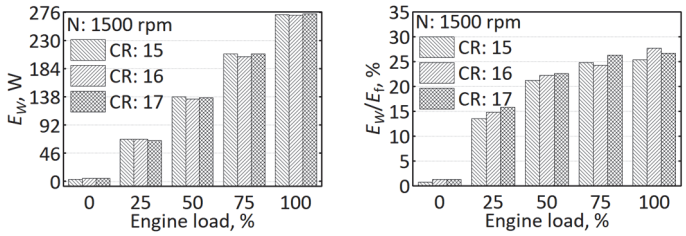

Fig. 4. Variations in: a) energy converted to work and b) ratio of energy converted to work.

Fig. 5a and b shows the variations in energy lost by heat transfer (E_{cw}) and the ratio of E_{cw} (E_{cw}/E_f) with engine load at 1500 rpm for different *CR*s. As shown in Fig. 5a, the amount of E_{cw} increases notably with rising load, which is attributed to higher combustion temperatures resulting from greater fuel supply to the cylinder. The E_{cw} ratio was lower at minimum and maximum loads (0 and 100 %), while it exhibited an increasing trend at medium loads (25–75 %). This behavior is explained by lower combustion temperatures at low loads and shorter combustion durations at high loads. Conversely, although the absolute E_{cw} values increased with *CR*, the E_{cw} ratio generally showed a stronger tendency to rise with higher *CR*s. This is attributed to increased heat loss caused by elevated combustion temperatures and longer combustion durations at higher *CR*s.[24] It was determined that the E_{cw} ratio increased by 6.4–19.5 and 5.8–24.7 % for *CR*s of 16 and 17, respectively, compared to a *CR* of 15 depending on engine load, while a reduction of 2.3 % was also observed at a *CR* of 16.

Fig. 6a and b shows the variations in energy lost through exhaust (E_{exh}) and the ratio of E_{exh} (E_{exh}/E_f) with engine load at 1500 rpm for different *CR*s. As illustrated, both the amount and ratio of E_{exh} increase notably with rising load. This is attributed to the greater fuel supply at higher loads, which results in an increase in combustion energy release, elevated combustion temperatures, and extended combustion duration.[20] Conversely, the amount and the ratio of E_{exh}

(CC) 2026 Serbian Chemical Society.

generally exhibited a slight upward trend with increasing *CR*, which is explained by higher in-cylinder pressures and temperatures at elevated *CR*s. These conditions lead to higher exhaust gas temperatures, and consequently greater energy carried away by the exhaust gases.[25] It was determined that the E_{exh} ratio increased by 4.4–17.1 and 13–21 % for *CR*s of 16 and 17 respectively, compared to a *CR* of 15 depending on engine load, while reductions of 0.6–3.6 and 0.7 % were also observed at the same *CR*s.

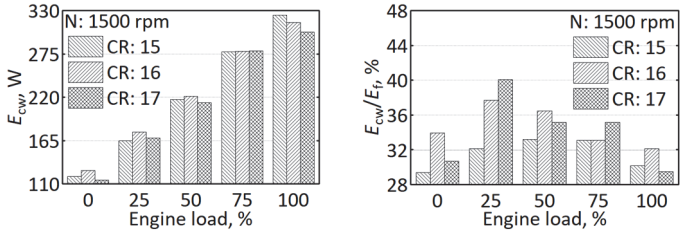

Fig. 5. Variations in: a) energy lost with heat transfer and b) ratio of energy lost by heat transfer.

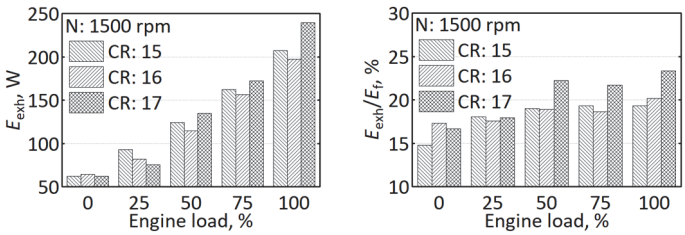

Fig. 6. Variations in: a) energy lost with exhaust and b) ratio of energy lost with exhaust.

Fig. 7a and b illustrates the variations in other energy losses (E_{other}) and the ratio of E_{other} (E_{other}/E_f) with engine load at 1500 rpm for different *CR*s. In ICEs, most other energy losses arise from combustion inefficiencies, friction losses, auxiliary power usage and fundamental thermodynamic limitations.[26] As shown in Fig. 7a, the amount of E_{other} initially decreases with rising load, then increases again, resulting in lower values at medium loads (50–75 %). This behavior is attributed to the fact that energy dissipated to auxiliary equipment remains relatively constant, even though the engine produces more work as load increases. Conversely, both the amount and ratio of E_{other} generally tend to decrease with higher *CR*s. This reduction is explained by the increase in E_W and the improvement in combustion efficiency at elevated *CR*s, which lead to lower losses.[27] It was determined that the E_{other} ratio decreased by 15.5–20.2 and 8.6–28 % for *CR*s of 16 and 17, respectively, compared to a *CR* of 15 depending on engine load, while an increase of 5.4 % was also observed at a *CR* of 16.

(CC) 2026 Serbian Chemical Society.

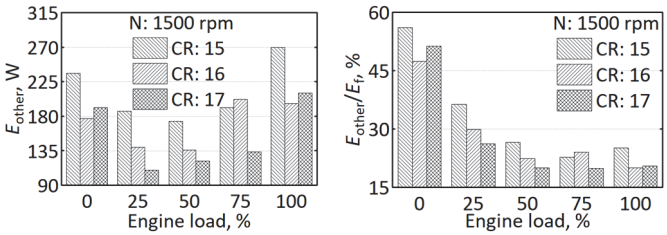

Fig. 7. Variations in: a) other energy losses and b) ratio of other energy losses.

Fig. 8a and b shows the variations in brake specific fuel consumption (*BSFC*) and energy (thermal) efficiency with engine load at 1500 rpm for different *CR*s. As shown in Fig. 8a, *BSFC* decreases significantly with rising engine load, which is attributed to the increase in work (power) produced at higher loads. Conversely, *BSFC* generally tends to decrease with increasing *CR*, due to elevated cylinder pressure and temperature that promote a more homogeneous fuel–air mixture and enhance combustion efficiency.[23] *BSFC* was reduced by 2.5–9.4 and 5–15.6 % for *CR*s of 16 and 17, respectively, compared to a *CR* of 15, depending on engine load. Furthermore, higher *CR*s were noted to improve volumetric efficiency and reduce *BSFC*, as a shortened ignition delay enhances combustion efficiency.[21] A higher *CR* compresses the air–fuel mixture further before ignition, leading to increased cylinder temperature and pressure, which results in greater energy conversion and higher power output. As shown in Fig. 8b, energy efficiency increased with both rising load and *CR*, which was attributed to improved combustion efficiency and consequently higher work output. It was observed that increasing *CR* reduces the fuel required to achieve the same power, while simultaneously improving combustion efficiency and reducing losses, thereby enhancing energy efficiency.[28] It was determined that energy efficiency increased by 4.7–9.8 and 4.9–17.4 % for *CR*s of 16 and 17, respectively, compared to a *CR* of 15, depending on engine load, while a reduction of 2.2 % was also observed at a *CR* of 16.

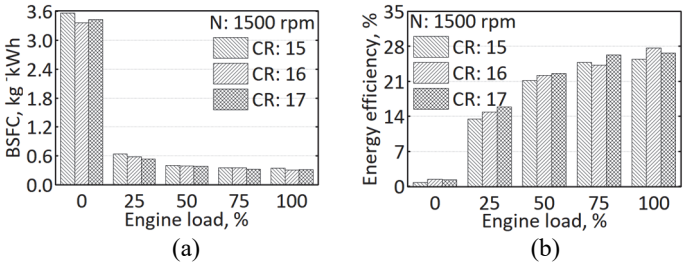

Fig. 8. Variations in: a) *BSFC* and b) energy efficiency.

Fig. 9a and b presents the variations in exergy converted to work ($E_{\chi W}$) and the ratio of $E_{\chi W}$ ($E_{\chi W}/E_{\chi f}$) with engine load at 1500 rpm for different *CR*s. As

(CC) 2026 Serbian Chemical Society.

seen in Fig. 9a, both the amount of $E_{\chi W}$ and its ratio increase significantly with rising engine load. This behavior is attributed to the greater fuel supply at higher loads, and the enhanced work output resulting from improved combustion efficiency. Conversely, although the absolute $E_{\chi W}$ values did not vary considerably with *CR*, the $E_{\chi W}$ ratio generally exhibited an increasing trend with higher *CR*s. This improvement is explained by the rise in combustion efficiency at elevated *CR*s, which enables a larger fraction of exergy input ($E_{\chi f}$) to be converted into useful work. The $E_{\chi W}$ ratio was found to increase by 9.9–22.1 and 4.9–17.4 % for *CR*s of 16 and 17, respectively, compared to a *CR* of 15, depending on engine load.

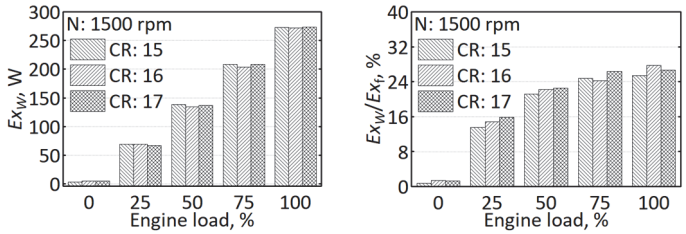

Fig. 9. Variations in: a) exergy converted to work and b) ratio of exergy converted to work.

Fig. 10a and b illustrates the variations in exergy lost through heat transfer ($E_{\chi cw}$) and the ratio of $E_{\chi cw}$ ($E_{\chi cw}/E_{\chi f}$) with engine load at 1500 rpm for different *CR*s. As shown in Fig. 10a, both the amount and the ratio of $E_{\chi cw}$ increased significantly with rising engine load. This behavior is attributed to higher combustion temperatures and changes in combustion duration as more fuel is supplied to the cylinder at increased loads. Conversely, although the amount of $E_{\chi cw}$ did not vary considerably with *CR*, the $E_{\chi cw}$ ratio generally exhibited a notable upward trend with increasing *CR*. This is explained by the rise in combustion temperature at higher *CR*s, which leads to greater heat losses.[29] The $E_{\chi cw}$ ratio was found to increase by 19.1–37.6 and 5.6–40.9 % for *CR*s of 16 and 17, respectively, compared to a *CR* of 15, depending on engine load.

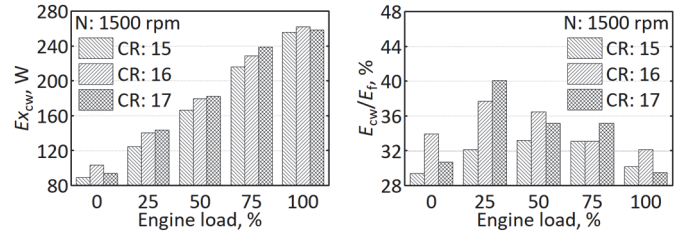

Fig. 10. Variations in: a) exergy lost by heat transfer and(b) ratio of exergy lost by heat transfer.

(CC) 2026 Serbian Chemical Society.

Fig. 11a and b illustrates the variations in exergy lost through exhaust ($E_{\chi exh}$) and the ratio of $E_{\chi exh}$ ($E_{\chi exh}/E_{\chi f}$) with engine load at 1500 rpm for different *CR*s. As shown in Fig. 11a, both the amount and the ratio of $E_{\chi exh}$ increased significantly with rising engine load. This is attributed to the greater fuel supply to the cylinder at higher loads, which results in elevated combustion temperatures and the expulsion of exhaust gases at higher pressures and temperatures. Conversely, although the amount of $E_{\chi exh}$ did not vary considerably with *CR*, the $E_{\chi exh}$ ratio generally exhibited a notable upward trend with increasing *CR*. This behavior is explained by the rise in combustion temperature at higher *CR*s, leading to exhaust gases being discharged at higher temperatures and pressures. It has been reported that improved combustion efficiency and elevated *CR*s contribute to increased combustion temperature and pressure, thereby causing higher $E_{\chi exh}$. Moreover, it has been noted that the energy carried by exhaust gases can be recovered and converted into mechanical energy through a turbocharger system, thus enhancing engine performance.[30] It was determined that the Ex_{exh} ratio increased by 7.8–17.5 and 1.8–20.9 % for *CR*s of 16 and 17, respectively, compared to a *CR* of 15, depending on engine load.

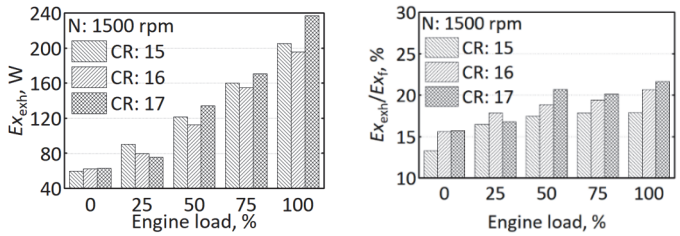

Fig. 11. Variations in: a) exergy lost with exhaust and b) ratio of exergy loss with exhaust.

Fig. 12a and b illustrates the variations in exergy destruction ($E_{\chi dest}$) and ratio of $E_{\chi dest}$ ($E_{\chi dest}/E_{\chi f}$) with engine load at 1500 rpm for different *CR*s. $E_{\chi dest}$ represents the losses arising from irreversible processes such as mixture formation, combustion, friction, and power dissipated by auxiliary equipment, and it is recognized as an important parameter for assessing the thermodynamic performance of an engine. Combustion, in particular, is a highly irreversible process; although the total energy remains constant during the conversion of fuel chemical energy to heat, exergy decreases significantly during combustion.[18] As shown in Fig. 12a, $E_{\chi dest}$ initially decreases with increasing engine load, reaches lower values at medium loads (25–75 %) and then rises again. This trend is attributed to the greater fuel consumption at higher loads, which leads to increased entropy production and consequently higher irreversibilities.[19] Moreover, longer combustion durations resulting from extended fuel injection at elevated loads cause the formation of more residual gas, thereby increasing exergy losses.[20] The $E_{\chi dest}$ ratio, however,

(CC) 2026 Serbian Chemical Society.

decreases notably with rising engine load, which is explained by higher combustion temperatures and improved combustion efficiency at increased engine loads. $E_{\chi dest}$ was found to decrease by 23.1–39.7 and 20.1–38.3 % for *CR*s of 16 and 17, respectively, compared to a *CR* of 15, depending on engine load. Conversely, both the amount and ratio of $E_{\chi dest}$ generally declined with increasing *CR*. This reduction is attributed to higher combustion temperatures and efficiency at elevated *CR*s. Enhanced thermal efficiency at higher *CR*s enables a larger portion of fuel chemical exergy to be converted into work, thereby reducing exergy losses.[31] It was found that the $E_{\chi dest}$ ratio decreased by 13.5–36.4 and 10.1–24.5 % for *CR*s of 16 and 17, respectively, compared to a *CR* of 15, depending on engine load.

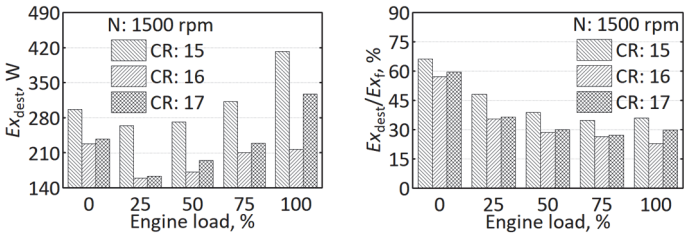

Fig. 12. Variations in: a) exergy destruction and b) ratio of exergy destruction.

Fig. 13a) and b presents the variations in $E_{\chi f}$ and exergy efficiency with engine load at 1500 rpm for different *CR*s. $E_{\chi f}$ increases with rising engine load, while it tends to decrease slightly with higher *CR*s, as shown in Fig. 13a. This behavior is attributed to the greater amount of fuel supplied to the cylinder and thus to higher fuel energy at increased loads.[32] $E_{\chi f}$ was found to decrease by 11.1–18.2 and 4.3––18.2 % for *CR*s of 16 and 17, respectively, compared to a *CR* of 15, depending on engine load. This reduction is thought to result from the lower fuel energy associated with higher *CR*s. Conversely, exergy efficiency increased with both engine load and *CR*, which is explained by improvements in combustion efficiency under these conditions. It has been reported that high combustion instability and low combustion temperature reduce exergy efficiency at low loads, whereas rising combustion temperature enhances combustion efficiency and stability, thereby improving exergy efficiency as load increases. Additionally, the higher quantity and temperature of residual exhaust gases generated at elevated loads preheat the fresh charge, increasing combustion temperature and efficiency, and contributing to higher exergy efficiency.[20] Although higher *CR*s increase combustion temperature, leading to greater heat losses and thermal irreversibilities, exergy efficiency may still improve because the gains in combustion and thermal efficiency outweigh these losses.[33] Exergy efficiency was observed to increase by 9.9–22.1 and 4.9–17.4 % for *CR*s of 16 and 17, respectively, compared to a *CR* of 15, depending on engine load. These variations highlight the dual effect of *CR*: although slight

(CC) 2026 Serbian Chemical Society.

reductions in efficiency occur at the highest *CR*, the overall trend demonstrates that increasing *CR* contributes to improved combustion efficiency and reduced irreversibilities, thereby enhancing exergy performance.

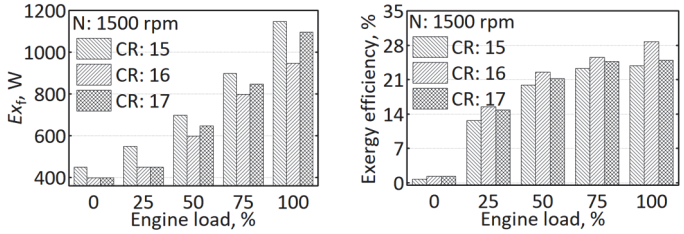

Fig. 13. Variations in: a) fuel exergy and b) exergy efficiency.

Fig. 14a and b illustrates the variations in the exergy performance coefficient (*EPC*) and sustainability index (*SI*) with engine load at 1500 rpm for different *CR*s. Both *EPC* and *SI* increased with rising engine load and *CR*, which is attributed to improved combustion stability, resulting in higher work output and exergy efficiency. It has been reported that the greater amount of fuel and air supplied to the cylinder at higher loads enhances the energy potential in the combustion chamber, thereby increasing *EPC*.[18] Conversely, an *SI* value greater than one indicates more efficient energy utilization with minimal losses in ICEs. *SI* increases with higher power output while decreasing with rising exergy destruction. Exergy efficiency also positively influences *SI*, and a higher *SI* value makes the energy source or process under investigation more attractive.[22] *EPC* was found to decrease by 45.3––110.9 and 26.7–99.9 % for *CR*s of 16 and 17, respectively, compared to a *CR* of 15, depending on engine load. Similarly, *SI* increased by 0.6–6.9 and 0.5–2.6 % for *CR*s of 16 and 17, respectively, compared to a *CR* of 15, depending on engine load. Based on these results, a *CR* of 16 appears to provide more favorable exergetic outcomes among the tested *CR*s. These findings indicate that although minor reductions occur at the highest *CR*, the overall trend demonstrates that higher *CR*s enhance *EPC* and *SI*, reflecting improved combustion stability, reduced irreversibilities, and more suitable energy utilization.

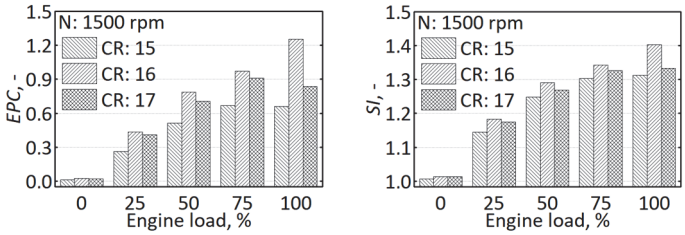

Fig. 14. Variations in: a) exergy performance coefficient and b) sustainability index.

(CC) 2026 Serbian Chemical Society.

CONCLUSION

This study provides a comprehensive thermodynamic analysis of the effects of the compression ratio (*CR*) on the combustion, performance, energy, and exergy characteristics of a diesel engine. Based on the findings, the following conclusions can be drawn.

– It was found that increasing the *CR* shortened the ignition delay, initiated combustion earlier, and completed the combustion process in a shorter duration. Consequently, higher *CR* values resulted in increased cylinder pressure and temperature, leading to improvements in efficiency and reduced fuel consumption. However, elevated pressure and temperature levels may raise production costs, as the engine requires stronger and higher–quality components during manufacturing.

– It was observed that increasing engine load and *CR* enhanced the conversion of fuel energy into work, thereby improving thermal efficiency. On the other hand, while energy losses due to heat and exhaust rose with higher engine load and *CR*, other forms of energy losses generally declined as *CR* increased.

– It was determined that increasing the engine load and *CR* enhanced the exergy converted into work, thereby improving exergy efficiency. On the other hand, while heat transfer and exergy losses through exhaust increased with higher *CR*s, exergy destruction decreased, and both the exergy performance and sustainability index showed notable improvements with rising *CR*.

CR was identified as a key parameter influencing losses, efficiency, exergy, and sustainability. Among the tested *CR*s, a *CR* of 16 was found to deliver the most favorable outcomes, particularly in terms of exergy performance. Specifically, exergy efficiency, exergy performance coefficient and sustainability index increased by 9.9–22.1, 45.3–110.9 and 0.6–6.9 %, respectively, for a *CR,* of 16 depending on engine load.

NOMENCLATURE

η_{ex}	exergy efficiency, %
BP	brake power, W
$BSFC$	brake specific fuel consumption, g / kW h
$BTE(\eta_e)$	brake thermal (energy) efficiency, %
$c_{p,cw}$	specific heat of cooling water, J / kg K
$c_{p,exh}$	specific heat of exhaust gases, J / kg K
CR	compression ratio, –
E_{cw}	energy loss with heat transfer, W
E_{exh}	energy loss with exhaust, W
E_f	fuel energy, W
E_{other}	other energy loss, W
E_W	energy converted to work, W
EPC	exergy performance coefficient, –
$E_{\chi cw}$	exergy loss with heat transfer, W
$E_{\chi dest}$	exergy destruction, W

(CC) 2026 Serbian Chemical Society.

$E_{\chi exh}$	exergy loss with exhaust, W
$E_{\chi f}$	fuel exergy, W
$E_{\chi W}$	exergy converted to work, W
FP	friction power, W
IP	indicated power, W
$ISFC$	indicated specific fuel consumption, g / kW h
$ITE(\eta_i)$	indicated thermal efficiency, %
CC	cycle coefficient, CC = 1 and CC = 2 for two and four stroke engines
LHV_f	lower heating value of fuel, J
M_{cw}	flow rate of cooling water, kg / s
m_f	flow rate of fuel, kg / s
N	engine speed, rpm
SI	sustainability index, –
T	temperature, °C or K
U	uncertainty, –
V_h	stroke volume, L or m^3
W	work, W
Z	number of cylinder, –

ИЗВОД

ДЕТАЉНА ТЕРМОДИНАМИЧКА АНАЛИЗА РАДА ДИЗЕЛ-МОТОРА ПРИ РАЗЛИЧИТИМ СТЕПЕНИМА КОМПРЕСИЈЕ

HAKAN BAYRAKTAR[1] и İSMET SEZER[2]

[1]Karadeniz Technical University, Department of Mechanical Engineering, Faculty of Engineering, Trabzon, Türkiye и [2]Gümüşhane University, Department of Mechanical Engineering, Faculty of Engineering and Natural Sciences, Gümüşhane, Türkiye

У овом раду експериментално је испитан утицај степена компресије (*CR*) на карактеристике сагоревања, као и енергетске и ексергетске карактеристике дизел-мотора. У испитивањима је коришћен четворотактни, атмосферски, водом хлађени, једноцилиндрични дизел-мотор са директним убризгавањем и могућношћу промене степена компресије. Експерименти су спроведени при константној брзини обртања од 1500 rpm, при различитим оптерећењима и степенима компресије од 15:1, 16:1 и 17:1. Софтвер у оквиру експерименталне поставке израчунава аритметичку средину резултата за десет радних циклуса како би се смањио утицај варијација између појединачних циклуса и повећала тачност резултата. На основу експериментално добијених података спроведена је детаљна термодинамичка анализа у циљу испитивања карактеристика сагоревања, као и енергетских и ексергетских карактеристика мотора при различитим степенима компресије. Резултати су показали да степен компресије има значајан утицај на наведене карактеристике. Са повећањем степена компресије повећавали су се параметри сагоревања, као што су удео сагореле масе, брзина ослобађања топлоте, притисак у цилиндру и температура гасова. Слично томе, са повећањем степена компресије уочена је и тенденција побољшања показатеља перформанси мотора, укључујући ефикасност, потрошњу горива, као и укупне енергетске и ексергетске перформансе. Од испитиваних степена компресије, степен компресије 16:1 показао је најповољније резултате са аспекта ексергетске анализе. Конкретно, при степену компресије 16:1, у зависности од оптерећења мотора, ексергетска ефикасност побољшана је за 9,9–22,1 %, коефицијент ексергетских перформанси за 45,3––110,9 %, а индекс одрживости за 0,6–6,9 %.

(Примљено 31. марта, ревидирано 25. маја, прихваћено 6. октобра 2026)

(CC) 2026 Serbian Chemical Society.

REFERENCES

1. A. B. Koc, M. Abdullah, *Fuel Process. Technol.* **109** (2013) 70 (https://doi.org/10.1016/j.fuproc.2012.09.039)
2. R. Beerge, S. Devarmani, in *Diesel Engines – Current Challenges and Future Perspectives*, IntechOpen, Rijeka, 2024 (https://doi.org/10.5772/intechopen.110936)
3. L. Wargula, A. Kadirov, D. Aimukhanov, D. Ulbrich, P. Kaczmarzyk, D. Bak, B. Wieczorek, *Sustainability* **17** (2025) 10435 (https://doi.org/10.3390/su172310435)
4. H. Liu, S. Yu, T. Wang, J. Li, Y. Wang, *J. Clean. Prod.* **451** (2024) 141996 (https://doi.org/10.1016/j.jclepro.2024.141996)
5. P. J. Megía, A. J. Vizcaíno, J. A. Calles, A. Carrero, *Energy Fuels* **35** (2021) 16403 (https://doi.org/10.1021/acs.energyfuels.1c02501)
6. M. H. Bhuiyan, Z. Siddique, *Int. J. Hydrogen Energy* **102** (2025) 1026 (https://doi.org/10.1016/j.ijhydene.2025.01.033)
7. M. E. M. Soudagara, S. Shelared, D. Marghadef, P. Belkhodeh, M. Nur-E-Alami, T. S. Kiongk, S. Ramesha, A. Rajabik, H. Venuk, T. M. Y. Khanl, M. A. Mujtabam, K. Shahapurkara, M. A. Kalamo, I. M. R. Fattah, *Energy Convers. Manage.* **307** (2024) 118337 (https://doi.org/10.1016/j.enconman.2024.118337)
8. M. A. I. Malika, M. A. Kalama, M. M. Abbas, A. S. Silitonga, A. Ikram, *Energy Convers. Manage.* **313** (2024) 118643 (https://doi.org/10.1016/j.enconman.2024.118643)
9. P. C. Miles, Ö. Andersson, *Int. J. Engine Res.* **17** (2015) 6 (https://doi.org/10.1177/1468087415604754)
10. M. K. Allawi, *Int. J. Eng. Tech. Res.* **5** (2016) 66 (https://www.erpublication.org/published_paper/IJETR042155.pdf)
11. D. Lou, Y. Liu, Y. Zhang, *Energies* **18** (2025) 1656 (https://doi.org/10.3390/en18071656)
12. M. Kaplan, *Int. J. Automot. Eng. Technol.* **8** (2019) 83 (https://doi.org/10.18245/ijaet.1495032)
13. Ö. Can, E. Öztürk, E. Arcaklioğlu, *Int. J. Automot. Sci. Technol.* **5** (2021) 43 (https://doi.org/10.30939/ijastech..805531)
14. T. Grönstedt, M. Irannezhad, X. Lei, O. Thulin, A. Lundbladh, *J. Eng. Gas Turbines Power* **136** (2014) 31202 (https://doi.org/10.1115/1.4025727)
15. M. Özkan, *Entropy* **17** (2015) 244 (https://doi.org/10.3390/e17010244)
16. J. P. G. Montoya, *Appl. Therm. Eng.* **280** (2025) 128376 (https://doi.org/10.1016/j.applthermaleng.2025.128376)
17. https://www.apexinnovations.co.in/pdf/PSP240.pdf (03.04.2026)
18. K. Gupta, N. Singh, P. Goswami, A. Priyam, *Int. J. Hydrogen Energy* **163** (2025) 150712 (https://doi.org/10.1016/j.ijhydene.2025.150712)
19. R. B. Mshelia, R. Yusuf, S. Sudi, *Konya J. Eng. Sci.* **10** (2022) 18 (https://doi.org/10.36306/konjes.984008)
20. D. Erol, E. Gülcan, *Int. J. Automot. Eng. Technol.* **14** (2025) 154 (https://doi.org/10.18245/ijaet.1705733)
21. C. Tiwari, T. N. Verma, G. Dwivedi, P. Verma, *Appl. Sci.* **13** (2023) 1857 (https://doi.org/10.3390/app13031857)
22. M. Ünaldi, A. Uyaroglu, H. E. Gülcan, M. Ciniviz F. Aydin, *Int. J. Hydrogen Energy* **158** (2025) 150542 (https://doi.org/10.1016/j.ijhydene.2025.150542)
23. M. K. Rath, S. K. Acharya, P. P. Patnnaik, S. Roy, *Int. J. Eng.* **27** (2014) 1259 (https://www.ije.ir/article_72362_5cf5ccfabacae0fe6ee918ef6961bc99.pdf)

(CC) 2026 Serbian Chemical Society.

24. V. Gnanamoorthi, G. Devaradjane, *J. Energy Inst.* **88** (2015) 19 (https://doi.org/10.1016/j.joei.2014.06.001)
25. S. Verma, L. M. Das, S. C. Kaushik, *Energy Convers. Manage.* **138** (2017) 346 (https://doi.org/10.1016/j.enconman.2017.01.066)
26. V. Gajjar, V. Patel, *Int. J. Eng. Sci. Invention* **13** (2024) 38 (https://www.ijesi.org/papers/Vol(13)i6/D13063846.pdf)
27. P. Bridjesh, G. Arunkumar, *Int. J. Chem. Sci.* **13** (2015) 997
28. S. S. Bhatti, S. Verma, S. K. Tyagi, *Therm. Sci. Eng. Prog.* **9** (2019) 332 (https://doi.org/10.1016/j.tsep.2018.12.006)
29. H. Yaman, *Process. Saf. Environ. Prot.* **158** (2022) 607 (https://doi.org/10.1016/j.psep.2021.12.014)
30. S. G. Chaudhari, M. A. Modi, T. M. Patel, G. P. Rathod, *IOSR J. Eng.* **6** (2016) 13 (https://iosrjen.org/Papers/vol6_issue4%20(part-3)/D06431319.pdf)
31. M. K. Yesilyurt, *Fuel* **278** (2020) 118319 (https://doi.org/10.1016/j.fuel.2020.118319)
32. B. Wang, M. Pamminger, T. Wallner, *Appl. Energy* **254** (2019) 113645 (https://doi.org/10.1016/j.apenergy.2019.113645)
33. Z. M. Yao, Z. Q. Qian, R. Li, E. Hu, *Energy* **176** (2019) 991 (https://doi.org/10.1016/j.energy.2019.04.027).

(CC) 2026 Serbian Chemical Society.

Journal of the Serbian Chemical Society
JSCS-info@shd.org.rs • www.shd.org.rs/JSCS
J. Serb. Chem. Soc. 91 (10) 1043–1057 (2026)
JSCS–5543
Original scientific paper
Published 16 November, 2026

Influence of fly ash fineness on cesium immobilization in geopolymers

GORDANA G. STANOJEVIĆ[1]*, MIROSLAV M. KOMLJENOVIĆ[1], JANA LJ. PETROVIĆ[2] and RADA D. PETROVIĆ[3]

[1]*Institute for Multidisciplinary Research, National Institute of the Republic of Serbia, University of Belgrade, Kneza Višeslava 1, 11030 Belgrade, Serbia,* [2]*Innovation Center of the Faculty of Technology and Metallurgy, Ltd, 11060 Belgrade, Serbia and* [3]*Faculty of Technology and Metallurgy, University of Belgrade, Karnegijeva 4, 11060, Belgrade, Serbia*

(Received 16 May, revised 27 May, accepted 2 June 2026)

Abstract: The influence of fly ash (FA) fineness on cesium immobilization in geopolymers was investigated by comparing samples synthesized in this study with those reported previously, as all samples were prepared at 95 °C with Cs contents of 2 and 5 wt. %. The effect of FA particle size distribution on physicomechanical properties, gel structure development, and Cs leaching behavior was evaluated. Results show that FA fineness significantly affects the kinetics of geopolymerization and the development of mechanical properties. In general, Cs addition prolongs the setting time of G-FA, with longer setting times observed in G-FA based on the coarser FA sample. These samples also showed lower compressive strengths, indicating that finer FA particles promote faster dissolution of aluminosilicate species and more rapid formation of the geopolymeric gel. Leaching behavior revealed that Cs release is diffusion-controlled regardless of FA fineness and Cs content, but the mean leachability index (L_{mean}) was lower in samples based on coarser FA particles, although in all cases it was higher than 9, which indicates effective Cs immobilization and satisfactory long-term stability of the material. Overall, FA fineness influences geopolymer reactivity, gel structure, and thus mechanical performance and effectiveness of Cs immobilization.

Keywords: alkaline activation; particle size distribution; radioactive waste; leaching; physicomechanical properties.

INTRODUCTION

Geopolymers are formed as a product of alkaline activation of aluminosilicate materials, including fly ash (FA) from thermal power plants.[1] The main product of the reaction is a cross-linked, three-dimensional, predominantly amorphous aluminosilicate gel, consisting of SiO_4 and AlO_4 tetrahedra that are connected by

* Corresponding author. E-mail: gordana@imsi.bg.ac.rs
https://doi.org/10.2298/JSC260516030S

Available online at https://www.shd.org.rs/JSCS/
(CC) 2026 Serbian Chemical Society.

oxygen. The negative charge resulting from the incorporation of the AlO_4 units into the silicate structure is compensated by alkali metal cations from the activator solution,[2–4] mainly Na^+, which leads to the formation of N-A-S-H gel. Due to such a structure, these materials exhibit a high capacity for binding and stabilizing ionic species, which is why they have recently been intensively investigated for the immobilization of radionuclides.[10,11] Among the key radionuclides resulting from nuclear activities, ^{137}Cs is characterized by a moderate half-life (about 30 years),[7,8,12] high specific activity (3.2 TBq/g),[13] and high-energy decay,[14] which makes it highly dangerous and harmful to both the environment and human health.

Previous studies have investigated the influence of temperature and curing time, as well as Cs sources such as $CsNO_3$ and $CsOH{\cdot}H_2O$, on Cs immobilization in FA-based geopolymers.[15] It was observed that flexural strengths increased with increasing curing time, but no significant differences were observed with changes in curing temperature. However, in both cases (when Cs was added as $CsOH{\cdot}H_2O$ and as $CsNO_3$), the presence of Cs reduced flexural strengths. This effect was more significant when Cs was added as $CsNO_3$, probably due to the lower pH compared to with that of $CsOH{\cdot}H_2O$. Moreover, these studies suggest that Cs is immobilized within the aluminosilicate gel matrix, which represents the main product of alkali activation. Li *et al.*[16] reported a similar immobilization mechanism and demonstrated that geopolymers exhibit higher Cs immobilization efficiency than that of Portland cement. Jang et al.[17] also evaluated Cs immobilization efficiency using different types of FA with varying chemical compositions, where the Al_2O_3 content ranged from approximately 22 to 27 wt.% and the CaO content from about 2.9 to 5.2 wt.%. Granulometric characteristics were not reported. Despite these compositional variations, the leachability index remained similar, reaching approximately 10 after 90 days of leaching. The influence of Cs on physicochemical properties, such as setting time and mechanical strength, was not assessed. Jain *et al.*[18] demonstrated, using analysis of variance (ANOVA), that curing temperature has the most significant influence on Cs immobilization, contributing approximately 84.64 % to the overall effect, followed by the interaction between Cs content and temperature. The concentration of sodium hydroxide as an activator had only a minor influence (approximately 0.35 %). It was also found that at Cs concentrations higher than 8 %, pollucite ($CsAlSi_2O$) formation occured, which likely resulted in a very high leachability index ranging from 11 to 14.[18,19]

Despite numerous studies, the utilization of geopolymers for the immobilization of radioactive waste, including Cs, remains largely unexploited in practice. This is mainly because the wide range of synthesis conditions makes it difficult to clearly identify the key factors governing FA reactivity and the resulting geopolymer's structure and properties. In addition to chemical and mineralogical composition,[2,21,22] which can differ significantly between sources and even within the same source, FA fineness is considered an important parameter which influences

(CC) 2026 Serbian Chemical Society.

FA reactivity. However, its role in Cs immobilization has not yet been investigated. In this study, FA from the thermal power plant "Nikola Tesla A", Obrenovac (Serbia), was used as the starting material for synthesizing Cs-containing geopolymers. During pneumatic transport at the thermal power plant, FA is separated into several fractions. In our previous study,[22] the FA-4 fraction (finer particles) was used to synthesize Cs-containing geopolymers. In contrast, the present study uses the FA-3 fraction (coarser particles) to evaluate the influence of granulometric composition on Cs immobilization efficiency and physicomechanical properties.

EXPERIMENTAL

Materials

The chemical composition of FA-3 was determined using the classical alkali melting method, while the particle size distribution was determined by wet sieving. The obtained results are presented in Table I. According to the international ASTM C618 classification,[23] FA-3 belongs to Class F. Compared to FA-4,[22] FA-3 has a slightly higher SiO_2 content and a slightly lower Al_2O_3 content. The proportion of fine particles (< 45 μm) in FA-3 is lower than in FA-4 (92.5 %).

TABLE I. Chemical composition (wt. %) and particle size distribution (%) of FA-3

Chemical composition	
SiO_2	58.2
Al_2O_3	20.2
Fe_2O_3	5.3
MnO	0.03
CaO	7.6
MgO	2.0
SO_3	2.2
Na_2O	0.5
K_2O	1.5
Loss on ignition at 1000 °C	1.6
Particle size distribution	
< 45 μm	82.5
45–63 μm	6.8
63–100 μm	6.7
>100 μm	4.0

The geopolymers without and with Cs were prepared under the same conditions as in our previous study.[22] A sodium silicate solution with a modulus (oxide mass ratio, $n = SiO_2/Na_2O$) of 1.5 was used as the activator. The solution was prepared by mixing a commercial sodium silicate solution (13.60 % Na_2O, 26.25 % SiO_2, 60.15 % H_2O; "Galenika-Magmasil", Serbia), with an initial modulus of 1.93, and sodium hydroxide (NaOH) (98.5 %, "Lach-Ner", Czech Republic).

Cesium chloride (99.9 % CsCl, Superlab, Serbia) was used as a source of the non-radioactive isotope $^{133}Cs^+$. Concentrated nitric acid (65 % HNO_3, Analar Normapur, EC) was used to adjust the pH of the solutions obtained by the leaching and filtration procedure, and was intended for the determination of the concentrations of Cs, Si and Al.

Available online at https://www.shd.org.rs/JSCS/

(CC) 2026 Serbian Chemical Society.

Synthesis of geopolymer pastes and mortars

The geopolymer pastes without and with Cs were prepared by mixing FA-3, alkaline activator and water or CsCl solution. The geopolymer mortars were prepared by mixing FA-3, alkaline activator, water or CsCl solution, and standard sand, following the procedure of EN 196-1[24] as closely as possible. Depending on the Cs content (0, 2 and 5 %), the samples were designated as G-FA-3-0Cs, G-FA-3-2Cs and G-FA-3-5Cs, respectively. The procedures for paste and mortar preparation were the same as in the previous research[22] and are given in the Supplementary material to this paper.

Physicomechanical properties

The setting time was monitored on geopolymer paste samples using Vicat penetrating needle, according to EN 196-3 standard procedure.[25]

Compressive strengths of geopolymer mortars were determined according to the EN 196-1[24] standard, using a Matest device.

Characterization of geopolymers

Mineralogical characterization was performed by XRD analysis using an X-ray diffractometer (Proto AXRD Benchtop) with CuKα X-rays, with 0.015° 2θ steps, in the 5–80° 2θ range. Crystal phases were identified using the "Crystallographica Search Match" software and the JCPDS-ICDD powder diffraction database.

Fourier transform infrared spectroscopy (FTIR) measurements were performed using a Perkin Elmer Spectrum Two spectrometer in attenuated total reflection (ATR) mode using a diamond crystal, in the range of 400–4000 cm^{-1}, with a resolution of 4 cm^{-1} and 4 replicates per sample.

Microstructural characterization was carried out using field-emission scanning electron microscopy (FESEM) on a Tescan Mira3 XMU electron microscope. Energy-dispersive spectroscopy (EDS) analysis was performed on an INCAx-act LN2-free analytical silicon drift characteristic X-ray detector with PentaFET® Precision and Aztec 4.3 software package (Oxford Instruments) interfaced with a Tescan Mira3 XMU. EDS analysis was conducted at 17 points per sample. Unreacted FA particles were excluded from the analyzed areas.

Leaching process

Leaching tests for the G-FA-3 samples were conducted according to the ANSI/ANS-16.1--2003 semi-dynamic leaching test,[26] the details of which are presented in the Supplementary material. Based on the Cs leaching results, the leaching rates (*LR*), diffusion coefficient (*D*) and mean leachability index (L_{mean}) were calculated according to Eqs. (S1), (S3) and (S5), which are presented in the Supplementary material.

RESULTS AND DISCUSSION

Physicomechanical properties

Fig. 1 shows the setting times of G-FA-3 pastes at different Cs contents. All tested pastes met the requirement defined by the EN 197-1[27] standard, which states that the start of setting should not be earlier than 60 min. As can be seen, increasing the Cs content prolonged both the initial and final setting times compared to the sample G-FA-3-0Cs. According to the relevant EN 197-1 standard, the final setting time must not exceed 600 min; however, both samples exceeded this limit. The

(CC) 2026 Serbian Chemical Society.

deviation was more pronounced for the sample G-FA-3-5Cs, which showed the greatest delay in setting.

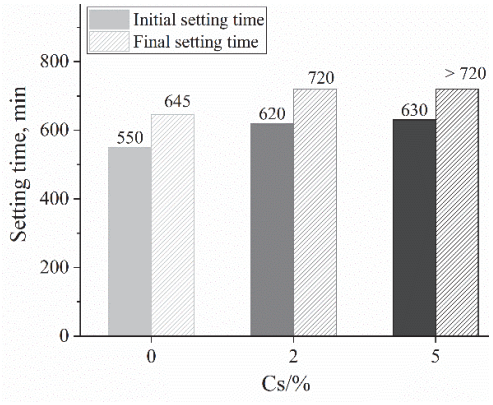

Fig. 1. Setting times of G-FA-3 samples.

Also, in a previous study using a finer fraction of FA,[22] longer setting times were observed in samples containing Cs, which were mainly attributed to the slowing of condensation reactions. In the present study, the setting times were approximately twice as long as in the previous study. This can be attributed to a lower proportion of particles smaller than 45 μm in the FA used here, since the setting behavior depends on the dissolution rate of the starting material. This process is likely governed by the granulometric composition of FA, which influences the specific surface area of the particles and, consequently, the reactivity of the FA. Finer FA particles, due to their higher specific surface area, promote faster release of Si and Al species,[2,28] leading to accelerated gel formation and shorter setting times.

The compressive strengths of G-FA-3 mortars at different Cs contents are shown in Table II. All G-FA-3 samples, regardless of Cs content, exhibited compressive strengths far above the minimum requirement of 3.4 MPa specified by NRC regulations for the immobilization of radioactive waste.[29] Increasing the Cs content to 5 % leads to a slight increase in compressive strength, in contrast to previous research,[22] which reported no significant change in mechanical properties with the addition of cesium. This behavior may be attributed to enhanced dissolution of FA and partial structural reorganization of the aluminosilicate gel in the presence of a larger amount of Cs. This is evident in samples based on FA-3, which has lower intrinsic reactivity, where Cs likely promotes additional dissolution and contributes to a higher degree of gel formation. In the case of the finer system,[22] gel phase formation is predominantly governed by the matrix itself, limiting any additional influence of Cs, although a prolonged setting time was observed, as in this study.

(CC) 2026 Serbian Chemical Society.

TABLE II. Compressive and flexural strengths of G-FA-3 samples

Sample	G-FA-3-0Cs	G-FA-3-2Cs	G-FA-3-5Cs	G-FA-4-0Cs[22]
Compressive strength, MPa				
Value	40.4±1.00	40.8±0.44	44.4±0.53	58.9±1.59
Relative compressive strength, MPa (relative to the sample G-FA-3-0Cs)				
Value	1.00	1.00	1.11	1.45
Relative compressive strength, MPa (relative to the sample G-FA-4-0Cs*)				
Value	0.68	0.69	0.75	1.00

Overall, the G-FA-3 samples exhibited lower compressive strength values compared to G-FA-4 (Table II), which can be attributed to differences in granulometric composition. Obviously, finer particles enable faster formation of aluminosilicate gel and thus better mechanical properties. These results indicate that granulometry plays a key role in governing the mechanical performance of geopolymers.

XRD

The XRD patterns of FA-3 and G-FA-3 samples with varying Cs contents are presented in Fig. S-1 in the Supplementary material. The XRD pattern of FA-3 shows crystalline phases characteristic of FA, as in the case of FA-4: quartz (SiO_2; JCPDS #89-8934), mullite ($Al_{5.33}Si_{0.67}O_{9.33}$; JCPDS #85-1460), hematite (Fe_2O_3; JCPDS #88-2359), anhydride ($CaSO_4$; JCPDS #72-0916) and feldspar ($NaAlSi_3O_8$; JCPDS #89-6423). In addition to these crystalline phases, calcite ($CaCO_3$; JCPDS #72-1937) is observed in G-FA-3 samples due to carbonation, which was also observed in previous research.[12,22] The reflection at 2θ 31.7° in the patterns of the Cs-containing samples increases with increasing Cs content and probably indicates a newly formed crystalline phases with Cs, similar to that in the previous research.[12,22] These results show that granulometric composition does not affect the phase composition of FA and FA-based geopolymers.

FTIR

In Fig. 2, the FTIR spectra of FA-3 and G-FA-3 samples, which are very similar to those of FA-4 and G-FA-4, are shown. The most intense band in the FTIR spectrum of FA-3 is located at 1058 cm^{-1} and originates from the asymmetric stretching vibrations of T–O–Si (T = Al, Si).[30] The bands of the symmetric stretching vibrations of Si–O–Si and Si–O–Al are observed at about 796, 780, 676 and 611 cm^{-1}, while the bands of the symmetric bending vibrations of Si–O–Si and Si–O–Al are located at about 594, 555 and 450 cm^{-1},[30] very similar to those for FA-4. The doublet at 796 and 780 cm^{-1} is mainly attributed to quartz, which remains inert during geopolymerization.[31] In the FTIR spectrum of the G-FA-3-0Cs sample, the most intense band becomes sharper and more intense, and is shifted toward a lower wavenumber, from 1058 cm^{-1} in FA-3 to 1005 cm^{-1} in the G-FA-3-0Cs sample (Fig. 2a). The shift of the most intense band indicates a

(CC) 2026 Serbian Chemical Society.

decrease in the T–O–T angle and elongation of the T–O–Si bonds, and is most often associated with the incorporation of Al into the gel structure during the formation of an aluminosilicate gel.[30,32–35] Such a shift was also observed in the case of the FA-4-based geopolymer. The bands at 676 and 594 cm^{-1} in the G-FA--3-0Cs sample cannot be observed, probably due to the dissolution of FA-3 during geopolymerization, while the band at 555 cm^{-1} remains unchanged during geopolymerization (Fig. 2b). This band probably belongs to mullite.[36] A similar observation was made when using FA-4.[22] The bands at 1443 and 875 cm^{-1} are attributed to the stretching vibrations of the C–O bond in the carbonate group, indicating the presence of carbonate,[15,30] which is also consistent with the XRD analysis. The broad band at about 3390 cm^{-1} and the band at 1641 cm^{-1} originate from the bending and stretching vibrations of the O–H and H–O–H water molecules, which are physically and chemically bound in the N-A-S-H gel structure.[15,30]

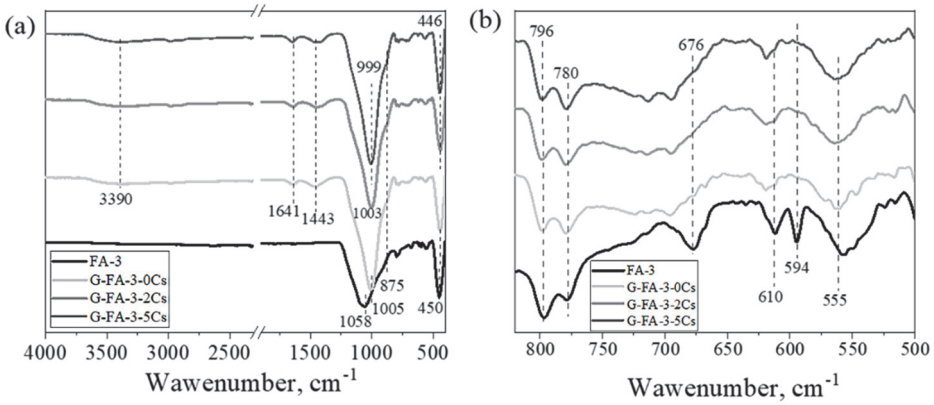

Fig. 2. FTIR spectra of FA-3 and G-FA-3 samples: a) full spectral range and b) expanded view in the 820–500 cm^{-1} range.

In the FTIR spectra of G-FA-3 samples with the addition of Cs, a slight shift of the most intense band was observed from 1005 cm^{-1} (for the G-FA-3-0Cs sample) to 1003 and 999 cm^{-1} for the G-FA-3-2Cs and G-FA-3-5Cs samples, respectively (Fig. 2a). This slight shift of the most intense band with an increase in the Cs content in the G-FA-3 samples could indicate some kind of structural reorganization of the N-A-S-H gel, *i.e.*, an increase in the proportion of Si–O–Al bonds and a higher degree of crosslinking within the gel network. This structural reorganization leads to the formation of a more compact and stable matrix, which is in agreement with the observed increase in strength, especially at higher Cs contents (5 %). The shift to lower wavenumbers was not observed in samples prepared with FA-4, which can be attributed to the higher proportion of finer particles (particles smaller than 45 μm), resulting in a less pronounced effect of Cs addition, which could not be detected by FTIR analysis.

(CC) 2026 Serbian Chemical Society.

FESEM/EDS

As shown in Fig. S-2 in the Supplementary material, the addition of Cs did not significantly affect the microstructure of G-FA-3 samples, as was the case with FA-4-based samples.

Fig. 3 presents the distribution of atomic ratios for the main elements present in the aluminosilicate gel. Overall, the high variability in the measured atomic ratios, as in the case of FA-4-based samples, indicates the heterogeneous nature of the aluminosilicate gel. Notwithstanding, the findings reveal a decrease in the Si/Al ratio with the incorporation of Cs, consistent with previous research,[22] which indicates an increase in Al content in the gel. This aligns with the FTIR analysis, where a shift of the most intense band toward lower wavenumbers was observed (Fig. 2a). The decrease in the Na/Al ratio with the addition of Cs suggests partial substitution of charge-balancing Na^+ by Cs^+ in the aluminosilicate gel structure. Similar trends were observed in the G-FA-4 samples. However, due to the potential migration of Na^+ under the electron beam during EDS analysis, the Na/Al ratio should be interpreted as a relative trend rather than an absolute value.[37] This may also explain the Na/Al ratio lower than 1 in the G-FA-3-0Cs sample.

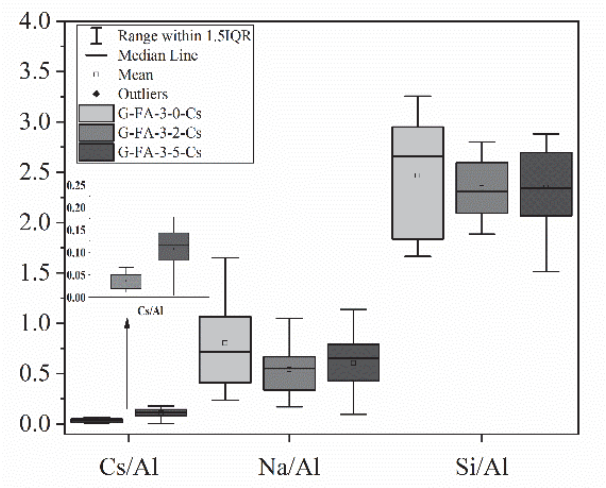

Fig. 3. Distribution of the atomic ratios of the main elements in G-FA-3 samples with varying Cs contents. The inset shows the Cs/Al ratio.

It is evident that Si/Al ratios are lower for G-FA-3 than for G-FA-4 samples, indicating a higher proportion of Al in the G-FA-3 gel. It is known that, in the initial phase of the reaction, a gel with higher aluminum content is formed, due to the greater solubility of aluminum from the amorphous phase of FA in comparison to silicon. As the reaction progresses, a gel with a higher proportion of silicon is formed. Consequently, it can be hypothesized that the alkaline activation reaction

(CC) 2026 Serbian Chemical Society.

is slower in FA-3 due to its coarser particles, resulting in less developed gel formation. Due to a lower degree of geopolymerization, G-FA-3 samples exhibited lower compressive strength in comparison with the G-FA-4 samples, as discussed in the preceding paragraph.

Leaching process

Leaching of Cs. The leaching kinetics of Cs from G-FA-3 samples were investigated based on the cumulative leached concentration and the leaching rate, calculated according to Eq. (S1) in the Supplementary material, as a function of leaching time. The obtained cumulative concentrations and corresponding leaching rates are presented in Fig. 4.

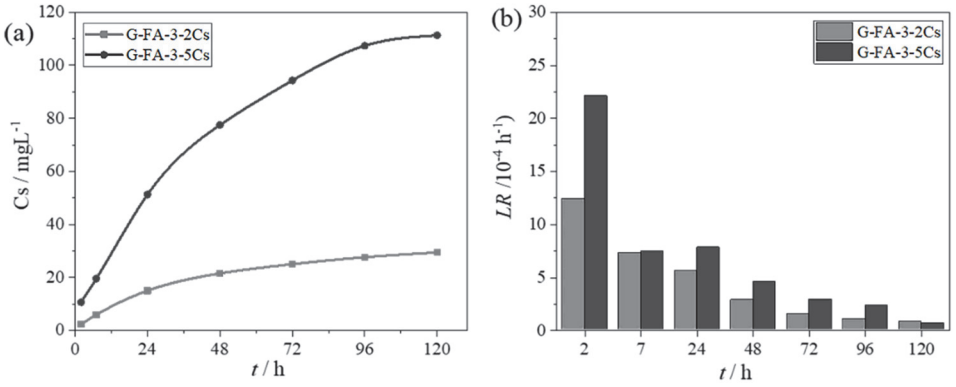

Fig. 4. a) The cumulative concentration of leached Cs and b) the leaching rate of Cs. (Analytical uncertainty at each point is approximately 1 %).

The leaching rate of Cs was highest during the first 2 h (Fig. 4b), similar to the case of G-FA-4 samples.[22] This trend is characteristic of diffusion-controlled leaching, where, after the initial leaching of surface-available ions, the transport of Cs^+ occurs by diffusion through the increasingly compact geopolymer matrix. In general, Cs leaching rates were higher when the Cs content in the sample was 5 %, indicating that the degree of Cs immobilization decreases with increasing Cs content, probably due to a higher proportion of weakly bound Cs^+. These ions are most likely located on the surface or in the pore solution of the aluminosilicate gel, which enables their faster leaching. This effect is also clearly reflected in the cumulative Cs leaching values in samples with higher Cs content. After five days of leaching, the cumulative leached Cs concentration was approximately 3.8 times higher in the sample with 5 % Cs compared to the sample with 2 % Cs, although the Cs content in sample G-FA-3-5Cs is 2.5 times greater than in sample G-FA-3--2Cs. In comparison to G-FA-4 samples (Fig. S-3), cumulative concentrations of leached Cs were higher, regardless of the comparable initial leaching rates.[22] It can be seen that *LR* values in later periods are higher for G-FA-3 samples, which

(CC) 2026 Serbian Chemical Society.

indicates their less compact matrix and easier Cs leaching, meaning lower immobilization efficiency.

Leaching of Si and Al. The cumulative leached concentrations of Si and Al are presented in Fig. 5. The very low concentration of leached Al indicates the stability of the formed gel in deionized water, regardless of the high concentration of leached Si. As hypothesized in previous research,[22] the leached Si originated mainly from unreacted sodium silicate used as the alkaline activator. This assumption is further supported by the consistently high pH values (11–11.5) of the leaching solution throughout the entire leaching period, which indicates the leaching of unreacted alkaline activation solution. Higher concentrations of leached Si in the case of G-FA-3 (Figs. 5a and S-4a) are probably the result of a slower alkaline activation reaction, resulting in larger amounts of residual, unreacted sodium silicate in the gel pores compared to G-FA-4.[22] It was also observed that the addition of Cs leads to a decrease in the leaching of Si and Al, particularly at a Cs content of 5 %, indicating an acceleration of alkaline activation and the formation of a more stable gel structure, consistent with the observed increase in compressive strength.

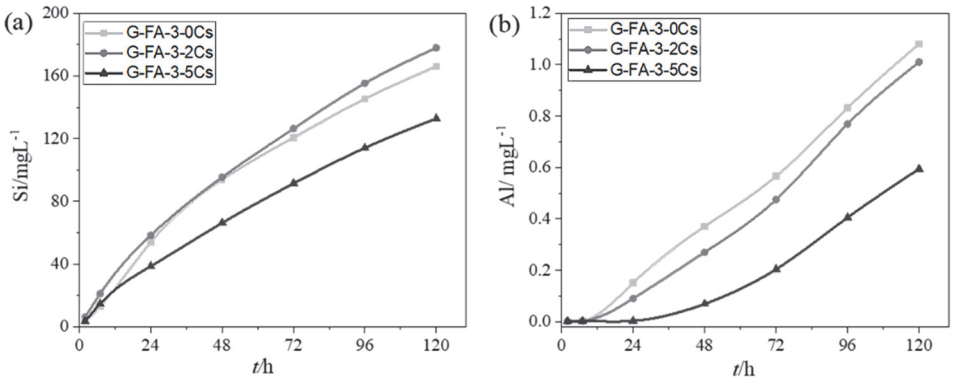

Fig. 5. Cumulative leaching behavior of the main aluminosilicate gel components: a) Si and b) Al. (Analytical uncertainty at each point is approximately 1 %).

Mechanism of Cs leaching and effectiveness of Cs immobilization

The diffusion model proposed by de Groot and van der Sloot was used to determine the primary mechanism of Cs leaching, based on the slope of the relationship between the logarithm of the cumulative leached Cs (B_t) and the logarithm of time (t).[38,39] The value of B_t can be obtained from:

$$B_t = \frac{c_t V_t}{S} \tag{1}$$

(CC) 2026 Serbian Chemical Society.

where B_t is the cumulative concentration of leached Cs over time t, mg m^{-2}); t is the contact time, s; C_t is the concentration of leached Cs over time t, mg L^{-1}; V_t is the volume of the leaching medium, L; S is the geometric surface area of the sample, m^2. A slope value between 0.4 and 0.6 indicates diffusion-controlled leaching. When the slope value is greater than 0.6, the primary leaching mechanism is dissolution (it implies that dissolution on the surface is faster than the diffusion of ions from the interior of the sample), while for a slope value less than 0.4, surface leaching is the primary mechanism. The obtained values are shown in Fig. 6.

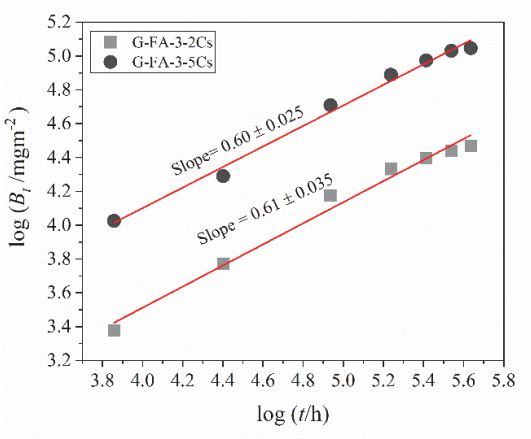

Fig. 6. The leaching mechanism of Cs from G-FA-3.

As can be seen from Fig. 6, the primary mechanism of Cs leaching is diffusion, regardless of the Cs content. Similar Cs leaching behavior was observed for G-FA-4 samples, but the slopes were slightly lower (Fig. S-2).[22] This indicates that the difference in the granulometry of the FA has no significant effect on the mechanism of Cs leaching from the geopolymer, as observed for the physicomechanical characteristics.

The mean leachability index (L_{mean}) of Cs from G-FA-3-2Cs and G-FA-3--5Cs was calculated according to Eq. (S5) in the Supplementary material. The L_{mean} values were 9.4 and 9.1 for samples with 2 and 5 % Cs, respectively. The obtained L_{mean} values are higher than 6, which is the minimum value for a material to be considered suitable for Cs immobilization, according to the NRC criterion.[29]

The corresponding values for G-FA-4-2Cs and G-FA-4-2Cs were 9.7 and 9.3 for 5 days of leaching. Based on the presented results, the slightly lower L_{mean} for G-FA-3 can be attributed to the formation of a less compact and more permeable gel structure due to the lower reactivity of the coarser FA particles.

(CC) 2026 Serbian Chemical Society.

CONCLUSION

In this study, the influence of fly ash (FA) particle size distribution on Cs immobilization was investigated. Geopolymers were synthesized using fly ash (FA-3) with approximately 82 wt. % of particles smaller than 45 μm, at 95 °C for 24 h, with Cs contents of 2 and 5 wt. %. The obtained results were compared with literature data for geopolymers prepared under identical experimental conditions using the finer FA-4, with approximately 92 wt. % of particles smaller than 45 μm.

The FA-3-based geopolymers (G-FA-3) showed that the addition of Cs prolonged the initial and final setting times, indicating a slowdown of condensation reactions, similar to that observed in G-FA-4 samples. However, longer setting times were recorded for G-FA-3 compared to FA-4-based geopolymers (G-FA-4). The addition of Cs also increased compressive strength at 5 wt. % Cs in the G-FA-3 samples, but the compressive strengths were lower than those of G-FA-4, which is attributed to the slower reaction of coarser FA-3 particles. The slower reaction kinetics likely led to the formation of a less compact aluminosilicate gel structure, which is reflected in the generally lower compressive strength values of G-FA-3 compared to G-FA-4.

The leaching behavior confirmed that Cs release was diffusion-controlled in all systems, independent of FA granulometry, with mean leachability index (L_{mean}) values of 9.7 and 9.3 for G-FA-3 at 2 and 5 wt. % Cs, respectively. Nevertheless, the slightly higher Cs release observed for G-FA-3 compared to G-FA-4 is consistent with the formation of a less compact gel network resulting from the lower reactivity of the coarser FA particles.

Overall, the results confirm that both FA fractions with different particle size distributions can be successfully applied for Cs immobilization. Although the influence of Cs on setting behavior, mechanical performance, and leaching resistance follows the same general trends as those observed for G-FA-4, these effects are more pronounced in G-FA-3 due to the lower reactivity of the coarser FA fraction. These findings highlight the importance of optimizing FA granulometry to improve matrix compactness and mechanical performance without compromising long-term environmental stability.

SUPPLEMENTARY MATERIAL

Additional data and information are available electronically at the pages of journal website: https://www.shd-pub.org.rs/index.php/JSCS/article/view/13976, or from the corresponding author on request.

Acknowledgement. This research was financially supported by the NATO SPS programme (project G5402) and the Ministry of Science, Technological Development and Innovation of the Republic of Serbia through project contracts No. 451-03-33/2026-03/200053, 451-03-34/2026-03/200135 and 451-03-33/2026-03/200287. The authors would like to thank Dr. Ljiljana Kostić-Kravljanac (Institute for Multidisciplinary Research, National Institute of the Republic of Serbia, Belgrade, Serbia) for assistance in acquiring the ICP-OES data.

(CC) 2026 Serbian Chemical Society.

ИЗВОД

ИСПИТИВАЊЕ УТИЦАЈА ГРАНУЛОМЕТРИЈСКОГ САСТАВА ЕЛЕКТРОФИЛТЕРСКОГ ПЕПЕЛА НА ИМОБИЛИЗАЦИЈУ ЦЕЗИЈУМА ГЕОПОЛИМЕРИМА

ГОРДАНА Г. СТАНОЈЕВИЋ[1], МИРОСЛАВ М. КОМЉЕНОВИЋ[1], ЈАНА Љ. ПЕТРОВИЋ[2] и РАДА Д. ПЕТРОВИЋ[3]

[1]Институт за мултидисциплинарна истраживања, Институт од националног значаја за Републику Србију, Универзитет у Београду, Кнеза Вишеслава 1, 11030 Београд, [2]Иновациони центар Технолошко-металуршког факултета, 11060 Београд и [3]Технолошко–металуршки факултет, Универзитет у Београду, Карнегијева 4, 11060, Београд

Утицај гранулометријског састава електрофилтерског пепела (FA) на имобилизацију цезијума геополимерима испитан је поређењем узорака синтетисаних у овом раду са резултатима датим у претходним истраживања. Сви узорци су припремани на 95 °C при уделу Cs од 2 и 5 теж. %. Испитан је утицај расподеле величине честица FA на физичко–механичка својства, структуру гела и излуживање Cs. Резултати показују да гранулометријски састав значајно утиче на кинетику геополимеризације и развој механичких својстава. Генерално, додавање Cs продужава време везивања G-FA, при чему су дужа времена везивања уочена код G-FA са крупнијим честицама FA. Такође, G-FA добијени коришћењем FA са крупнијим честицама су показали ниже чврстоће при притиску, што указује да финије честице FA подстичу брже растварање алуминосиликатних врста и брже формирање геополимерног гела. Излуживање Cs је дифузионо контролисано без обзира на величину честица FA и удео Cs, иако је средњи индекс излуживања (L_{sr}) био нешто нижи у узорцима са крупнијим честицама FA (L_{sr} за све узорке био је већи од 9). Генерално, гранулометријска својства FA утичу на реактивност геополимера и структуру гела, а самим тим и на механичка својства и ефикасност имобилизације Cs.

(Примљено 16. маја, ревидирано 27. маја, прихваћено 2. јуна 2026)

REFERENCES

1. J. Davidovits, *Geopolymer chemistry and applications*, 5th ed., Geopolymer Institute, Saint-Quentin, 2020, p. 311 (ISBN: 9782954453118)
2. P. Duxon, A. Fernández-Jiménez, J. L. Provis, G. C. Lukey, A. Palomo, J. S. J. van Deventer, *J. Mater. Sci.* **42** (2007) 2917 (https://doi.org/10.1007/s10853-006-0637-z)
3. J. L. Provis, J. S. J. van Deventer, *Geopolymers: Structure, Processing, Properties and Industrial Applications,* Woodhead Publishing, Cambridge, 2009, p. 89 (https://doi.org/10.1533/9781845696382)
4. J. L. Provis, J. S. J. van Deventer, *Alkali-Activated Materials: State-of-the-Art Report*, RILEM TC 224-AAM. Springer/RILEM, Dordrecht, 2014, p. 98 (https://doi.org/10.1007/978-94-007-7672-2)
5. C. Shi, A. Fernández-Jiménez, *J. Hazard. Mater*., *B* **137** (2006) 1656 (https://doi.org/10.1016/j.jhazmat.2006.05.008)
6. R. O. Abdel Rahman, R. Z. Rakhimov, N. R. Rakhimova, M. I. Ojvan, *Cementitious Materials for Nuclear Waste Immobilization*, John Wiley & Sons Ltd., Chichester, 2015, p. 8 (https://doi.org/10.1002/9781118511992)
7. Y. Zhu, Z. Zheng, Y. Deng, C. Shi, Z. Zhang, *Cem. Concr. Compos*. **126** (2022) 104377 (https://doi.org/10.1016/j.cemconcomp.2021.104377)
8. J. Liu, Y. Xu, J. Wang, W. Zhang, J. Ye, R. Wang, *J. Aust. Ceram. Soc*. **60** (2024) 1131 (https://doi.org/10.1007/s41779-024-01018-6)
9. S. Jain, O. Onuaguluchi, N. Banthia, T. Troczynski, *J. Am. Ceram. Soc*. **108** (2024) e20131 (https://doi.org/10.1111/jace.20131)

(CC) 2026 Serbian Chemical Society.

10. E. Mukiza, Q. T. Phung, S. C. Seetharam, T. N. Nguyen, C. Bruggeman, G. De Schutter, *J. Environ. Manage.* **370** (2024) 122746 (https://doi.org/10.1016/j.jenvman.2024.122746)
11. M. Houhou, N. Leklou, H. Ranaivomanana, J. D. Penot, S. de Barros, *Discov. Appl. Sci.* **7** (2025) 126 (https://doi.org/10.1007/s42452-025-06536-x)
12. M. Komljenović, G. Tanasijević, N. Džunuzović, J. L. Provis, *J. Hazard. Mater.* **388** (2020) 121765 (https://doi.org/10.1016/j.jhazmat.2019.121765)
13. S. Jain, N. Banthia, T. Troczznski, *Cem. Concr. Compos.* **133** (2022) 104679 (https://doi.org/10.1016/j.cemconcomp.2022.104679)
14. M. I. Ojovan, W. Lee, S. Kalmykov, in *An introduction to nuclear waste immobilization*, Elsevier, Oxford, 2019, p. 8 (https://doi.org/10.1016/C2017-0-03752-7)
15. A. Fernández-Jiménez, D. E. Macphee, E. E. Lachowski, A. Palomo, *J. Nucl. Mater.* **346** (2005) 185 (https://doi.org/10.1016/j.jnucmat.2005.06.006)
16. Q. Li, SZ. Sun, D. Tao, Y. Xu, P. Li, H. Cui, J. Zhai, *J. Hazard. Mater.* **262** (2013) 325 (https://doi.org/10.1016/j.jhazmat.2013.08.049)
17. J. G. Jang, S. M. Park, H. K. Lee, *J. Hazard. Mater.* **318** (2016) 339 (https://doi.org/10.1016/j.jhazmat.2016.07.003)
18. S. Jain, N. Banthia, T. Troczynski, *J. Clean. Prod.* **380** (2022) 134984 https://doi.org/10.1016/j.jclepro.2022.134984)
19. S. Jain, N. Banthia, T. Troczynski, *Cem. Concr. Compos.* **133** (2022) 104679 (https://doi.org/10.1016/j.cemconcomp.2022.104679)
20. M. Komljenovic, Z. Bascarevic, V. Bradic, *J. Hazard. Mater.* **181** (2010) 35 (https://doi.org/10.1016/j.jhazmat.2010.04.064)
21. V. Nikolić, M. Komljenović, Z. Baščarević, N. Marjanović, Z. Miladinović, R. Petrović, *Constr. Build. Mater.* **94** (2015) 361 (https://doi.org/10.1016/j.conbuildmat.2015.07.014)
22. G. G. Stanojević, M. M. Komljenović, N. M. Džunuzović, S. S. Lazarević, J. L. Provis, R. D. Petrović, *Constr. Build. Mater.* **500** (2025) 144217 (https://doi.org/10.1016/j.conbuildmat.2025.144217)
23. *ASTM C618-25a: Standard Specification for Coal Fly Ash and Raw or Calcined Natural Pozzolan for Use in Concrete*, 2025
24. *EN 196-1:2008: Methods of testing cement - part 1: determination of strength*, 2008
25. *EN 196-3:2010: Methods of testing cement Part 3: Determination of setting times and soundness*, 2010
26. *ANSI/ANS-16.1-2003 (R2017): Measurement of the leachability of solidified low-level radioactive wastes by a short-term test procedure*, 2003
27. *EN 197–1:2011: Cement - Part 1: Composition, specifications and conformity criteria for common cements*, 2011
28. R. Gao, Z. Zhou, J. Yang, J. Zhang, *Open Ceram.* **20** (2024) 100680 (https://doi.org/10.1016/j.oceram.2024.100680)
29. NRC, Wasteform Technical Position, Revision 1, 1991
30. P. Rozek, M. Król, W. Mozgawa, *Spectrochim. Acta, A* **198** (2018) 283 (https://doi.org/10.1016/j.saa.2018.03.034)
31. W. K. W. Lee, J. S. J. van Deventer, *Langmuir* **19** (2003) 8726 (https://doi.org/10.1021/la026127e)
32. G. Kovalchuk, A. Fernández-Jiménez, A. Palomo, *Fuel* **86** (2007) 315 (https://doi.org/10.1016/j.fuel.2006.07.010)
33. C. A. Rees, J. L. Provis, G. C. Lukey, J. S. J. van Deventer, *Langmuir* **23** (2007) 8170 (https://doi.org/10.1021/la700713g)

(CC) 2026 Serbian Chemical Society.

34. A. Hajimohammadi, J. L. Provis, J. S. J. van Deventer, *Chem. Mater.* **22** (2010) 5199 (https://doi.org/10.1021/cm101151n)
35. S. L. A. Valcke, P. Pipilikaki, H. R. Fischer, M. H. W. Verkuijlen, E. R. H. van Eck, *Mater. Struct.* **48** (2014) 557 (https://doi.org/10.1617/s11527-014-0432-2)
36. M. Criado, A. Fernández-Jiménez, A. Palomo, *Micropor. Mesopor. Mater.* **106** (2007) 180 (https://doi.org/10.1016/j.micromeso.2007.02.055)
37. M. Rowles, B. O'Connor, *J. Mater. Chem.* **13** (2003) 1161 (https://doi.org/10.1039/b212629j)
38. G.J. de Groot, H. A. van der Sloot, in ASTM *Selected Technical Papers STP1123, Stabilization and Solidification of Hazardous, Radioactive, and Mixed Wastes,* 2nd Vol., T.C. Gilliam, C.C. Wiles, Eds., ASTM, West Conshohocken, PA, 1992, p. 149 (https://doi.org/10.1520/stp19548s)
39. H.A. van der Sloot, J.J. Dijkstra, *Development of Horizontally Standardized Leaching Tests for Construction Materials: A Material Based or Release Based Approach?*, Energy Research Centre of the Netherlands, Petten, 2004 **(**https://doi.org/10.13140/RG.2.2.11986.76486).

(CC) 2026 Serbian Chemical Society.

Journal of the Serbian Chemical Society
JSCS-info@shd.org.rs • www.shd.org.rs/JSCS
J. Serb. Chem. Soc. 91 (10) S305–S308 (2026) *Supplementary material*

SUPPLEMENTARY MATERIAL TO

Influence of fly ash fineness on cesium immobilization in geopolymers

GORDANA G. STANOJEVIĆ[1]*, MIROSLAV M. KOMLJENOVIĆ[1], JANA LJ. PETROVIĆ[2] and RADA D. PETROVIĆ[3]

[1]*Institute for Multidisciplinary Research, National Institute of the Republic of Serbia, University of Belgrade, Kneza Višeslava 1, 11030 Belgrade, Serbia,* [2]*Innovation Center of the Faculty of Technology and Metallurgy, Ltd, 11060 Belgrade, Serbia and* [3]*Faculty of Technology and Metallurgy, University of Belgrade, Karnegijeva 4, 11060, Belgrade, Serbia*

J. Serb. Chem. Soc. 91 (10) (2026) 1043–1057

EXPERIMENTAL PROCEDURE

Synthesis of geopolymers pastes and mortars

The geopolymer pastes were prepared by mixing FA-3, alkaline activator, and water. For Cs containing geopolymers, CsCl was first dissolved in water and then mixed with FA-3 and the alkaline activator. The Cs content was 2.0 % and 5.0 % relative to the mass of FA-3. The water/binder ratio was 0.39. In this ratio, water refers to the total amount of water in the system, including water from the activator and any additional water added to achieve comparable paste consistency, while the binder represents the sum of the FA mass and the solid part of the activator. The flow of the pastes was measured on a flow table and found to be 195 ± 10 mm, according to the standard method described in,[1] to ensure comparable workability of all samples. The concentration of Na_2O for all samples was 10 % relative to the mass of FA-3.[2]

The pastes were mixed for about 3 min, then poured into plastic cylindrical molds (62.5 x 15 mm), after which air bubbles were removed on a vibrating table. The prepared pastes were cured, covered with plastic bags at 95 °C for 24 h, and then at room temperature (20 ± 2 °C) until the testing.[2]

The geopolymer mortar was prepared by mixing FA-3, alkaline activator, water, and standard sand, following the procedure of EN 196-1[3] as closely as possible. The FA-3: sand ratio was 1:3. In the case of geopolymers with added Cs, the mortars were prepared by dissolving CsCl in water, then mixing with FA-3, alkaline activator, and finally sand. The Cs content and the concentration of Na_2O were the same as in the corresponding pastes.

The water:binder ratio was 0.43 for the G-FA-3-0Cs, 0.44 for the G-FA-3-2Cs, and 0.42 for the G-FA-3-5Cs sample. The water/binder ratio was determined as for the pastes. The mortars were homogenized in an automatic mixer for approximately 3 min, then poured into molds containing three mortar prisms of standard dimensions (40 x 40 x 160 mm) on a vibrating table, and cured under the same conditions as the pastes.

* Corresponding author. E-mail: gordana@imsi.bg.ac.rs

Available online at https://www.shd.org.rs/JSCS/

(CC) 2026 Serbian Chemical Society.

Leaching process

Deionized water was used as the leaching medium, with an electrical conductivity of less than 5 μS/cm on 25 °C. The ratio of the volume of the leaching medium to the total geometric surface area of the samples was kept constant at 10 ± 0.2 cm.

All paste samples were completely immersed in deionized water. The leaching test was conducted for 5 days at 23 ± 2 °C, with the leaching medium being fully replaced after cumulative leaching times of 2, 7, 24, 48, 72, 96, and 120 h.

At the end of each interval, the solution was filtered through a 0.45 μm membrane filter under vacuum. The pH of the filtrate was measured with a pH meter (HANNA Instruments HI 991001). Before measuring the concentrations of leached Cs, Al, and Si, the pH of the filtrate was lowered to below 2 by adding concentrated HNO_3. The concentrations of leached Cs, Al, and Si were measured using an Inductively Coupled Plasma-Optical Emission (ICP-OES) instrument (Spectro-Genesis EOP II 991001).

According to the ANSI/ANS-16.1-2003 standard,[4] the individual leaching rates of Cs were calculated according to equation (S1):

$$LR = \frac{a_n/A_o}{(\Delta t)_n} \tag{S1}$$

where, a_n is the amount of cesium released from the sample during leaching interval n, g; A_0 is the total amount of cesium in the sample at the beginning of the first leaching interval, g, and

$$(\Delta t)_n = t_n - t_{n-1} \tag{S2}$$

is the duration of the nth leaching interval, h.

The diffusion coefficient (D) was calculated using the mass transport equation (Fick's second law):

$$D = \pi \left[\frac{a_n/A_o}{(\Delta t)_n}\right]^2 \left[\frac{V}{S}\right]^2 T \tag{S3}$$

where D is the diffusion coefficient, cm^2/s; a_n is the amount of Cs released from the sample during the leaching interval *n,* g; A_0 is the total amount of Cs in the sample at the beginning of the first leaching interval, g; $(\Delta t)_n$ is the duration of the n-th leaching interval, s; V is the sample volume, cm^3; T is the leaching time, s, represented by the geometric mean time of the nth leaching interval, calculated as follows

$$T = \left[1/2\left({t_n}^{1/2} + {t_{n-1}}^{1/2}\right)\right]^2 \tag{S4}$$

The mean leachability index (L_{mean}) of Cs from G-FA-2%Cs and G-FA-5%Cs was calculated according to the following equation [S5]:

$$L_{mean} = 1/n \sum_{n=1}^{n_{max}\Sigma} [log(\beta/D)]_{n_{max}} \tag{S5}$$

where, n_{max} is the number of D values used for the calculation (7), β is defined constant (1.0 cm^{2}s^{-1}), and D is the diffusion coefficient of Cs calculated from equation (S3), for each step n.

(CC) 2026 Serbian Chemical Society.

RESULTS AND DISCUSSION

XRD

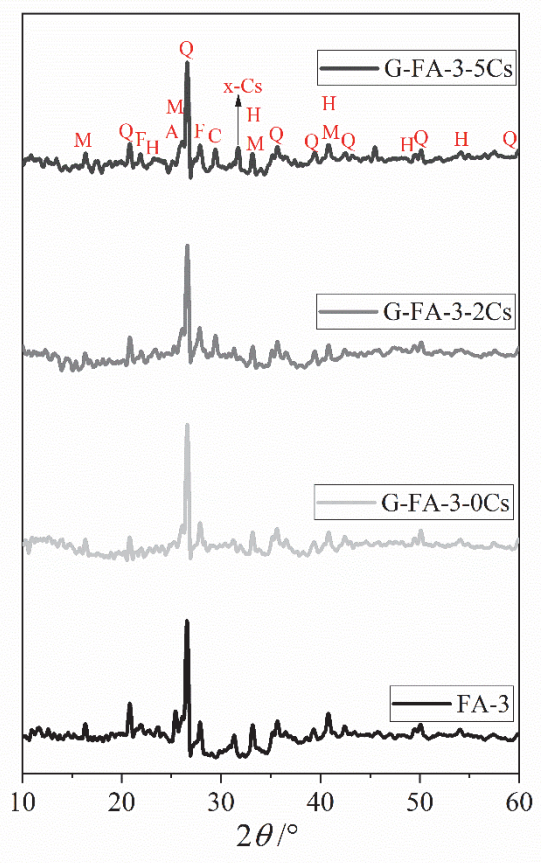

Fig. S-1. XRD patterns of FA-3 and G-FA-3 samples (Legend: M-mullite, Q-qurtz, H-hematite, A-anhydrite, F-feldspar, C-calcite, X-Cs-$Cs_2Al(OH)(SiO_4)_2$)

FESEM

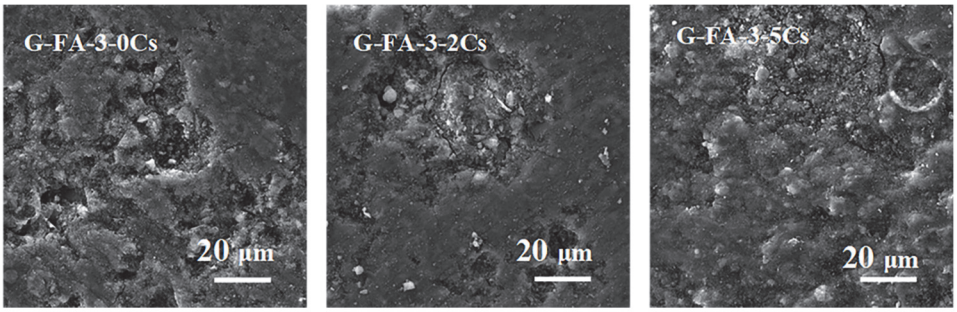

Fig. S-2. SEM images of G-FA-3

(CC) 2026 Serbian Chemical Society.

Leaching of Cs from G-FA-4

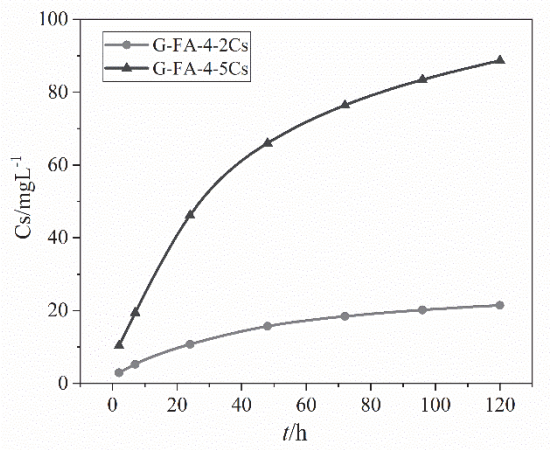

Fig.S-3. Cumulative concentration of leached Cs from G-FA-4

Leaching of Si and Al from G-FA-4

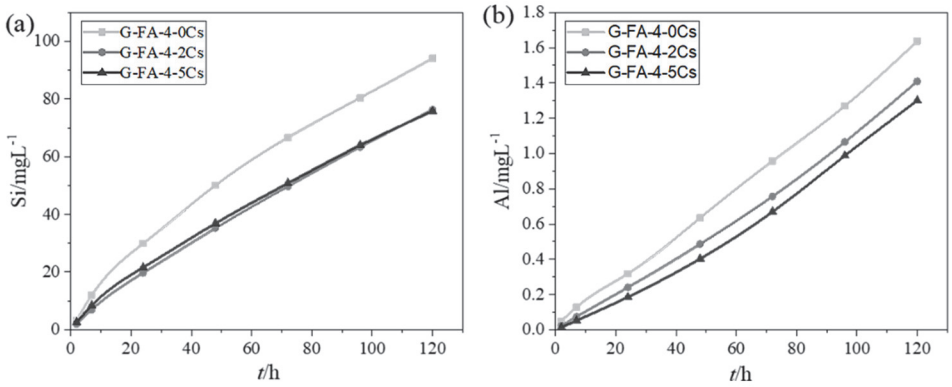

Fig.S-4. Cumulative concentration of leached (a) Si and (b) Al from G-FA-4

REFERENCE

1. *EN 1015-3:2008: Methods of test for mortar for masonry - Part 3: Determination of consistence of fresh mortar (by flow table)*, 2008
2. G. G. Stanojević, M. K. Komljenović, N. M. Džunuzović, S. S. Lazarević, J. L. Provis, R. D. Petrović, *Constr. Build. Mater*. **500** (2025) 144217 (https://doi.org/10.1016/j.conbuildmat.2025.144217)
3. *EN 196-1:2008: Methods of testing cement - part 1: determination of strength*, 2008
4. *ANSI/ANS-16.1-2003 (R2017): Measurement of the leachability of solidified low-level radioactive wastes by a short-term test procedure*, 2003.

(CC) 2026 Serbian Chemical Society.

Journal of the Serbian Chemical Society
JSCS-info@shd.org.rs • www.shd.org.rs/JSCS
J. Serb. Chem. Soc. *91* (10) 1059–1081 (2026)
JSCS–5544
Original scientific paper
Published 16 November, 2026

Chemical technology aspects of non-equilibrium microwave heating for phase separation in multiphase liquid systems

AYSEL V. GASIMZADE[1]*, VALI KH. NURULLAYEV[2] and RASHAD R. KHALILZADE[1]

[1]*Azerbaijan State Oil and Industry University, Baku, Azerbaijan and* [2]*State Oil Company of Azerbaijan Republic, Baku, Azerbaijan*

(Received 9 March, revised 7 May, accepted 11 June 2026)

Abstract: Microwave-assisted demulsification is a promising method for separating water-in-oil emulsions because it provides rapid and volumetric energy transfer. However, the mechanism of separation under non-equilibrium heating conditions remains insufficiently understood. In this study, the kinetic factors governing microwave-assisted phase separation were investigated at microwave powers of 200–800 W and water fractions of 0.12–0.45. Temperature evolution, heating rate (dT/dt), separated water volume, and specific energy consumption were analysed. The results showed a pronounced non-monotonic dependence of separation efficiency on microwave power. The highest separation efficiency was observed at intermediate powers of 400–600 W, while further power increases reduced performance despite continued temperature rise. The findings demonstrate that heating rate, rather than final temperature, is the main controlling parameter, providing a basis for more energy-efficient microwave demulsification.

Keywords: dielectric heating; heating-rate control; specific energy consumption; contour optimization; kinetic destabilization.

INTRODUCTION

Water–oil emulsions are an unavoidable consequence of crude oil production, particularly in mature reservoirs where the water cut increases and fluids remain in contact for extended periods. Under such conditions, natural surface-active components of crude oil promote the formation of dispersed systems that are kinetically stable and difficult to separate. These emulsions complicate transportation, reduce processing efficiency and increase energy consumption in surface facilities. Their behaviour is controlled not only by temperature, but also by interfacial properties, phase distribution and the time-dependent response of the system.[1–3] In industrial practice, separation is commonly achieved through thermal treatment and

* Corresponding author. E-mail: qasimzade92@inbox.ru
https://doi.org/10.2298/JSC260309032G

Available online at https://www.shd.org.rs/JSCS/
(CC) 2026 Serbian Chemical Society.

chemical demulsifiers.[4–6] While these methods are widely used, they often require elevated temperatures or substantial chemical dosages, which increase operational costs and raise environmental concerns. For this reason, there is growing interest in physical methods that can enhance separation efficiency without excessive energy input or chemical dependency.[7–11]

Microwave heating provides a distinct alternative to conventional conductive heating. Instead of transferring heat from the surface inward, microwave energy is deposited directly within the volume of the material and interacts preferentially with polar components.[12–15] In heterogeneous systems such as water-in-oil emulsions, where the dispersed and continuous phases possess different dielectric properties, this selective interaction can lead to localized heating and transient non-uniform conditions. As a result, the structural response of the emulsion cannot be described solely by its average temperature.[16–19] The efficiency of microwave-assisted separation depends on several coupled parameters, including applied power, heating rate, phase connectivity and interfacial relaxation dynamics. When energy input is balanced with structural relaxation, phase separation is enhanced, whereas excessive power or rapid heating may increase molecular mobility and reduce coalescence efficiency.[20,21] Although this study uses crude oils from the Absheron oilfields, the analysis is based on general physical parameters, making the approach applicable to a wide range of water-in-oil systems in petroleum processing.[22–26]

In this study, water-in-oil emulsions prepared from Absheron crude oils were subjected to controlled microwave irradiation at power levels between 200 and 800 W. Systems with different water volume fractions were examined. Temperature evolution, heating rate, separated water volume, and specific energy consumption were evaluated in order to identify operating conditions that promote efficient phase separation. By linking separation performance to both kinetic behaviour and energy input, the work aims to clarify the mechanisms governing microwave interaction with multiphase liquid systems. From a mechanical and industrial engineering standpoint, microwave-assisted demulsification can be regarded as an energy-driven separation process in which power delivery and dynamic response play a more decisive role than bulk temperature alone.

EXPERIMENTAL

The experimental methodology was designed to evaluate the influence of microwave power and emulsion structure on phase separation under controlled laboratory conditions. Water-in-oil emulsions prepared from Absheron crude oils with different water fractions were subjected to controlled microwave irradiation, and their heating behaviour, separation efficiency and energy consumption were analysed.[27-33]

Materials and sample preparation. Crude oil samples were obtained from producing wells Nos. 533, 623, 629, and 628 located in the Absheron oilfields (Azerbaijan), representing mature onshore reservoirs with moderate density and elevated resin–asphaltene content that promote

(CC) 2026 Serbian Chemical Society.

stable water-in-oil emulsions. The oils were stored in sealed glass containers at 20 °C and protected from light prior to use, while distilled water (pH ≈ 5.5) was used as the dispersed phase. Emulsions were prepared at controlled water volume fractions (ϕ from 0.12 to 0.45) by mixing oil and water with a mechanical impeller at 2000 rpm for 8–10 min at 20 °C, followed by a short stabilization period. The emulsion type was verified using the standard drop-dispersion test, confirming that all systems were water-in-oil (W/O). The internal structure of the emulsions varied with water fraction, evolving from isolated droplets at low ϕ to partially connected networks at intermediate fractions and highly connected structures at high water content. For microwave experiments, 70±0.5 g of emulsion was transferred into a 100 mL borosilicate glass beaker used as the standard sample container.[27-30]

Microwave treatment procedure. Microwave irradiation was performed using a laboratory-scale microwave reactor (Milestone ETHOS microwave reactor, Italy) operating at a fixed frequency of 2.45 GHz. The output power was adjustable and set to four discrete levels: 200, 400, 600 and 800 W. Experiments were conducted in an open reaction vessel under atmospheric pressure conditions. The emulsion sample (70±0.5 g) placed in a 100 mL borosilicate glass beaker was positioned at the geometric centre of the microwave cavity using a non-metallic holder to ensure reproducible electromagnetic exposure. Each sample was irradiated for a predetermined time interval controlled with an accuracy of ±0.5 s. Temperature–time profiles were monitored during microwave irradiation. The temperature of the emulsion was monitored using a calibrated K-type thermocouple (accuracy ±0.1 °C). Immediately after irradiation (within 2––3 s), the bulk temperature of the emulsion was measured. The probe was inserted along the central axis of the sample to a depth of approximately 15 mm below the surface to minimize surface-related temperature deviations. All experiments were carried out under identical geometric and environmental conditions to ensure reliable comparison of heating behaviour and phase separation efficiency across different microwave power levels.[31-33]

Dielectric characterization methodology. To further evaluate the electromagnetic response of the emulsions during microwave-assisted heating, additional dielectric characterization was performed for W/O systems with different water fractions (ϕ from 0.12 to 0.45). The dielectric constant (ε'), dielectric loss factor (ε''), dissipation factor (tan δ), and effective microwave wavelength (λ_{eff}) were determined under microwave treatment conditions corresponding to the main demulsification experiments. The analysis was carried out at microwave powers of 200, 400, 600 and 800 W using the bulk temperatures measured after 60 s of irradiation (T_{60}). The dielectric behaviour of the aqueous phase, oil phase and emulsion mixture was evaluated using temperature-dependent dielectric correlations commonly applied for heterogeneous liquid systems under microwave exposure. The obtained dielectric parameters were used to assess the influence of microwave power and water fraction on microwave energy absorption and dissipation behaviour in the emulsion system.[34-36]

Viscosity measurement methodology. To investigate the contribution of thermal-viscosity effects to microwave-assisted phase separation, viscosity measurements were additionally performed before and after microwave treatment. W/O emulsions with different water fractions (ϕ from 0.12 to 0.45) were subjected to microwave irradiation at powers of 200–800 W under the same experimental conditions used in the demulsification tests. Following microwave exposure, the apparent dynamic viscosity of the emulsions was measured after thermal stabilization under controlled laboratory conditions. Viscosity reduction (%) was calculated relative to the initial viscosity of the untreated emulsion samples. The separated water volume obtained after microwave treatment was additionally recorded in order to evaluate the relationship between viscosity reduction and demulsification efficiency.[37-39]

(CC) 2026 Serbian Chemical Society.

Interfacial tension methodology. To evaluate the influence of microwave irradiation on interfacial destabilization, the interfacial tension (IFT) of the W/O emulsions was measured before and after microwave treatment. Emulsions with different water fractions (ϕ from 0.12 to 0.45) were treated at microwave powers of 200, 400, 600 and 800 W using the same irradiation conditions applied in the phase-separation experiments. Interfacial tension measurements were carried out under controlled temperature conditions using standard tensiometric procedures. The obtained IFT values were used to assess the effect of microwave power on interfacial properties and their possible relationship with phase separation behaviour.[40-42]

Energy consumption analysis. To evaluate the energetic performance of the microwave-assisted separation process, the specific energy consumption per unit volume of separated water (E/A in kWh/m^3) was calculated.

The parameter E/A represents the electrical energy supplied to the system that is required to separate a unit volume of water from the emulsion and is commonly used for comparative assessment of thermal and electromagnetic separation processes.[43] The specific energy consumption was determined as:

$$E/A = Pt / A \quad (1)$$

where P is the microwave power in kW, t is the irradiation time in h, and A is the separated water volume in m^3.

Nominal microwave power levels (200–800 W) were converted to kW for calculations. The irradiation time was measured experimentally for each test. The separated water volume was determined gravimetrically and converted to volumetric units under standard conditions. All energy calculations were performed under identical operating conditions to ensure consistency and reliable comparison between different power regimes.

RESULT AND DISCUSSION

Microwave interaction with heterogeneous liquid systems arises from a coupled interplay between electromagnetic energy absorption, interfacial polarization phenomena and phase-dependent thermal responses. In dispersed media composed of immiscible liquid phases, such as emulsions, microwave energy input induces spatially non-uniform heating and localized structural rearrangements that cannot be adequately captured by bulk temperature evolution alone. For this reason, elucidating the interdependence between applied microwave power, the resulting temperature increase and phase separation behaviour is critical for identifying the physical mechanisms that govern structural destabilization and phase evolution.

A substantial body of microwave demulsification studies illustrates enhanced phase separation with increasing supplied energy, achieved either through elevated power levels or prolonged irradiation durations, a behaviour commonly attributed to viscosity reduction and accelerated droplet coalescence.

In the present study, by contrast, the structural response exhibits a pronounced non-monotonic character. Maximum separation is attained within an intermediate power range, beyond which further increases in power lead to a decline in separation efficiency despite continued temperature rise. Such behaviour demonstrates that demulsification cannot be interpreted as a purely thermal process; rather, it reflects

(CC) 2026 Serbian Chemical Society.

a dynamic balance between microwave energy deposition and the rate of interfacial structural relaxation, as illustrated in Fig. 1.

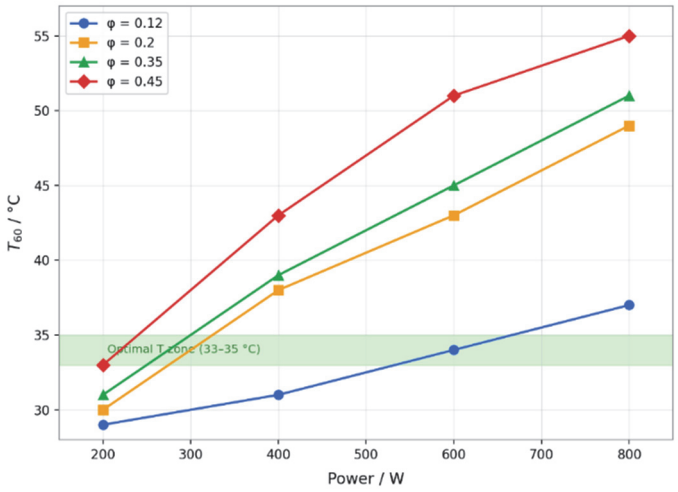

Fig. 1. Temperature at 60 s (T_{60}) *versus* microwave power for emulsions with ϕ from 0.12 to 0.45. Shaded region indicates the optimal temperature range.

Fig. 1 shows the dependence of bulk temperature measured after 60 s of microwave exposure on the applied power level for emulsions with varying water volume fractions. For all investigated systems, the bulk temperature increased progressively with increasing microwave power. However, the magnitude of the temperature rise appears to depend strongly on the water fraction of the emulsion.

At the lowest water content (ϕ = 0.12), the temperature increase remained relatively moderate across the investigated power range. Even at 800 W, the bulk temperature reached only approximately 37 °C, which may be associated with limited microwave absorption due to the relatively low volume of the polar aqueous phase. Under intermediate power conditions, the emulsion remained within or near the experimentally observed temperature interval associated with favourable phase separation behaviour.

As the water fraction increased (ϕ = 0.20 or 0.35), the temperature response became more pronounced. The larger dispersed aqueous phase likely enhanced dielectric losses and volumetric microwave energy absorption, resulting in higher apparent heating rates. At microwave powers of 600–800 W, the measured bulk temperature exceeded 45 °C, indicating intensified energy dissipation within the emulsion system.

For the highest water fraction (ϕ = 0.45), the most significant temperature increase was observed, reaching approximately 55 °C at 800 W. This behaviour may be related to enhanced electromagnetic interaction associated with increased

(CC) 2026 Serbian Chemical Society.

water-phase connectivity and interfacial density. At the same time, the results suggest that operation at excessively high microwave powers may shift the system beyond the experimentally favourable temperature region for stable phase separation.

The shaded region in Fig. 1 highlights the temperature interval (33–35 °C) associated with relatively favourable demulsification behaviour under the investigated conditions. At moderate microwave powers (200–400 W), several emulsions passed through this interval, which may indicate a balance between interfacial destabilization and controlled molecular mobility. In contrast, at higher power levels, the systems rapidly exceeded this temperature range, where excessive heating may contribute to increased phase mobility and less efficient droplet coalescence.

From a heat-transfer perspective, the results indicate that microwave heating behaviour in heterogeneous emulsions depends strongly on dielectric composition and water fraction. Nevertheless, since the present analysis is based on bulk temperature measurements obtained after microwave irradiation, possible local thermal gradients and transient hot-spot formation could not be directly resolved. Therefore, the proposed interpretation of non-equilibrium heating effects should be considered an indirect phenomenological interpretation derived from macroscopic experimental observations rather than direct local thermal characterization.

Although temperature remains a key parameter influencing phase stability, through its effects on interfacial tension, molecular mobility and phase connectivity, its role under microwave irradiation cannot be considered in isolation. Rather, thermal effects are inherently coupled with kinetic and electromagnetic contributions, giving rise to strongly nonlinear responses. Identifying temperature ranges associated with effective structural transformation is therefore essential for elucidating the mechanisms governing microwave-induced phase separation, as further illustrated in Fig. 2.

Fig. 2 shows the relationship between separated water volume and bulk temperature after 60 s of microwave exposure for emulsions with different water fractions. The obtained results indicate that phase separation efficiency does not increase monotonically with temperature but instead exhibits a composition-dependent optimum behaviour.

At low water content ($\phi = 0.12$), phase separation remained relatively limited throughout the investigated temperature range, which may be associated with weaker dielectric interaction and lower microwave energy absorption due to the reduced amount of dispersed aqueous phase. For intermediate water fractions (ϕ from 0.20 to 0.35), the separated water volume increased progressively within a moderate temperature interval, with the highest separation efficiency for $\phi = 0.35$ observed at approximately 45 °C before declining at higher temperatures.

At the highest investigated water fraction ($\phi = 0.45$), phase separation initially increased rapidly with temperature but subsequently decreased beyond a certain

(CC) 2026 Serbian Chemical Society.

temperature range. This behaviour may indicate that excessively rapid heating and increased phase mobility partially suppress stable droplet coalescence under high-energy microwave conditions.

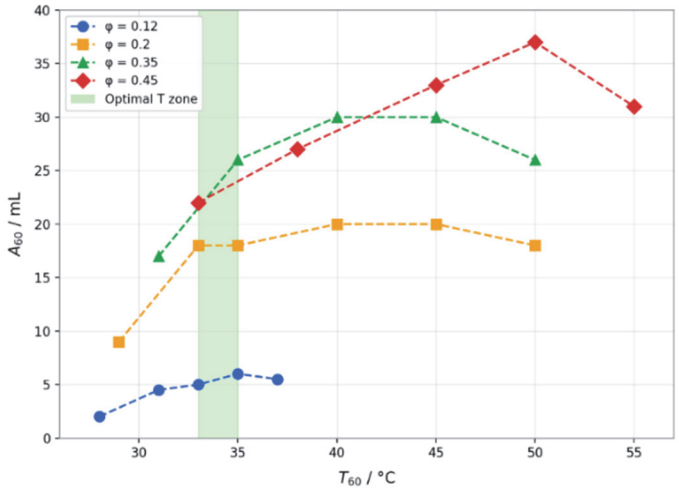

Fig. 2. Separated water volume (A) *versus* bulk temperature (T_{60}) for emulsions with ϕ from 0.12 to 0.45. Shaded region indicates the optimal range.

The obtained results suggest that microwave-assisted demulsification may operate within a limited temperature and heating regime rather than following a purely temperature-controlled separation trend. At the same time, since the analysis was based primarily on bulk temperature measurements obtained after microwave irradiation, the possible influence of local thermal gradients, transient overheating, and non-uniform energy distribution could not be directly resolved. Therefore, the proposed interpretation should be considered an indirect phenomenological explanation of the experimentally observed separation behaviour.

To further clarify the role of dynamic heating effects, the separation performance was analysed as a function of heating rate rather than bulk temperature alone. The heating rate ($\mathrm{d}T/\mathrm{d}t$) was determined from the temperature rise during the initial 60 s of microwave exposure. The relationship between separated water volume and heating rate for different water fractions is illustrated in Fig. 3.

Fig. 3 illustrates the relationship between separated water volume and apparent heating rate ($\mathrm{d}T/\mathrm{d}t$) for emulsions with different water fractions. The obtained results suggest that phase separation efficiency may be more strongly influenced by heating dynamics than by bulk temperature alone. For all investigated systems, an initial increase in heating rate was generally associated with improved phase

(CC) 2026 Serbian Chemical Society.

separation behaviour. However, beyond a certain range, further increases in heating rate did not result in proportional enhancement of separated water volume and, in several cases, led to reduced separation efficiency.

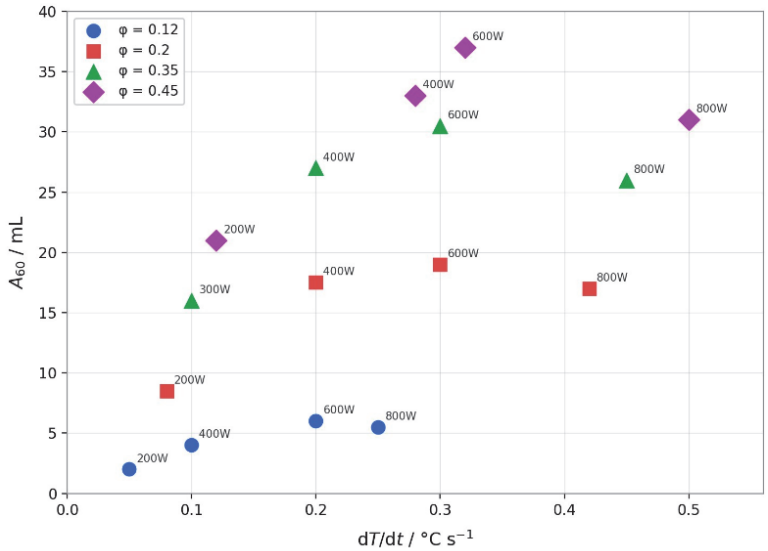

Fig. 3. Separated water after 60 s (A_{60}) *versus* heating rate (dT/dt) for emulsions with ϕ from 0.12 to 0.45. Power levels: 200–800 W.

At low water content (ϕ = 0.12), the apparent heating rate remained relatively small across the investigated microwave power range, and only moderate improvement in separation efficiency was observed. This behaviour may be associated with limited dielectric losses and reduced interfacial area, which likely restrict the conversion of absorbed microwave energy into efficient droplet coalescence.

For intermediate water fractions (ϕ = 0.20 or 0.35), a more pronounced optimum heating-rate region was observed. The separated water volume increased progressively as dT/dt increased from low to moderate values, reaching maximum separation efficiency at intermediate microwave powers (400–600 W). At the highest investigated heating rates corresponding to 800 W, a reduction in separated water volume became apparent despite continued energy input. This behaviour may indicate that moderate microwave heating promotes interfacial destabilization and droplet interaction, whereas excessively rapid heating could increase molecular mobility and partially suppress stable phase disengagement.

The emulsion with the highest water fraction (ϕ = 0.45) exhibited the strongest apparent sensitivity to heating rate. Maximum separation efficiency was observed at approximately 0.4–0.45 °C/s (600 W), followed by a decline at higher heating rates. Although this behaviour may suggest the existence of an optimal dynamic

(CC) 2026 Serbian Chemical Society.

heating regime for microwave-assisted demulsification, the present results should be interpreted cautiously because the heating-rate analysis was derived from bulk temperature measurements rather than direct local thermal characterization.

From an engineering perspective, the obtained data indicate that the rate of microwave energy delivery may play an important role in determining phase separation behaviour. The results further suggest that separation efficiency depends not only on the total energy supplied to the system but also on the dynamic conditions under which energy is deposited into the heterogeneous emulsion structure. At the same time, possible local overheating effects, transient thermal gradients and interfacial relaxation processes were not directly measured in the present study. Therefore, the proposed interpretation of non-equilibrium heating effects should be considered an indirect phenomenological interpretation derived from macroscopic experimental observations.

Microwave-assisted demulsification has frequently been interpreted as a predominantly thermally driven process. Numerous studies report that increasing microwave power or irradiation time enhances separation efficiency due to selective heating of the aqueous phase, reduction in viscosity and accelerated droplet coalescence. For example, Binner *et al.*[44] demonstrated that selective dielectric heating of dispersed saline droplets generates localized thermal gradients that promote phase disengagement. In such interpretations, separation efficiency typically increases monotonically with supplied energy.

However, the present results contradict this simplified thermal paradigm. A distinct non-monotonic separation behaviour was observed: separation efficiency reached a maximum within an intermediate power window (approximately 400––600 W), while further power increase (800 W) resulted in reduced performance despite continued temperature rise. This behaviour indicates that microwave demulsification cannot be explained solely by bulk heating effects.[45]

Studies such as Fang *et al.*[37] suggest that microwave irradiation may alter interfacial electrostatic properties by modifying droplet surface charge and zeta potential. While these findings highlight the importance of interfacial destabilization mechanisms, they do not explicitly account for kinetic limitations associated with rapid energy deposition.

The present work extends beyond both purely thermal explanations (*e.g.*, Binner) and electrostatic interpretations (*e.g.*, Fang) by identifying heating rate ($\mathrm{d}T/\mathrm{d}t$) as a governing engineering parameter. The observed divergence between peak and final heating rates further demonstrates that microwave-assisted demulsification operates within a finite kinetic window controlled by the balance between electromagnetic energy input and structural relaxation time.[45–49]

Moreover, unlike earlier studies that primarily evaluate separation yield, this investigation introduces a multi-criteria optimization framework incorporating separation efficiency, productivity and specific energy consumption. The resulting

(CC) 2026 Serbian Chemical Society.

contour-based efficiency mapping demonstrates that maximum power application does not correspond to maximum process efficiency. Instead, optimal performance occurs within a localized composition–power interaction region.[47–49]

These findings suggest that microwave demulsification should be interpreted as a non-equilibrium energy-controlled separation mechanism rather than a purely temperature-dominated process, offering a more rigorous engineering basis for industrial scale-up.

In order to distinguish the influence of microwave power intensity on separation dynamics, the temperature–separation relationship was examined separately for 400 and 600 W operating conditions. These two regimes represent intermediate and elevated energy input levels, respectively, and allow evaluation of the structural response under different heating intensities. The corresponding results are presented in Fig. 4.

Fig. 4 compares phase separation behaviour at two microwave power levels, 400 and 600 W, illustrating the influence of microwave energy intensity on the temperature–separation relationship. At 400 W, separation efficiency exhibited a moderate and composition-dependent response, with relatively pronounced maxima observed for intermediate water fractions (ϕ from 0.20 to 0.35) within a limited temperature interval.

At 600 W, the faster apparent heating conditions generally produced larger separated water volumes; however, the temperature interval associated with favourable separation behaviour became noticeably narrower, particularly for emulsions with ϕ = 0.35 or 0.45. In several cases, phase separation increased up to an intermediate temperature range and subsequently decreased despite continued temperature rise.

These observations suggest that increasing microwave power does not simply enhance demulsification efficiency in a linear manner but may additionally modify the dynamic balance between microwave energy deposition, interfacial destabilization, and the transient structural response of the emulsion system. Under higher-power conditions, excessively rapid heating may contribute to increased molecular mobility and less stable phase disengagement despite higher bulk temperatures.

At the same time, the present interpretation should be considered cautiously because the analysis was based primarily on bulk temperature measurements obtained after microwave irradiation. Direct characterization of local thermal gradients, transient hot spots and structural relaxation phenomena was not performed. Therefore, the proposed interpretation represents an indirect phenomenological explanation of the experimentally observed separation behaviour rather than direct mechanistic confirmation.

To further evaluate the dynamic characteristics of microwave heating under high-power conditions, the peak heating rate and the final heating rate were compared as a function of water fraction at 600 W. This comparison allows assessment

(CC) 2026 Serbian Chemical Society.

of transient versus stabilized heating behaviour and provides insight into structural relaxation effects during microwave exposure. The results are illustrated in Fig. 5.

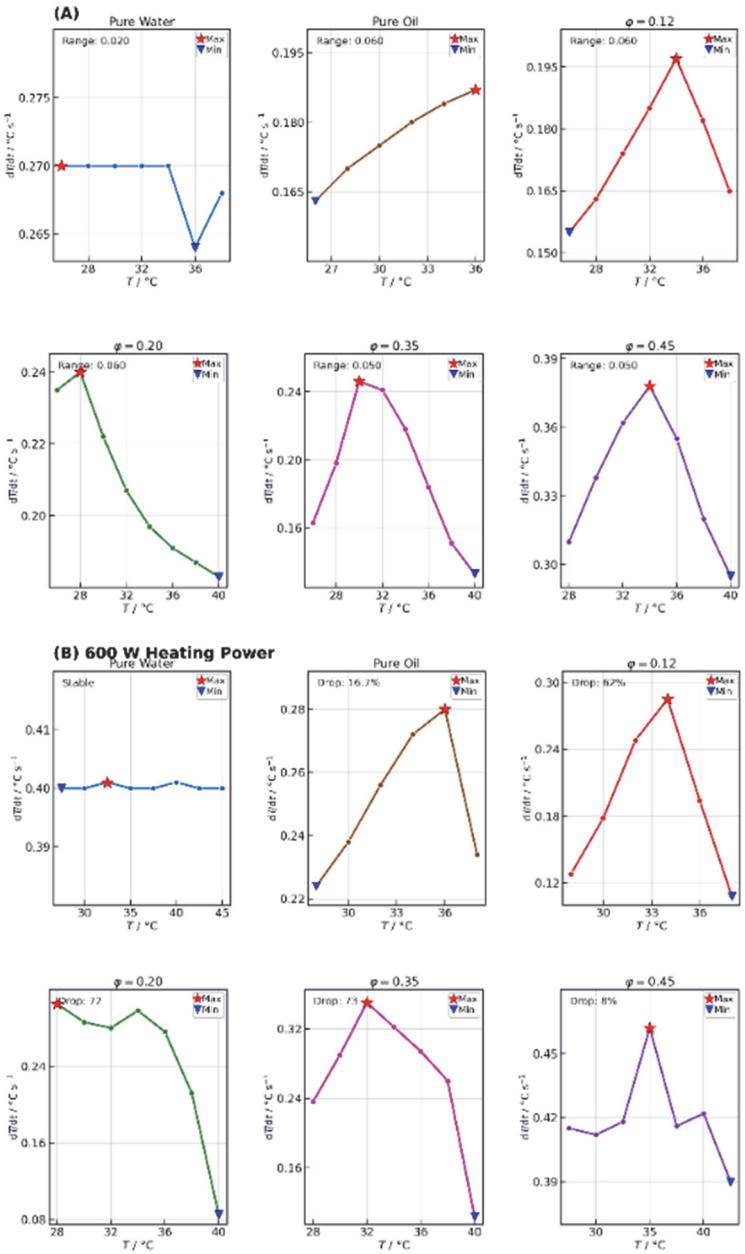

Fig. 4. Separated water volume (A_{60}) as a function of temperature at 400 (A) and 600 W (B) for emulsions with different water fractions (ϕ from 0.12 to 0.45).

(CC) 2026 Serbian Chemical Society.

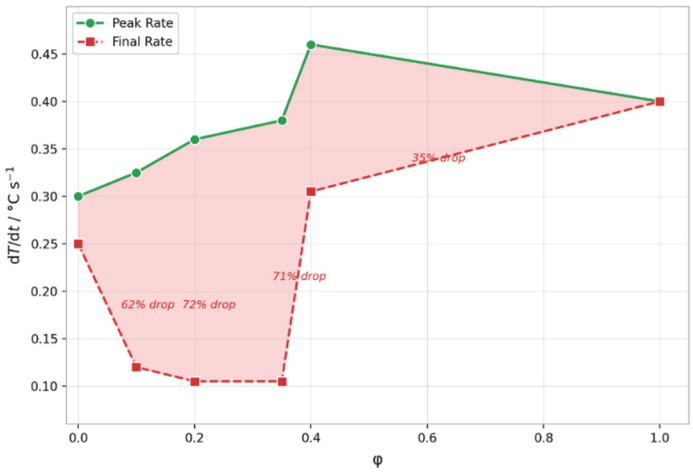

Fig. 5. Peak and final heating rates as a function of water fraction (ϕ) at 600 W.

Fig. 5 illustrates the variation of apparent peak and final heating rates with water fraction at a constant microwave power of 600 W. The obtained results show that the peak heating rate generally increased with increasing water fraction up to approximately $\phi \approx 0.45$, which may be associated with enhanced dielectric losses and stronger microwave energy absorption within the aqueous phase of the emulsion.

In contrast, the final heating rate exhibited a less uniform behaviour, with a noticeable decrease relative to the peak heating rate at intermediate water fractions (ϕ in the range 0.12–0.35). This behaviour may indicate the presence of transient heating effects during microwave irradiation, where the initial energy absorption rate exceeds the subsequently stabilized thermal response of the system.

At higher water fractions ($\phi \geq 0.45$), the difference between peak and final heating rates became smaller, suggesting a comparatively more stable apparent energy absorption behaviour under the investigated conditions. These observations indicate that transient heating dynamics may play an important role in microwave-assisted phase separation processes.

At the same time, the present interpretation should be considered cautiously because the heating-rate analysis was derived from bulk temperature measurements obtained after microwave irradiation rather than from direct local thermal monitoring. Consequently, possible local overheating effects, transient thermal gradients, and interfacial relaxation phenomena could not be directly resolved. Therefore, the proposed interpretation of transient structural response represents an indirect phenomenological explanation of the experimentally observed behaviour rather than direct mechanistic verification.

To quantify the relative impact of microwave power on separation performance and energy efficiency, the percentage changes in separated water volume and

(CC) 2026 Serbian Chemical Society.

specific energy consumption (E/A) were evaluated with respect to the baseline condition (200 W). This comparative analysis enables assessment of performance gains and associated energy penalties across different water fractions. The results are summarized in Fig. 6.

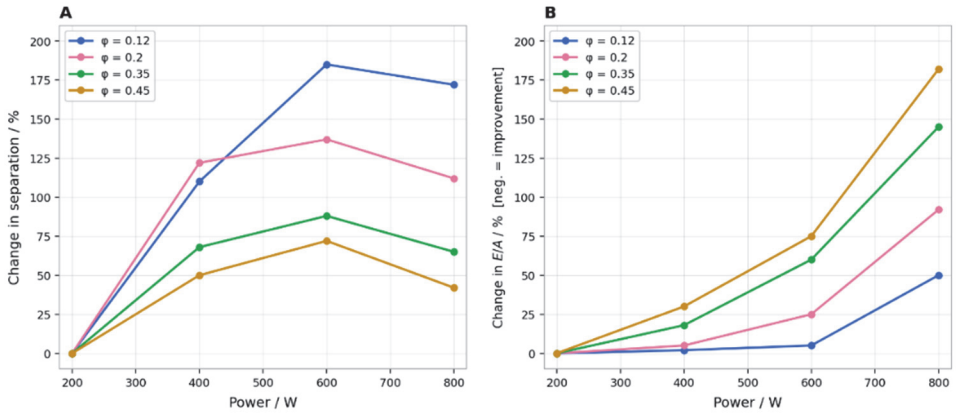

Fig. 6. Relative variation of separated water (A) and specific energy consumption (E/A, B) with microwave power for ϕ from 0.12 to 0.45 (reference: 200 W).

Fig. 6 compares the influence of microwave power on phase separation efficiency and specific energy consumption for emulsions with different water fractions. The obtained results show that increasing microwave power from 200 to 400 and 600 W generally improved phase separation efficiency for all investigated systems. The strongest relative improvement was observed at low water content (ϕ = 0.12), where the separated water volume increased substantially at intermediate microwave powers.

For intermediate water fractions (ϕ 0.20–0.35), separation efficiency also increased with microwave power; however, the improvement became less pronounced beyond approximately 600 W. At the highest investigated water fraction (ϕ = 0.45), the increase in separation efficiency remained comparatively moderate despite continued power increase.

In contrast, the specific energy consumption increased significantly with increasing microwave power, particularly for emulsions with higher water fractions (ϕ 0.35–0.45). These results indicate that additional microwave energy input does not necessarily translate proportionally into improved phase separation performance under all operating conditions.

At the highest investigated microwave power (800 W), the increase in energy consumption became substantially more pronounced, whereas the corresponding separation improvement remained limited. This behaviour suggests that excessively high microwave power may reduce the overall energetic efficiency of the

(CC) 2026 Serbian Chemical Society.

demulsification process despite continued temperature increase and intensified energy deposition.

From an engineering perspective, the obtained results suggest that favourable microwave-assisted demulsification performance may occur within an intermediate microwave power range of approximately 400–600 W under the investigated conditions. At the same time, since the present analysis was based on macroscopic measurements of bulk temperature, separated water volume, and energy consumption, possible local overheating effects and transient non-uniform energy redistribution could not be directly characterized. Therefore, the proposed interpretation should be considered an indirect phenomenological assessment of the experimentally observed process behaviour rather than direct mechanistic verification.

To further clarify the role of electromagnetic interactions during microwave-assisted demulsification, additional dielectric characterization of the W/O emulsions was performed. Since microwave heating in heterogeneous systems is governed by selective interaction between the electromagnetic field and polar components, evaluation of dielectric parameters is essential for understanding the relationship between microwave power, energy absorption, and phase separation behaviour. For this reason, dielectric constant (ε'), dielectric loss factor (ε''), dissipation factor ($\tan \delta$), and effective microwave wavelength (λ_{eff}) were analysed for emulsions with different water fractions under microwave irradiation conditions. The measurements were carried out for microwave powers of 200–800 W using the temperature conditions corresponding to the experimental separation tests. The obtained dielectric parameters are summarized in Table I.

The dielectric analysis demonstrates that the electromagnetic response of the emulsion strongly depends on both water fraction and microwave power. The dielectric constant of the aqueous phase remained substantially higher than that of the oil phase throughout the investigated temperature range, confirming that microwave energy absorption occurs predominantly within the dispersed water domains. Simultaneously, the gradual increase in dielectric loss factor (ε'') and dissipation factor ($\tan \delta$) with increasing microwave power indicates intensified microwave energy conversion into heat within the heterogeneous emulsion structure.

The results further show that the dielectric properties of the emulsion evolve dynamically during heating. Although increased microwave power enhanced dielectric losses and energy dissipation, the highest phase separation efficiency was not observed at the maximum power level (800 W). This behaviour suggests that enhanced electromagnetic energy deposition alone cannot fully explain the observed demulsification behaviour. Instead, excessive power input may promote transient overheating and increased molecular mobility, which can partially suppress stable droplet coalescence.

(CC) 2026 Serbian Chemical Society.

TABLE I. Dielectric parameters of W/O emulsions at different water fractions and microwave powers; ϕ – water volume fraction in the emulsion; T_{60} – bulk temperature measured after 60 s of microwave irradiation; ε' – dielectric constant; ε'' – dielectric loss factor; tan δ – dielectric dissipation factor; λ_{eff} – effective microwave wavelength in the emulsion medium

Water fraction, ϕ	Power W	T_{60} °C	ε' water	ε'' water	ε' oil	ε'' oil	ε' mixture	ε'' mixture	tan δ mixture	λ_{eff} cm
0.12	200	29.8	75.2	9.70	2.218	0.0068	3.42	0.025	0.0073	6.61
	400	33.6	73.9	8.60	2.216	0.0082	3.48	0.029	0.0083	6.55
	600	35.4	73.3	8.15	2.214	0.0090	3.51	0.032	0.0091	6.52
	800	37.0	72.8	7.80	2.213	0.0094	3.54	0.034	0.0096	6.49
0.20	200	31.6	74.6	9.15	2.217	0.0075	4.12	0.033	0.0080	6.04
	400	37.8	72.5	7.60	2.212	0.0088	4.25	0.040	0.0094	5.95
	600	43.5	70.6	6.60	2.208	0.0103	4.36	0.047	0.0108	5.87
	800	48.9	68.8	5.85	2.205	0.0106	4.45	0.052	0.0117	5.81
0.35	200	34.2	73.7	8.45	2.215	0.0085	5.24	0.041	0.0078	5.33
	400	42.8	70.8	6.69	2.209	0.0099	5.25	0.050	0.0095	5.32
	600	47.3	69.3	6.04	2.206	0.0104	5.22	0.051	0.0098	5.34
	800	54.0	67.1	5.27	2.201	0.0114	5.17	0.053	0.0103	5.36
0.45	200	36.2	73.0	7.95	2.214	0.0093	6.05	0.052	0.0086	4.96
	400	44.1	70.4	6.49	2.208	0.0106	6.12	0.060	0.0098	4.93
	600	50.4	68.3	5.66	2.203	0.0104	6.18	0.066	0.0107	4.91
	800	61.3	64.6	4.62	2.195	0.0130	6.26	0.074	0.0118	4.88

At the same time, the present dielectric characterization represents averaged bulk behaviour of the emulsion system. Spatially resolved dielectric mapping and local electromagnetic field distribution were not directly measured. Therefore, the proposed interpretation of non-equilibrium microwave effects should be considered a phenomenological rather than a direct mechanistic confirmation.

To evaluate whether the observed demulsification behaviour can be explained solely by thermal viscosity effects, additional viscosity measurements were performed before and after microwave treatment. Since viscosity strongly influences droplet mobility, collision frequency, and coalescence probability in W/O emulsions, investigation of viscosity evolution under microwave irradiation provides important insight into the contribution of thermal effects to phase separation. The experiments were carried out for emulsions with different water fractions at microwave powers of 200–800 W under the same irradiation conditions used in the separation experiments. The obtained viscosity values and corresponding separated water volumes are presented in Table II.

Microwave treatment resulted in a substantial reduction in emulsion viscosity for all investigated water fractions and power levels. The viscosity decrease became progressively more pronounced with increasing microwave power, reflecting enhanced thermal activation and reduced resistance to flow.

(CC) 2026 Serbian Chemical Society.

However, despite the continuous reduction in viscosity, the separated water volume did not increase monotonically at the highest microwave power level (800 W). In several systems, phase separation efficiency decreased even though viscosity reduction remained significant. This observation indicates that viscosity reduction alone cannot fully explain the demulsification behaviour under microwave irradiation.

TABLE II. Influence of microwave power on viscosity reduction and phase separation efficiency of W/O emulsions; ϕ – water volume fraction in the emulsion; MW – microwave treatment; separated water – volume of water separated after microwave treatment

Water fraction, ϕ	Microwave power, W	Viscosity before MW, mPa·s	Viscosity after MW, mPa·s	Viscosity reduction, %	Separated water, mL
0.12	200	42.5	37.8	11.1	8.4
	400		32.4	23.8	13.9
	600		28.7	32.5	16.2
	800		24.1	43.3	15.4
0.20	200	58.7	49.5	15.7	15.8
	400		39.8	32.2	24.6
	600		33.2	43.4	29.1
	800		27.6	53.0	27.5
0.35	200	84.3	67.4	20.0	24.8
	400		50.1	40.6	33.9
	600		41.5	50.8	34.8
	800		32.6	61.3	31.2
0.45	200	116.8	89.5	23.4	30.5
	400		65.7	43.8	41.2
	600		52.4	55.1	46.7
	800		39.3	66.4	42.5

The obtained results therefore support the assumption that microwave-assisted phase separation is influenced not only by thermal viscosity effects but also by dynamic non-equilibrium phenomena associated with rapid energy deposition and transient interfacial restructuring. Excessively rapid heating may exceed the characteristic relaxation time of the emulsion structure, thereby limiting stable droplet coalescence despite lower viscosity values.

In order to further investigate the role of interfacial phenomena during microwave-assisted demulsification, the interfacial tension (IFT) of W/O emulsions was additionally analysed before and after microwave treatment. Since destabilization of the water–oil interface is one of the key factors controlling droplet coalescence and phase disengagement, evaluation of IFT variation under microwave exposure provides additional information regarding the contribution of interfacial effects to

(CC) 2026 Serbian Chemical Society.

the separation process. The measurements were performed for emulsions with different water fractions treated at microwave powers of 200–800 W. The obtained results are illustrated in Fig. 7.

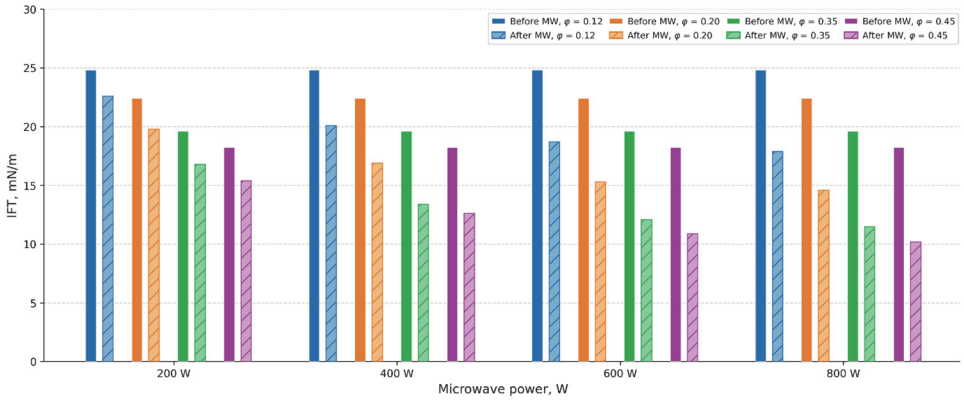

Fig. 7. Interfacial tension (IFT) of W/O emulsions with different water fractions before and after microwave treatment at different power levels.

The interfacial tension measurements additionally confirm that microwave irradiation promotes destabilization of the water–oil interface. For all investigated systems, interfacial tension decreased after microwave treatment and the magnitude of reduction increased with microwave power.

Nevertheless, the decrease in interfacial tension did not correspond directly to maximum phase separation efficiency at the highest power level. Although the lowest IFT values were observed at 800 W, the separated water volume did not increase proportionally and, in some cases, decreased relative to intermediate power conditions.

This divergence suggests that interfacial tension reduction alone is insufficient to describe the complex behaviour of microwave-assisted demulsification. The results support the interpretation that the process is governed by a coupled interaction between dielectric energy absorption, heating dynamics, and transient structural response of the emulsion system.

To integrate the effects of power input and composition into a unified performance framework, an efficiency optimization map was constructed. The map combines separation yield and specific energy consumption into a single energy efficiency metric and illustrates its dependence on microwave power and oil concentration. The resulting performance landscape is shown in Fig. 8.

Fig. 8 presents the energy-efficiency contour map as a function of water volume fraction (ϕ) and microwave power. The obtained contour distribution indicates that process efficiency does not increase monotonically with either parameter. Instead,

(CC) 2026 Serbian Chemical Society.

a localized efficiency maximum appears within an intermediate region of water fraction and microwave power.

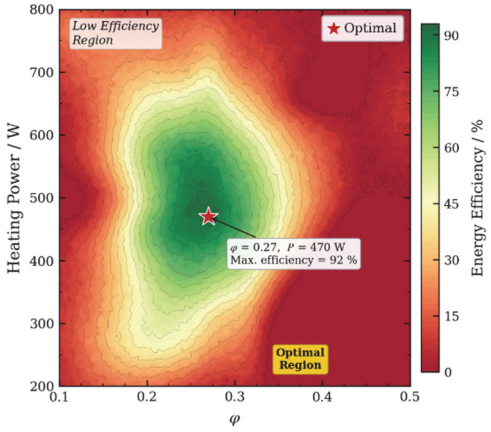

Fig. 8. Energy efficiency contour map as a function of water fraction (ϕ) and microwave power. The marked point indicates the optimal condition.

The highest apparent efficiency was observed at $\phi \approx 0.27$ and $P \approx 470$ W, where η_{max} reached approximately 92 % under the investigated experimental conditions. This region may correspond to a comparatively favourable balance between microwave energy absorption, dielectric response, and phase-separation dynamics within the emulsion system.

At lower microwave powers (< 300 W), the supplied energy appeared insufficient to achieve efficient destabilization of the water–oil interface, resulting in relatively limited phase separation across the investigated compositions. In contrast, at higher microwave powers (> 700 W), the overall efficiency decreased despite continued energy input and elevated bulk temperatures. This behaviour may indicate that excessively rapid heating contributes to increased molecular mobility and less efficient phase disengagement while simultaneously increasing specific energy consumption.

The influence of water fraction also exhibited a non-linear behaviour. At low water fractions, the reduced dielectric contrast likely limited effective microwave coupling and energy absorption. At high water fractions, increased phase connectivity and structural complexity may have reduced efficient phase disengagement under high-energy conditions. Consequently, the experimentally favourable operating region appeared within intermediate emulsion compositions, where microwave absorption and phase destabilization remained relatively balanced.

The contour map was constructed using interpolated experimental data within the investigated parameter range. Therefore, the identified optimal condition should be interpreted as an approximate practical operating region rather than a strict theoretical maximum. In addition, because the present analysis was based primarily on bulk thermal and separation measurements, local thermal gradients,

(CC) 2026 Serbian Chemical Society.

transient electromagnetic field redistribution and microscopic interfacial processes were not directly characterized.

From a process-engineering perspective, the obtained results suggest that microwave-assisted demulsification may be more effectively operated within a controlled efficiency window rather than at the maximum available microwave power. Proper selection of both microwave power and emulsion composition appears important for achieving a favourable balance between phase separation performance and energy consumption under the investigated conditions.

Although the present study demonstrates clear relationships between microwave power, dielectric behaviour, viscosity reduction, interfacial tension variation and phase separation efficiency, several limitations should be acknowledged. The kinetic analysis was primarily based on bulk temperature measurements obtained immediately after microwave irradiation. Direct spatial characterization of local temperature gradients, transient hot spots, droplet evolution and interfacial charge redistribution was not performed.

Consequently, the proposed mechanisms related to structural relaxation, transient overheating and non-equilibrium destabilization should be interpreted as indirect phenomenological interpretations derived from macroscopic experimental observations. Further investigations involving infrared thermal imaging, dielectric field mapping and *in situ* droplet-size characterization are required for direct mechanistic validation.

CONCLUSION

The obtained results indicate that microwave-assisted demulsification does not appear to follow a purely temperature-driven mechanism under the investigated conditions. The combined analysis of bulk temperature evolution, dielectric behaviour, viscosity reduction, interfacial tension variation and phase separation efficiency suggests that heating dynamics may play an important role in determining demulsification performance. The experimentally favourable phase separation behaviour was observed mainly at intermediate microwave powers of approximately 400–600 W. At higher microwave power levels (≈800 W), separation efficiency decreased despite continued increases in bulk temperature, dielectric losses, viscosity reduction and interfacial tension reduction. This behaviour may indicate that excessively rapid microwave heating contributes to transient non-equilibrium effects and less efficient phase disengagement.

The combined evaluation of separation yield, productivity, dielectric response and specific energy consumption showed that the most favourable operating region under the investigated conditions occurred at intermediate water fractions (ϕ 0.20–0.35) and moderate-to-high microwave powers (470–600 W). The obtained contour-based efficiency analysis suggests that maximum microwave power input does not necessarily correspond to maximum process efficiency. Instead, efficient

(CC) 2026 Serbian Chemical Society.

microwave-assisted demulsification appears to require a balanced interaction between microwave energy absorption, heating dynamics and emulsion structure.

At the same time, the present analysis was based primarily on macroscopic measurements, including bulk temperature evolution, dielectric characteristics, viscosity, interfacial tension and separated water volume. Direct characterization of local thermal gradients, transient hot spots, droplet evolution and interfacial relaxation phenomena was not performed. Therefore, the proposed interpretation of non-equilibrium microwave effects should be considered an indirect phenomenological interpretation derived from experimental observations rather than direct mechanistic confirmation. Further studies involving spatial thermal mapping, in situ droplet-size analysis and localized dielectric characterization are required for more detailed mechanistic validation of microwave-assisted phase separation processes.

Acknowledgements. This work was carried out within the framework of the research program on corrosion mitigation in microbiologically active oilfield environments conducted at Azerbaijan State Oil and Industry University in collaboration with the State Oil Company of Azerbaijan Republic (SOCAR). The authors gratefully acknowledge the technical support provided during electrochemical and microbiological testing. The authors also thank colleagues for valuable discussions related to impedance analysis and adsorption modelling.

И З В О Д

ТЕХНОЛОШКИ АСПЕКТИ НЕРАВНОТЕЖНОГ МИКРОТАЛАСНОГ ЗАГРЕВАЊА У ЦИЉУ ФАЗНОГ РАЗДВАЈАЊА ВИШЕФАЗНИХ ТЕЧНИХ СИСТЕМА

AYSEL V. GASIMZADE[1], VALI KH. NURULLAYEV[2] и RASHAD R. KHALILZADE[1]

[1]Azerbaijan State Oil and Industry University, Baku, Azerbaijan u [2]State Oil Company of Azerbaijan Republic, Baku, Azerbaijan

Микроталасно потпомогнута деемулгација представља перспективну методу за раздвајање емулзија типа вода-у-уљу, јер омогућава брз пренос енергије по целој запремини. Међутим, механизам раздвајања у условима неравнотежног загревања још увек није довољно разјашњен. У овом истраживању испитивани су кинетички фактори који управљају микроталасно потпомогнутим фазним раздвајањем при снази микроталасног зрачења од 200 до 800 W и уделу воде од 0,12 до 0,45. Анализирани су промена температуре током времена, брзина загревања (dT/dt), запремина издвојене воде и специфична потрошња енергије. Резултати су показали изражену немонотону зависност ефикасности раздвајања од снаге микроталасног зрачења. Највећа ефикасност раздвајања постигнута је при средњим снагама од 400 до 600 W, док је даље повећање снаге довело до смањења ефикасности упркос даљем порасту температуре. Добијени резултати показују да је брзина загревања, а не крајња температура, главни параметар који управља процесом, што пружа основу за развој енергетски ефикаснијих поступака микроталасне деемулгације.

(Примљено 9. марта, ревидирано 7. маја, прихваћено 11. јуна 2026)

REFERENCES

1. Z. Zhao, H. Li, X. Gao, *Chem. Rev.* **124** (2024) 2651 (https://doi.org/10.1021/acs.chemrev.3c00794)

(CC) 2026 Serbian Chemical Society.

2. N. Hassanshahi, G. Hu, J. Li, *ACS Omega* **7** (2022) 33397 (https://doi.org/10.1021/acsomega.2c04022)
3. Husain, A. A. Adewunmi, M. S. Kamal, M. Mahmoud, M. A. Al-Harthi, *Energy Fuels* **35** (2021) 16527 (https://doi.org/10.1021/acs.energyfuels.1c02286)
4. H. Díaz Velázquez, D. Guzmán-Lucero, R. Martínez-Palou, *J. Disp. Sci. Technol.* **44** (2023) 1884 (https://doi.org/10.1080/01932691.2022.2049293)
5. H. Nour, M. S. Omer, S. F. Pang, *J. Appl. Sci.* **10** (2010) 2935 (https://doi.org/10.3923/jas.2010.2935.2939)
6. L. Wei, L. Zhang, S. Guo, X. Jia, Y. Zhang, C. Sun, X. Dai, *ACS Omega* **6** (2021) 25518 (https://doi.org/10.1021/acsomega.1c03530)
7. S. K. Nandwani, N. I. Malek, M. Chakraborty, S. Gupta, *Energy Fuels* **34** (2020) 9411 (https://doi.org/10.1021/acs.energyfuels.0c01331)
8. Z. Jia, Z. Niu, Z. Yang, X. Li, J. Wang, X. He, H. Sui, L. He, *Energy Fuels* **34** (2020) 1259 (https://doi.org/10.1021/acs.energyfuels.9b02679)
9. M. M. S. Abdullah, H. A. Al-Lohedan, *Energy Fuels* **33** (2019) 12916 (https://doi.org/10.1021/acs.energyfuels.9b03148)
10. O. Ezzat, A. M. Atta, H. A. Al-Lohedan, M. M. S. Abdullah, A. I. Hashem, *Energy Fuels* **32** (2018) 214 (https://doi.org/10.1021/acs.energyfuels.7b02955)
11. D. Alves, E. Lourenço, E. Franceschi, A. F. Santos, C. C. Santana, G. Borges, C. Dariva, *Energy Fuels* **31** (2017) 9132 (https://doi.org/10.1021/acs.energyfuels.7b01418)
12. M. S. Bin Dahbag, M. E. Hossain, A. A. AlQuraishi, *Energy Fuels* **30** (2016) 9260 (https://doi.org/10.1021/acs.energyfuels.6b01712)
13. X. He, Q. Liu, Z. Xu, *Chem. Eng. Sci.* **230** (2021) 116215 (https://doi.org/10.1016/j.ces.2020.116215)
14. A. Adewunmi, M. S. Kamal, T. I. Solling, *J. Petrol. Sci. Eng.* **196** (2021) 107680 (https://doi.org/10.1016/j.petrol.2020.107680)
15. H. Bao, H. Xing, M. Liu, Q. Zhang, H. Yan, J. Liu, *J. Disp. Sci. Technol.* **41** (2020) 2116 (https://doi.org/10.1080/01932691.2019.1651204)
16. A. Husain, M. A. Al-Harthi, *J. Petrol. Sci. Eng.* **220** (2023) 111089 (https://doi.org/10.1016/j.petrol.2022.111089)
17. D. S. Miller, T.-C. Kuo, D. Brennan, A. Schmitt, K. Grzesiak, R. Jenkins, H. Singh, H. Wiles, T. Martin, A. Banks, D. Hayes, R. Gupta, J. Moore, J. Mendenhall, T. Kalantar, *J. Surf. Deterg.* **28** (2025) 977 (https://doi.org/10.1002/jsde.12850)
18. Z. Song, W. Pan, S. Wang, X. Lv, X. Zhao, J. Sun, Y. Mao, X. Wang, W. Wang, *Energy Sources, A* **47** (2025) 9720 (https://doi.org/10.1080/15567036.2021.1956019)
19. K. Ji, Y. Tian, J. Jiang, X. Yan, J. Tian, J. Yang, Z. He, X. Lu, *Fuel* **386** (2025) 134247 (https://doi.org/10.1016/j.fuel.2024.134247)
20. S. Tahami, K. Movagharnejad, *J. Mol. Liq.* **411** (2024) 125748 (https://doi.org/10.1016/j.molliq.2024.125748)
21. H. Sadighian, Z. Mohamadnia, E. Ahmadi, *Carbohyd. Polym.* **327** (2024) 121697 (https://doi.org/10.1016/j.carbpol.2023.121697)
22. F. Ye, X. Zhang, X. Jiang, H. Liu, Y. Tang, Q. Qu, L. Shen, Z. Zhang, Y. Mi, X. Yan, *Geoenergy Sci. Eng.* **230** (2023) 212265 (https://doi.org/10.1016/j.geoen.2023.212265)
23. P. Schacht, P. Torres-Mancera, J. Ancheyta, in *Catalytic* In-Situ *Upgrading of Heavy and Extra-Heavy Crude Oils*, J. Ancheyta, M. Varfolomeev, C. Yuan, Eds., Wiley OnLine Library, 2023, p. 237 (https://doi.org/10.1002/9781119871507.ch5)

(CC) 2026 Serbian Chemical Society.

24. M. Lei, H. Huang, J. Liu, F. Peng, *Colloids Surfaces, A* **671** (2023) 131696 (https://doi.org/10.1016/j.colsurfa.2023.131696)
25. F. Song, J. Zhou, Z. Jia, L. He, H. Sui, X. Li, *J. Mol. Liq.* **382** (2023) 121864 (https://doi.org/10.1016/j.molliq.2023.121864)
26. K. Azizollah, *Petrol. Chem.* **63** (2023) 338 (https://doi.org/10.31857/S002824212303005X) (in Russian)
27. T. Wei, X. Zhong, X. Chen, Z. Guo, *Langmuir* **41** (2025) 16139 (https://doi.org/10.1021/acs.langmuir.5c01225)
28. H. Sadighian, Z. Mohamadnia, E. Ahmadi, *Langmuir* **39** (2023) 9627 (https://doi.org/10.1021/acs.langmuir.3c00564)
29. S. Rasouli, N. Rezaei, S. Zendehboudi, X. Duan, R. L. Legge, I. Chatzis, *Langmuir* **39** (2023) 4100 (https://doi.org/10.1021/acs.langmuir.2c03480)
30. N. Parmar, C. A. Kavale, H. Goyal, *Ind. Eng. Chem. Res.* **62** (2023) 2561 (https://doi.org/10.1021/acs.iecr.2c03877)
31. H. Tang, L. Hao, J. Chen, F. Wang, H. Zhang, Y. Guo, *Energy Fuels* **32** (2018) 3627 (https://doi.org/10.1021/acs.energyfuels.7b03344)
32. T. Assenheimer, A. Barros, K. Kashefi, J. C. Pinto, F. W. Tavares, M. Nele, *Energy Fuels* **31** (2017) 6587 (https://doi.org/10.1021/acs.energyfuels.7b00275)
33. H. Bahmani, Y. Hojjat, A. Yazdian, M. Shirkosh, *Petrol. Sci. Technol.* **43** (2025) 1293 (https://doi.org/10.1080/10916466.2024.2326167)
34. D. M. Hagl, D. Popovic, S. C. Hagness, J. H. Booske, M. Okoniewski, IEEE *Trans. Microwave Theory Tech*. **51** (2003) 1194 (https://doi.org/10.1109/TMTT.2003.809626)
35. U. Kaatze, *Meas. Sci. Technol*. **18** (2007) 967 (https://doi.org/10.1088/0957-0233/18/4/002)
36. J. O. Alvarez, D. Jacobi, S. Althaus, S. Elias, *Fuel* **288** (2021) 119679 (https://doi.org/10.1016/j.fuel.2020.119679)
37. *ASTM D7042-21a, Standard Test Method for Dynamic Viscosity and Density of Liquids by Stabinger Viscometer*, ASTM International, West Conshohocken, PA, 2021 (https://doi.org/10.1520/D7042-21A)
38. *ASTM D445-20, Standard Test Method for Kinematic Viscosity of Transparent and Opaque Liquids*, ASTM International, West Conshohocken, PA, 2020 (https://doi.org/10.1520/D0445-20)
39. K. Paso, T. Kompalla, N. Aske, H. P. Rønningsen, J. Sjöblom, *J. Dispers. Sci. Technol*. **30** (2009) 757 (https://doi.org/10.1080/01932690802643220)
40. B. Vonnegut, *Rev. Sci. Instrum*. **13** (1942) 6 (https://doi.org/10.1063/1.1769937)
41. H. M. Princen, I. Y. Z. Zia, S. G. Mason, *J. Colloid Interface Sci*. **23** (1967) 99 (https://doi.org/10.1016/0021-9797(67)90090-2)
42. M. Hoorfar, A. W. Neumann, *Adv. Colloid Interface Sci*. **121** (2006) 25 (https://doi.org/10.1016/j.cis.2006.06.001)
43. S. Manholi, S. Athiyanathil, *J. Poly. Res.* **31** (2024) 1 (https://doi.org/10.1007/s10965-024-04212-z)
44. E. R. Binner, J. P. Robinson, S. A. Silvester, S. W. Kingman, E. H. Lester, *Fuel* **116** (2014) 516 (https://doi.org/10.1016/j.fuel.2013.08.042)
45. E. B. da Silva, D. Santos, M. P. de Brito, R. C. L. Guimarães, B. M. S. Ferreira, L. S. Freitas, M. C. V. de Campos, E. Franceschi, C. Dariva, A. F. Santos, M. Fortuny, *Fuel* **128** (2014) 141 (https://doi.org/10.1016/j.fuel.2014.02.076)

(CC) 2026 Serbian Chemical Society.

46. Y. Wang, C. Liu, H. Lang, Z. Hu, X. Wang, Z. Yang, Z. Wang, Z. Guo, L. Jiang, *Food Chem. X* **19** (2023) 100861 (https://doi.org/10.1016/j.fochx.2023.100861)
47. H. Xu, C. Hu, M. Gantumur, H. Li, N. Sukhbaatar, L. Zhang, Z. Jiang, *J. Food Eng.* **403** (2026) 112707 (https://doi.org/10.1016/j.jfoodeng.2025.112707)
48. Z. Li, X. Zhong, C. Luan, N. Wen, C. Shi, S. Liu, Y. Xu, Q. He, Y. Wu, J. Yang, *Food Chem. X* **21** (2024) 101149 (https://doi.org/10.1016/j.fochx.2024.101149)
49. L. O. Diehl, D. P. Moraes, F. G. Antes, J. S. F. Pereira, M. F. P. Santos, R. C. L. Guimarães, É. M. M. Flores, *Sep. Sci. Technol.* **46** (2011) 1358 (https://doi.org/10.1080/01496395.2011.560590).

(CC) 2026 Serbian Chemical Society.

Journal of the Serbian Chemical Society
JSCS-info@shd.org.rs • www.shd.org.rs/JSCS
J. Serb. Chem. Soc. 91 (10) 1083–1097 (2026)
JSCS–5545
Original scientific paper
Published 18 November, 2026

Corrosion studies of stainless steel and carbon steel in aqueous solutions of sodium glycinate used for CO_2 capture

MUHAMMAD SHUAIB SHAIKH[1]*, AZMI MOHD SHARIFF[2,3], INAMULLAH BHATTI[1], ABDUL QADEER LAGHARI[1], ABDUL SATTAR JATOI[4], ARSHAD IQBAL[4], GHULAM MUSTAFA MEMON[5] and TANWEER HUSSAIN[6]

[1]Department of Chemical Engineering, Mehran University of Engineering and Technology, Jamshoro,76062, Sindh, Pakistan, [2]CO2 Research Centre (CO2RES), Universiti Teknologi PETRONAS, Bandar Seri Iskandar 32610, Perak, Malaysia, [3]Advance Safety Management Services Sdn. BHD, 50450 Kuala Lumpur, Malaysia, [4]Chemical Engineering Department, Dawood University of Engineering and Technology, Karachi, 74800, Sindh, Pakistan, [5]IRC for Industrial Nuclear Energy, King Fahd University of Petroleum & Minerals, Saudi Arabia and [6]Department of Mechanical Engineering, Mehran University of Engineering and Technology, Jamshoro,76062, Sindh, Pakistan

(Received 16 May, revised 19 June, accepted 2 August 2026)

Abstract: Corrosion is a well-known and serious issue in the carbon dioxide (CO_2) absorption process, which causes high maintenance cost for the restoration of corroded equipment and pipelines. Aqueous sodium glycinate (SG) is a potential solvent for CO_2 capture. A corrosion study of SG solvent is very crucial for its practical applications, as such data are very limited in the open literature. Therefore, to address this significant gap, the corrosion rates of stainless steel (SS304) and carbon steel (CS1018) were investigated in this study by employing the weight loss method using SG solvent at three different temperatures (303.15, 313.15 and 333.15 K) and concentrations (0.10, 0.20 and 0.30 mass fraction) of industrial importance. The results revealed that SS304 showed negligible corrosion in SG solvent with marginal effects of temperature and concentration. However, significant effects of temperature and concentration were observed on the corrosion rate of CS1018 in SG solvent. At the highest studied temperature of 333.15 K and the highest concentration (0.30 mass fraction), the corrosion rates of SS304 and CS1018 in SG solvent were 3.291 and 32.203 mpy, respectively. Moreover, the corrosion rate of CS1018 in SG solvent was compared with methyldiethanolamine (MDEA), monoethanolamine (MEA) and diethanolamine (DEA). It was found that SG solvent showed lower corrosivity than various amine solvents. The findings of this study provide guidance for the practical application for SG solvent in the CO_2 capture process. Also, the data obtained

* Corresponding author. E-mail: shuaib.shaikh@faculty.muet.edu.pk
https://doi.org/10.2298/JSC260516055S

Available online at https://www.shd.org.rs/JSCS/
(CC) 2026 Serbian Chemical Society.

could significantly help design engineers establish appropriate operating conditions for the CO_2 capture process to control corrosion.

Keywords: corrosion behavior; metallic materials; weight loss method; amino acids; CO_2 absorption.

INTRODUCTION

Corrosion is a well-known issue in acid gas (CO_2) removal operations, which is considered one of the most serious problems in CO_2 absorption. The corrosion of equipment, pipelines and other utilities in the CO_2 absorption process cause unscheduled downtime, loss of production; reduced equipment life and sometimes even fatal injuries. The production loss for a typical plant due to corrosion varies from 10,000 to 30,000 USD per day. Additionally, various management expenses are also incurred for the restoration of corroded systems and corrosion mitigation. Although it is virtually impossible to eliminate corrosion, however, it can be minimized and controlled. Chemical and design engineers always strive for the minimization of corrosion in CO_2 capture plants. To accomplish this, prior knowledge of chemical solvents, and the materials of construction for CO_2 capture plant fabrication is always important, especially when new chemical solvents are designed for CO_2 capture.[1–4] Therefore, in order to minimize and control corrosion in a CO_2 absorption plant, it is essential to evaluate the corrosion tendency of the new solvents to be used for the absorption of CO_2. Aqueous SG solvent shows promising CO_2 absorption characteristics. Various studies on SG solvent have been carried out, including studies on physical properties and CO_2 solubility.[5,6] However, these studies are not sufficient for commercial applications of SG solvent. It is crucial to investigate corrosion rate of stainless steel and carbon steel using SG solvent for its commercial applications. Based on a comprehensive literature review, such data are rarely available in the open literature. Therefore, in order to address this research gap, systematic corrosion studies on aqueous SG solvent have been carried out in this study. The corrosion data on the SG solvent are very useful for the selection of appropriate materials for the fabrication of plants and utilities. Besides, the evaluation of the corrosion tendency of SG solvent and its comparison with conventional amine solvents is also a key criterion for the commercial suitability of the SG solvent.

MATERIALS AND METHODS

In this study, the weight loss method was used for measuring the corrosion rate. The weight loss method is a simple and established technique for investigating general corrosion. This technique is used for long-term exposure of test metal in solutions. Weighed test specimens are immersed in the test solutions for a particular time, and then removed to determine the loss in weight of the specimen.

(CC) 2026 Serbian Chemical Society.

Chemicals and gases

Various chemicals and gases were used in this work, such as glycine, sodium hydroxide, monoethanolamine, acetone and double-distilled water. These chemicals were supplied by Merck Sdn Bhd., Malaysia. Gases such as CO_2 and N_2 were supplied by Air Products Sdn Bhd. Malaysia. All the chemicals and gases were used without further purification. Double-distilled water was used for preparing the samples. The detailed specifications of the chemicals and gases used in this study are summarized in Table I.

TABLE I. Specifications of chemicals and gases

Chemicals/gases	Chemical formula	Purity	Method of purification	Supplier
Glycine	H_2NCH_2COOH	≥ 99 %	None	Merck
Sodium hydroxide	NaOH	≥ 99 %	None	Merck
Monoethanolamine	C_2H_7NO	≥ 99 %	None	Merck
Water	H_2O	99 %	Double distillation	–
Acetone	C_3H_6O	≥ 99.5 %	None	Merck
Carbon dioxide	CO_2	99 %	None	Air Products
Nitrogen	N_2	99 %	None	Air Products

Preparation of solvent samples

Aqueous solutions of SG were prepared by neutralizing glycine dissolved in double-distilled water with an equimolar amount of sodium hydroxide. The solutions were stirred continuously until complete dissolution.[7] The concentrations of the solutions were expressed as mass fractions, denoted by w. An electronic analytical balance (Sartorius, model BSA-224S-CW) was used for all mass measurements with an accuracy of $\pm 1\times10^{-4}$ g. The solvent concentrations were 0.10, 0.20 and 0.30 mass fractions, which are relevant to commercial applications for the CO_2 removal process. Moreover, the selected concentration range represented the low, medium and high concentrations of amino acid salts, which are commonly used for systematic investigation of concentration effects on the corrosion rate and comparison with the literature. In addition, the purpose of selecting these solvent concentration ranges was to avoid solvent precipitation during CO_2 absorption.[8,9]

Specimen description and preparation

Two types of specimens were used in this work, stainless steel (SS304) and carbon steel (CS1018). These specimens are also called corrosion coupons. The coupons can be rectangular, cylindrical, or disc-shaped, with various dimensions. The dimensions of the test coupons are selected according to the conditions of the tests and the facilities available for corrosion testing. Carbon steel and stainless steel are selected in this study because they are widely used in the fabrication of equipment, accessories, and pipelines in CO_2 capture plants.[1] The corrosion coupons were purchased from Metals Samples Inc., USA. The coupons were shipped in individual vapor corrosion inhibition (VCI) bags to prevent vapor and atmospheric corrosion of the coupons. The coupons are rectangular, having dimensions of (1/16″ thick×1/2″ wide×3″ length). The coupons have 3/16″ diameter hole located 1/4″ from an end centered with 1/8″ radius corners. Besides, all the coupons were pre-weighed and stenciled with sequential numbers and alloy codes to avoid confusion during exposure. As an example, the coupons used in this study are shown in Fig. 1a (SS304) and b (CS1018). The chemical composition of the coupons SS304 and CS1018 is given in Table II.

(CC) 2026 Serbian Chemical Society.



Fig. 1. Corrosion coupons.

TABLE II. Chemical composition (%) of corrosion coupons used in this study

Element	Sample	
	SS304	CS1018
Carbon	0.0575	0.1900
Manganese	1.6540	0.6700
Phosphorus	0.0330	0.0300
Sulfur	0.0010	0.0010
Chromium	18.1630	0.0300
Nickel	8.0340	0.0400
Copper	0.4700	0.0800
Molybdenum	0.3370	0.0200
Nitrogen	0.0650	0.0070
Iron	Balance	Balance

The specimens were prepared before use by grinding with silicon carbide waterproof abrasive papers with a grit range from 120 to 600, supplied by Saie Brand, China. The specimens were then cleaned with deionized water, degreased with acetone and dried with dry air. Finally, the prepared specimens were stored in a desiccator for corrosion experiments. The prepared specimens were handled carefully with gloves and tweezers to avoid contamination of the specimen surface. The method of preparing the specimens was performed according to ASTM G1-90.[10] The prepared specimens were used within 24 h of preparation.

Weight loss method for corrosion measurement

Corrosion testing using weight loss technique is the simplest and longest-established method to measure uniform corrosion. In this method, a weighed coupon of metal or alloy is immersed in the test solution under certain conditions (which var according to the objectives of the study) for a reasonable period, depending upon the experimental objectives and test design. Later, the coupons were removed and cleaned of all corrosion materials and reweighed. The weight loss of the metal was then used for the calculation of the corrosion rate.[11,12] In this study, the weight loss technique was used because it is widely used in laboratories and industries due to a number of attractive features.[12] The corrosion experiments are easy to conduct using the weight loss method because no sophisticated or complex instruments are required. The measurement is direct and does not require theoretical assumptions. This technique is applicable to all kinds of corrosion environments, which makes it versatile. Apart from these, it is a low-cost technique, flexible with respect to experimental facilities available in laboratories, and allows simultaneous evaluation of various materials and test solutions under various test conditions. Despite being the oldest method of corrosion measurement, the weight loss method remains widely used due to the versatile features described above.

Experimental procedure

The simple immersion corrosion method was used in this study, and the general corrosion rate was calculated using the weight loss method. The fundamental procedure of immersion

(CC) 2026 Serbian Chemical Society.

corrosion tests was followed according to the guidelines of ASTM G-31-72 (Standard Practice for Laboratory Immersion Corrosion Testing of Metals),[11] The setup consisted of a corrosion bottle (250 mL, Schott Duran), nylon strings (0.45mm, No.2, Ofmer Company) for holding the corrosion coupon, a pH meter (SCHOTT instruments), and a heating system (hot plate/water bath/oven). In this study, an oven was used for heating. All the corrosion experiments were carried out at atmospheric pressure. The test solutions were prepared as described. The corrosion bottles filled with 250 mL of test solution were purged with CO_2 until saturation at ambient temperature. Later, before immersing the coupons in the test solution, the coupons were weighed using an electronic analytical balance (Sartorius, model BSA-224S-CW) with an accuracy of $\pm 1\times10^{-4}$ g. The corrosion coupons were immersed in the corrosion bottles by hanging them with a nylon string across the opening of the corrosion bottle. The coupons were suspended and positioned at the center of the corrosion bottle to ensure complete immersion of the coupons in the test solution and prevent them from touching the bottom of the bottles. The bottles were then firmly closed with the screw lid.[13] The corrosion bottle was labeled with the name of the test solution, identification of the coupons (type of alloy and coupon number), while the date, and time of immersion were recorded.[11,14,15] Finally, the corrosion bottle was placed in the preheated oven at 303.15 K for 240 h.[12,13,16] Similarly, other experiments were conducted at 313.15 and 333.15 K for the same exposure time. The temperature range (303.15, 313.15 and 333.15 K) was selected based on the practical range of absorption temperatures in CO_2 capture plants and to study systematic effect of temperature on the corrosion rate.[17,18] The time of exposure in these types of experiments can vary from 24 to 240 h.[19] A short exposure time may sometimes give erroneous results. It is recommended to use a longer exposure time (240 h) in order to get more realistic results.[11-13,18] The selected time duration of 240 h is sufficient and considered a long exposure time that produces a measurable corrosion rate and stable corrosion behavior[11-13,18] This exposure time is also suggested in ASTM G-31-72.[12] Each experiment was performed in triplicate to obtain reproducible results, and the average results were reported. The results were accurate within ±10 %.

Post-exposure cleaning of specimens

After completion of the test duration (240 h), the test bottles were removed from the oven and the specimens were withdrawn from the bottles. Before cleaning the coupons, their appearance was observed and recorded properly. The variation in the test solutions was also observed. Although these observations are qualitative, they can provide useful information during analysis of the corrosion results. Cleaning the coupons after a test is an important step in corrosion measurement. The procedure for post-cleaning of coupons was followed according to ASTM G1--90 standard.[10] The coupons were washed with running tap water, cleaned with a non-metallic brush and chemically washed. Later, the coupons were scraped with at least two different grit abrasives until the surfaces were free of the remaining corrosion products. The coupons were then washed with acetone, dried and weighed using an analytical balance. The cleaning cycles were repeated few times until the constant weight loss was obtained by plotting the number of cleaning cycles versus a mass.[8] During the post-cleaning, care should be taken to avoid the removal of base metal.

Calculation of corrosion rate

The corrosion rate of SS304 and CS1018 in the test solutions was calculated according to ASTM G1-90 (Standard Practice for Preparing, Cleaning and Evaluation Corrosion Test Specimen). Since the weight loss method was used in this study, the initial and final weights of the

(CC) 2026 Serbian Chemical Society.

specimen were used for estimating the corrosion rate. The following equation was used to calculate the corrosion rate:[9,10]

$$CR = \frac{KW}{ATD} \tag{1}$$

where CR is the corrosion rate in mpy, K is the constant factor (5.34×10^5), W is the mass loss in g, A is the area (3.38 square inches), T is the time of exposure (240) in h and D is the density of the alloy (SS304: 7.94; CS1018: 7.87) in $g\cdot cm^{-3}$.

RESULT AND DISCUSSION

Comparison of corrosion rate of monoethanolamine with the literature

The corrosion rate of MEA at a mass fraction of 0.30 was measured at various temperatures (303.15, 313.15 and 333.15 K) in order to compare the results with literature. The corrosion rate of MEA at 313.15 K was compared with previous work,[20] since the data are not available in the literature at other temperatures. The comparison is shown in Fig. 2. The experimental values of the corrosion rate at 313.15 K are in the range of those reported in the literature for MEA at a mass fraction of 0.30 at 313.15 K.[20]

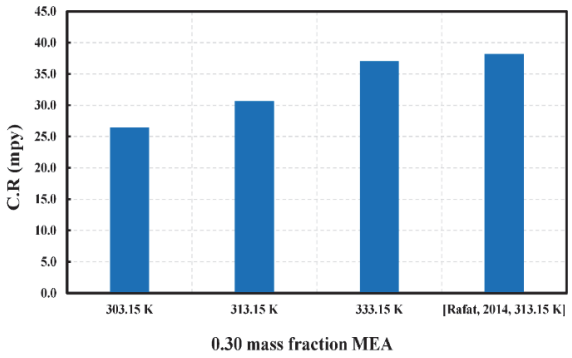

Fig. 2. Corrosion rate of 0.30 mass fraction MEA and comparison with the literature.

Corrosion rate of aqueous SG solutions

The corrosion rate of SS304 and CS1018 in aqueous SG solutions was measured by weight loss technique at three different temperatures (303.15, 313.15 and 333.15 K) and at various mass fractions (0.10, 0.20 and 0.30). Each experiment was conducted three times, and the average results were reported. The process parameters of interest in this study for corrosion measurement are temperature, concentration and type of metal. Therefore, the effects of these parameters on the corrosion rate were studied using the weight loss technique.

Effect of temperature on corrosion rate

Temperature is an essential parameter that influences the rate of corrosion. Therefore, in this study, the effect of temperature on the corrosion rate of SS304

(CC) 2026 Serbian Chemical Society.

and CS1018 was investigated at the three different temperatures mentioned above. From the analysis of the corrosion results, it was found that temperature has a significant influence on the corrosion rate of both SS304 and CS1018 in aqueous SG solutions. The rate of corrosion increases with an increase in the system temperature, as shown in Fig. 3a and b. This suggests that increasing the solution temperature increases the kinetic energy of the species, thereby accelerating the iron dissolution and thus enhancing the corrosion rate.[21,22] The corrosion reaction (iron dissolution) is:

$$\mathrm{Fe{+}HCO_3^-} \rightarrow \mathrm{FeCO_3} + \mathrm{H^+} + 2\mathrm{e^-} \tag{2}$$

Moreover, increasing the temperature increases the mobility of reacting species by increasing the diffusion of ions of the reactive species to the metal surface, thereby increasing the corrosion rate.[4,24] Moreover, passive oxide films may become unstable and more porous at elevated temperatures, thereby accelerating the iron dissolution process.[21–23] Similar trends have been observed for various amine solutions.[3,4,24,25] By further investigating the effect of temperature on the corrosion rate, it was observed from Fig. 3a and b that the effect of temperature from 303.15 to 313.15 K is smaller than that from 313.15 to 333.15 K for both metals and at various concentrations. The corrosion rate increased significantly from 313.15 to 333.15 K, which suggests that the corrosion process is dependent on temperature. This trend could be due to increase in corrosion reaction kinetics at high temperatures. These trends are the same as those reported in the literature for various solvents used for CO_2 capture.[3,4,24,25] Moreover, the effect of temperature on the corrosion rate of SS304 is smaller than that on CS1018 for aqueous SG solutions. This could be due to the fact that SS304 is significantly less susceptible to corrosion than CS1018. Therefore, an increase in temperature does not greatly affect the corrosion of SS304 in aqueous SG solutions. At the highest studied temperature (333.15 K) and the highest concentration (0.30 mass fraction), the corrosion rate of SS304 in aqueous SG solutions was 3.291 mpy. Similarly, the corrosion rate of CS1018 under the same conditions was 32.203 mpy in aqueous SG solutions.

Furthermore, the effect of temperature on the corrosion rate of SS304 and CS1018 followed Arrhenius behavior:

$$\log C.R = \log A - \left(\frac{E_\mathrm{a}}{2.303RT} \right) \tag{3}$$

where $C.R$ is the corrosion rate (mpy), A is the Arrhenius pre-exponential factor, $E_\mathrm{a}/2.303R$ is the slope of the equation, in which E_a is the activation energy (J/mol), R is the universal gas constant (J/(K mol)), and T is the temperature in K. From Eq. (3), the plot of log $C.R$ *versus* $1/T$ gives straight lines, as shown in Fig. 3a and b. From the Arrhenius plots, the effect of temperature on the corrosion rate of SS304 and CS1018 in aqueous solutions of SG is more obvious.

(CC) 2026 Serbian Chemical Society.

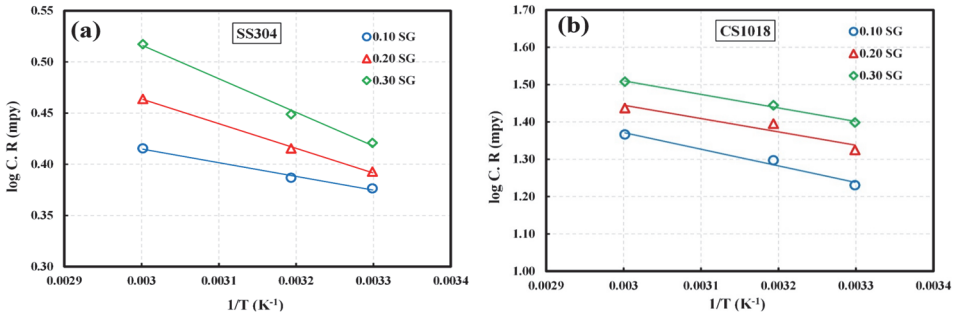

Fig. 3. Arrhenius plot for corrosion rate of: a) SS304 and b) CS1018 in aqueous SG solutions at various concentrations.

Moreover, the Arrhenius equation given above can also be used for the prediction of the corrosion rate of SS304 and CS1018 in aqueous SG solutions. Therefore, for the validation of experimental results, the corrosion rate data of the studied solvent were also predicted using Eq. (3) and its coefficients. The validity of experimental and predicted data was assessed statistically by estimating the deviation between the two datasets. The values of Arrhenius pre-exponential factors (A), slopes of the lines ($E_a/(2.303R)$, R^2 and SD are given in Table III for aqueous SG solutions.

TABLE III. Corrosion rate correlation parameters for aqueous SG solutions

w(SG)	$E_a/2.303R$	A	R^2	SD
		SS304		
0.10	133.72	6.547869	0.9909	0.0088
0.20	240.73	15.34264	0.9984	0.0071
0.30	328.45	31.75411	0.9948	0.0188
		CS1018		
0.10	445.82	511.564	0.9762	0.3802
0.20	357.74	329.6856	0.9048	0.7842
0.30	362.91	397.1001	0.994	0.2195

Effect of concentration on corrosion rate

It is essential to study the effect of the concentration of SG on the corrosion rate of SS304 and CS1018. Different concentrations of the solvent give different corrosion rates of both metals. Therefore, in this study, the corrosion rate of SS304 and CS1018 in aqueous SG solutions was measured at different concentrations (0.10, 0.20 and 0.30 mass fractions). The graphical representation of the effect of concentration on the corrosion rate of SS304 and CS1018 in aqueous SG solutions at various temperatures is shown in Fig. 4a and 4b.

From the analysis of corrosion results, it was found that the corrosion rate increases with increasing concentration of SG in the solution. This trend is due to

(CC) 2026 Serbian Chemical Society.

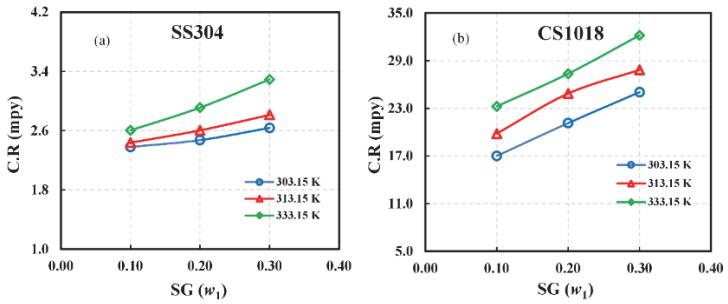

Fig. 4. Effect of concentration on the corrosion rate of: a) SS304 and b) CS1018 in aqueous SG solutions at various temperatures.

the fact that when the concentration increases, the absolute amount of CO_2 absorbed increases, which results in a higher number of bicarbonate ions and protonated amines. The increasing number of bicarbonates and protonated amines causes a greater rate of iron dissolution and hence increases the corrosion rate. Moreover, a higher concentration also increases the ionic strength and electrical conductivity, thus facilitating the charge transfer and increasing the iron dissolution. Additionally, the increased concentration of amino acid salts helps to form metal–amino acid complexes. The formation of these complexes restricts the development of protective layers on the metal surface, thereby exposing the metal to the reacting species and increasing corrosion.[26,27] The same trend has been observed in the literature for various amines.[20,24] Moreover, the effect of concentration on the corrosion rate of SS304 is much lower than that on CS1018. This may be due to the fact that SS304 is significantly less susceptible to corrosion than CS1018. However, the trend still shows an increasing tendency similar to that observed for CS1018. On further analyzing the results, it was observed that at a fixed temperature (303.15 K), the corrosion rate of SS304 in aqueous SG solution increased from 2.379 to 2.636 mpy (10.80 % increase) when the concentration was increased from 0.10 to 0.30 mass fraction. However, the effect of concentration on the corrosion of CS1018 in SG solution is significantly higher than that observed for SS304. At a fixed temperature (303.15 K), an increase of about 47.26 % in the corrosion rate of CS1018 in aqueous SG solution was observed when increasing the concentration from 0.10 to 0.30 mass fraction. From the above facts, it is quite apparent that corrosion rate of CS1018 is largely influenced by the concentration of aqueous SG solutions. On average, the corrosion rate increased by almost 40 % when the concentration increased from 0.10 to 0.30 mass fraction. These results suggest that SS304 is corrosion resistant even at high concentrations, while CS1018 is significantly susceptible to corrosion at high SG concentrations. These results could significantly aid the selection of appropriate materials of construction for CO_2 capture plants. Moreover, the results also provide significant guidance for selecting

(CC) 2026 Serbian Chemical Society.

the appropriate solvent concentration for the CO_2 capture process, so that the corrosion problem could be minimized.

Effect of the type of metal on corrosion rate

The appropriate material selection for a CO_2 absorption column is essential because it affects the capital and operational costs of the CO_2 capture process.[28] In general, two types of metals, SS304 and CS1018, are widely used for the fabrication of CO_2 capture plants.[1,2,4] For every new solvent, it is very important to investigate the corrosion rate of these two materials in the new solvent prior to solvent selection.[29] Therefore, in this study, the corrosion rate of SS304 and CS1018 in aqueous solutions of SG was investigated at three different temperatures (303.15, 313.15 and 333.15 K) and at various concentrations. The comparison of corrosion rate data of SS304 and CS1018 at various temperatures and concentrations is presented in Fig. 5 for aqueous SG solutions.

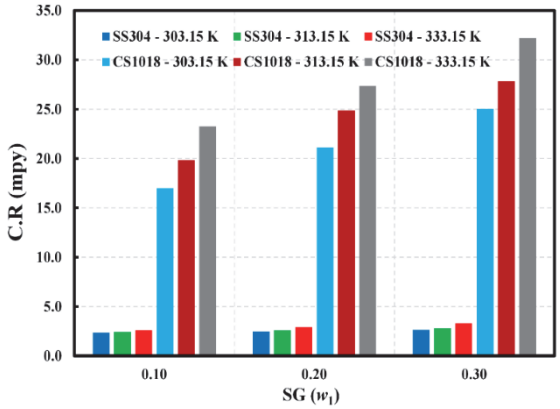

Fig. 5. Comparison of the corrosion rates of SS304 and CS1018 in aqueous SG solutions at various temperatures.

From the analysis of the data, it was found that SS304 is significantly less susceptible to corrosion than CS1018, as is evident from Fig. 5, at various temperatures and concentrations. The highest corrosion rate of SS304 at the highest temperature (333.15 K) and the highest concentration (0.30 mass fraction) was 3.291 mpy in aqueous SG solutions. This corrosion rate of SS304 is considered negligible.[24] In other words, it can be said that the corrosion rate of SS304 in aqueous solutions of SG is negligible and can be neglected. This evidence suggests that SS304 is a highly corrosion-resistant material in aqueous SG solutions. On the other hand, CS1018 is more susceptible to corrosion than SS304. Moreover, the highest corrosion rate of CS1018 at the highest temperature (333.15 K) and the highest concentration (0.30 mass fraction) was 32.203 mpy in aqueous SG solutions. Based on this comparative analysis of the two metals, SS304 can be a better

(CC) 2026 Serbian Chemical Society.

material for the construction and fabrication of a CO_2 absorption plant than CS1018.[30,31]

The higher corrosion resistance of SS304 can be attributed to the fact that under the test conditions of this study, SS304 did not significantly undergo active dissolution process, whereas CS1018 was in the active dissolution state. Alloys such as SS304 can easily form passive films (chromium oxide), which provide corrosion protection.[24] Initially, during the immersion of corrosion coupon specimens in the test solutions, these specimens were clean and film-free and exposing these fresh test specimens with more anodic and cathodic sites to the aqueous SG solution favored the corrosion process.[24] Since the passive film layer on the SS304 surface forms more readily, no severe dissolution occurred even after long immersion time. The formation of passive films suppressed the iron dissolution process, thereby reducing the corrosion rate.[32–34] In the case of CS1018, the active dissolution process continued for some time, and passive films did not form readily, resulting in greater dissolution and a higher corrosion rate of CS1018. This suggests that passive film formation plays a crucial role in corrosion protection.[32,34,35] In this study, passive films on CS1018 did not form; therefore, a higher corrosion rate was observed for CS1018. Similar trends in the corrosion behavior of SS304 and CS1018 in aqueous amine solvents have been observed and reported elsewhere.[17,18] The above findings indicate that SS304 is the superior and preferred material of construction for the fabrication of CO_2 capture plant and accessories compared with CS1018.

Comparison of corrosion rate of the solvents

The corrosion rates of various solvents studied in this work are compared in terms of their performance in corrosion protection. It is crucial to analyze and compare the corrosion tendency of various solvents to be used for CO_2 capture. Since an alloy like SS304 is considered slightly corrosive, the comparison is only made for the corrosion rate of CS1018 in solvents such as SG, MEA, MDEA and DEA. Moreover, since the data on the corrosion rate of CS1018 in amine solvents are also very scarce and scattered, a possible comparison of the corrosion rate in the solvents studied in this work is made with amine solvents at 313.15 K. Fig. 6 shows the comparison of corrosion rates among various solvents. The concentration of the solvents expressed as a mass fraction. From Fig. 6, it is apparent that the solution of SG is less corrosive than amine-based solvents. Among the amines, DEA has lower corrosion rate than other amines, however, it is still higher than that of amino acid salts. Aqueous SG solution has a lower corrosion rate than MEA and DEA. From the above observations, the corrosion rate of the solvents shown in Fig. 6. follows the order MDEA > MEA > DEA > SG. These results suggest that aqueous amino acid salts could potentially be used for CO_2 capture from various gas streams. The comparative analysis of the corrosion data of different solvents will

(CC) 2026 Serbian Chemical Society.

design engineers and corrosion consultants in the selection of an appropriate material of construction for the fabrication of a CO_2 absorption plant and accessories.

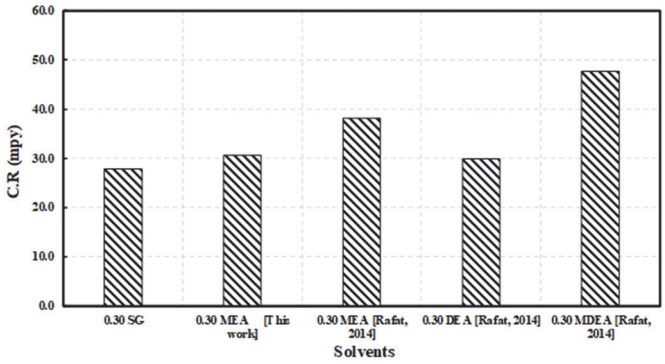

Fig. 6. Comparison of corrosion rates of different solvents at 313.15 K.

CONCLUSION

The corrosion study of two metals, SS304 and CS1018, in aqueous SG solutions was carried out at different temperatures (303.15 K, 313.15 K and 333.15 K) and concentrations (0.10, 0.20 and 0.30 mass fractions). The measured corrosion rates of SS304 and CS1018 in aqueous SG solutions showed an increasing trend with increasing temperature and concentration. The effect of temperature on the corrosion rate of SS304 was marginal; however, this effect was significant for CS1018. Similar to the temperature effect, the concentration effect on SS304 was also trivial, but significant in the case of CS1018. The corrosion rate data of aqueous SG solutions were correlated by an Arrhenius type equation, and good agreement was found between the predicted and experimental data, as shown by low values of the estimated standard deviation (*SD*). Therefore, the Arrhenius type correlation can be used for the prediction of the corrosion rate of SS304 and CS1018 in various solvents. Moreover, it is worth mentioning that SS304 much less susceptible to corrosion; hence, SS304 can be considered non-corrosive. However, CS1018 was considerably more susceptible to corrosion in the studied solvents. The corrosion rates of various solvents were compared and followed the order MDEA > MEA > > DEA > SG. Overall, solvents studied in this work showed a lower corrosion rate than the amine solvents. Therefore, these solvents could potentially be used for commercial applications in CO_2 removal. Additionally, the corrosion rate data obtained in this study can be used for the appropriate selection of solvents for CO_2 capture, and materials of construction for the fabrication of a CO_2 absorption plant and accessories. An additional notable contribution of the present work is the investigation of the corrosion rate of metals in aqueous SG solution using SS304 and CS1018 at various temperatures. This provides a large corrosion database, which would help design engineers and corrosion consultants in the selection of

(CC) 2026 Serbian Chemical Society.

an appropriate material of construction for the fabrication of a CO_2 absorption plant and accessories. Moreover, the reported experimental data on the corrosion rate will also guide the selection of an appropriate solvent for CO_2 capture.

Acknowledgement. This manuscript is derived from the first author's PhD thesis. The authors are thankful to the CO2 Research Centre (CO2RES), Universiti Teknologi PETRONAS, Malaysia, for technical support in completing the present research work.

ИЗВОД

СТУДИЈЕ КОРОЗИЈЕ НЕРЂАЈУЋЕГ ЧЕЛИКА И УГЉЕНИЧНОГ ЧЕЛИКА У ВОДЕНИМ РАСТВОРИМА НАТРИЈУМ-ГЛИЦИНАТА КОЈИ СЕ КОРИСТЕ ЗА ВЕЗИВАЊЕ CO_2

MUHAMMAD SHUAIB SHAIKH[1], AZMI MOHD SHARIFF[2,3], INAMULLAH BHATTI[1], ABDUL QADEER LAGHARI[1], ABDUL SATTAR JATOI[4], ARSHAD IQBAL[4], GHULAM MUSTAFA MEMON[5] и TANWEER HUSSAIN[6]

[1]Department of Chemical Engineering, Mehran University of Engineering and Technology, Jamshoro,76062, Sindh, Pakistan, [2]CO2 Research Centre (CO2RES), Universiti Teknologi PETRONAS, Bandar Seri Iskandar 32610, Perak, Malaysia, [3]Advance Safety Management Services Sdn. BHD, 50450 Kuala Lumpur, Malaysia, [4]Chemical Engineering Department, Dawood University of Engineering and Technology, Karachi, 74800, Sindh, Pakistan, [5]IRC for Industrial Nuclear Energy, King Fahd University of Petroleum & Minerals, Saudi Arabia u [6]Department of Mecheniccal Engineering, Mehran University of Engineering and Technology, Jamshoro,76062, Sindh, Pakistan

Корозија је добро познат и озбиљан проблем у процесу апсорпције угљен-диоксида (CO_2), што узрокује огромне трошкове одржавања за санацију кородиране опреме и цевовода. Водени раствор натријум-глицината (SG) је потенцијални растварач за хватање CO_2. Студија корозије SG растварача је веома важна за његову практичну примену, јер су такви подаци веома ограничени у доступној литератури. Стога, да би се решио овај значајан јаз, у овој студији су испитане брзине корозије нерђајућег челика (SS-304) и угљеничног челика (CS-1018) применом методе губитка тежине коришћењем SG растварача на три различите температуре (303,15, 313,15 и 333,15 K) и концентрације од индустријског значаја (масени удео од 0,10, 0,20 и 0,30). Резултати су показали да је SS304 показао занемарљиву корозију у НГ растварачу са маргиналним утицајем температуре и концентрације. Међутим, значајан утицај температуре и концентрације је примећен на брзину корозије CS1018 у SG растварачу. На највишој проучаваној температури од 333,15 K и високој концентрацији (0,30 масени удео), брзина корозије SS304 и CS1018 у SG растварачу је 3,291 и 32,203 mpy, редом. Штавише, брзина корозије CS1018 у SG растварачу је упоређена са метилдиетаноламином (MDEA), моноетаноламином (MEA) и диетаноламином (DEA). Утврђено је да SG растварач показује мању корозивност од различитих аминских растварача. Резултати ове студије пружају смернице за практичну примену SG растварача у процесу хватања CO_2. Такође, добијени подаци би могли значајно помоћи инжењерима пројектантима да успоставе одговарајуће радне услове процеса хватања CO_2 како би се контролисала корозија.

(примљено 16. маја, ревидирано 19. јуна, прихваћено 2. августа 2026)

REFERENCES

1. S. Ahn, H.-J. Song, J.-W. Park, J. H. Lee, I. Y. Lee, K.-R. Jang, *Korean J. Chem. Eng.* **27** (2010) 1576 (https://doi.org/10.1007/s11814-010-0246-z)
2. K. M. DuPart, T. Bacon, D. Edwards, *Hydrocarb. Process.* **72** (1993) 75 (https://www.osti.gov/biblio/6824217)

(CC) 2026 Serbian Chemical Society.

3. A. Veawab, P. Tontiwachwuthikul, S. D. Bhole, *Ind. Eng. Chem. Res*. **36** (1997) 264 (https://doi.org/10.1021/ie9504563)
4. A. Veawab, P. Tontiwachwuthikul, A. Chakma, *Ind. Eng. Chem. Res*. **38** (1999) 3917 (https://doi.org/10.1021/ie9901630)
5. A. M. Shariff, M. S. Shaikh, in *Energy Efficient Solvents for CO_2 Capture by Gas-Liquid Absorption: Compounds, Blends and Advanced Solvent Systems*, W. M. Budzianowski, Ed., Springer International Publishing, Cham, 2017, p. 117 (https://doi.org/10.1007/978-3-319-47262-1_6)
6. M. S. Shaikh, A. M. Shariff, M. A. Bustam, G. Murshid, *Chinese J. Chem. Eng*. **23** (2015) 536 (https://doi.org/10.1016/j.cjche.2013.11.001)
7. J.-G. Lu, F. Fan, C. Liu, H. Zhang, Y. Ji, M.-d. Chen, *J. Chem. Eng. Data* **56** (2011) 2706 (https://doi.org/10.1021/je101192x)
8. B. El Ibrahimi, E. Berdimurodov, in *Electrochemical and Analytical Techniques for Sustainable Corrosion Monitoring*, J. Aslam, C. Verma, C. M. Hussain, Eds., Elsevier, Amsterdam, 2023, p. 81 (https://doi.org/10.1016/B978-0-443-15783-7.00011-6)
9. M. E. Majchrowicz, S. Kersten, W. Brilman, *Ind. Eng. Chem. Res.* **53** (2014) 11460 (https://doi.org/10.1021/ie501083v)
10. ASTM, *Standard Practice for Preparing, Cleaning, Evaluation Corrosion Test Specimens*, in *ASTM G1-**90***, 1999 (15-21)
11. R. Babonian, Corrosion Tests and Standards: Applications and Interpretaions, 2nd ed., ASTM International, West Conshohocken, PA, 2005
12. *Standard practice for laboratory immersion corrosion testing of metals*, ASTM International, West Conshohocken, PA, 2004
13. S. Papavinasam, R. W. Revie, M. Attard, A. Demoz, H. Sun, J. C. Donini, K. Michaelian, in *Proceedings of the CORROSION 2000*, Orlando, FL, 2000, pp. 1–30 AMPP(https://doi.org/10.5006/C2000-00055)
14. W. L. Mathay, R. B. Hoxeng, *Corros.* **12** (1956) 72 (https://doi.org/10.5006/0010-9312-12.11)
15. Y. Ga-Er, Y-Wei Yang, Z Yang, D. Attwood, C. Booth, V. Mark Nace, *Langmuir* **12** (1996) 3404 (https://doi.org/10.1021/la9509108)
16. P. Munn, *Corr. Sci*. **35** (1993) 1495 (https://doi.org/10.1016/0010-938X(93)90377-S)
17. S. A. Mazari, B. Si Ali, B. M. Jan, I. M. Saeed, S. Nizamuddin, *Int. J. Greenhouse Gas Control* **34** (2015) 129 (https://doi.org/10.1016/j.ijggc.2014.12.017
18. G. T. Rochelle, *Science* **325** (2009) 1652 (https://doi.org/10.1126/science.1176731)
19. Q. Li, D. Wang, M. Zhao, M. Yang, J. Tang, K. Zhou, *Process. Saf. Environ. Prot.* **147** (2021) 300 (https://doi.org/10.1016/j.psep.2020.08.035)
20. A. Rafat, M. Atilhan, R. Kahraman, *Ind. Eng. Chem. Res.* **55** *(*2016) 446 (https://doi.org//10.1021/acs.iecr.5b01794)
21. K. M. Emran, I. M. A. Omar, S. T. *Arab*. *Sci. Rep.* **12** (2022) 6432 (https://doi.org/10.1038/s41598-022-10462-y
22. R. Felix-Contreras, J. de la Vega Olivas, C. D. Arrieta-Gonzalez. *Materials* **17** (2024) 5776 (https://doi.org/10.3390/ma17235776
23. S. M. Mouneir, A. M. El-Shamy, *Multiscale Multidis. Model Exp. Des.* **9** (2026) 131 (https://doi.org/10.1007/s41939-026-01185-y
24. L. Xiao, S. Liu, H. Gao, H. Liao, Paitoon, T. Z. Liang, *Sep. Purif. Technol.* **169** (2016) 279 (https://doi.org/10.1016/j.seppur.2016.06.018)

(CC) 2026 Serbian Chemical Society.

25. M. Hasib-ur-Rahman, H. Bouteldja, P. Fongarland, M. Siaj, F.c.a. Larachi, *Ind. Eng. Chem. Res.* **51** (2012) 8711 (https://doi.org/10.1021/ie2019849)
26. A. Momeni, R. V. McQuillan, M. S. Alivand, A. Zavabeti, G. W. Stevens, K. A. Mumford, *Chem. Eng. J.* **480** (2024) 147934 (https://doi.org/10.1016/j.cej.2023.147934)
27. A. Kiani, W. Conway, M. H. Abdellah, G. Puxty, A.-J. Minor, G. Kluivers, R. Bennett, P. Feron, *Greenhouse Gas Sci. Technol.* **14** (2024) 859 (https://doi.org/10.1002/ghg.2302)
28. S. Ó. Garðarsdóttir, F. Normann, R. Skagestad, F. Johnsson, *Int. J. Greenhouse Gas Control* **76** (2018) 111 (https://doi.org/10.1016/j.ijggc.2018.06.022)
29. Y. Wang, Y., M. Fang, J. Gao, C. Li, Y. Huang, L. Yang, S. Li, X. Hu, T. Wang, *Int. J. Greenhouse Gas Control* **136** (2024) 104186 (https://doi.org/10.1016/j.ijggc.2024.104186)
30. R. E. Tataru-Farmus, M. Harja, L. Tonucci, F. Coccia, M. Ciulla, L. Lazar, G. Soreanu, I. Cretescu, *Clean Technol*. **7** (2025) 99 (https://doi.org/10.3390/cleantechnol7040099)
31. P. Zhang, Y. Gao, Y. Zhao, B. Gao, X. Ding, R. Wang, Y. Yang, J. Wang, K. Zhao, D. Fu, L. Wang, *Sep. Purif. Technol.* **362** (2025) 131674 (https://doi.org/10.1016/j.seppur.2025.131674)
32. Y. Hong, D. D. Dong, G. P. Zou, Y. Li, S. S. Lin, T. C. Kuang, Y. Z. Wu, M. J. Dai, *Corros. Sci.* **218** (2023) 111188 (https://doi.org/10.1016/j.corsci.2023.111188)
33. Z. Dong, C. Fu, B. Dong, X. R. Nóvoa, U. Angst, *Electrochim. Acta* **518** (2025) 146996 (https://doi.org/10.1016/j.electacta.2025.146996)
34. Y. Feng, J. Chen, J. Luo, *Resour. Policy* **92** (2024) 104996 (https://doi.org/10.1016/j.resourpol.2024.104996)
35. Q. Zhou, Z. Liu, X. Wang, Y. Li, X. Qin, L. Guo, L. Zhou, W. Xu, *J. Energy Chem.* **89** (2024) 336 (https://doi.org/10.1016/j.jechem.2023.10.035).

(CC) 2026 Serbian Chemical Society.

Journal of the Serbian Chemical Society
JSCS-info@shd.org.rs • www.shd.org.rs/JSCS
J. Serb. Chem. Soc. *91* (10) 1099–1111 (2026)
JSCS–5546
Original scientific paper
Published 16 November, 2026

Adsorption–desorption behaviour of clomazone in Planosol and Vertisol agricultural soils

RADA D. ĐUROVIĆ-PEJČEV[1]*, LJILJANA R. ŠANTRIĆ[1], LAZAR M. KALUĐEROVIĆ[2] and SVJETLANA B. RADMANOVIĆ[2]

[1]*Institute of Pesticides and Environmental Protection, Banatska 31b, 11080 Belgrade, Serbia and* [2]*University of Belgrade, Faculty of Agriculture, Nemanjina 6, 11080 Belgrade, Serbia*

(Received 22 January, revised 13 March, accepted 18 August 2026)

Abstract: Understanding of the processes that affect soil herbicide behaviour enables the prediction of their fate in the environment. Soil–herbicide interactions are governed by adsorption–desorption processes as only the free herbicide fraction participates in all other processes occurring in or on the soil. Given the agricultural and environmental significance of clomazone, its adsorption–desorption behaviour was investigated in two widely distributed Serbian agricultural soil types, Planosol and Vertisol. Both processes were well-described by Freundlich isotherms, and the obtained sorption parameters show that clomazone sorbed to both organic matter and mineral soil components. Vertisol, characterized by higher organic matter and clay content, demonstrated greater sorption capacities (3.67–21,23 $mg^{(n-1)/n}$ $dm^{3/n}$ kg^{-1} for 1.5–15 mg dm^{-3}) and lower desorption rates (the amounts desorbed of 29.49–28.48 % during 72 h for 1.5–15 mg dm^{-3}) compared to Planosol (3.15–18.35 $mg^{(n-1)/n}$ $dm^{3/n}$ kg^{-1} and 33.32–29.97 % for 1.5––15 mg dm^{-3}). The more pronounced desorption hysteresis observed in Vertisol is likely attributable to the presence of a higher number of high-energy sorption sites compared to Planosol. These findings highlight the crucial role of soil composition in determining the environmental fate of clomazone, providing a valuable basis for developing agronomically effective and environmentally safe application recommendations.

Keywords: pesticides; sorption; soil; Freundlich modelling.

INTRODUCTION

Chemical weed control is essential for large-scale agriculture, but given the manner and amount of herbicide application, soil contamination is a central concern. The retention time of herbicides in soil depends on many factors, including especially the soil's sorption capacity, fluid flow dynamics and the solute transport

* Corresponding author. E-mail: rada.djurovic@pesting.org.rs
https://doi.org/10.2298/JSC260122050D

Available online at https://www.shd.org.rs/JSCS/
(CC) 2026 Serbian Chemical Society.

in addition to degradation rates. Understanding the processes that herbicide molecules undergo after contact with soil is crucial for predicting herbicide efficacy and the fate of these agrochemicals in the environment.[1]

Soil–herbicide interactions after the herbicide is found in the soil and/or soil solution are driven by sorption processes (sorption/desorption) of this compound, since all detoxification mechanisms, such as mobility, degradation (primarily microbiological) and plant uptake, relate only to the free (unsorbed) fraction of the molecules.[2] Knowledge of sorption constants (K_d, K_{OC}, K_{OM}) and sorption isotherms (described by the Freundlich coefficients K_f and n_f) enables assessment of the mobility of pesticide molecules in the environment, especially their potential to enter groundwater.

In general, herbicides of concern for aquatic systems are those with water solubility ≥ 30 mg dm^{-3}, a sorption coefficient (K_d) < 5 dm^3 kg^{-1} or a sorption coefficient normalized to organic carbon content (K_{OC}) in the range of 300–500 dm^3 kg^{-1}, a hydrolytic half-life ($t_{1/2}$) > 6 months, a photolytic half-life ($t_{1/2}$) > 3 days, and/or a microbiological degradation half-life ($t_{1/2}$) > 2–3 weeks.[3–5] Clomazone (IUPAC: 2-(2-chlorobenzyl)-4,4-dimethyl-1,2-oxazolidin-3-one), an isoxazolidinone herbicide, is a good example of such a herbicide.

Clomazone is a nonionic herbicide with relatively high water solubility (1100 mg dm^{-3}), moderate mobility (K_{OC}: 150–562 dm^3 kg^{-1}) and persistence in soil (DT_{50}: 30–135 days), and moderate resistance to photolytic degradation ($t_{1/2}$: > 30 days).[6] These properties, along with the potentially harmful effects this compound may have on cultivated plants after crop rotation,[7] make clomazone a possible environmental contaminant of agricultural relevance.

Literature data indicate that clomazone sorption in soil occurs either through organic matter (OM)[8–13] or through both OM and soil clay.[14] López-Piñeiro *et al.*[15] found that clomazone sorption to soil increased with increasing soil acidity, while Gunasekara *et al.*[10] and Xu *et al.*[16] reported that soils with a history of fire events tend to have higher clomazone retention. Some studies indicate that clomazone sorption to soil decreases as herbicide concentration increasing,[10,17,18] while some authors found that OM contained in various biochars used as soil amendments significantly increases clomazone sorption.[12,15,16,19–23] The desorption of pesticides is also an important process, as it affects the amount of pesticide released from the soil to the soil solution and can further contribute to the processes of mobility, degradation and plant uptake, thereby determining the activity of the compound in the environment. However, with the exception of our earlier study on clomazone desorption from Regosol and Chernozem soils,[9] to our knowledge, there are only a few papers addressing clomazone desorption from soil.[10,12,15,20] All of these studies have been conducted in rice production and flooded conditions, where clomazone may pose a particular environmental risk due to its relatively high solubility in water. Considering that these studies, as well as all other previously

(CC) 2026 Serbian Chemical Society.

referenced papers, have examined clomazone adsorption behaviour in waterlogged soils, it is clear that further research is needed on the adsorption/desorption behaviour of this herbicide in agricultural soils.

As previously mentioned, our previous study[9] included Chernozem and Regosol, both developed under terrestrial environmental conditions without water excess. These alkaline, loam soils differed in humus content and clay mineralogy. The present study extends to Vertisols and Planosols[24] which are also widespread in crop production, predominantly occurring on level plains and covering 335 and 130 million ha worldwide[25] and approximately 700,000 and 400,000 ha in Serbia, respectively.[26] Natural Vertisols and Planosols are characterised by a challenging water regime, where water excess and moisture stress alternate according to distinct wet and dry seasons. Vertisols are heavy soils, with a high proportion of swelling clays that cause a difficult water regime but also confer high chemical fertility. The waterlogging problem in Planosols can be mitigated by tillage practices in agricultural crop production.[25] Compared to the alkaline Chernozem and Regosol, investigated Vertisols and Planosols are acidic. Considering all the above mentioned, the aim of this study was to determine the adsorption/desorption behaviour of clomazone in Planosol and Vertisol,[24] two Serbian widespread soils used in crop production that may have problematic water regimes. The main objective was to establish whether or not, and to what extent, the amount of OM and clay in these soils influence the retention and release of clomazone, as well as to assess the extent to which different clomazone concentrations affect its adsorption/desorption behaviour.

EXPERIMENTAL

Reagents and materials

Analytical standard of clomazone (99.5 % purity) was supplied by Dr. Ehrenstorfer, Germany. Its stock solution (1.5 g dm^{-3}) was prepared in acetonitrile (J. T. Baker, Holland) and stored at –18 °C until further use.

Calcium chloride was purchased from Merck (Germany), and highly purified deionized water (Purelab Option – R7, Elga, UK) was used for preparation of 0.01 M $CaCl_2$ solution.

Working standard solutions of clomazone (0.5, 1.5, 3, 6, 9, 12 and 15 mg dm^{-3}) were prepared by diluting its stock solution with 0.01 M $CaCl_2$ solution.

Samples of two agricultural soils, Planosol and Vertisol, were collected in October 2022 from the top 25 cm soil layer in fields where soybean had been grown that year. Planosol was sampled in Varna (44°41′N, 19°38′E; 110 m a.s.l.), and Vertisol in Umka (44°39′N, 20°17′E; 111 m a.s.l)). Clomazone had not been applied to these fields for at least 3 years prior to sampling. Soil samples were air-dried and sieved (2 mm mesh), and subsequently characterized by standard methods: soil texture by combining the sieving and pipette methods, using 0.1 M sodium pyrophosphate as a dispersing agent; organic carbon (OC) by the dichromate method; soil pH by the potentiometric method (soil/water, 1/2.5);[27] the soil textural class according to the USDA triangle[28] (Table I).

Planosol is a clay loam, strongly acidic, with low OC, and clay composed mainly of illite, with a small amount of smectite and chlorite. Vertisol is a clay, moderately acidic, with moderate

(CC) 2026 Serbian Chemical Society.

OC, and clay consisting mainly of smectite, but also containing illite and kaolinite. Mineralogical composition of the clay fraction was determined previously by XRD analysis and reported elsewhere.[29] Clay mineral composition was determined by X-ray diffraction (XRD) analysis of the clay fraction (<2 μm), following standard oriented aggregate preparation procedures including, ethylene glycol saturation and heating treatments.[30]

TABLE I. General soil properties

Soil	pH (H_2O)	Content of soil components, %			
		OC	Sand	Silt	Clay
Planosol	5.20	1.28	24.7	39.8	35.5
Vertisol	6.08	1.91	20.7	34.1	45.2

Sorption experiments

Adsorption/desorption isotherms of clomazone were obtained using the batch equilibration method.[31] Duplicate 2 g soil samples were mixed with 10 cm^3 of 0.01 M $CaCl_2$ solution with initial clomazone concentrations ranging from 0.5 to 15 mg dm^{-3} in 50 cm^3 polypropylene centrifuge tubes. Samples were equilibrated by shaking at 20±1 °C on a rotary shaker during 24 h. Although our previous research showed that apparent equilibrium was reached within 8 h in Planosol and 6 h in Vertisol).[18] The suspensions were then centrifuged at 3000 rpm for 5 min, and the resulting supernatants were filtered through 0.22 μm membranes before further analysis. The amounts of clomazone adsorbed by the soils were calculated from the difference between the initial and supernatant concentrations in each sample.

For initial clomazone concentrations of 1.5, 6 and 15 mg dm^{-3}, desorption studies were conducted immediately after the adsorption process was completed, by replacing 5 cm^3 of the obtained supernatants with 5 cm^3 of clomazone-free 0.01 M $CaCl_2$ solution. The tubes were equilibrated for an additional 24 h on the rotary shaker, followed by centrifugation at 3000 rpm for 5 min, filtration of the obtained supernatants and chromatographic analysis. For all concentrations, three successive desorption steps were examined.

All sorption and desorption measurements were performed in triplicate.

Chromatographic analysis

Quantification of clomazone in the obtained adsorption/desorption supernatants was performed using the Shimadzu Prominence high performance liquid chromatography (HPLC) system, equipped with a pump model LC-20AD and diode array detector (DAD), model SPD--M20A. The following conditions were used: Eclipse XDB-C18 column (4.6 mm×150 mm, 3.5 μm), acetonitrile/water (70:30 by volume) as the mobile phase at 1.0 cm^3 min^{-1} the flow rate, 40 mm^3 injection volume, and quantification at 214 nm. The detection and quantification limits were 0.0009 and 0.003 mg dm^{-3}, respectively.

Data analysis

Adsorption/desorption coefficients (K_d / dm^3 kg^{-1}) were calculated as the ratio of the clomazone concentration in soil after completion of the adsorption/desorption experiments (c_s / mg kg^{-1}) and equilibrium concentration in the solution (c_e / mg dm^{-3}) according to:

$$K_d = \frac{c_s}{c_e} \quad (1)$$

The K_{OC} coefficients were calculated by normalizing K_d coefficients to the soil OC contents according to equation:

(CC) 2026 Serbian Chemical Society.

$$K_{OC} = \frac{100K_d}{\text{Content of OC}} \quad (2)$$

Adsorption/desorption isotherms were fitted using the Freundlich equation:

$$c_s = K_f c_e^{1/n_f} \quad (3)$$

and the Freundlich constants K_f and n_f were calculated from the linear form of the Eq. (3):

$$\log c_s = \log K_f + \frac{1}{n} \log c_e \quad (4)$$

The desorption percentage (D) for all desorption steps was calculated as:

$$D = 100 \frac{c_{s(ads)} - c_{s(des,1)}}{c_{s(ads)}} \quad (5)$$

$$D = 100 \frac{c_{s(des,i)} - c_{s(des,i+1)}}{c_{s(des,i)}} \quad (6)$$

where $c_{s(ads)}$ and $c_{s(des,i)}$ are the clomazone concentrations in the soil after the completion of adsorption and desorption steps, respectively, and i is the number of desorption steps (i = 1,2,3).

The hysteresis coefficients (H) were calculated for the adsorption/desorption isotherms according to:

$$H = \frac{1/n_{des}}{1/n_{ads}} \quad (7)$$

where $1/n_{ads}$ and $1/n_{des}$ are the Freundlich slopes obtained for the adsorption and desorption isotherms, respectively.

RESULTS AND DISCUSSION

Clomazone adsorption studies

In order to compare the experimental results with previously published ones for Chernozem and Regosol. Clomazone adsorption/desorption isotherms for the two agricultural soils studied are shown in Fig. 1. Distribution coefficients and Freundlich parameters obtained for clomazone adsorption are presented in Table II.

As Table II shows, clomazone adsorption behaviour is well described by the Freundlich model with correlation coefficients (r^2) of 0.999 and 0.998 for Planosol and Vertisol soils, respectively. According to the Giles classification,[32] the obtained isotherms (Fig. 1) are C-type, indicating that their slopes are independent of the initial clomazone concentration in the solution. This is further confirmed by the $1/n_{(ads)}$ parameters with values close to 1 for both soils studied (Table II). The same type of isotherms was obtained for Regosol and Chernozem, two other widespread Serbian soils used in crop production,[9] which indicates constant partition of clomazone molecules between all the studied soils and soil solutions.

(CC) 2026 Serbian Chemical Society.

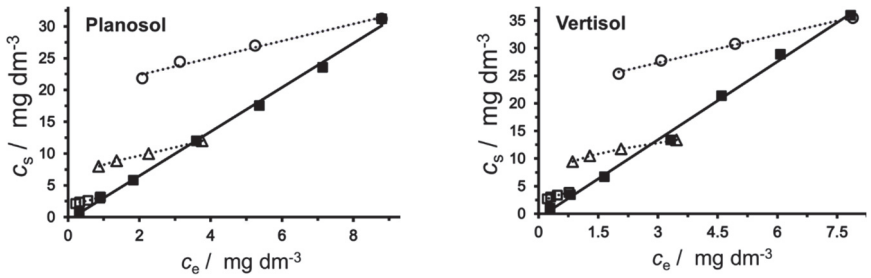

Fig. 1. Adsorption/desorption isotherms of clomazone in two Serbian agricultural soils: ■) adsorption; □) desorption for 1.5 mg dm^{-3}; Δ) desorption for 6 mg dm^{-3}; ○) desorption for 15 mg dm^{-3}

TABLE II. Distribution coefficients and Freundlich parameters for clomazone adsorption on the soils; value in parentheses is the 95 % confidence interval

Parameter	Soil	
	Planosol	Vertisol
$K_{d(ads)}$ / dm^3 kg^{-1}	3.41 (±0.05)	4.59 (±0.08)
r^2	0.998	0.998
$K_{OC(ads)}$ / dm^3 kg^{-1}	266.40	240.30
$K_{f(ads)}$ / mg$^{(n-1)/n}$ dm$^{3/n}$ kg^{-1}	3.14 (±0.01)	4.05 (±0.01)
$1/n_{(ads)}$	1.04 (±0.01)	1.07 (±0.02)
r^2	0.999	0.998

Across the entire initial clomazone concentration range studied (0.5–15 mg dm^{-3}), adsorption in Vertisol was consistently higher than in Planosol (Fig. 1). This observation is further supported by the adsorption coefficients K_d and Freundlich adsorption constants $K_{f(ads)}$, which were higher for Vertisol than for Planosol (Table II). According to the universal hypothesis, organic matter is the dominant component involved in pesticide adsorption in soils where its content exceeds 5 %, while in soils with lower organic matter content, adsorption can occur on both the organic and inorganic fractions of the soil, primarily humic acids and clays.[33–35] Therefore, considering the higher OC and clay contents in Vertisol compared to Planosol (Table I), higher adsorption could be expected in Vertisol, as was experimentally confirmed by K_d and $K_{f(ads)}$. However, if we assume that OC is the dominant soil component involved in clomazone adsorption, the values of the $K_{OC(ads)}$ coefficients calculated for both soils should be very similar. Comparing the $K_{OC(ads)}$ constants presented in Table II, it is clear that clay also plays a role in clomazone adsorption in both tested soils. The lower $K_{OC(ads)}$ constant obtained for Vertisol, which based on the K_d and $K_{f(ads)}$ coefficients adsorbs clomazone more strongly than Planosol, is probably a consequence of partial coverage of organic matter, that is blocking of the active adsorption centres of organic matter by clay. Additionally, differences in soil mineral composition and texture may also influence the sorption process. Vertisols are rich in the clay fraction, dominated by

(CC) 2026 Serbian Chemical Society.

expansive smectite minerals that swell with increased moisture, whereas Planosols are clay loams with illite as the dominant clay mineral.[18] In general, clay minerals may contribute to clomazone retention through hydrogen bonding, dipole–dipole interactions, and surface adsorption on hydroxylated mineral surfaces. Although clomazone does not undergo cation exchange because it occurs predominantly as a neutral molecule, its polar functional groups can interact with exposed hydroxyl groups located on clay mineral edges and external surfaces.[36] Although raw smectite is not the most effective sorbent for clomazone, it still exhibits a higher sorption capacity than illite or kaolinite.[37] On other side, non-ionic herbicides such as clomazone can be adsorbed to organic matter by physical and chemical sorption mechanisms, including van der Waals forces, ligand exchange, and hydrogen bonding.[37] There are only a few experimental results on clomazone–OM component binding mechanisms. Loux *et al.*[37] indicated that hydrophobic bonding is one mechanism of clomazone adsorption on OM, based conclusions on mean K_{OC} values.

Linear and multiple regression analyses between selected soil properties and the distribution coefficients ($K_{d(ads)}$ and $K_{OC(ads)}$) as well as the Freundlich parameters ($K_{f(ads)}$ and $1/n_{(ads)}$) were conducted (Supplementary material to this paper, Tables S-I and S-II) based on data from this study and previously published source[9] using the Data Analysis Tool Pak in Microsoft Excel 2016.

A significant correlation ($p < 0.05$) was found only between the constant $K_{OC(ads)}$ and soil pH ($r = 0.997$, $p = 0.003$) (Table S-I), indicating that $K_{OC(ads)}$ decreases with increasing soil pH ($K_{OC(ads)} = -27.5418\text{pH} + 409.0384$). A decrease in clomazone sorption with increasing soil pH was reported by López-Piñeiro *et al.*[15] who studied the impacts of fresh and aged holm oak biochar on clomazone behaviour in rice cropping soils. A multiple correlation analysis between the sorption data and combinations of two soil parameters showed a significant correlation ($p < 0.05$) of $K_{OC(ads)}$ with both OC and sand contents, as well as with soil acidity and silt content (Table S-II). Therefore, these multiple correlation analyses provide linear predictive models for $K_{OC(ads)}$. Considering all multiple linear functions of sorption data that were significantly or relatively well correlated with combinations of soil properties (Table S-II), it is clear that in addition to the OC content and acidity of the tested soils, soil texture has a significant influence on clomazone adsorption. A similar conclusion was drawn in a kinetic study of clomazone sorption in four agricultural soils.[18]

By comparing our results with literature data, a relatively good agreement between adsorption coefficients $K_{d(ads)}$, $K_{OC(ads)}$ and $K_{f(ads)}$ can be found (Table S-III of the Supplementary material).[9,17–19] However, as the clomazone concentration ranges[8,10] and soil/soil solution ratios[8,10–12,14–16,20,23,37,38] used in other studies are often not uniform and differ from ours, some discrepancies between our results and those previously published are not surprising. For example, Gunasekara *et al.*[10], Xu *et al.*[16] and Pena *et al.*[19] obtained L-type isotherms, while the

(CC) 2026 Serbian Chemical Society.

reported $K_{d(ads)}$ and $K_{OC(ads)}$ coefficients were higher[10,14] or lower[11,12,15,20,21,23] than our findings. Similarly, previously reported $K_{f(ads)}$ values were higher[10,14] or lower[16,21,23] than those obtained in this study.

Clomazone desorption studies

Clomazone desorption isotherms for the two agricultural soils studied are presented in Fig. 1, while the Freundlich desorption parameters, hysteresis coefficients and desorption percentages obtained by applying Eqs. (4)–(7) to the experimental data are listed in Table III.

TABLE III. Freundlich parameters ($K_{f(des)}$ and $1/n_{(des)}$), hysteresis coefficients (H) and desorption percentages (D) for clomazone desorption in Planosol and Vertisol; value in parentheses is the 95 % confidence interval

Parameter	Planosol			Vertisol		
	Initial concentration, mg dm^{-3}					
	1.5	6	15	1.5	6	15
$K_{f(des)}$ mg$^{(n-1)/n}$ dm$^{3/n}$ kg^{-1}	3.15 (±0.01)	8.22 (±0.01)	18.35 (±0.01)	3.67 (±0.01)	9.82 (±0.00)	21.23 (±0.01)
$1/n_{(des)}$	0.27 (±0.03)	0.28 (±0.03)	0.24 (±0.01)	0.19 (±0.03)	0.25 (±0.00)	0.24 (±0.02)
r^2	0.965	0.973	0.992	0.933	0.999	0.987
H	0.261	0.266	0.232	0.176	0.237	0.228
D (I) / %	17.18	16.42	13.55	11.86	12.25	13.29
D (II) / %	9.06	11.45	9.49	10.25	10.72	9.88
D (III) / %	11.47	9.82	10.50	10.87	9.99	8.49
Total D (I–III), %	33.32	33.26	29.97	29.49	29.49	28.48

The data indicate that clomazone desorption behaviour is well described by Eq. (4) for all three initial concentration levels of clomazone, with r^2 ranging from 0.965 to 0.992, and 0.933 to 0.999 for Planosol and Vertisol, respectively.

By comparing the $1/n$ Freundlich parameters obtained for adsorption (Table II) and desorption (Table III), it can be concluded that $1/n_{(ads)}$ values are much higher than $1/n_{(des)}$, regardless of both the initial clomazone concentration and the soil types studied. This indicates that a significant amount of adsorbed clomazone is not easily desorbed and that desorption cannot be predicted on the basis of adsorption isotherms. It has also been reported previously that the sorption of clomazone to soil is not a reversible process.[9,10,15,20]

The calculated hysteresis coefficients (Eq. 7) range from 0.232–0.266 and 0.176–0.237 for Planosol and Vertisol, respectively (Table III), which are comparable with the values obtained for Regosol and Chernozem in our previous study.[9] However, these values were somewhat higher than those reported for clomazone adsorption-desorption behaviour in four American soils,[10] but given their different origins, types of land use, and management practices, this inconsistency was to be

(CC) 2026 Serbian Chemical Society.

expected. As shown in Table III, for each initial clomazone concentration in the study, the *H* value obtained for Planosol was higher than that for Vertisol, indicating that Vertisol, with its higher adsorption capacity (Table II), has a lower tendency to desorb clomazone. Considering that only the free fraction (unsorbed) of clomazone molecules can participate in detoxification mechanisms such as mobility, degradation (primarily microbiological) and uptake of pesticides by plants, *i.e.,* target organisms, it is obvious that there is a greater tendency for Planosol pollution, including a bigger potential for leaching, i.e. pollution of deeper soil layers and even groundwater.

The desorption percentages (*D* / %) for all three successive desorption steps, as well as the total percentage of clomazone desorbed calculated by Eqs. (5) and (6) are presented in Table III. As shown, regardless of soil type and initial clomazone concentration in the adsorption-desorption study, the amount desorbed decreases with each subsequent desorption step in most cases. These results confirm the hypothesis of bound residues, which states that only clomazone molecules weakly bound to soil can be easily desorbed. Considering the total amounts of clomazone desorbed during all three consecutive desorption cycles (*D* (I–III)) for both soils studied, it seems that these fractions are highly dependent on the initial clomazone concentration. For both soils, the decrease in *D* (I–III) values with increasing initial clomazone concentration in the soil-solution system, indicates that high-energy binding sites are limited, and become progressively saturated as the solute concentration increases. By comparing the *D* (I–III) values obtained for Planosol (33.32–29.97 %) and Vertisol (29.49–28.48 %), it can be stated that desorption is higher from Planosol regardless of the initial clomazone concentration. These results were expected, considering the higher adsorption capacity (Table II) of Vertisol compared to Planosol. The results obtained along with the possible water saturation of Planosols in some parts of the year, highlight the necessity for responsible clomazone application in this soil.

Comparison of our results with literature data (Table S-III) indicates good agreement of obtained $K_{f(des)}$, $n_{(des)}$ and *D* values with those obtained for Chernozem and Regosol soils.[9] However, Gámiz *et al.*[23] obtained $K_{f(des)}$ coefficient lower than our findings, Gámiz *et al.*[23] and Gunasekara *et al.*[10] reported lower $n_{(des)}$ values than those presented in this study, while *D* values obtained in this study are lower than those published by Vicente *et al.*[12], López-Piñeiro *et al.*[15] and Pena *et al.*[19] Considering that soil/soil solution ratios[12,15,19,23] and the clomazone concentration range[10] are not uniform and differ from ours, discrepancies between our results and those previously published are not surprising.

CONCLUSION

The study of the adsorption–desorption behaviour of clomazone in two widespread Serbian agricultural soil types showed that, in addition to organic matter

(CC) 2026 Serbian Chemical Society.

and clay as the main sorbing soil components, soil acidity and overall soil texture significantly influence the extent of this herbicide sorption. Regardless of soil type, the distribution of clomazone molecules between the soil and the soil solution is linear, and does not depend on the initial concentration of the herbicide in the system. Clomazone was found to adsorb more to Vertisol, which has a higher content of both organic matter and clay compared to Planosol. At the same time Vertisol showed a lower tendency to desorb herbicide molecules than Planosol. The greater hysteresis effect (lower H values) observed in Vertisol can be explained by the high-energy bonding hypothesis, which suggests that this soil contains more high-energy sorption sites than Planosol. Significant correlations established between the constant $K_{OC(ads)}$ and soil pH, as well as between the $K_{OC(ads)}$ and both OC and sand contents, soil acidity and silt content, provide predictive linear models for calculating the $K_{OC(ads)}$ constant based on soil characteristics. In order to provide more reliable models for predicting the adsorption/desorption behaviour of clomazone in agricultural soils, future studies must include a larger number of agricultural soil types in the type of research presented in this paper. These data are important for making reliable recommendations from both agronomic and environmental perspectives, especially for the protection of groundwater as a source of drinking water.

SUPPLEMENTARY MATERIAL

Additional data and information are available electronically at the pages of journal website: https://www.shd-pub.org.rs/index.php/JSCS/article/view/13741, or from the corresponding author on request.

Acknowledgement. The study was funded by the Ministry of Science, Technological Development and Innovation of the Republic of Serbia (grants 451-03-33/2026-03/200214 and 451-03-34/2026-03/200116).

ИЗВОД

АДСОРПЦИОНО–ДЕСОРПЦИОНО ПОНАШАЊЕ КЛОМАЗОНА У ПОЉОПРИВРЕДНОМ ЗЕМЉИШТИМА ПЛАНОСОЛ И ВЕРТИСОЛ

РАДА Д. ЂУРОВИЋ-ПЕЈЧЕВ[1], ЉИЉАНА Р. ШАНТРИЋ[1], ЛАЗАР М. КАЛУЂЕРОВИЋ[2] и СВЈЕТЛАНА Б. РАДМАНОВИЋ[2]

[1]Институт за пестициде и заштиту животне средине, Банатска 31б, 11080 Београд и [2]Пољопривредни факултет, Универзитет у Београду, Немањина 6, 11080 Београд

Познавање процеса који утичу на понашање хербицида у земљишту омогућава разумевање и предвиђање њихове судбине у животној средини. Интеракције земљиште–хербицид су вођене процесима адсорпције-десорпције, с обзиром на то да у свим осталим процесима који се одвијају у/на земљишту учествује само слободна фракција хербицида. С обзиром на пољопривредни и еколошки значај кломазона, његово адсорпционо–десорпционо понашање је проучавано у два широко распрострањена пољопривредна земљишта у Србији, Планосолу и Вертисолу. Оба процеса су добро описана Фројндлиховим изотермама, при чему добијени параметри сорпције указују да се кломазон везује и за органску материју и за минералне компоненте земљишта. Вертисол, који карактерише

(CC) 2026 Serbian Chemical Society.

већи садржај органске материје и глине, карактерише већи капацитет сорпције (3,67–21,23 $mg^{(n-1)/n}$ $dm^{3/n}$ kg^{-1} за 1,5–15 mg dm^{-3}) и нижи степен десорпције (десорбована количина од 29,49–28,48 % у току 72 h за 1,5–15 mg dm^{-3}) у односу на Планосол (3,15––18,35 $mg^{(n-1)/n}$ $dm^{3/n}$ kg^{-1} и 33,32–29,97 % за 1,5–15 mg dm^{-3}). Израженији десорпциони хистерезис добијен за Вертисол се може објаснити већим бројем високоенергетских сорпционих центара присутних у овом земљишту у односу на Планосол. Приказани резултати указују да судбина кломазона у животној средини у великој мери зависи од састава земљишта, при чему представљају и значајну основу за развој агрономски ефикасних и еколошки безбедних препорука за примену.

(Примљено 22. јануара, ревидирано 13. марта, прихваћено 18. августа 2026)

REFERENCES

1. Lj. Radivojević, S. Gašić, Lj. Šantrić, J. Gajić Umiljendić, D. Marisavljević, *J. Serb. Chem. Soc.* **77** (2012) 845 (https://doi.org/10.2298/JSC110825004R)
2. R. Đurović, *Pestic. Phytomed. (Belgrade)* **26** (2011) 9 (https://doi.org/10.2298/PIF1101009D)
3. S. Hatrík, J. Tekel, *J. Chromatogr., A* **733** (1996) 217 (https://doi.org/10.1016/0021-9673(95)00725-3)
4. R. Wintersteiger, B. Goger, H. Krautgartner, *J. Chromatogr., A* **846** (1999) 349 (https://doi.org/10.1016/S0021-9673(99)00429-X)
5. R. Zanella, E. G. Primel, F. F. Gonçalves, M. H. S. Kurz, C. M. Mistura, *J. Sep. Sci.* **26** (2003) 935 (https://doi.org/10.1002/jssc.200301309)
6. C. MacBean, *The Pesticide Manual, A World Compendium*, 14th ed., British Crop Protection Council, Hampshire, 2006 (ISBN: 1-901396-14-2)
7. A. Andres, G. Concenço, G. Theisen, F. Vidotto, A. Ferrero, *Crop Prot.* **53** (2013) 103 (https://doi.org/10.1016/j.cropro.2013.06.012)
8. H. A. Lins, M. de Freitas Souza, L. P. Batista, L. L. L. da Silva Rodrigues, F. D. da Silva, B. C. C. Fernandes, S. B. de Melo, P. S. F. das Chagas, D. V. Silva, *Smart Agric. Technol.* **9** (2024) 100699 (https://doi.org/10.1016/j.atech.2024.100699)
9. R. Đurović-Pejčev, S. Radmanović, Z. P. Tomić, L. Kaluđerović, V. Bursić, Lj. Šantrić, *J. Serb. Chem. Soc.* **85** (2020) 809 (https://doi.org/10.2298/JSC190917122D)
10. A. Gunasekara, I. Dela Cruz, M. Curtis, V. Claassen, R. Tjeerdema, *Pest. Manage. Sci.* **65** (2009) 711 (https://doi.org/10.1002/ps.1733)
11. K. Kirksey, R. Hayes, W. Krueger, C. Mullins, T. Mueller, *Weed Sci.* **44** (1996) 959 (https://www.jstor.org/stable/4045767)
12. L. A. Vicente, D. Peña, D. Fernández-Rodríguez, Á. Albarrán, J. M. R. Nunes, A. López--Piñeiro, *J. Environ. Manage.* **386** (2025) 125761 (https://doi.org/10.1016/j.jenvman.2025.125761)
13. M. Pereira, A. Rodrigues, V. Fonseca, D. J. Passos, M. Da Silva, V. Silva, A. Da Silva, *Biosci. J.* **34** (2018) 1496 (https://doi.org/10.14393/BJ-v34n6a2018-39492)
14. L. F. Li, G. X. Li, R. B. Yang, Z. Y. Guo, X. Y. Liao, *J. Environ. Sci.* **16** (2004) 678 (https://pubmed.ncbi.nlm.nih.gov/15495980/)
15. A. López-Piñeiro, J. Sánchez-Terrón, C. Martín-Franco, D. Peña, L. A. Vicente, S. Gómez, D. Fernández-Rodríguez, Á. Albarrán, *Geoderma* **413** (2022) 115768 (https://doi.org/10.1016/j.geoderma.2022.115768)
16. C. Xu, W. Liu, G. Sheng, *Sci. Total Environ.* **392** (2008) 284 (https://doi.org/10.1016/j.scitotenv.2007.11.033)

(CC) 2026 Serbian Chemical Society.

17. T. L. Mervosh, G. K. Sims, E. W. Stoller, T. R. Ellsworth, *J. Agric. Food Chem.* **43** (1995) 2295 (http://dx.doi.org/10.1021/jf00056a062)
18. R. Đurović-Pejčev, S. Radmanović, Z. P. Tomić, L. Kaluđerović, T. Đorđević, *Environ. Sci.: Processes Impacts* **25** (2023) 542 (https://doi.org/10.1039/D2EM00272H)
19. D. Pena, A. Lopez-Pineiro, A. Albarran, J. Sanchez-Lerena, L. Cox, J. Rato-Nunes, M. Rozas, S. Gaytan, *Int. J. Energy Environ.* **9** (2015) 237 (https://www.naun.org/main/NAUN/energyenvironment/2015/b542011-072.pdf)
20. D. Fernández, S. Gómez, Á. Albarrán, D. Peña, M. Á. Rozas, J. M. Rato-Nunes, A. López-Piñeiro, *Pest. Manage. Sci.* **76** (2020) 1795 (https://doi.org/10.1002/ps.5705)
21. M. Da Silva, M. De Queiroz, A. Neves, A. Da Silva, A. De Oliveira, R. De Oliveira, M. Azevedo, *An. Acad. Bras. Ciênc.* **90** (2018) 3745 (http://dx.doi.org/10.1590/0001-3765201820180135)
22. M. Da Silva, M. De Queiroz, A. Neves, A. Da Silva, A. De Oliveira, R. De Oliveira, M. Azevedoa, G. Pereira, *J. Braz. Chem. Soc.* **30** (2019) 2386 (https://doi.org/10.21577/0103-5053.20190149)
23. B. Gámiz, P. Velarde, K. Spokas, M. Hermosín, L. Cox, *J. Agric. Food Chem.* **65** (2017) 3109 (https://doi.org/10.1021/acs.jafc.7b00458)
24. IUSS Working Group WRB, *World Reference Base for Soil Resources. International soil classification system for naming soils and creating legends for soil maps*, 4th ed., International Union of Soil Sciences (IUSS), Vienna, 2022, https://www.isric.org/sites/default/files/WRB_fourth_edition_2022-12-18.pdf (accessed 25 June 2025)
25. IUSS Working Group WRB, *World reference base for soil resources 2014 – International soil classification system for naming soils and creating legends for soil maps, update 2015*, Rome, 2025, http://www.fao.org/3/i3794en/I3794en.pdf (accessed 4 June 2026)
26. A. Đorđević, S. Radmanović, *Pedology*, Faculty of agriculture, Belgrade, 2018 (ISBN: 978-86-7834-300-1) (in Serbian)
27. M. R. Carter, E. G. Gregorich, *Soil sampling and methods of analysis*, 2nd ed., CRC Press Taylor & Francis Group, Boca Raton, FL, 2008 (ISBN: 978-0-8493-3586-0)
28. Soil Survey Staff, *Field book for describing and sampling soils, version 4.0. USDA, Natural Resources Conservation Service*, U.S. Government Printing Office, Washington, DC, 2025, https://www.nrcs.usda.gov/sites/default/files/2025-05/Field-Book-for-Describing-and-Sampling-Soils-Ver4.pdf (accessed 5 June 2026)
29. L. Kaluđerović, R. Đurović-Pejčev, S. Radmanović, in *Proceedings of AGRORES 2024, 13th International Symposium of Agricultural Sciences*, 27-30 May 2024, Trebinje, Book of abstracts, 2024, p. 147
30. D. M. Moore, R. C. Jr. Reynolds, *X-Ray Diffraction and the Identification and Analysis of Clay Minerals*, 2nd ed., Oxford University Press, New York, 1997
31. OECD standard, *OECD guidelines for testing of chemicals, proposal for updating guideline 106 – Adsorption/desorption using a batch equilibrium method*, 1997
32. D. L. Sparks, *Environmental Soil Chemistry*, 1st ed., Academic Press, Inc., San Diego, CA, 1995 (ISBN: 0-12-656445-0)
33. M. Arienzo, A. Buondonno, *Toxicol. Environ. Chem.* **39** (1993) 193 (https://doi.org/10.1080/02772249309357917)
34. B. M. Jenks, F. W. Roeth, A. R. Martin, D. L. McCallister, *Weed Sci.* **46** (1998) 132 (https://doi.org/10.1017/S0043174500090299)

(CC) 2026 Serbian Chemical Society.

35. M. Bekbölet, O. Yenigün, I. Yücel, *Water Air Soil Poll.* **111** (1999) 75 (https://doi.org/10.1023/A:1005089612111)
36. B. K. G. Theng, *The Chemistry of Clay-Organic Reactions*, Adam Hilger, London, 1974 (ISBN: 0852742118)
37. M. M. Loux, R. A. Liebl, F. W. Slife, *Weed Sci.* **37** (1989) 440 (http://www.jstor.org/stable/4044736)
38. A. Di Marsico, L. Scrano, M. Amato, B. Gàmiz, M. Real, L. Cox, *Sci. Total Environ.* **625** (2018) 531 (https://doi.org/10.1016/j.scitotenv.2017.12.078).

(CC) 2026 Serbian Chemical Society.

Journal of the Serbian Chemical Society
JSCS-info@shd.org.rs • www.shd.org.rs/JSCS
J. Serb. Chem. Soc. 91 (10) S309–S310 (2026) *Supplementary material*

SUPPLEMENTARY MATERIAL TO

Adsorption–desorption behaviour of clomazone in Planosol and Vertisol agricultural soils

RADA D. ĐUROVIĆ-PEJČEV[1]*, LJILJANA R. ŠANTRIĆ[1], LAZAR M. KALUĐEROVIĆ[2] and SVJETLANA B. RADMANOVIĆ[2]

[1]*Institute of Pesticides and Environmental Protection, Banatska 31b, 11080 Belgrade, Serbia and* [2]*University of Belgrade, Faculty of Agriculture, Nemanjina 6, 11080 Belgrade, Serbia*

J. Serb. Chem. Soc. 91 (10) (2026) 1099–1111

Linear and multiple regression analyses between selected soil properties and the distribution coefficients ($K_{d(ads)}$ and $K_{OC(ads)}$) as well as the Freundlich parameters ($K_{f(ads)}$ and $1/n_{(ads)}$) were conducted (Tables S-I and S-II) based on data from this study and previously published source[9] using the Data Analysis Tool Pak in Microsoft Excel 2016. Comparative overview of the main sorption parameters obtained in this study and previously published data was presented in Table S-III.

TABLE S-I. Linear regression analysis between clomazone adsorption data and selected soil properties

	$K_{d\ (ads)}$	$K_{f\ (ads)}$	$1/n_{(ads)}$	$K_{OC\ (ads)}$
OC	0.860 (0.140)[a]	0.854 (0.146)	0.927 (0.073)	0.004 (0.996)
Clay	0.859 (0.141)	0.871 (0.129)	0.667 (0.333)	0.741 (0.259)
pH	0.467 (0.533)	0.473 (0.527)	0.291 (0.709)	0.997[b] (**0.003**)
Silt	0.676 (0.324)	0.663 (0.337)	0.709 (0.291)	0.777 (0.223)
Sand	0.880 (0.120)	0.882 (0.118)	0.771 (0.229)	0.852 (0.148)

[a] Values in parentheses are p values of the correlations; [b] Significance at the 0.05 level.

* Corresponding author. E-mail: rada.djurovic@pesting.org.rs
https://doi.org/10.2298/JSC260122050D

Available online at https://www.shd.org.rs/JSCS/

(CC) 2026 Serbian Chemical Society.

TABLE S-II. Multiple linear regression results for clomazone adsorption

Regression equation	r[a]	p[b]
$K_d = 2.2041 \times OC - 0.3860 \times pH + 2.6462$	0.997	0.070
$K_d = 1.3736 \times OC - 0.0417 \times sand + 2.7380$	0.997	0.080
$K_d = 0.6326 \times pH - 0.1105 \times sand + 2.9187$	0.995	0.095
$K_{f\,(ads)} = 1.6339 \times OC - 0.2920 \times pH + 2.6196$	0.995	0.099
$1/n_{(ads)} = 0.0619 \times OC + 0.0019 \times silt + 0.8840$	0.999	0.053
$K_{OC\,(ads)} = 4.3364 \times OC - 27.5998 \times pH + 402.6336$	0.998	0.067
$K_{OC\,(ads)} = -55.2564 \times OC - 2.9965 \times sand + 409.9218$	0.998	**0.049**[c]
$K_{OC\,(ads)} = 0.0066 \times clay - 27.5073 \times pH + 408.5849$	0.997	0.083
$K_{OC\,(ads)} = -25.1549 \times pH + 0.6342 \times silt + 371.8211$	1.000	**0.004**[c]
$K_{OC\,(ads)} = -25.5141 \times pH - 0.2265 \times sand + 402.9237$	0.998	0.066

[a] Multiple correlation coefficient; [b] Significance level; [c] Significance at the 0.05 level.

TABLE S-III. Comparative overview of the main sorption parameters obtained in this study and previously published data

$K_{d\,(ads)}$ / $dm^3\ kg^{-1}$	$K_{OC\,(ads)}$ / $dm^3\ kg^{-1}$	$K_{f\,(ads)}$ / $mg^{(n-1)/n}\ dm^{3/n}\ kg^{-1}$	$n_{(ads)}$	$K_{f\,(des)}$ / $mg^{(n-1)/n}\ dm^{3/n}\ kg^{-1}$	$n_{(des)}$	D / %	Data source
3.41-4.59	266.40-240.30	3.14-4.05	0.93-0.96	3.15-21.23	3.57-5.26	28.48-33.32	This study
2.30-11.0	129.00-887.00	5.06-9.20	0.83-0.89		0.05-0.24		Ref[10]
	354.00-767.00	6.10-11.25	1.25-1.49				Ref[14]
2.34-5.23	90.00-201.15	3.29	1.25				Ref[17]
		1.11	0.82				Ref[16]
		2.82-3.74	0.74-0.79			32.20-43.70	Ref[19]
0.47-5.30	60.00-573.00		1.02-1.10				Ref[37]
0.92-1.12	29.58-31.20						Ref[11]
2.14-3.83	186.09-198.45	2.21-3.43	0.93-1.00	2.34-18.95	3.70-5.26	29.12-35.58	Ref[9]
3.00-5.58	201.55-313.28						Ref[18]
1.27-1.69	14.51-17.89		0.84-0.95			37.60-50.00	Ref[12]
		1.33-18.44					Ref[8]
1.16-1.66	12.43-16.44		0.83-0.88			32.70-48.60	Ref[15]
1.24-1.85	8.21-18.14		0.77-0.95				Ref[20]
		1.49-2.97	2.47-3.69				Ref[13]
0.47	34.19	0.77	1.37				Ref[21]
0.41-6.40	75.09-462.43						Ref[38]
1.14	88.00	1.14	1.00	2.04	0.53		Ref[23]

(CC) 2026 Serbian Chemical Society.